

IMPROVE THE STABILITY OF ORGANIC-INORGANIC HYBRID
PEROVSKITE BY VAPOR-SOLID REACTION

by

XIAOZHOU YU

QING PENG, COMMITTEE CHAIR

YUPING BAO

ARUNAVA GUPTA

QIANG HUANG

FENG YAN

A DISSERTATION

Submitted in partial fulfillment of the requirements
for the degree of Doctor of Philosophy
in the Department of Chemical and Biological Engineering
in the Graduate School of
The University of Alabama

TUSCALOOSA, ALABAMA

2019

Copyright Xiaozhou Yu 2019

ALL RIGHTS RESERVED

ABSTRACT

Organic-inorganic hybrid perovskites, such as $\text{CH}_3\text{NH}_3\text{PbI}_3$ and $\text{NH}_2\text{CH}=\text{NH}_2\text{PbI}_3$, emerge as a new class of low-cost semiconductors that have the potential applications in high-efficiency photovoltaic cells, light emitting diodes, lasers, and sensors. However, hybrid perovskites can be easily degraded by H_2O , O_2 , and light in ambient conditions. To improve the stability of hybrid perovskites, we carried out a comprehensive study including the degradation kinetics and surface modification by vapor-solid reactions for encapsulation.

The degradation kinetics of perovskites were studied by using *in situ* methods. We found $\text{CH}_3\text{NH}_3\text{PbI}_3$ perovskite degrades slowly at 85°C . This result indicates hybrid perovskites alone is not stable in the working conditions. We enhanced the stability of perovskites by surface modification through studying the surface reaction mechanism on perovskites. We found that by increasing the partial pressure of vapor reactants such as pyridine, the vapor-perovskite reactions will change from surface terminated reaction to bulk transformation reactions.

A thin pin-hole free oxide barrier layer can not only block H_2O and O_2 from meeting perovskites but also encapsulate the gas byproducts from the degradation reactions to stop the reversible degradation reaction. Atomic layer deposition (ALD) is a promising method to deposit a pinhole-free metal oxide barrier film onto perovskites. Although there are numerous reports in applying ALD on hybrid perovskites, the nucleation mechanism of ALD on these perovskites are poorly understood. Herein, we will present our findings about the atomic level surface reaction mechanism during ALD on perovskite-related substrates. Collectively, we are able to create a couple of new pathways to improve the stability of perovskite materials.

LIST OF ABBREVIATIONS AND SYMBOLS

ALD	Atomic layer deposition
FTIR	Fourier transform infrared spectroscopy
SEM	Scanning electron microscopy
QCM	Quartz crystal microbalance
QMS	Quadrupole mass analyzer
XRD	X-ray powder diffraction
XPS	X-ray photoelectron spectroscopy
DRIFTS	Diffuse reflectance infrared fourier transform spectroscopy
UV-vis	ultraviolet–visible spectrophotometry
TMA	Tri-methyl aluminum
DEZ	Diethylzinc
MAPbI ₃	Methylammonium lead iodide
FAPbI ₃	Formamidinium lead iodide
Py	Pyridine
PCBM	Phenyl-C61-butyric acid methyl ester
MAI	Methylammonium iodide

ACKNOWLEDGMENTS

First and foremost, I would like to express my gratitude to my advisor Dr. Qing Peng for his invaluable guidance and providing great opportunities for me to finish my Ph.D. studies. He is always paying great attention to my dissertation project and in all my experiments. His altitude in science, research, and life supply me valuable inspiration and guide me to improve myself.

Secondly, I would like to thank my colleague Haoming who supply me selfless help in my experiment and test. I would like to thank Johnny Goodwin, Rob Holler, and Dr. Qin Yin. They give me very patient instruction in the instrument using and valuable advice to further improve the test result.

Finally, I would thank my wife Siyuan Zhang and my parents who support me to go through the whole Ph.D. process. Thanks for their care and time in my life. Without them, no matter what I achieve is meaningless. Hope them happy and enjoy life.

CONTENTS

ABSTRACT.....	ii
LIST OF ABBREVIATIONS AND SYMBOLS	iii
ACKNOWLEDGMENTS	iv
LIST OF FIGURES	viii
CHAPTER 1: INTRODUCTION	1
1.1 Brief history of solar cell.....	2
1.2 Perovskite solar cells.....	2
1.2.1 Perovskite crystal structure.....	3
1.2.2 Perovskite synthesis methods	6
1.3 The stability challenges of perovskite materials	6
1.3.1 Heat degradation.....	7
1.3.2 Humidity degradation	8
1.3.3 UV degradation.....	9
1.3.4 O ₂ degradation	10
1.4 The current methods for addressing the poor stability and their limitations.....	10
1.4.1 Substitution of the A Cation and X Anion	10
1.4.2 2D perovskite.....	12
1.4.3 Polymer or carbon encapsulation	13
1.5.1 Surface passivation of perovskite	16
1.5.2 Surface coating of perovskite by atomic layer deposition (ALD).....	17
1.6 Overview of the dissertation	20

CHAPTER 2: EXPERIMENTAL METHODS AND RESEARCH METHODS	22
2.1 Materials.....	22
2.2 Base substrate cleaning	22
2.3 Hybrid perovskite film fabrication.....	23
2.3.1 CH ₃ NH ₃ PbI ₃ (MAPbI ₃) film synthesized by solvent engineering method.....	23
2.3.2 MAPbI ₃ powder synthesized by drop-casting method.....	23
2.3.3 Formamidinium Lead Iodide (FAPbI ₃) HC(NH ₂) ₂ PbI ₃ film fabrication.....	23
2.4 Characterization methods.....	24
2.4.1 In situ Diffuse reflectance infrared Fourier transform spectroscopy (DRIFTS)	24
2.4.2 X-ray diffraction (XRD).....	25
2.4.3 Ultraviolet–visible spectroscopy (UV–Vis)	25
2.4.4 Scanning electron microscope (SEM)	25
2.4.5 In situ QCM Measurement.	25
2.4.6 In-situ QMS	26
2.4.7 In-situ FTIR	26
2.4.8 XPS.....	26
CHAPTER 3: PROBE DECOMPOSITION OF METHYLAMMONIUM LEAD IODIDE PEROVSKITE IN N ₂ AND O ₂ BY IN SITU INFRARED SPECTROSCOPY	28
3.1 Introduction	28
3.2 Experimental results:.....	30
3.3 Conclusion.....	39
Support information	41
CHAPTER 4 : INSPECT THE SURFACE PROPERTY OF MAPBI ₃ BY PROBE MOLECULAR OF PYRIDINE.....	47
4.1 Introduction.	47

4.2 Results and discussions.....	49
4.3 Discussion.....	67
4.4 Conclusion.....	71
Support information:.....	72
CHAPTER 5: IMPROVE THE STABILITY OF METHYLAMINE LEAD PEROVSKITE BY ATOMIC LAYER DEPOSITION OF AL₂O₃ AT 25°C.....	77
5.1 Introduction.....	77
5.2 Result and discussion.....	79
5.3 Discussion.....	91
5.4 Conclusions.....	95
Supporting information:.....	96
CHAPTER 6: IMPROVE THE STABILITY OF HYBRID HALIDE PEROVSKITE VIA ATOMIC LAYER DEPOSITION ON ACTIVATED PHENYL-C61 BUTYRIC ACID METHYL ESTER.....	99
6.1 Introduction.....	99
6.2 Results and discussion.....	100
6.3 Conclusion.....	111
Support information:.....	112
CHAPTER 7: SUMMARY AND FUTURE DIRECTION.....	116
7.1 Summary:.....	116
7.2 Future direction:.....	118
7.2.1 ALD Al ₂ O ₃ on formamidinium lead iodide (FAPbI ₃).....	118
7.2.2 ALD on MAPbI ₃ quantum dots (QDs).....	119
REFERENCES.....	121
APPENDIX: LIST OF PUBLISHED, SUBMITTED, AND UNDER-PREPARATION PAPERS.....	139

LIST OF FIGURES

Figure 1.1 Evolution of the best-reported lab-cell ($\leq 0.1 \text{ cm}^2$) efficiencies with time.....	3
Figure 1.2 Perovskite cubic crystal structure of ABX_3 . ¹⁴ For $\text{CH}_3\text{NH}_3\text{PbI}_3$ perovskite, A is CH_3NH_3^+ , B is Pb^{2+} and X is I.	4
Figure 1.3 The preparation of MAPbX_3 films by gas and solution deposition methods:(a) dual source co-evaporation using PbCl_2 and MAI sources; (b) vapor-assisted solution process using MAI organic vapors to react with pre-deposited PbI_2 films;(c) one-step and two-step sequential solution spin-coating method; (d) dipping the PbI_2 film into MAI solution. Reproduced with permission from reference ¹⁷	6
Figure 1.4 The decomposition routes of perovskite materials under different environmental factors including: heat, humidity, oxygen and light. ¹²	7
Figure 1.5 a) Possible decomposition pathway of hybrid halide perovskites in the presence of water. ²⁹ b) Water degrades MAPbI_3 by forming monohydrate phase ($\text{CH}_3\text{NH}_3\text{PbI}_3 \cdot \text{H}_2\text{O}$) and dihydrate ($(\text{CH}_3\text{NH}_3)_4\text{PbI}_6 \cdot 2\text{H}_2\text{O}$). Reproduced with permission from reference ³⁰ . c) UV-vis spectra of $\text{CH}_3\text{NH}_3\text{PbI}_3$ exposed in 98% humidity environment. Reproduced with permission from reference ³³	9
Figure 1.6 a) The efficiency development of mixed perovskite with specified chemical compositions ⁴³ . b) Stability improvement of FAPbI_3 with Cs^+ cation doping. Reproduced with permission from reference ⁴³	11
Figure 1.7 a) Unit crystal structure of quasi-2D perovskite with different PbI_6^{4-} layer amounts values, showing the evolution of dimensionality from 2D ($n = 1$) to 3D ($n = \infty$), b) power conversion efficiency of devices based on MAPbI_3 and quasi-2D perovskites before and after 1440 h storage. Reproduced with permission from reference ⁴⁸	13
Figure 1.8 a) Photographs of perovskite films after water-spraying for 60 s. With PEG modification, the color can convert back to black in ambient air in 45s. Reproduced with permission from reference ⁵⁴ . b) Photo illustrating the visible degradation of the perovskite layer. The color shifts from almost black to yellow for all organic HTLs except for the films covered with PMMA only or a composite of carbon nanotubes and PMMA. Reproduced with permission from reference ⁵¹ . c) Triple-layer architecture of perovskite device with a thick carbon electrode. Reproduced with permission from reference ⁵⁵	14
Figure 1.9. a) Typical Al_2O_3 ALD reaction mechanism. ⁷⁵ b) Improve the stability of perovskite solar cell by the encapsulation of ALD metal oxide.....	19
Figure 2.1 The image of in-situ DRIFTS system.....	24
Figure 2.2 Homemade ALD system with the capability of in-situ QMS.	27

Figure 2.3 ALD system with in-situ FTIR instrument.....27

Figure 3.1. IR spectra of MAPbI₃ samples diluted with KBr powder to weight percentages of 1:1600 to 1:50. All the spectra were obtained at 25 °C. The inset shows the variation of the intensity of the N–H stretch (3179 cm⁻¹) from MAPbI₃/KBr with the weight percentage of MAPbI₃. All the spectra are referenced to that of a pure KBr powder sample at 25 °C..... 31

Figure 3.2. IR spectra of MAPbI₃/KBr samples at 95 °C in N₂ for 2 min and 18 h. All the spectra are referenced to the spectrum of a pure KBr sample at 25 °C. 32

Figure 3.3. Time-evolved differential IR spectra of MAPbI₃/KBr samples at 95 °C. The spectrum labeled 10min ref 2min was obtained at 10 min with the spectrum at 2 min as the reference. The labels of the other spectra follow the same principle..... 33

Figure 3.4. Normalized intensity of the N–H peak (~3179 cm⁻¹) vs reaction time in N₂ at 75 °C (black ■), 85 °C (red ●), 95 °C (blue ▲), 100 °C (green ▼), 120 °C (magenta ◻), and 150 °C (brown ◆). Solid lines are guides for the eyes. We extracted the reaction rates α t d d from the slopes of the initial linear portions of these data sets (e.g., the dashed line for the data from 120 °C). 34

Figure 3.5. Plots of ln (da/dt) vs 1/T for degradation in N₂ and O₂ with a laser (633 nm). The laser with O₂ greatly increases the decomposition rate. Lines are linear fits to the data points. We use the symbol -r_P to represent da/dt. 38

Figure 4.1. Optical images of a CH₃NH₃PbI₃/FTO sample (a) before pyridine exposure; (b, c) after 10 s and 1 min of exposure to autogenic pyridine vapor (~20 torr at 25 °C) in a glovebox; (d–f) 1, 5, and 30 min in N₂ (glovebox) after removal of the pyridine vapor..... 50

Figure 4.2. Time-evolved IR spectra of a CH₃NH₃PbI₃/Si after P_20 torr treatment. The spectra were recorded at 3 min, 30 min, 1, 6, and 12 h in a dry-air purged IR chamber. IR spectrum of a clean CH₃NH₃PbI₃/Si is added for the comparison. All spectra use Si as the reference. Blue dash lines are peaks from Py⁺H. Red dash lines are peaks from Py-H. Green dash line is the ring-vibration mode from Py-Pb²⁺. Brown dash lines are H-deformation from all pyridine species. Black dash lines are peaks from CH₃NH₃PbI₃. * represents the ring vibration modes of Py⁺H..... 51

Figure 4.3. Differential IR spectra of CH₃NH₃PbI₃/Si (after P_20 torr treatment) at 18, 21, 24, 27, and 30 min in dry air with the spectrum at 15 min in dry air as the reference. A negative peak means the related species is removed during the period in dry air. A positive peak means the related species are generated. Blue dash lines are peaks from Py⁺H. The black dash lines are peaks from CH₃NH₃⁺. The broad negative peak centered around 3100 cm⁻¹ is due to the removal of CH₃NH₃⁺..... 53

Figure 4.4. SEM images of a pure CH₃NH₃PbI₃/Si sample (a) and CH₃NH₃PbI₃/Si after P_20 torr treatment and sitting in N₂ for 30 min (b). The SEM images show that P_20 torr treatment changes the surface morphology of CH₃NH₃PbI₃. 55

Figure 4.5. XRD patterns of CH₃NH₃PbI₃ (red, ●, red dash-dot lines) and CH₃NH₃PbI₃/Si after P_20 torr treatment and sitting in N₂ for 30 min (black, *, black dashlines) after. The XRD patterns

of CH₃NH₃I (green, ▼, green dashlines) and PbI₂ (blue, ■, blue dash-dot lines) are shown for comparison.....56

Figure 4.6. (a) The mass gain occurred on a CH₃NH₃PbI₃ film measured by QCM in exposure to 16 pulses of pyridine vapor (1 s each). The blue trace is the reactor’s pressure, with the spike from pyridine pulses, and the black trace is the mass gain from the in situ QCM. (b) XRD pattern of CH₃NH₃PbI₃/Si after 16 pyridine pulses. (blue, ■) and (red, ●) are peaks from PbI₂ and CH₃NH₃PbI₃. (c, d) SEM images show that surface morphology of CH₃NH₃PbI₃/Si sample is similar before (c) and after (d) the pyridine pulses.....58

Figure 4.7. IR spectrum of CH₃NH₃PbI₃ after 16 pulses of pyridine vapor. It shows that Py⁺H is formed and CH₃NH₃⁺ is removed.....59

Figure 4.8. (a) Mass gain (black line) vs time for a CH₃NH₃PbI₃ film before, during and after exposure to pyridine vapor at partial pressures of 0.5 torr (blue).....62

Figure 4.9. (a) Overall view of the time-evolved mass gain (black trace) occurred onto a CH₃NH₃PbI₃ film during the exposure of pyridine vapor of 1.38 torr in a vacuum reactor. It is termed P_1.3 torr treatment. The measured mass gain suddenly jumps to 74 × 10³ μg/cm². It is an artifact due to the short of the back and front electrodes of QCM crystal by the reaction product. (b) The enlarged view of dash line window in (a). The mass gain behavior changes with reaction time and is categorized into three Zones (1–3) as shown by shadowed areas. (c) The enlarged view of transient mass gain behavior in Zone 1. Zone 1 consists of two Stages (1–2). (d) The transient mass gain behavior during the evacuation of the pyridine vapor. The mass gain stabilizes at ~20 μg/cm² and is from the absorbed pyridine molecules. (a–d) The mass gain is the black trace, and the pressure is the blue trace.....63

Figure 4.10. (a) IR spectrum of CH₃NH₃PbI₃/Si after the exposure to 1.3 torr pyridine vapor as shown in **Figure 9**. (b) XRD spectra of CH₃NH₃PbI₃/Si sample in (a). Inset **Figure** is the optical image CH₃NH₃PbI₃/FTO after 1.3 pyridine treatment (Brown). (Black, *) and (Red, ●) are peaks from new unknown species and CH₃NH₃PbI₃. (c, d) SEM images of the CH₃NH₃PbI₃/Si in (a) at different magnifications. Red arrows point to the flakes, and white arrows points to the voids.....65

Figure 4.11. (a) QCM result from the stepwise increases of the partial pressure pyridine, 0.5, 0.8, 1.15, and 1.3 torr, then stepwise reduce the pressure of pyridine. Zone 2 region is shadowed. (b) Zoom-in view of the region enclosed by the dash-box in (a). The mass gain and duration at each pressure are labeled accordingly.....67

Figure 4.12. Schematic mechanism of the reaction between the pyridine vapor and CH₃NH₃PbI₃ when the vapor pressure of pyridine is 1.15 torr or lower (a) and 1.3 torr or higher (b). In (a), at low pressure, PbI₂ shell acts as a barrier to protect CH₃NH₃PbI₃ from pyridine. Liquid film and catalytic reaction are observed when pyridine vapor is 1.3 torr or higher.....69

Figure 5.1. *In situ* QCM measurement of the mass gain behavior (a) during 50 pulses of TMA onto CH₃NH₃PbI₃ and (b) during the first eight pulses of TMA vapor on CH₃NH₃PbI₃. The experiment is carried at 25 °C. Each TMA exposure step consists of 1s pulse of TMA vapor (partial pressure of ~0.1 torr) followed by 30s N₂ purge.....80

Figure 5.2. In situ QMS measurement of 50 pulses of TMA vapor on the CH ₃ NH ₃ PbI ₃ powder at 25 °C. The signal intensity of TMA (m/z = 57) and CH ₃ I (m/z = 142) is magnified by 200 times. .	81
Figure 5.3. XRD spectrum of a CH ₃ NH ₃ PbI ₃ film before (top) and after (bottom) 50 pulses of TMA vapor at 25°C.	82
Figure 5.4. Nucleation and growth behavior of ALD Al ₂ O ₃ on CH ₃ NH ₃ PbI ₃ at 25 °C. (a) The overview of mass gain during 50 ALD Al ₂ O ₃ cycles; (b) the detailed mass gain behavior during the initial 7 cycles.	83
Figure 5.5. (a) The mass change during TMA pulse on CH ₃ NH ₃ PbI ₃ at 75°C; (b) The mass change during the initial 6 pulses of TMA as shown by the dash box in (a).	84
Figure 5.6. The gas product of the reaction between CH ₃ NH ₃ PbI ₃ and TMA vapor at 75 °C by QMS.	85
Figure 5.7. XRD spectrum of CH ₃ NH ₃ PbI ₃ before (black) and after (red) TMA pulse treatment at 75°C. PbI ₂ can be detected after 50 pulses TMA.	86
Figure 5.8. Nucleation and growth of Al ₂ O ₃ ALD on CH ₃ NH ₃ PbI ₃ at 75°C measured by <i>in situ</i> QCM, (a) successive 50 cycles; (b) initial 5 cycles.	86
Figure 5.9. XPS spectrum of Pb _{4f} (a), I _{3d} (b), N _{1s} (c) and O _{1s} (d) in fresh CH ₃ NH ₃ PbI ₃ (black trace) and after treated by 50 pulses TMA vapor at 25°C (red trace) and 75°C (blue trace). For all spectra, the lower C _{1s} peak is set at 284.8 eV.	87
Figure 5.10. XPS spectrum of CH ₃ NH ₃ PbI ₃ before (a) and after treated by 50 pulses TMA vapor at 25°C (b) and 75°C (c).	87
Figure 5.11. Optical image of CH ₃ NH ₃ PbI ₃ and CH ₃ NH ₃ PbI ₃ after treated by 50 pulses TMA vapor treatment at 75°C and 25°C. The samples are sitting in the lab ambient environment.	89
Figure 5.12. SEM images of top views of CH ₃ NH ₃ PbI ₃ films grown on the silicon wafer, (a) before and (b) after 50 pulses of TMA vapor of 0.1 torr at 25°C, (c) before and (d) after TMA vapor of 0.1 torr at 75 ° C.	90
Figure 5.13. Mass change of CH ₃ NH ₃ PbI ₃ during the long exposure to TMA vapor of high partial pressure at 25°C. Black line is the mass gain and blue trace is the partial pressure of TMA.	91
Figure 6.1. (a) Mass change measured by QCM in 100 cycles ALD ZnO on CH ₃ NH ₃ PbI ₃ at 25°C (DEZ and water), (b) the initial 6 cycles of ALD ZnO on CH ₃ NH ₃ PbI ₃	101
Figure 6.2. Differential IR spectrum of CH ₃ NH ₃ PbI ₃ after 100 cycles of ALD ZnO at 25 °C. The fresh CH ₃ NH ₃ PbI ₃ is used as the reference. Negative peaks represent removed species.	102
Figure 6.3. Mass change on the CH ₃ NH ₃ PbI ₃ substrate by repeating pulses of DEZ vapor at 60 °C. The inset image (top left) is QCM crystal with a fresh CH ₃ NH ₃ PbI ₃ film. The same sample after 50 pulses of DEZ vapor is shown in the inset image (bottom right). Bottom red trace illustrates the DEZ pulses.	103

Figure 6.4. Mass change during ALD ZnO (DEZ/N₂/H₂O/N₂ =1:5:1:15s) on the CH₃NH₃PbI₃ substrate with PCBM coating (~65 nm) at 80 °C (black). The reference is the mass change of a similar sample in the vacuum at 80 °C without ZnO ALD (red). The bottom trace (blue) shows the transient pressure increase during the pulse of DEZ and H₂O..... 104

Figure 6.5. IR spectra of fresh CH₃NH₃PbI₃/PCBM before and after 200 cycles of ZnO ALD process at 80 °C. Dash-dot lines are peaks from CH₃NH₃PbI₃ and black dash line is the peak from PCBM. A clean Si substrate was used as the reference. 105

Figure 6.6. Mass change during ALD ZnO on PCBM at 100 °C. 107

Figure 6.7. Mass change on the surface of the CH₃NH₃PbI₃/PCBM substrate: (a) during 40 cycles of ALD Al₂O₃ and (b) following ALD ZnO cycles..... 107

Figure 6.8. (a) Mass change during the long exposure of TMA vapor on PCBM at 100 °C; (b) differential FTIR spectrum of PCBM after TMA vapor treatment with reference to the PCBM film, and (c) mechanism for the improved nucleation of ALD ZnO on PCBM by TMA..... 109

Figure 6.9. (a) IR spectra of (a) CH₃NH₃PbI₃ and (b) CH₃NH₃PbI₃/PCBM before (black) and after (red) 40 cycles of ALD Al₂O₃ and then 200 cycles of ALD ZnO at 100 °C. A clean Si substrate was used as the reference. 110

Figure 6.10. (a,b) Optical image of CH₃NH₃PbI₃ with and without the ALD treatment; (c,d) CH₃NH₃PbI₃/PCBM with and without the ALD treatment. These images were taken after the samples sit in ambience (20 °C and 40% RH) for 14 days. (e) Stability of CH₃NH₃PbI₃/PCBM with ALD treatment under the impact of a water droplet. ALD treatment: 40 cycles of ALD Al₂O₃ and 200 cycles of ALD ZnO..... 111

Figure 7.1. The proposed reaction mechanism of FA⁺ with TMA/water chemistry. 119

Figure 7.2. In situ QCM measurement of (a) the overall mass gain behavior during 30 pulses of TMA (1 s, partial pressure 0.1 torr, followed by 30s N₂ purge) onto FAPbI₃ at 75 °C..... 119

Figure 7.3 the PL performance of MAPbI₃ before and after ALD Al₂O₃..... 120

CHAPTER 1: INTRODUCTION

The energy crisis and global warming have become a growing interwind problem in civilization. Currently, 85% of global energy supply is from fossil fuels including natural gas, coal, and petroleum. Although the proved gas and oil reserves have increased by 70% and 40% respectively in the past two decades, fossil fuels are dwindling because of fast consumption and environmentally damaging mining technology. Meanwhile, the usage of fossil fuels dumps million tons of carbon dioxide into the atmosphere, resulting in the global climate change, such as extreme weather and the rising sea level. The situation becomes a significant threat to human society.

The development of renewable energy technologies is widely recognized as a crucial component in providing an integrated solution to limit greenhouse gas emissions and improve the sustainability of human society.¹⁻³ Renewable energy derives from a unlimited energy sources including solar, wind, biomass, geothermal, hydropower and tidal energy. One biggest challenge is to develop a renewable energy technology which is cheaper than fossil fuel in terms of per kWh. The utilization of solar energy is considered as the ultimate way to solve the problem of energy crisis. Sunlight is the most abundant clean energy and is sustainable for economic growth with a minimum detrimental impact on the environment. Significant efforts have been devoted to harvest solar energy through a sustainable and efficient way.

1.1 Brief history of solar cell

Since the photovoltaic (PV) effect was discovered by Alexander Edmond Becquerel,⁴ 3 generations of PV technologies have been developed. The first-generation silicon solar modules were available commercially in 1956. The cost was around \$300 for a one-watt solar module, which was far beyond an acceptable level for consumers. After more than 70 years` development, silicon solar cells can now produce electricity from sunlight at a comparable cost to that from fossil fuels. Although the high efficiency and stable energy output make the silicon solar cell the most successful commercialized PV technology, people are still trying to find cheaper alternatives with shorter payback period. Thin film based solar cells, for example, cadmium telluride (CdTe), copper indium gallium sulfide/selenide (CIGS/Se), and copper zinc tin sulfide/selenide (CZTS/Se) are second-generation solar cells. This generation of solar cells has high power conversion efficiencies and high stability. Moreover, they can be applied to flexible substrates. However, the price and toxic materials limit its further exploration. The third-generation solar cells including organic solar cells, quantum dots solar cells, and organic-inorganic hybrid solar cell are low-cost and solution processable. Among these emerging technologies, organic-inorganic hybrid lead halide perovskite-based solar cells show impressive high-power conversion efficiency. The solar-to-power conversion efficiency of $\text{CH}_3\text{NH}_3\text{PbI}_3$ -based perovskite solar cells has reach ~22.1%, which is close to the efficiency of state-of-the-art polycrystalline Si solar cells.⁵⁻⁸ The manufacturing of perovskites solar cell is much less energy-intensive than Si solar cells because the perovskites can be fabricated by solution methods, which are suitable for large-scale roll-to-roll production.^{9,10}

1.2 Perovskite solar cells

Since Miyasaka and co-workers first reported methylammonium lead iodide as the sensitizer in liquid-electrolyte-based Dye-sensitized solar cells in 2009, perovskite materials have attracted

increasing attention due to their low-cost fabrication and excellent photovoltaic (PV) performance. Progress in the efficiency of lab-scale perovskite solar cell device is summarized in **Figure 1.1**.¹⁰ In 2017, the efficiency of perovskite solar cells had climbed to 22.1%, and the energy payback period is less than 3 months. The advantage of perovskite material makes it very promising to be the next generation of the solar cell.

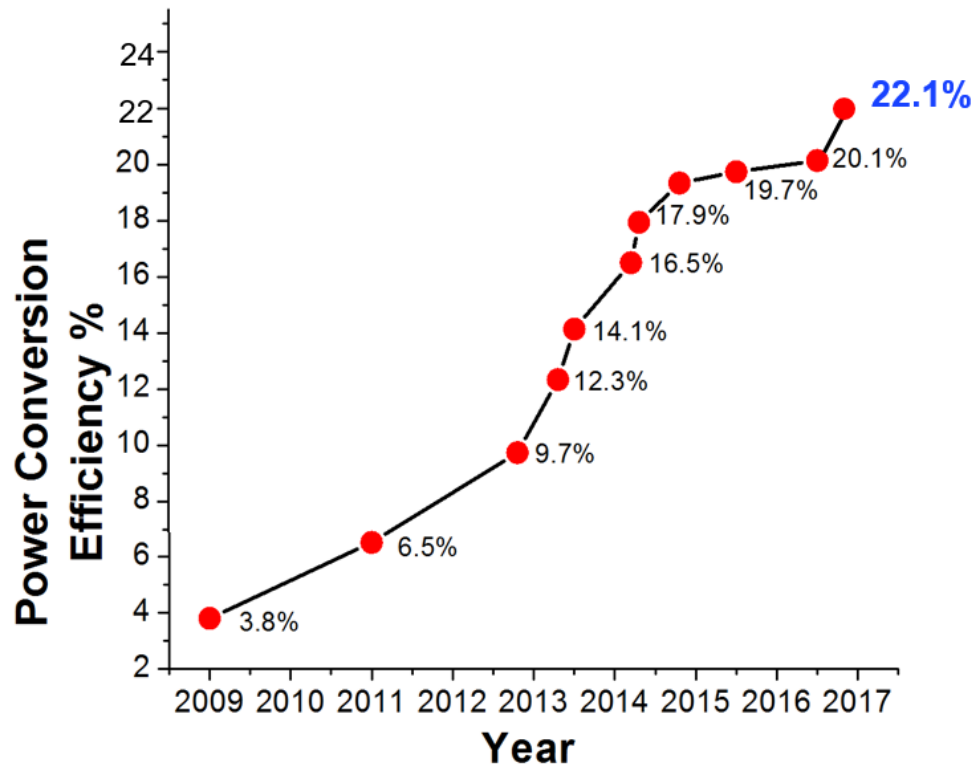


Figure 1.1 Evolution of the best-reported lab-cell ($\leq 0.1 \text{ cm}^2$) efficiencies with time.¹¹

1.2.1 Perovskite crystal structure

Perovskite is a family of material that shares a crystal structure of ABX_3 , A is the organic part such as CH_3NH_3^+ (MA), $\text{CH}(\text{NH}_2)_2^+$ (FA); B is the metal cation such as Pb^{2+} , Sn^{2+} , Ge^{2+} ; and X represents halides ion such as I, Br^- , Cl^- . In the early 1920s, Goldschmidt proposed a “tolerance factor” as follow¹²:

$$t = \frac{(r_A + r_x)}{\sqrt{2}(r_B + r_x)}$$

In the equation , r_A , r_B and r_X are the ionic radii for the ions in the A, B and X sites, the perovskite crystal lattice structure is shown in **Figure 1.2**. Up to now, almost all perovskites have the values in the range 0.75–1.00. Tolerance factor is an empirical formula and helps researchers to choose atoms with suitable radii for the perovskite structure. Each A, B, X component has different effects on the solar cell performance and crystal stability.

A is the organic amine cation, which balance the charge neutrality within the inorganic lattice. It also affects the lattice size of the inorganic lattice. In general, materials with a tolerance factor of 0.9-1.0 have an ideal cubic structure with better lattice stability. The tolerances are 0.84 and 0.88 respectively for MAPbI_3 and FAPbI_3 . Compared to MAPbI_3 , FAPbI_3 has lower band gap and better thermal stability. For instance, FAPbI_3 can stay stable in air at 150°C , but MAPbI_3 degrades rapidly at 100°C . The thermogravimetric analysis (TGA) result also pointed out that FAPbI_3 is stable up to 300°C in argon.¹³

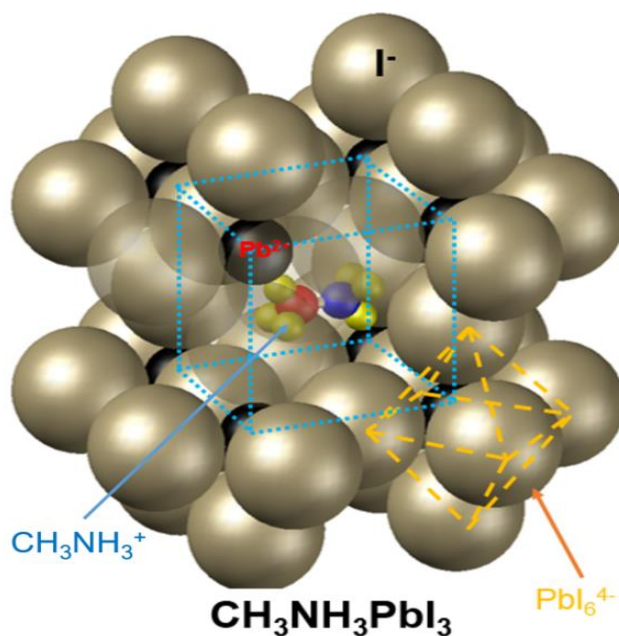


Figure 1.2 Perovskite cubic crystal structure of ABX_3 .¹⁴ For $\text{CH}_3\text{NH}_3\text{PbI}_3$ perovskite, A is CH_3NH_3^+ , B is Pb^{2+} and X is I.

B part is a metal cation including Pb^{2+} , Sn^{2+} , and Ge^{2+} . Compare to the Sn and Ge perovskite, MAPbI_3 perovskite obtain the best power conversion efficiency. However, MAPbI_3 perovskite is not stable in ambience. MAPbI_3 easily degrades into PbI_2 , which can dissolve in water and contaminate the earth. Thus, researchers worked on finding Pb-free perovskites. Sn and Ge were regarded as good candidates due to their similar electronic structures with Pb. However, the power conversion efficiencies for MASnI_3 and MAGeI_3 perovskite are less than 7% and both of them are very easy to be oxidized.¹⁵ Transition metals, such as Cu, Mn, Ge, Co, and Ni, are also very promising alternatives. For instance, $(\text{CH}_3\text{NH}_3)_2\text{CuCl}_4$, $(\text{CH}_3\text{NH}_3)_2\text{CuCl}_{0.5}\text{Br}_3$, and $(\text{RNH}_3)_2\text{FeX}_4$ also have perovskite structures. Although these materials have high open circuit voltage (V_{oc}), the low efficiency and oxidation resistance are significant drawbacks, which limiting their usage and demanding more work to solve these problems.¹⁵

X part is the halide ion (F^- , Cl^- , Br^- , I^-). B and X form BX_6^- Octahedral structure. The bond length of B-X not only decides the band gap of perovskite but also the stability of perovskite. Jun Hong Noh and co-workers synthesized $\text{CH}_3\text{NH}_3\text{Pb}(\text{I}_{1-x}\text{Br}_x)_3$ with a different mole ratio of I and Br.¹⁶ They found that as Br content increased, the sample would stay stable for longer time. When Br content is 20%, the efficiency would stay stable even after 20 days` exposure in 55% humidity environment at room temperature. The substitution of larger I atoms with smaller Br atoms in $\text{CH}_3\text{NH}_3\text{Pb}(\text{I}_{1-x}\text{Br}_x)_3$ leads to the reduction of the lattice constant and a transition to a cubic phase. Lattice structure change would have a significant effect on the stability of perovskite.

1.2.2 Perovskite synthesis methods

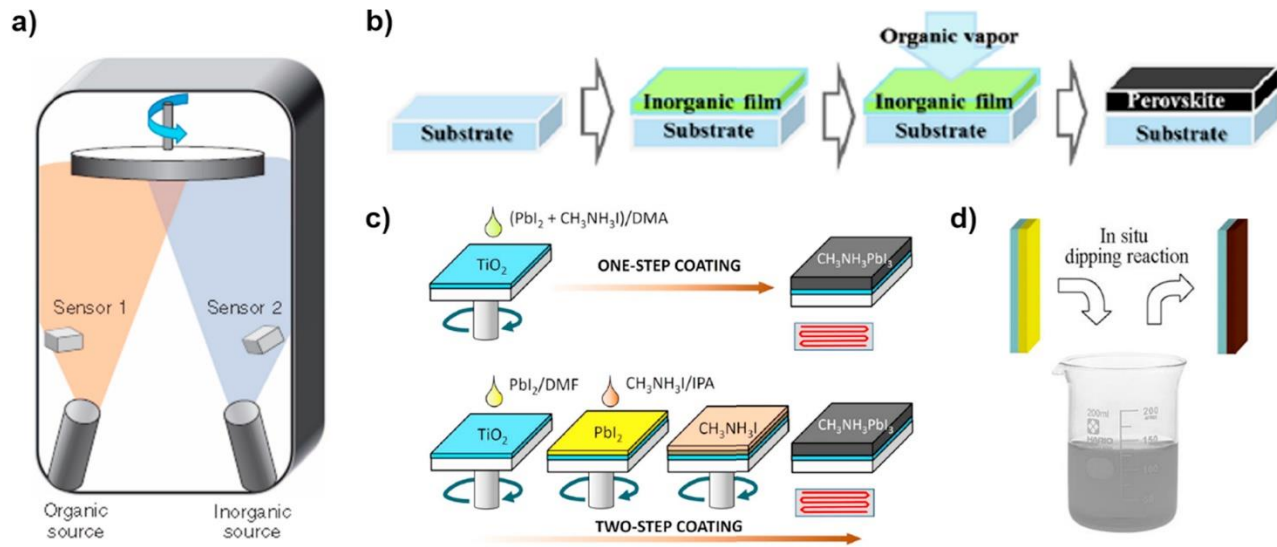


Figure 1.3 The preparation of MAPbX₃ films by gas and solution deposition methods: (a) dual source co-evaporation using PbCl₂ and MAI sources; (b) vapor-assisted solution process using MAI organic vapors to react with pre-deposited PbI₂ films; (c) one-step and two-step sequential solution spin-coating method; (d) dipping the PbI₂ film into MAI solution. **Reproduced with permission from reference**¹⁷.

Uniform and pinhole free perovskite absorber films are the key to achieve high power conversion efficiency and stability. Currently, there are two major methods in preparing perovskite films: vacuum deposition⁷ and solution processing.^{5,18} Although gas vacuum deposition has better thickness control and offers better film uniformity (shown in **Figure 1.3a, b**), the higher fabrication cost and difficulties in the large-scale manufacturing needs to be addressed. Compared to vacuum deposition, the cost of solution processing is much lower (shown in **Figure 1.3 c, d**). The solution processing includes the preparation of precursor solution, film coating, and annealing. The detail steps will show in Chapter 2.

1.3 The stability challenges of perovskite materials

As a promising photovoltaic technology, enormous progress in improving the PV performance has been achieved on hybrid perovskite in the last several years. However, the toxicity of Pb metal and the stability in the working condition become barriers for its commercialization.

The problem of heavy metal Pb pollution could be solved by encapsulation and recycling program, but people still did not find a solution to extend the lifetime of perovskite absorber to more than 25 years in the working condition. Because of the poor chemistry stability, hybrid perovskite is easily degraded to PbI_2 when exposed in the ambient environment and lose the light-absorb property in the visible light range. It's found that heat, humidity, UV light, and O_2 will degrade perovskite in a couple of days by various pathways shown in **Figure 1.4**.¹² Hybrid perovskite is easy to lose the organic group, for instance CH_3NH_3^+ , and then degrade to PbI_2 . More fundamental studies about the stabilization of perovskites in different environmental conditions are still in urgent need to realize its industrial commercialization.

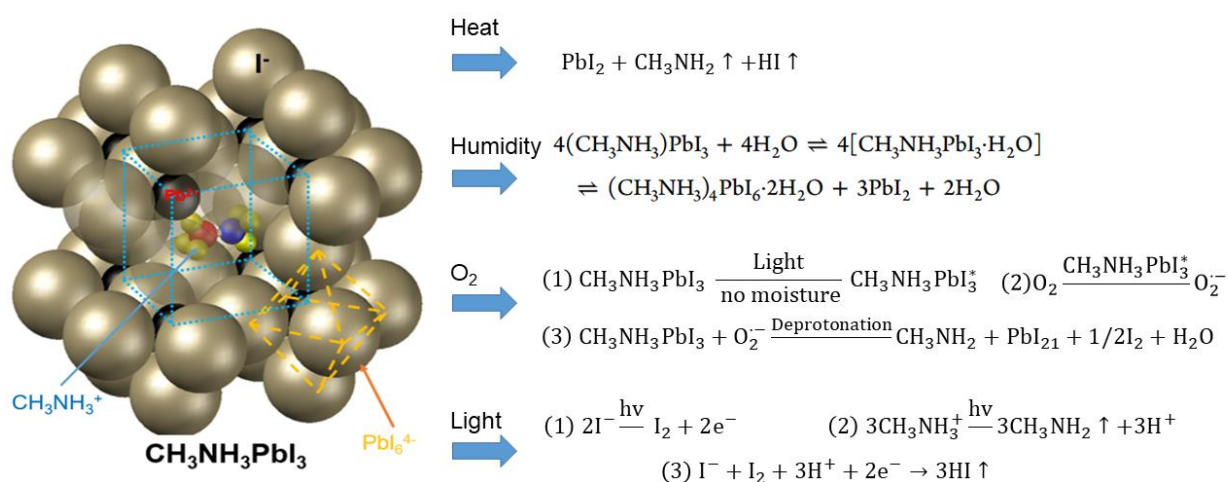


Figure 1.4 The decomposition routes of perovskite materials under different environmental factors including: heat, humidity, oxygen and light.¹²

1.3.1 Heat degradation

The synthesis of perovskites involves an annealing process in all the developed methods.¹⁹⁻
²⁴ Based on the test standard of the International Electrotechnical Commission (IEC) 61646 “Thin-film terrestrial photovoltaic (PV) modules design qualification and type approval”, perovskite material should survive under the temperature cycling of -40 and 85°C.²⁵ Whether perovskite

material can keep stable at high temperatures, such as 85°C, is under debated. Michael Gratzel *et al.* reported MAPbI₃ can be stable up to 300 °C based on the TGA data.²⁶ But during the synthesis process, if the annealing temperatures are above 120 °C, perovskite can thermally degrade to PbI₂, CH₃NH₂ and HI gas.²¹ The process is shown below:



Qi Yabing *et al.* showed that the CH₃NH₃PbI₃ decomposed into methyl-iodide (CH₃I) and ammonia (NH₃) by heat.²⁷ Boyen *et al.* demonstrated that significant decomposition of perovskite already occurs during annealing at 85 °C even in inert atmosphere.²⁸ Thus, CH₃NH₃PbI₃ perovskite suffers from the thermal degradation in the working condition of solar cells. We also studied the thermal degradation kinetics in different packaging gas and the result will be discussed in detail in Chapter 3.

1.3.2 Humidity degradation

During the fabrication and cell operation procedures, perovskite materials are inevitably exposed to the moisture in the air. Humidity affects the perovskite solar cells in both positive and negative ways. Moisture can accelerate the crystallization speed of perovskite, which facilitates to form dense and uniform film morphology. Therefore, fabricating perovskite solar cells in the ambient environment will help to achieve better power conversion efficiency. However, humidity also causes the degradation of perovskite, which become one of the biggest barriers to push perovskite material to the market. Frost and co-workers proposed an acid-base reaction between water and MAPbI₃ shown in **Figure 1.5a**.²⁹ Water will react with MAPbI₃, degrade perovskite into HI, CH₃NH₂ gas and PbI₂. A different degradation mechanism was proposed by Barnes *et al.* where water will form a hydrate with perovskite reversibly.³⁰ The hydrate will convert the crystal structure of perovskite from 3D to 1D, and 0D (Shown in **Figure 1.5b**). After forming perovskite dihydrate, the extra water will degrade MAPbI₃ to PbI₂. In the low humidity (<13%) environment,

perovskite material can stay stable for a long time and no hydrate structure could be detected by FTIR.³¹ However, in relatively high humidity (>13%), the formation of monohydrate has been proved by FTIR and QCM.³² The water induced degradation rate dramatically increased with the increase of humidity. MAPbI₃ will totally lose light absorbance after one-day storage in the 98% humidity environment. (Shown in **Figure 1.5c**).

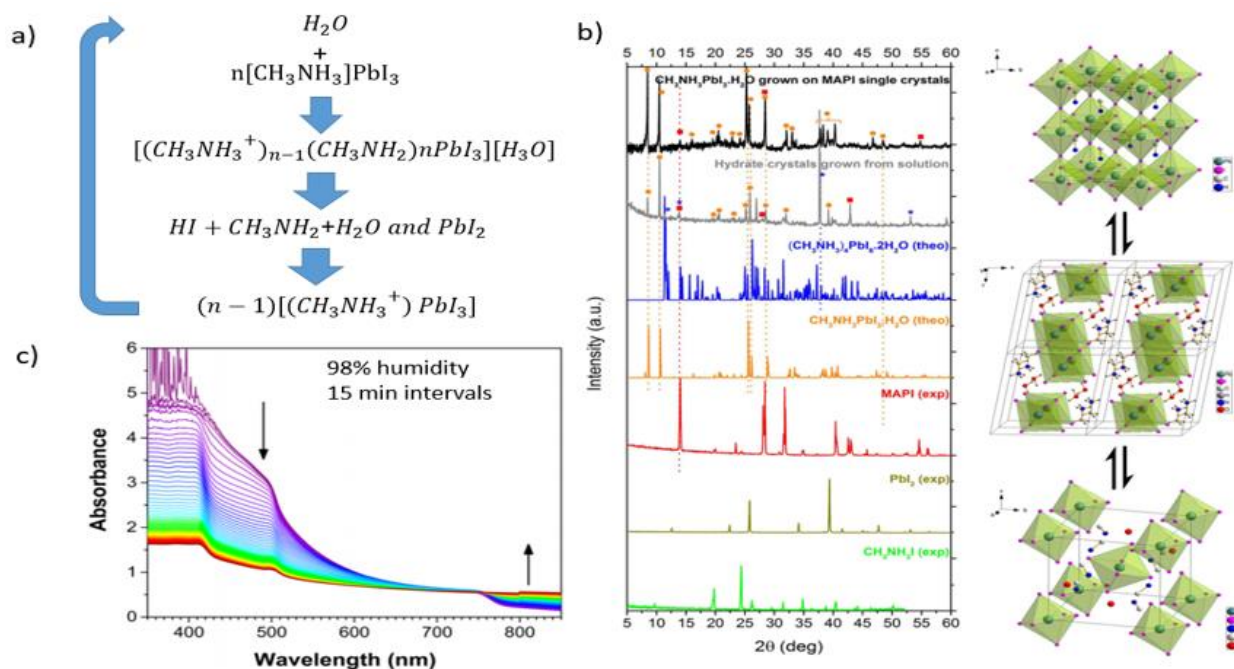


Figure 1.5 a) Possible decomposition pathway of hybrid halide perovskites in the presence of water.²⁹ b) Water degrades MAPbI₃ by forming monohydrate phase ($\text{CH}_3\text{NH}_3\text{PbI}_3 \cdot \text{H}_2\text{O}$) and dihydrate ($(\text{CH}_3\text{NH}_3)_4\text{PbI}_6 \cdot 2\text{H}_2\text{O}$). **Reproduced with permission from reference**³⁰. c) Uv-vis spectra of $\text{CH}_3\text{NH}_3\text{PbI}_3$ exposed in 98% humidity environment. **Reproduced with permission from reference**³³.

1.3.3 UV degradation

It was found that UV light will accelerate the decomposition of MAPbI₃. The stability of perovskite solar cell under UV radiation was firstly studied by H. J. Snaith's group.³⁴ They claimed that UV light will cause the desorption of surface-adsorbed oxygen from TiO₂ layer and following oxidation reaction of I. Jiangning Ding group proved that UV irradiation could accelerate the degradation rate of perovskite in the humidity environment.³⁵

1.3.4 O₂ degradation

When the light shines on the perovskite material, electrons would be excited and separated with holes. O₂ molecular would grab the excited electron and forms superoxide (O₂⁻) on the surface of perovskite. The degradation is initiated by the reaction of superoxide (O₂⁻) with the methylammonium cations. The O₂ degradation mechanism is shown in **Figure 1.4**. The synergistic effects of water with O₂ and UV-vis light with O₂ dramatically accelerate the degradation rate of the perovskite.^{36,37} For instance, when exposed to both light and dry air, unencapsulated MAPbI₃ solar cells rapidly degrade within minutes.³⁸

1.4 The current methods for addressing the poor stability and their limitations

Although the degradation mechanisms of perovskite by the environmental factors are still under debated, various strategies have been proposed to improve stability.

1.4.1 Substitution of the A Cation and X Anion

It is hypothesized that substitution of the A cation and X anion will offer a more-stable cubic phase of perovskite. Base on the tolerance factor, A cation such as CH(NH₂)₂⁺ (FA⁺), Cs⁺ and X anion such as Cl⁻, Br⁻ and SCN⁻ can also fit to the perovskite crystal.

FA⁺ and PbI₆⁴⁻ can also form a 3D perovskite with a lower band gap of about 1.47 eV.¹² Compared to the MA⁺, FA⁺ enhanced hydrogen bonding to the inorganic matrix and thus alters the covalent/ ionic character of Pb-I bonds, which enhances the thermal stability of perovskite. Park *et al.* demonstrated FAPbI₃ perovskite has good thermal stability at a temperature of 150°C.^{13,39} Because of the appropriate ionic radius of Cs⁺ for the perovskite 3D structure, inorganic perovskite CsPbI₃ has also been intensively investigated. Snaith *et al.* first demonstrated that cubic CsPbI₃ perovskite can be formed over 310°C and it is very stable at room temperature for 200 days.⁴⁰ However, both FAPbI₃ and CsPbI₃ suffer a fast crystal phase change. In the ambient environment,

α -FAPbI₃ phase will convert to β -FAPbI₃ phase in a couple of days and lose all the PV performance.⁴¹

For the substitution of X anion, compared to MAPbI₃, MAPbBr₃ and MAPbCl₃ obtain better stability in the ambient environment. S. I. Seok group found that using bromide to dope MAPbI₃ can significantly improve the stability of the perovskite in humid atmosphere.¹⁶ Although the bandgap of MAPb(I_{1-x}Br_x)₃ was increased from 1.58 eV to 2.28 eV with x from 0 to 1, the humidity resistance was dramatically improved with Br doping amount increase. As SCN⁻ has a similar size of I, SCN⁻ is perfectly fit into the perovskite structure. Tao Xu groups reported that compared to MAPbI₃ perovskite, CH₃NH₃Pb (SCN)₂I has the similar band gap but better moisture tolerance.⁴²

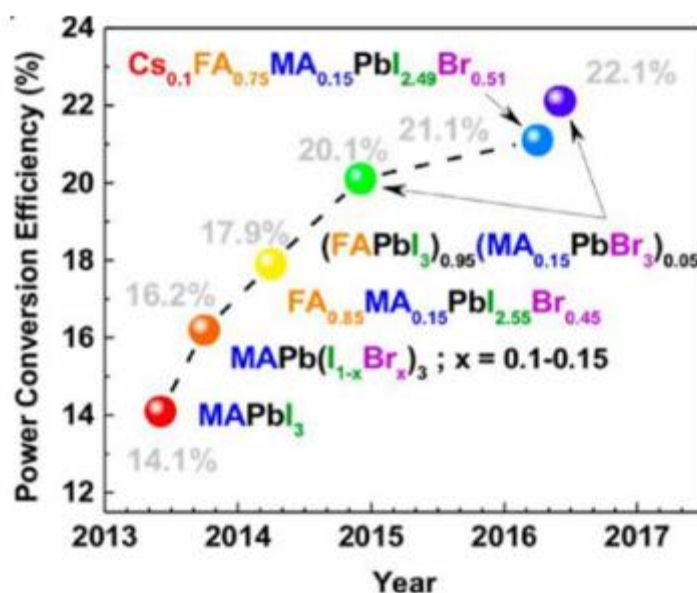


Figure 1.6 a) The efficiency development of mixed perovskite with specified chemical compositions⁴³. b) Stability improvement of FAPbI₃ with Cs⁺ cation doping. **Reproduced with permission from reference⁴³.**

Based on the study of the functions of A and X ion, tones of perovskite with mixed cations and halide anions was explored (shown in **Figure 1.6**).^{43,44} For instance, Cs_{0.1}FA_{0.75}MA_{0.15}PbI_{2.49}Br_{0.51} perovskite have been proved to not only obtain a very high power conversion efficiency (21.1%), but also maintain the stable performance in ambience for 3 months.

The efficiency and phase stability improved with the precise control to the ratio of each ion. However, the dope of A and X ion would increase the cost of material and make the preparation of precursor solution more complex. Therefore, although the substitution of A and X ion could improve the stability of perovskite, the lifetime of perovskite material without encapsulation needs to be further extended.

1.4.2 2D perovskite

The 3D perovskite would convert to a 2D layered structure when replacing the surface MA⁺ with the larger organic primary ammonium cation. Sargent *et al.* reported a reduced-dimensionality (quasi-2D) perovskite films with improved stability while retaining the high performance by mixing phenylethyl ammonium iodide (PEAI).⁴⁵⁻⁴⁷ They found that, with the molar ratio of PEA/MAI increasing, the crystal size of perovskite decreases but the humidity tolerance dramatically improved due to the surface coverage of large organic amine group. The stability and PV performance has the opposite trend when mixing PEA into the precursor. The improvement of stability should not scarify the PV performance.

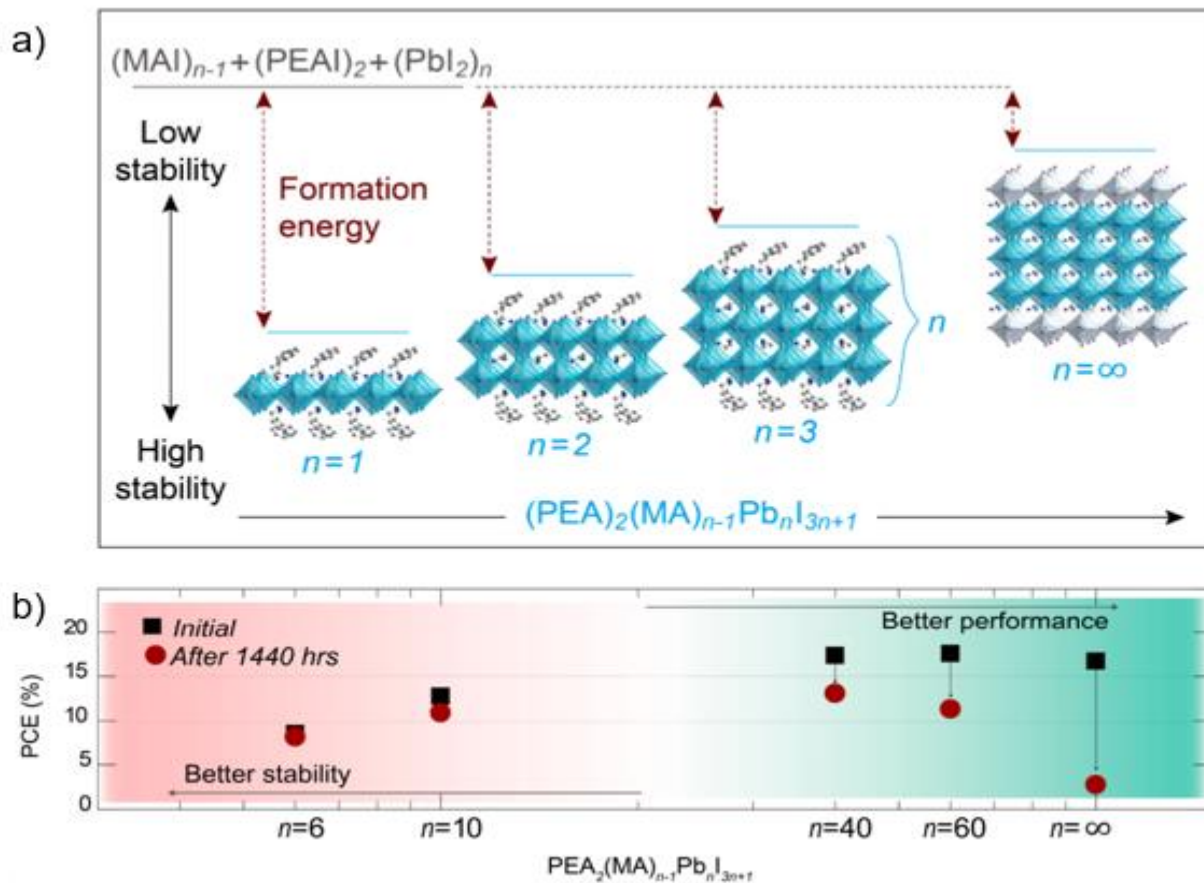


Figure 1.7 a) Unit crystal structure of quasi-2D perovskite with different PbI_6^{4-} layer amounts values, showing the evolution of dimensionality from 2D ($n = 1$) to 3D ($n = \infty$), **b)** power conversion efficiency of devices based on MAPbI_3 and quasi-2D perovskites before and after 1440 h storage. **Reproduced with permission from reference⁴⁸.**

1.4.3 Polymer or carbon encapsulation

The encapsulation of perovskite with polymer or carbon is an efficient method to block the contact between perovskite material with the environmental factors. Because of the hydrophobic property of polymer and carbon, the humidity resistance of perovskite is dramatically improved after polymer and carbon encapsulation.

Polymers, such as poly-(vinylpyrrolidone) (PVP)^{49,50}, Poly(methyl methacrylate) (PMMA)⁵¹, Polyvinylidene fluoride (PVDF)⁵², Polystyrene (PS)⁵³, polyethylene glycol (PEG)^{53,54} were used to work as a function layer or an additive to enhance the stability of perovskite material. Qing Zhao group reported that MAPbI_3 perovskite obtained strong humidity resistant and self-

healing capability upon the addition of PEG into the precursor solution (shown in **Figure 1.8a**).⁵⁴ Snaith *et al.* reported that, after coating the mixture of PMMA and carbon nanotube on the surface of perovskite, the film remained black over 96h.⁵¹ Without PMMA encapsulation, the perovskite films cover by other carrier transport layer degrade to yellow PbI_2 (shown in **Figure 1.8b**).

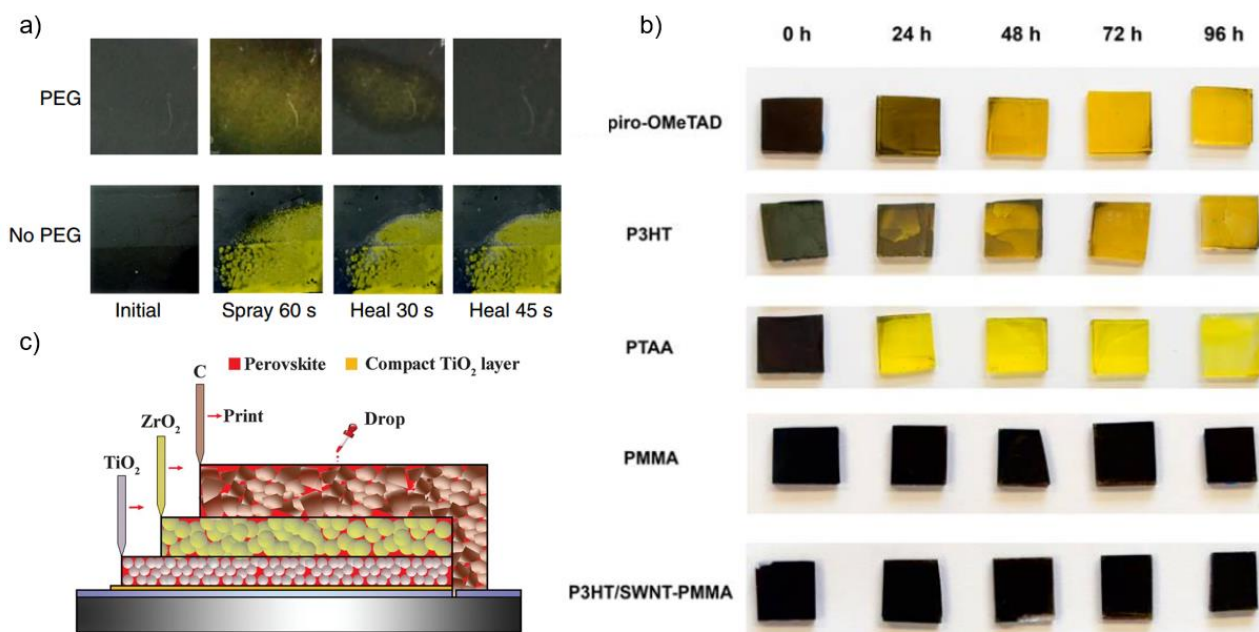


Figure 1.8 a) Photographs of perovskite films after water-spraying for 60 s. With PEG modification, the color can convert back to black in ambient air in 45s. **Reproduced with permission from reference**⁵⁴. b) Photo illustrating the visible degradation of the perovskite layer. The color shifts from almost black to yellow for all organic HTLs except for the films covered with PMMA only or a composite of carbon nanotubes and PMMA. **Reproduced with permission from reference**⁵¹. c) Triple-layer architecture of perovskite device with a thick carbon electrode. **Reproduced with permission from reference**⁵⁵.

Carbon materials including PCBM, carbon nanotube, graphene, and amorphous carbon were widely used to fabricate the electron transport layer or electrode in the solar cell. As the inherent passivation ability of reduced graphene oxide (RGO) against oxygen and moisture, the RGO layer cover on the surface of MAPbI_3 significantly reduced the decomposition rate.⁵⁶ Hongwei Han group reported a triple layer architecture($\text{TiO}_2\text{-ZrO}_2\text{-C}$) of the perovskite device. Because of the humidity resistance of carbon electrode, the unsealed perovskite worked stably under full AM 1.5 simulated sunlight in ambient air over 1008 hours (shown in **Figure 1.8c**).⁵⁵

Polymer and carbon encapsulation show promising to enhance the stability of perovskite film. However, most of the polymers are insulators, the coating of polymers will increase the resistance of the whole solar cell device. Carbon materials are hard to coat uniformly on the surface of perovskite film. The low coating quality and bad coverage increase the interface resistance resulting in the decrease of power conversion efficiency of the device. Therefore, polymer and carbon encapsulation works like a double-edged sword and better coating methods need to be explored.

1.5 Surface modification of perovskite

The surface of perovskite plays a very important role in the stability of perovskite. Because of the fast crystallization process, perovskite film is full of grain boundary and surface defects. Although currently, there are no direct evidence proving the degradation is caused by the surface defect, multiple indirect examples have demonstrated that the degradation rates are sensitive to the grain boundary sizes.^{57,58} Jinsong Huang et al. reported that the degradation of humidity is along the in-plane direction, which is initiated at the grain boundary.⁵⁷ Moisture will diffuse from the amorphous intergranular layer of the grain boundary to the bulk of perovskite film. Shuzhou Li group found that oxygen and water molecules both have strong interactions with PbI_2 -terminated surface of perovskite which cause the degradation of perovskite.³⁷ Filippo De Angelis *et al.* pointed out that the interaction of water molecules with Pb atoms changed MAI terminated surfaces through a rapid solvation process, which prompts the degradation of perovskite.⁵⁹ Therefore, understanding the surface chemistry of hybrid perovskite is crucial for the following surface modification. However, because of the complex of the surface group on the perovskite, the surface property of perovskite is not systematically studied yet. Although people proposed many strategies to modify the surface of perovskite, a comprehensive study about surface reaction mechanism is in urgent need.

1.5.1 Surface passivation of perovskite

The surface defect with higher surface energy is facile to react with water and O₂ molecular resulting in the degradation of perovskite. Moreover, the surface defect also acts as a trap which will cause the charge recombination. Therefore, surface passivation enables to improve both stability and efficiency of perovskite solar cell. In general, Lewis acid MA⁺, Pb₂⁺ and Lewis base I⁻ defect can be exposed on the surface of MAPbI₃ perovskite. Snaith and co-workers demonstrated uncoordinated lead ions defect sites passivated by sulfur atoms in thiophene or nitrogen atoms in pyridine through the coordinate bonding interactions.⁶⁰ After passivation, the rate of nonradiative recombination in perovskite film significantly decreased. As Lewis bases, thiophene and pyridine should coordinate with Lewis acid sites, such as Pb²⁺. The surface Lewis base defect, for instance halide ion defect, can also be passivated by the Lewis acid iodopentafluorobenzene (IPFB).⁶¹ After passivation, the efficiency and stability have been dramatically improved.

Based on above passivation mechanism, multiple passivation groups including fatty amine⁶², aromatic amine^{63,64}, acid⁶⁵, thiol⁶⁶, and phosphate⁶⁷ have been proposed to enhance the stability. For instance, Jianjun Tian *et al.* modified MAPbI₃ film with 2-Aminoethanethiol (2-AET) molecular. After surface passivation, the film could keep stability even after dipping into water for 5min.⁶⁶ Michael Grätzel and co-workers used butylphosphonic acid 4-ammonium chloride to crosslink the grain boundary of perovskite film.⁶⁷ The strong hydrogen bonding between the –PO(OH)₂ and –NH₃⁺ terminal groups and the perovskite surface significantly enhance the water tolerance of perovskite. Ni Zhao group tested the stability of FAPbI₃ film after modified by aniline, benzylamine, and phenethylamine.⁶³ They found benzylamine achieve the best stability due to the spaces steric effect. Perovskite film could keep the black color for 4 months in ambience because the water molecule is automatically repelled from the site of the Pb–I layer by the benzylamine layer.

Although a big step has moved forward to enhance the stability of perovskite by surface passivation, the fundamental understanding of surface reaction mechanism is still not clear. Currently, no direct evidence has been shown to verify which kind of functional groups are on the surface of perovskite and the reaction mechanism between function group, such as -NH_2 and -OH with perovskite is not clear. We use pyridine a kind of molecular probe to show that both Lewis and Bronsted acid sites are on the surface of perovskite by FTIR. The detailed content is discussed in Chapter 4.

1.5.2 Surface coating of perovskite by atomic layer deposition (ALD)

Atomic layer deposition (ALD) is a thin-film deposition technique for a variety of applications.⁶⁸ The sequential, self-limited, gas-surface reaction control deposition of ALD leads to excellent step coverage and conformal deposition on high aspect ratio structures. This property makes ALD an efficient method to coat a uniform, pinhole-free, ultra-thin metal oxide layer on the surface of perovskite.⁶⁹⁻⁷¹ The typical Al_2O_3 ALD process was shown in **Figure 1.9a**. For the ALD process, the key factor decides the growth behavior of the metal oxide film is the surface-active sites. For instance, trimethylaluminum/water chemistry can easily nucleate and form a uniform surface morphology on the surface with -OH group. If there are no active sites on the surface, for instance the surface covered by long-chain alkyl, there will be no mass growth or existing a long-time nucleation delay period. Therefore, understand the vapor-solid reaction mechanism between the ALD precursor and perovskite surface is crucial to achieve a conformal coating on the surface. The mechanism about how ALD metal oxide layer enhances the stability of perovskite is shown in **Figure 1.9b**. ALD metal oxide film could totally physically separate the contact between environmental factor (such as water, oxygen molecular) and perovskite film which dramatically extends the lifetime of perovskite.^{72,73}

Although people applied ALD metal oxide to enhance the stability of perovskite material, most of the experiments were still trial and error. Dibyashree Koushik *et al.* pointed out that, after ALD 10 cycles of Al_2O_3 on the surface of perovskite, the efficiency of perovskite device increased from 15.1% to 18% and perovskite solar cell device could keep 70% of the original efficiency in a series of humidity environment.⁷⁴ Alex B. F. Martinson *et al.* reported that after ALD TiO_2 onto PCBM film, perovskite solar cell device could not only survive under high thermal stress (100 °C) in ambient environments but also upon direct contact with a water droplet.⁷³ ALD encapsulation enables to enhance the stability of perovskite, however, the fundamental understanding of ALD growth behavior and nucleation mechanism on the perovskite related substrate is not clear yet. Here, we carried out a systematically study about ALD metal oxide growth behavior on perovskite related layers at different deposition condition by in-situ method. The detail discussion is shown in Chapter 5 and 6. The study about the ALD nucleation mechanism on the perovskite related surfaces will supply the inside understanding about the perovskite surface property and help to optimize the surface coating condition.

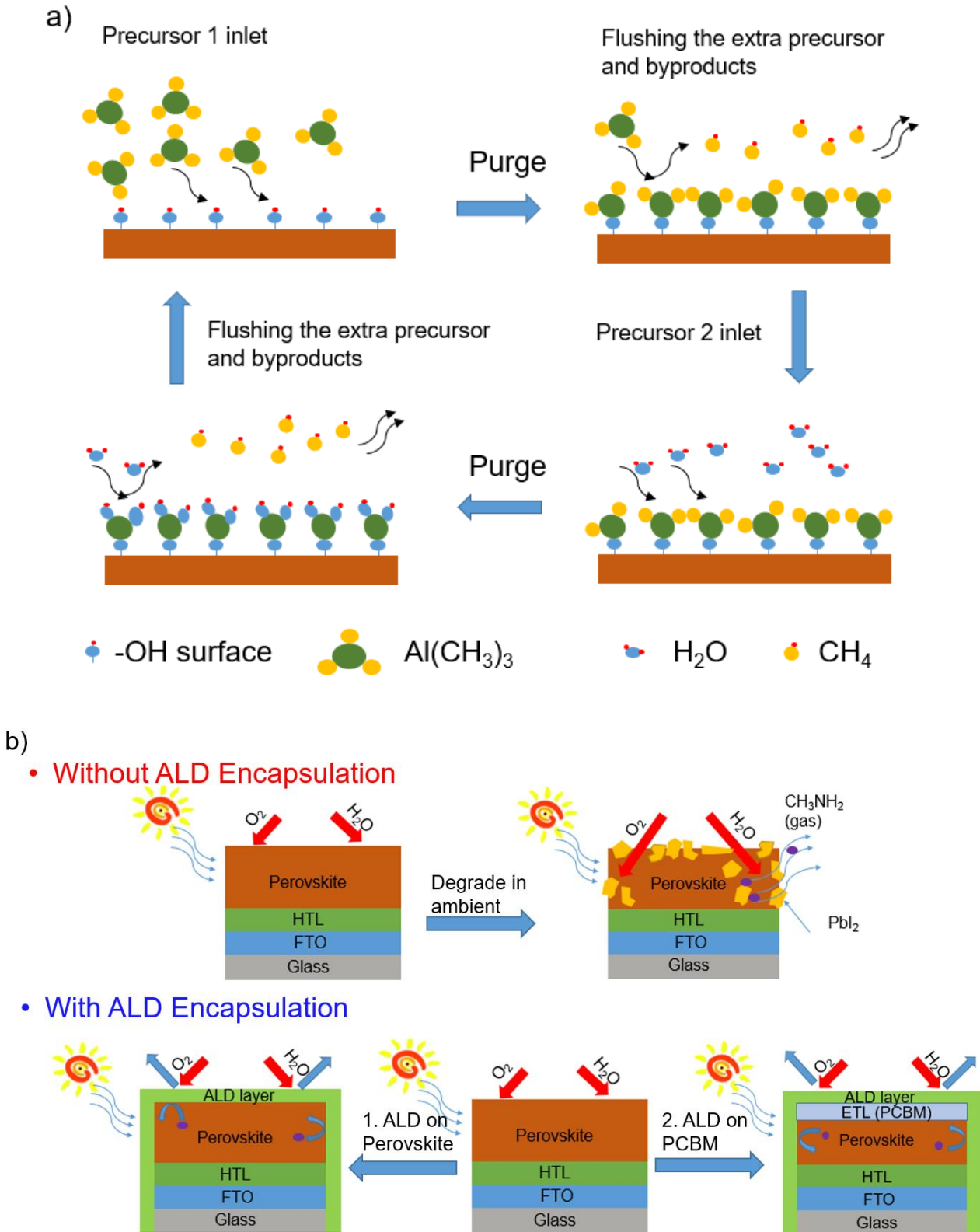


Figure 1.9. a) Typical Al_2O_3 ALD reaction mechanism.⁷⁵ b) Improve the stability of perovskite solar cell by the encapsulation of ALD metal oxide.

1.6 Overview of the dissertation

Despite the great success of hybrid perovskite has been achieved, many physical and chemical processes during the degradation have not been well understood yet. Thus, firstly, we studied the thermal degradation kinetics of MAPbI₃ in different gases environment by in-situ diffuse reflectance infrared Fourier transform spectroscopy (DRIFTS). The degradation kinetics is very helpful to elucidate the degradation mechanism and predict the degradation rate. Such information is critical not only for the outdoor applications of MAPbI₃ devices but also for my later surface modification. The detail results are discussed in Chapter 3.

Secondly, we use pyridine as the molecular probe to detect the function group bonding on the surface of perovskite. We also discuss the reaction mechanism of Lewis base Pyridine with perovskite. We found a strong pressure-dependent growth behavior between amine with perovskite. Low-pressure pyridine vapors passivate the surface of perovskite; however, high-pressure pyridine vapor could convert perovskite crystal to liquid. The detail discussion is shown in Chapter 4.

In the next step, we studied the nucleation mechanism and growth behavior of ALD Al₂O₃ on perovskite surface. Although people have proved that the ALD metal oxide layer extends the lifetime of perovskite, a systematic study about the reaction mechanism of ALD precursor and perovskite surface group is still lacking. Using in-situ quartz crystal microbalance (QCM) and quadrupole mass analyzer (QMS) measurement, we found the strong effects of reaction temperature and partial pressure of reactant on the nucleation of atomic layer deposition of Al₂O₃ on MAPbI₃. The present results are discussed in Chapter 5.

In addition to perovskite absorber, we also applied ALD on the Phenyl-C61-butyric acid methyl ester (PCBM) which is the most used electron transport layer material for the solar cell.⁷⁶ Different semiconductor metal oxides such as ZnO⁷⁷, SnO₂⁷⁸ and TiO₂ were coated onto PCBM by ALD to protect the perovskite solar cell device. However, no solid evidence showed the metal

oxide really grow onto the PCBM. Our in-situ QCM and FTIR data indicated that ALD ZnO by diethylzinc (DEZ)/water chemistry could not grow onto the PCBM film as the C=O bond cannot be broke by weak Lewis acid DEZ, resulting in no active sites for DEZ to react. In order to form a dense film, Al₂O₃ ALD was applied to the PCBM to supply active sites such as -OH for the following ZnO ALD regarding that trimethyl aluminum (TMA) as the precursor of Al₂O₃ ALD is more acidic. The detailed information is presented in Chapter 6.

Finally, we propose to apply the ALD to other perovskite systems such as NH₂CH=NH₂PbI₃ (FAPbI₃)¹³ and perovskite quantum dots^{79,80}. TMA could etch MAPbI₃ at 75°C; however, at 75°C NH₂CH=NH₂⁺ could form a stable coordinate structure with TMA which acts as a stable active site for the following ALD process. Due to the ultra-small size and the unstable chemical property, the iodine serial perovskite quantum dots will degrade in 15s at the ambient environment. With the ALD encapsulation, we observed the MAPbI₃ perovskite keeps photoluminescence property in ambient for more than 15min. The present results and future direction are shown in Chapter 7.

CHAPTER 2: EXPERIMENTAL METHODS AND RESEARCH METHODS

2.1 Materials

Most of the chemicals used in this dissertation are purchased from Sigma Aldrich. All the chemicals were directly used without further purification. Lead Iodide powder was purchased from TCI (99%). The ALD precursors including trimethylaluminum (TMA, 98%) and diethyl Zinc (DEZ,98%) were purchased from Strem Chemicals. The substrates including fluorine doped tin oxide (FTO) glass (TEC 8), double-side polished silicon wafers (500 μm thick, undoped, resistivity $> 20,000$ Ohm-cm), and AT-cut QCM crystals were purchased from Hartford Glass Co., University Wafer Inc, and Phillip Technologies LLC respectively.

2.2 Base substrate cleaning

Fluorine-doped tin oxide (FTO) glass substrates (TEC 8) of $1\text{ cm} \times 2\text{ cm}$ was purchased from Hartford Glass Co. Inc. FTO glass was cleaned by ultrasonication in soapy water, DI H_2O , acetone, and isopropyl alcohol (IPA) for 10 min, respectively, and then subjected to oxygen plasma (Plasma Cleaner, PDC32G) for 15 min.

Double-side polished, undoped silicon wafers (500 μm thick and resistivity of $>20\,000$ Ohm-cm) were purchased from University Wafer, Inc. Double-side polished silicon wafers were sonicated in acetone and isopropyl alcohol, then dried by blowing with N_2 . The Si was further cleaned by oxygen plasma to remove adventitious carbon.

2.3 Hybrid perovskite film fabrication

2.3.1 CH₃NH₃PbI₃ (MAPbI₃) film synthesized by solvent engineering method

CH₃NH₃PbI₃ films were synthesized by the solvent engineering method.⁸¹ The procedure is as the following. First, the precursor solution of CH₃NH₃PbI₃ was prepared by dissolving 0.154 g PbI₂ and 0.053 g CH₃NH₃I in the mixed solvent of 212 μl DMF and 23.6 μl DMSO. Second, the precursor solution was spin-coated on the substrate at 4000 rpm for 30 s. At ~10 s into the spin-coating, 500 μl toluene was dropped on the surface to accelerate the crystallization of CH₃NH₃PbI₃ films. Third, the film was then annealed at 100 °C for 3 min in ambient. The final CH₃NH₃PbI₃ films have bright black color.

2.3.2 MAPbI₃ powder synthesized by drop-casting method

The precursor solution is prepared by the one-step method. PbI₂ and CH₃NH₃I were dissolved in DMF solvent with the concentration of (1 mmol/ml). Drop casting the precursor solution onto the glass substrate which was cleaned through sequential sonication in DI Water, acetone, and isopropanol. The film totally converts to black color after annealing at 100°C in the glove box for 30min. The MAPbI₃ powder was collected by scratching the film.

2.3.3 Formamidinium Lead Iodide (FAPbI₃) HC(NH₂)₂PbI₃ film fabrication

FAPbI₃ films were synthesized followed the intramolecular exchange method.⁸² The PbI₂ solution was prepared by dissolving 0.154 g PbI₂ in the solvent mixture of 256 μl DMF and 23.6 μl DMSO. PbI₂ film forms by spin-coated PbI₂ solution onto a substrate at 3000 rpm for 30 seconds. Then FAI solution which prepared by dissolving 0.080g FAI in 1ml IPA was spin-coated on top of PbI₂ film at 5000 rpm for 30 sec. The films changed to dark brown color during annealing on a hot plate at 150 °C for 20 min.

2.4 Characterization methods

2.4.1 In situ Diffuse reflectance infrared Fourier transform spectroscopy (DRIFTS)

Drifts is an infrared spectroscopy technique used for measurement of particles and powders, as well as rough surface. When the IR beam enters the sample, it can either be reflected off the surface of a particle or be transmitted through a particle. The IR energy reflecting off the surface is typically lost. The IR beam that passes through a particle can either reflect off the next particle or be transmitted through the next particle. This transmission-reflectance process can repeat many times between the sample, which increases the pathlength. Finally, such scattered IR energy is collected by a spherical mirror that is focused onto the detector. The detected IR light is partially absorbed by particles of the sample, bringing the sample information.



Figure 2.1 The image of in-situ DRIFTS system.

All DRIFTS spectra were acquired with Nicolet™ iS50 interferometer (Thermo Fisher Scientific Inc.). All spectra were obtained at a resolution of 4 cm⁻¹ resolution averaging over 64 scans. For Drifts analyses, we employed a liquid-N₂-cooled mercury cadmium telluride (MCT)-A detector with the frequency range of 650 - 4000 cm⁻¹. The diffuse reflectance spectra were acquired

on a diffuse reflection accessory (DiffusIR™, Pike Technologies Inc.). Fresh $\text{CH}_3\text{NH}_3\text{PbI}_3/\text{KBr}$ samples were purged with UHP N_2 for around 1h to remove air from the gas-tight Drifts cell (Pike Technologies Inc). The temperature of Drifts cell can be controlled up to 900°C . For in-situ Drifts analyses, the $\text{MAPbI}_3/\text{KBr}$ sample will be analyzed under the continuous flow of UHP N_2 or O_2 of 20 standard cubic centimeters.

2.4.2 X-ray diffraction (XRD)

Perovskite films were obtained by XRD (Bruker D8 Advanced Diffractometer). The X-ray source is $\text{Co K}\alpha$ radiation (0.179 nm) and then the spectra were converted as the $\text{Cu K}\alpha$ radiation source (0.154 nm) as the source. The operating voltage and current are 40 kV and 35 mA.

2.4.3 Ultraviolet–visible spectroscopy (UV–Vis)

The UV–vis measurements were tested in absorbance mode on a Shimadzu UV-1800 UV–vis spectrophotometer. The perovskite samples were coated on the FTO glass. A clean FTO glass was used as the background in the UV–vis analyses. The scan range in UV–vis is 400–900 nm. The scan rate is 0.5 nm/ s with a resolution of 0.1 nm.

2.4.4 Scanning electron microscope (SEM)

The morphology of samples was analyzed by a JEOL 7000 FE SEM. Acceleration voltage (20 kV) was used in SEM measurements.

2.4.5 In situ QCM Measurement.

The in situ QCM measurements were performed using Eon-LT monitor with a temperature sensor. To stabilize the QCM signal, the samples were sitting in the reactor at vacuum for at least 1 h before we perform the pyridine adsorption experiment. The mass of MAPbI_3 films is $260 \pm 25 \mu\text{g}/\text{cm}^2$ on the QCM crystal.

2.4.6 In-situ QMS

In situ QMS measurement. The quadrupole mass spectrometer (Stanford Research Systems RGA300) was located at the downstream of the ALD reactor. The differentially pumped chamber was separated from the reactor tube by a 50 μm orifice and evacuated using a turbo-molecular pump (Agilent, TPS-compact). 0.5 g $\text{CH}_3\text{NH}_3\text{PbI}_3$ powder was sealed in a stainless-steel tube by quartz wool. The tube was connected to the inlet of the orifice by a Swagelok tube fitting. The $\text{CH}_3\text{NH}_3\text{PbI}_3$ powder was used to increase the concentration of desorbed byproducts from the reaction between $\text{CH}_3\text{NH}_3\text{PbI}_3$ and TMA vapor so that the mass spectrometer could detect these byproducts, because powder samples supply more surface area than thin film samples. The installing of the instrument was shown in **Figure 2.2**.

2.4.7 In-situ FTIR

All the experiments are done in a home-made ALD system (shown in **Figure 2.3**). The sample was mounted horizontally in the vacuum chamber. The FTIR measure follows by the transmission model. The testing sample was prepared by pressuring the mixture of perovskite powder and high surface area SiO_2 onto stainless steel mesh (34% open area, 1.1 mm thickness) by the jack under the pressure of 40MPa.

2.4.8 XPS

The surface chemical property was analyzed by XPS (Kratos AXIS 165), the analyzer pass energies were 160 eV and 80 eV for the survey scan and detail scan respectively. The perovskite was spin coated on the silicon wafer.

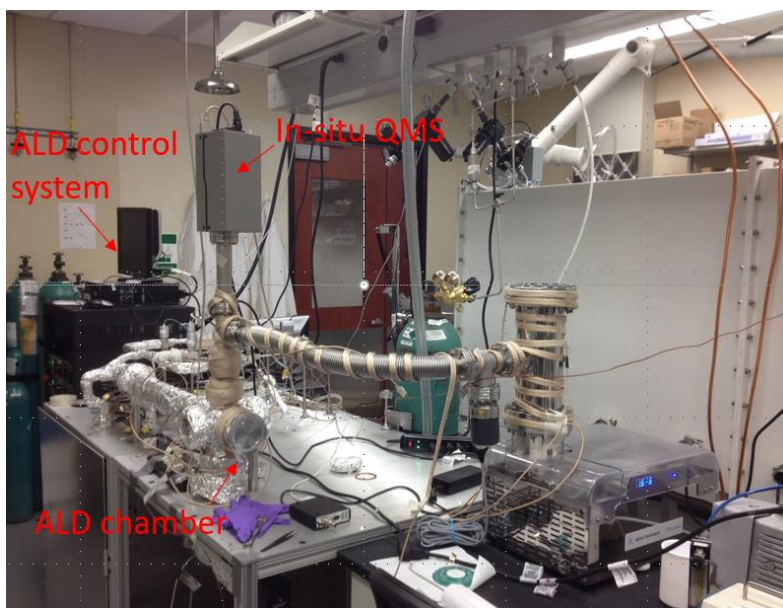


Figure 2.2 Homemade ALD system with the capability of in-situ QMS.

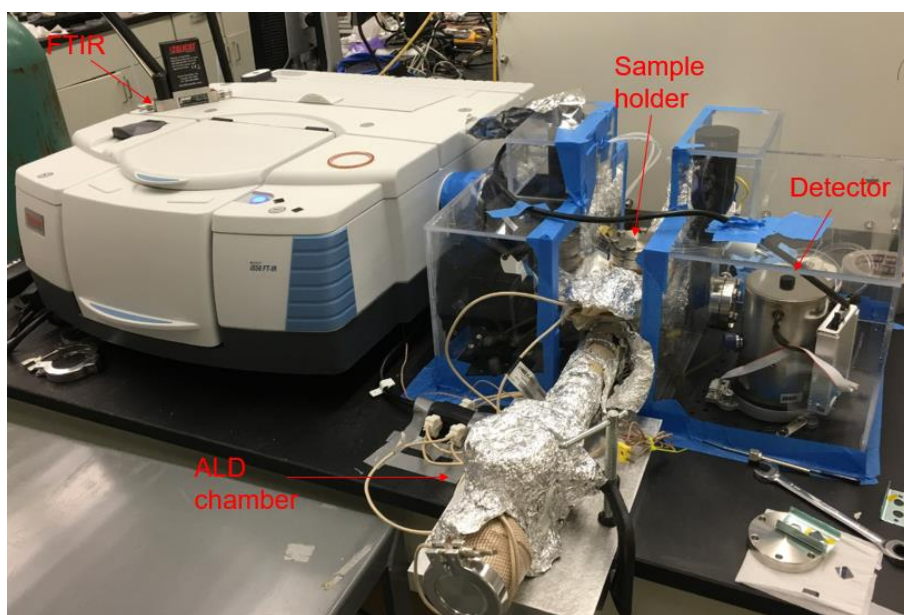


Figure 2.3 ALD system with in-situ FTIR instrument

CHAPTER 3: PROBE DECOMPOSITION OF METHYLAMMONIUM LEAD IODIDE PEROVSKITE IN N₂ AND O₂ BY IN SITU INFRARED SPECTROSCOPY

3.1 Introduction

While the field has been making great progress in improving the efficiency of methylammonium lead iodide (MAPbI₃)-based solar cells, the large-scale deployment of MAPbI₃ based solar cells still faces several major challenges.^{10,83-91} The instability of MAPbI₃ in a typical outdoor environment is one of the biggest challenges.^{10,84-86,88-91} Among various environmental factors, moisture, oxygen, light, and environmental temperatures are major concerns affecting the stability of MAPbI₃.²⁹ The threat of moisture can be addressed by packaging the solar cell with pure N₂ or dry air.⁹² According to international standards for thin-film photovoltaic modules (IEC 61646), a solar cell of any type will experience temperatures as high as 85 °C. Therefore, it is critical to understand the intrinsic thermal stability of MAPbI₃ in these potential packaging gases including N₂ or dry air.

The related studies are limited and have contradicting results. Thermogravimetric analyses show that MAPbI₃ is stable up to 300 °C in the N₂ environment.⁹³ Above 300 °C, MAPbI₃ decomposes into volatile CH₃NH₂ and HI and solid PbI₂. However, conductive atomic force microscopy measurements provide evidence that MAPbI₃ actually decomposes irreversibly at 85 °C in N₂ after 24 h. In situ scanning transmission electron microscopy (STEM) showed no detectible degradation up to 150 °C inside a complete MAPbI₃ solar cell.⁹⁴

These contradicting results could partially be ascribed to the degradation kinetics of MAPbI₃ in N₂, which unfortunately is not readily available. In terms of the effect of O₂ on the decomposition of MAPbI₃, the mechanism is not yet well-understood,^{33,95,96} and the reaction kinetics has rarely been studied. Time-evolved and temperature-evolved infrared (IR) spectroscopy can provide valuable insights about the decomposition chemistry and kinetics. For example, the time-evolved chemical composition of MAPbI₃ during the decomposition at various temperatures will provide the chemical identities of the products and help in understanding the mechanism. The temperature dependence of the degradation rates will provide the decomposition kinetics of MAPbI₃ to elucidate the degradation mechanism and predict the degradation rate. Such information is critical not only for the outdoor applications of MAPbI₃ devices but also the syntheses of MAPbI₃ (either in ambient conditions or a glovebox). To date, this type of study has not been carried out.

In this work, we employed in situ diffuse-reflectance infrared Fourier transform spectroscopy (DRIFTS) to probe the time-evolved and temperature-evolved chemical changes of MAPbI₃ during its decomposition in N₂ and O₂. In situ DRIFTS allowed us to quantify the amount of MAPbI₃ when it was well-dispersed in a KBr matrix as isolated particles with a concentration of less than 2 wt %. With the in-situ cell, we were able to carry out the IR experiment in an ultra-high-purity O₂ or N₂ environment. Through our study, we found that in N₂ the rate of decomposition increases from ~0.05% h⁻¹ at 75 °C to ~50% h⁻¹ at 150 °C. The effective activation energy of degradation of MAPbI₃ in N₂ is ~120 kJ/mol. Our kinetics results predict that MAPbI₃ could decompose at 60 °C or lower at a very low rate. Without illumination, O₂ accelerates the degradation rate. The synergistic effect of O₂ and photons (633 nm) further increases the rate and reduces the effective activation energy of decomposition of MAPbI₃ to ~50 kJ/mol. In addition, in situ DRIFTS analyses showed that a small amount of H₂O can be removed from MAPbI₃ by heating

and does not accelerate the decomposition. Moreover, there are no IR peaks ($650\text{--}4000\text{ cm}^{-1}$) from the solid product formed by decomposition of MAPbI_3 in N_2 and O_2 .

3.2 Experimental results:

MAPbI_3 was synthesized by a one-step solution method. Details about the experimental conditions are shown in the Supporting Information. X-ray diffraction of our MAPbI_3 films showed only MAPbI_3 crystals (**Figure S1**). The average crystal size was $\sim 60\text{ nm}$. For DRIFTS analyses^{84,86}, we scratched the MAPbI_3 films from glass substrates and gently mixed them with KBr powder in ambient conditions with concentrations of $<2\text{ wt } \%$. As all of the samples were processed in ambient conditions, moisture could react with MAPbI_3 to form hydrates.¹⁹⁻²¹ We characterized the chemical identity of $\text{MAPbI}_3/\text{KBr}$ by DRIFTS (DiffusIR900C, Pike Technology Inc.). The spectra of samples in **Figure 3.1** were taken after $\sim 1\text{ h}$ purge with N_2 . The IR spectra show peaks related to asymmetric and symmetric N-H stretching modes (3179 and 3132 cm^{-1}), asymmetric and symmetric C-H stretching modes (2958 and 2921 cm^{-1}), the C-H bending mode (1422 cm^{-1}), asymmetric and symmetric N-H bending modes (1577 and 1469 cm^{-1}), $\text{CH}_3\text{-NH}_3^+$ rocking modes (1249 and 910 cm^{-1}), the C-N stretching mode (962 cm^{-1}), and various resonant modes of MAPbI_3 (2817 , 2711 , 2488 , 2375 , and 1840 cm^{-1}).⁹⁷⁻⁹⁹ The positions of these peaks (Table S1) and their relative intensities match with the corresponding IR spectra of pure MAPbI_3 ,^{97,99} which verified the chemical nature of MAPbI_3 in our $\text{MAPbI}_3/\text{KBr}$ samples. UV-vis analysis of a $\text{MAPbI}_3/\text{KBr}$ pellet with a KBr pellet as the background shows the starting absorbance at $\sim 800\text{ nm}$ (**Figure S2**), which is consistent with the band gap of MAPbI_3 ($\sim 1.54\text{ eV}$). In comparison with the large N-H stretch mode ($\sim 3179\text{ cm}^{-1}$) from MAPbI_3 , the small -OH peak (centered at 3500 cm^{-1}) suggests that the amount of hydroxyl species, including hydrates, water, and hydroxide, is relatively small.^{100,101} The spectra confirmed the presence of MAPbI_3 and small amount of -OH species in our samples.

DRIFTS can be used to quantify the amount of an absorber (e.g., MAPbI₃) when it is diluted

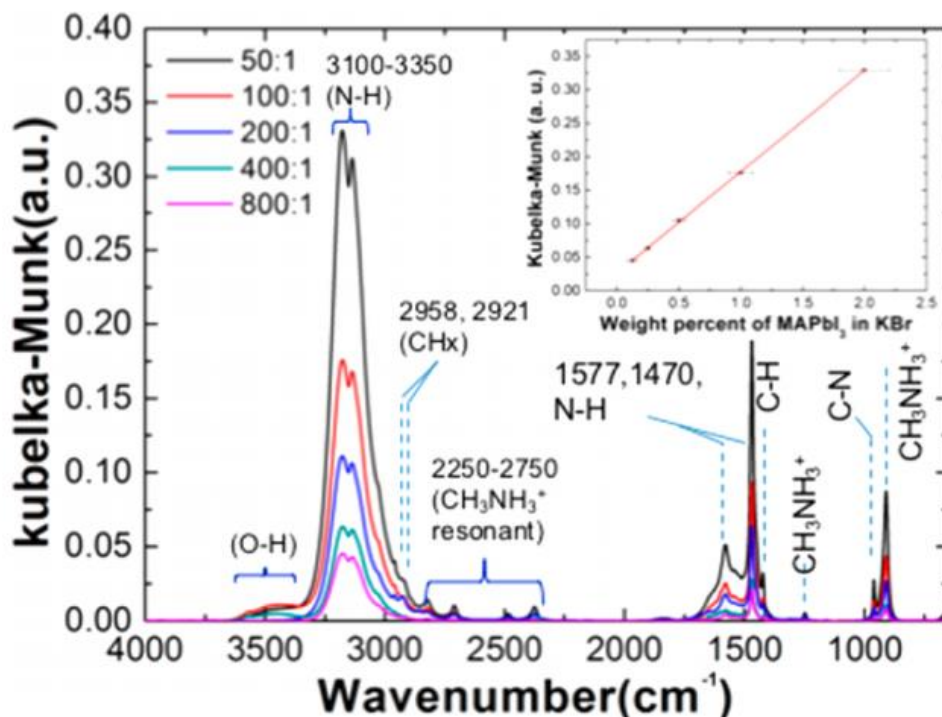


Figure 3.1. IR spectra of MAPbI₃ samples diluted with KBr powder to weight percentages of 1:1600 to 1:50. All the spectra were obtained at 25 °C. The inset shows the variation of the intensity of the N–H stretch (3179 cm⁻¹) from MAPbI₃/KBr with the weight percentage of MAPbI₃. All the spectra are referenced to that of a pure KBr powder sample at 25 °C.

in a nonabsorbing material such as KBr powder according to the Kubelka-Munk theory of diffuse reflectance of powdered samples (eq 1)¹⁰²:

$$f(R_{\infty}) = \frac{(1-R_{\infty})^2}{2R_{\infty}} = \frac{K}{S} = kC \quad (2.1)$$

wherein $f(R_{\infty})$ is the Kubelka-Munk unit of highly diluted MAPbI₃ dispersed in KBr; R_{∞} , K , and S are the spectral reflectance, absorption, and scattering components from the sample; k is a constant; and C is the concentration of dispersed MAPbI₃ in KBr. For any one wavelength, S is assumed to be constant and is determined by the KBr powder matrix, while K changes with the concentration of MAPbI₃. Our measurements showed that the intensity of the N-H stretching mode (i.e., 3179 cm⁻¹) increases quite linearly with the weight percentage of MAPbI₃ inside KBr up to 2 wt % at least

(inset in **Figure 3.1**). Therefore, we were able to use DRIFTS to quantify the amounts of MAPbI₃ in samples.

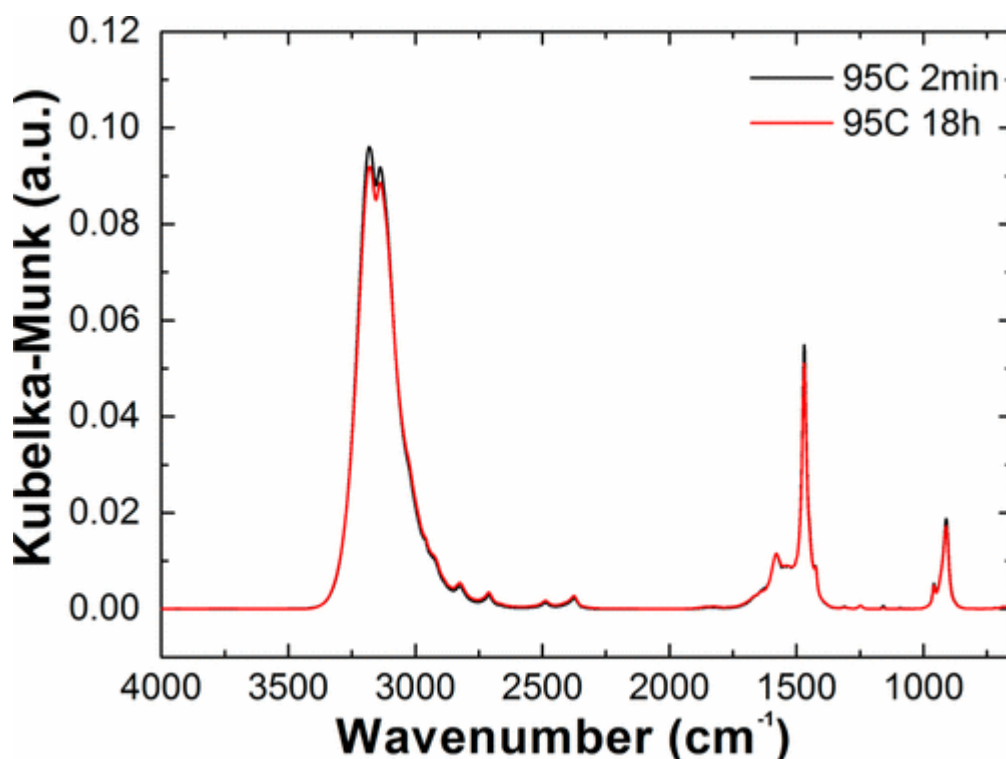


Figure 3.2. IR spectra of MAPbI₃/KBr samples at 95 °C in N₂ for 2 min and 18 h. All the spectra are referenced to the spectrum of a pure KBr sample at 25 °C.

The thermal stability of MAPbI₃ in N₂ was probed at different temperatures by DRIFTS in an in situ heated gas-tight sample chamber with a continuous flow of N₂ (99.999%). **Figure 3.2** shows the IR spectra of MAPbI₃ at 95 °C after 2 min and 18 h. The intensity of characteristic peaks of MAPbI₃ is reduced by increasing the heating time. This indicates that decomposition of MAPbI₃ happened in 95 °C. The IR spectrum of MAPbI₃ (95 °C, 18 h) resembles the spectrum of pure MAPbI₃ as shown in **Figure 3.1** and other reports.⁹⁷⁻⁹⁹ This suggests that the decomposed products either do not have IR absorbance in the probed range (e.g., PbI₂) or desorb from the samples (e.g., CH₃NH₂ or HI). These two spectra also indicate that hydrate is not a major component in the sample, because annealing at 95 °C will degrade hydrates, which will cause a shift of the N-H peak and generate a negative -OH IR peak centered ~3500 cm⁻¹.^{101,103}

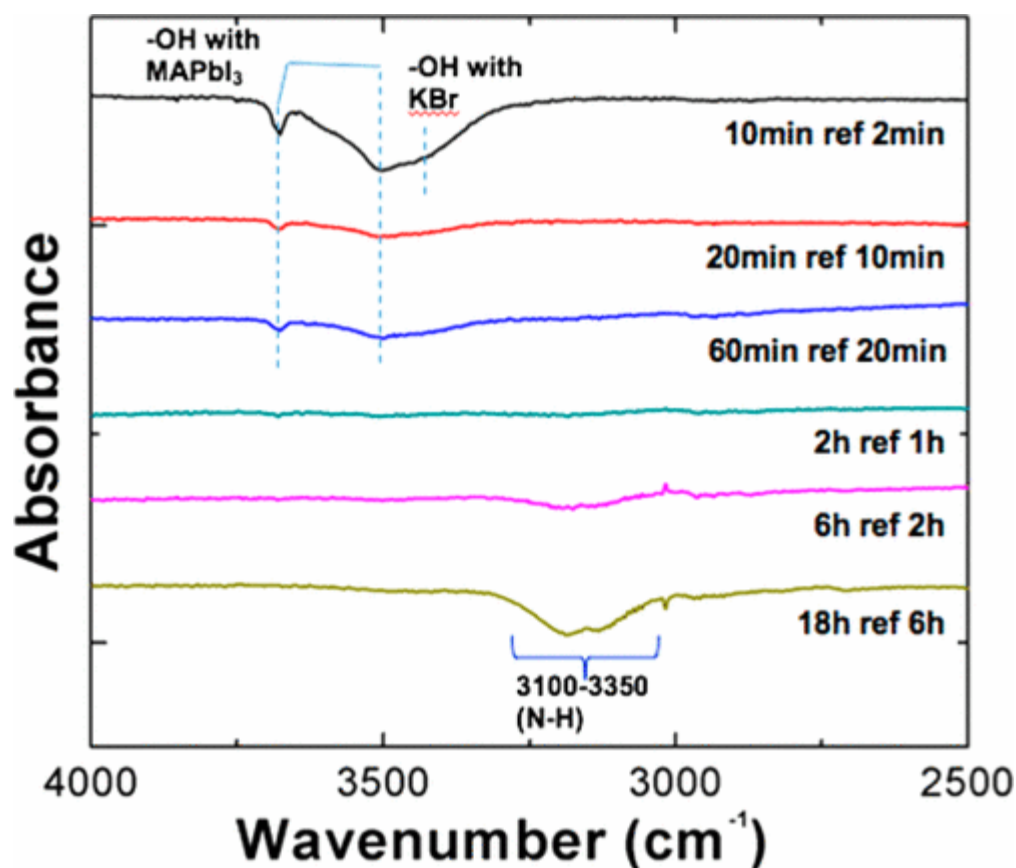


Figure 3.3. Time-evolved differential IR spectra of MAPbI₃/KBr samples at 95 °C. The spectrum labeled 10min ref 2min was obtained at 10 min with the spectrum at 2 min as the reference. The labels of the other spectra follow the same principle.

Time-evolved differential spectra show a subtle change of chemical bonds that are not observable with KBr as the background. **Figure 3.3** presents differential spectra of MAPbI₃/KBr at 95 °C for different periods. The negative peaks represent species that are removed from the sample. The -OH peaks (3250-3700 cm⁻¹) are removed during the first 60 min. The majority of -OH species are removed during the first 10 min. The free -OH at 3660 cm⁻¹ and H bonded -OH, a broad peak centered around 3500 cm⁻¹, are assigned to the surface bonded OH groups on MAPbI₃.¹⁰⁴ The peak for the desorbed -OH species in a pure KBr sample at 95 °C is centered at 3400 cm⁻¹, as shown in **Figure S3** Even though we tried to eliminate moisture from the sample by continuously purging the system with ultrahigh-purity N₂,¹⁰¹ it was not possible to completely eliminate water from the

system without damaging MAPbI₃ because of the sticky nature of water molecules.¹⁰⁵ It often takes a heating step to remove surface-bonded water molecules.

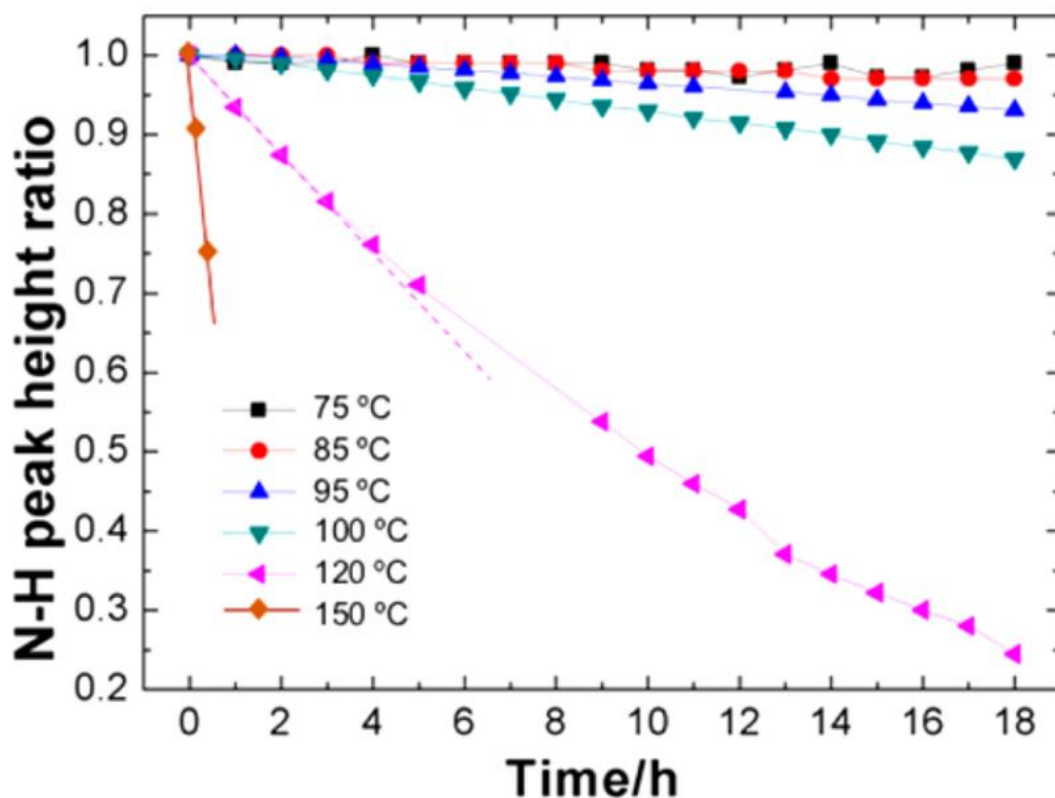


Figure 3.4. Normalized intensity of the N–H peak ($\sim 3179\text{ cm}^{-1}$) vs reaction time in N₂ at 75 °C (black ■), 85 °C (red ●), 95 °C (blue ▲), 100 °C (green ▼), 120 °C (magenta ◀), and 150 °C (brown ◆). Solid lines are guides for the eyes. We extracted the reaction rates $\alpha t d$ from the slopes of the initial linear portions of these data sets (e.g., the dashed line for the data from 120 °C).

It is noteworthy that the change in intensity of the N-H peaks is negligible during the first 60 min at 95 °C. In the second hour, the removal of N-H and -OH peaks are negligible. After a longer term of annealing, the removal of N-H peaks is clear. For example, the spectra at 6 h (referenced to that at 2 h) and at 18 h (referenced to 6 h) show the removal of N-H peaks (3179 and 3132 cm^{-1}) along with a very small amount of the -OH peak at 3500 cm^{-1} . This means that -OH and N-H are removed at different stages. Similar time-evolved differential spectra were obtained at other temperatures in N₂ (**Figure S4**). From the differential spectra in **Figure 3.3**, we draw several conclusions. First of all, these removed -OH species, probably water, do not dramatically accelerate

the degradation of MAPbI₃,¹⁰¹ although water has been proposed as a catalyst to accelerate the degradation of MAPbI₃.²⁹ Second, the surface bonded water does not form hydrates with MAPbI₃ as claimed by many literature reports,¹⁰⁶ because the removal of -OH peaks is not accompanied by a change in the N-H peaks. This is probably due to the fact that the relative amount of water in our system is much smaller than that in other studies. Third, the degradation of MAPbI₃ at 95 °C is mainly due to the thermally induced decomposition because the removal of -OH and N-H do not take place at the same time.

The time-evolved IR spectra of MAPbI₃ at different temperatures were used to probe the rates of decomposition of MAPbI₃ in a continuous flow of N₂. The intensity of the N-H peak (3179 cm⁻¹) was chosen to monitor the decomposition as a function of reaction time because it is the most pronounced peak from MAPbI₃ (**Figures 3.1** and **3.2**). For a clearer comparison, the intensities of the N-H peak are normalized to the intensity of N-H peak obtained at 2 min at that temperature.

Figure 3.4 summarizes the normalized N-H peak intensity versus reaction time at various temperatures. At 75 °C, the trend of the extent of degradation with time is not clear because of the low degradation rate (~1%/18h). The differential spectrum of 18 h - 2 min at 75 °C (**Figure S5**) clearly shows the reduction of peak intensities from MAPbI₃ due to the degradation. At 85 °C, the total reduction in the N-H peak intensity after 18 h is $3 \pm 1.5\%$. The error is from multiple experiments and may be caused by the sample preparation. The degradation rate at 85 °C in N₂ agrees reasonably well with reported marginal degradation of a MAPbI₃ film in N₂ at 85 °C for 24 h. Our own experiment also shows that the degradation rate of MAPbI₃/KBr substrate at 85 °C is similar to that of a MAPbI₃ thin film on a Si wafer with native oxide (**Figure S6**). These two pieces of evidence suggest that the KBr substrate does not strongly affect the degradation of MAPbI₃. At 95 and 100 °C, the normalized N-H peak intensity decreases with reaction time in a linear fashion up to at least 18 h. The constant slope suggests that the degradation rate does not change much with

small degree of degradation. The degradation rate at 120 °C is constant within 2 h and then decreases with the extent of decomposition, as shown by the less-steep slope at longer reaction times. The degradation rate is further increased at 150 °C. The degradation can also be observed by the reduction in the intensities of the C-N mode ($\sim 962\text{ cm}^{-1}$) and N-H bending mode ($\sim 1468\text{ cm}^{-1}$) with annealing time at various temperatures (**Figure S7**).

The rate of the MAPbI₃ decomposition reaction can generally be described by eq 2 according to the mole balance of solid-state decomposition kinetics theory:¹⁰⁷

$$r_p = \frac{da}{dt} = Ae^{-\left(\frac{E_a}{RT}\right)}f(a) \quad (2.2)$$

in which A is the pre-exponential factor, Ea is the activation energy, T is the absolute temperature, R is the gas constant ($8.314\text{ J mol}^{-1}\text{ K}^{-1}$), f(α) is the reaction model, and α is the conversion of the reaction, given by eq 3:

$$\alpha = \frac{N_0 - N_t}{N_0} = 1 - \frac{N_t}{N_0} \quad (2.3)$$

wherein N₀ and N_t are the molar amounts of MAPbI₃ at times 0 and t and N_t/N_0 is the intensity of the N-H peak at time t normalized to that at time 0 (**Figure 3.4**).

According to the data in **Figures 3.4** and **S7**, the degradation rate of MAPbI₃ does not change much with reaction time when the degradation fraction α is smaller than 10%. This suggests that da/dt is relatively constant within this range and that f(α) is relatively constant and has a very small impact on the reaction rate at this stage. Therefore, according to eq 2, it is possible to extract the effective activation energy from a plot of $\ln(da/dt)$ versus $1/T$ at the initial stage of degradation. It is noteworthy that the degradation rate extracted from the C-N mode (**Figure S7a**) is slightly different than the rates obtained from the N-H modes (**Figures 3.4** and **S7b**). This could be due to the impact of hydrogen bonding of N-H on its IR modes. We calculated the average rates from all of these IR modes with a standard deviation representing the variation of the rates from different modes. These calculated initial rates da/dt are $\sim 0.06\% \text{ h}^{-1}$, $0.17 \pm 0.06\% \text{ h}^{-1}$, $0.3 \pm 0.1\% \text{ h}^{-1}$, $0.8 \pm$

0.2% h⁻¹, 6 ± 0.5% h⁻¹, and 50% h⁻¹ at 75, 85, 95, 100, 120, and 150 °C respectively. We have plotted ln(dα/dt) versus 1/T in **Figure 3.5**. The data can be fitted well by linear regression. The residue of the fit is ~99%. We extracted the effective activation energy (E_a) from the slope (= - E_a/R) according to eq 2. The value of E_a is ~120 kJ/mol. On the basis of the value of E_a and eq 2, the calculated decomposition rate of MAPbI₃ at 60 °C should be ~5% of the rate at 85 °C for similar samples. The differential spectrum 18 h - 2 min at 60 °C (**Figure S5**) shows negligible N-H stretches, which agrees with the prediction. Our results predict that the extent of degradation of MAPbI₃ in N₂ should be within 10% after 1000 h of operation at 60 °C. This prediction is consistent with the lifetime study of MAPbI₃ solar cells in N₂.⁹² Furthermore, our kinetics results show that the low degradation rate in N₂ and a high heating rate (10 °C/min) are the reasons why researchers did not observe the degradation of MAPbI₃ up to 250 °C in the thermogravimetric analysis.⁹³

The decomposition rate of MAPbI₃ in pure oxygen without illumination is $\sim 1.1\% \text{ h}^{-1}$ at 85 °C (**Figure S8**), which is higher than the rate in N₂ ($0.17 \pm 0.06\% \text{ h}^{-1}$). This result suggests that O₂ affects the degradation of MAPbI₃. This relatively low rate is probably the reason why previous reports showed that oxygen alone does not accelerate the degradation.^{95,96} We further confirmed that the synergistic effect between O₂ and photons (633 nm)^{95,96} dramatically increases the degradation rate of MAPbI₃ in O₂. These 633 nm photons were from a HeNe laser in our IR bench

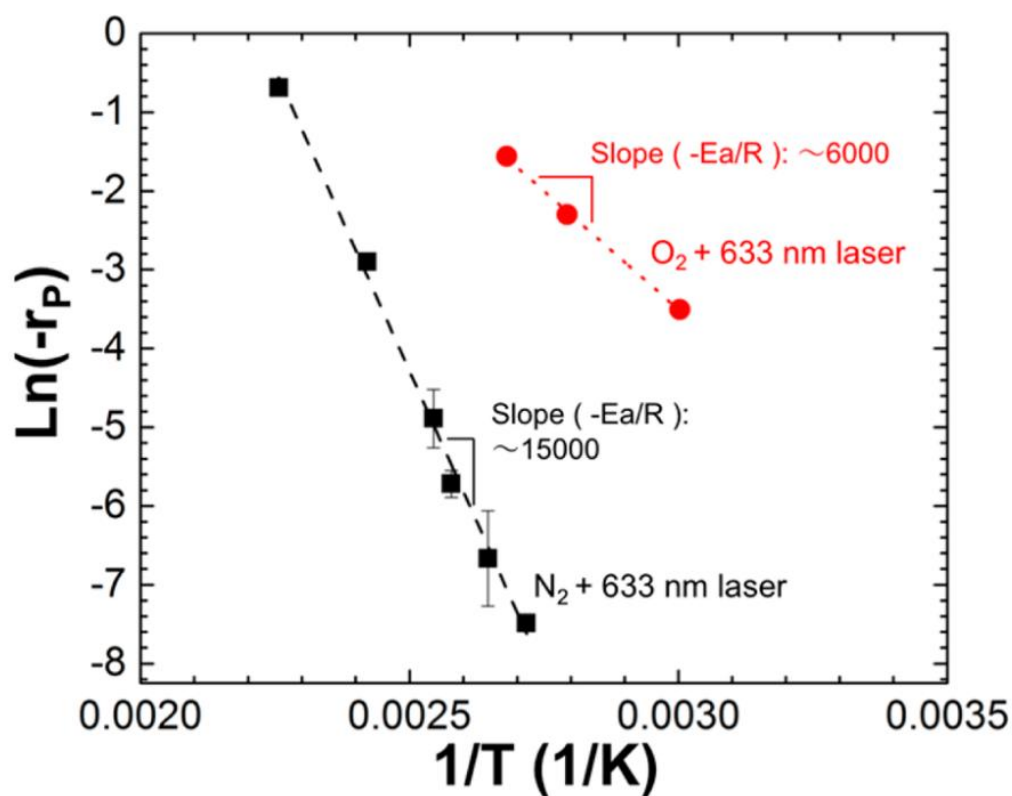


Figure 3.5. Plots of $\ln (da/dt)$ vs $1/T$ for degradation in N₂ and O₂ with a laser (633 nm). The laser with O₂ greatly increases the decomposition rate. Lines are linear fits to the data points. We use the symbol $-r_p$ to represent da/dt .

to help locate the IR beam. The laser beam was also on during the experiments with N₂, therefore the results in **Figure 3.5** suggests that the laser itself does not dramatically affect the degradation rate.

The IR spectra of MAPbI₃ with decomposition caused by O₂ and photons are similar to those of pure MAPbI₃ (**Figure S9**) but with reduced intensities of its characteristic peaks. We did not observe peaks associated with -OH species (3600-3400 cm⁻¹) and C-O species (1750-1900 cm⁻¹). These results suggest that the decomposed products from CH₃NH₃⁺ left MAPbI₃. This may be due to the deprotonation reaction between the reduced O₂ and CH₃NH₃⁺.

The proposed reaction rate model for the decomposition in O₂ is shown in eq 4:

$$r_p = \frac{da}{dt} = Ae^{-\left(\frac{E_a}{RT}\right)} f(a)g(O_2)h(a) \quad (2.4)$$

in which A, E_a, T, R, f(α), and α are defined as in eq 2, g(O₂) is a function of the partial pressure of O₂, and h(α) is the concentration of photoelectrons. When α is less than 10%, α is relatively constant (**Figure S10**). g(O₂) is a constant because of the constant flow rate of pure O₂. Because α is small and the photon flux is constant, the optical absorption of the sample is relatively constant, and thus, the concentration of photoelectrons h(α) is also nearly constant. We extracted the decomposition rate (dα/dt) at the initial decomposition stage, and ln(dα/dt) is plotted versus 1/T in **Figure 3.5**. The effective degradation activation energy is ~50 kJ/mol, which is smaller than the activation energy in N₂. This result indicates that visible photons coupled with O₂ can lower the barrier of the decomposition of MAPbI₃. The reduced barrier may result from deprotonation of CH₃NH₃⁺ facilitated by O₂⁻.

3.3 Conclusion

Our results show that the long-term stability of MAPbI₃ in a normal solar cell operating environment (up to 85 °C) even in N₂ is a concern. At 60 °C or below, >90% MAPbI₃ could be stable for up to 1000 h in N₂. O₂ accelerates the decomposition reaction. The synergistic effect between O₂ and solar irradiation may increase the decomposition rate further. Our results show that MAPbI₃ is very sensitive to temperature. Therefore, careful attention must be paid to monitor the

history of temperatures that MAPbI₃ has experienced. According to our results, it is very possible that the deprotonation of surface CH₃NH₂⁺ is the rate-limiting step in the decomposition of MAPbI₃ in N₂ and O₂.^{94,95} Therefore, one could increase the stability of MAPbI₃ by reducing the rate of this reaction. For example, a larger crystal size (fewer surface CH₃NH₂⁺ sites per unit mass) would lead to a lower degradation rate. It is also possible to improve the stability by replacing the surface CH₃NH₂⁺ sites with other ligands that have a higher bonding energy with the Pb-I matrix

Support information

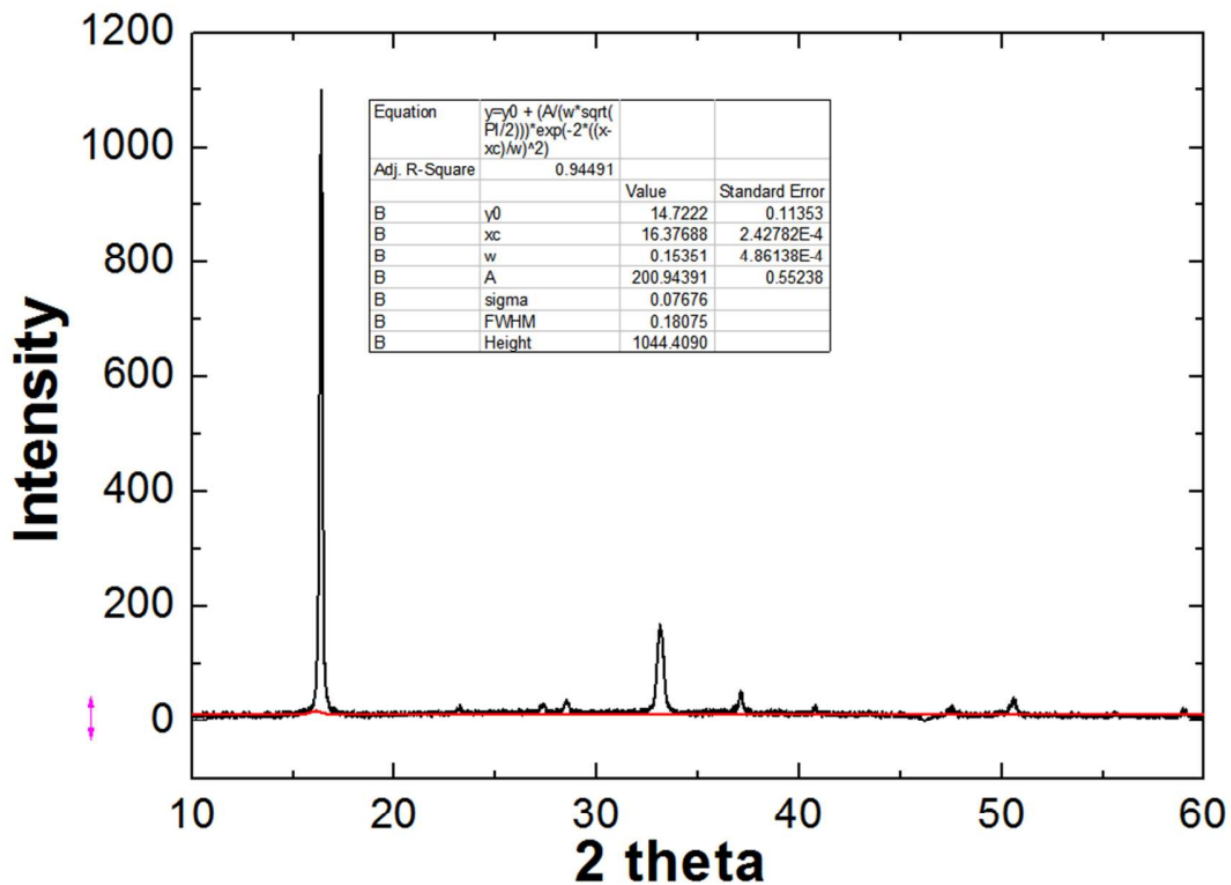


Figure S1. A representative XRD spectrum of MAPbI₃ thin film synthesized from one step method. There is no PbI₂ peak.

The crystal size of MAPbI₃ is calculated according to Scherrer formula

$$D = k\lambda / (\beta \cos(\theta))$$

In the above equation, k is 0.943 (cubic lattice). The λ is the X-ray wavelength from Co source (0.179 nm). D is the average diameter of perovskite crystal. Therefore, D is listed as following:
 $D = 0.943 * 0.179 / (0.18075 / 180 * 3.14 * \cos(16.37688/2)) = 54.1 \text{ nm}$

Table S1. Peak assignments for the IR spectra of $\text{CH}_3\text{NH}_3\text{PbI}_3$ and CH_3NH_2 ^[2-4]

Wavenumbers (cm^{-1})	Assignment
3660	Free -OH stretch
3500	H-bonded -OH stretch
3431	-OH stretch on KBr
3275	sym. N-H stretch in CH_3NH_2
3179	N-H a-str. in MAPbI_3
3132	N-H s-str. in MAPbI_3
2958	asym. CH_3 stretch,
2921	sym. CH_3 stretch,
2817	Asym. NH_3 bend + $\text{CH}_3\text{-NH}_3^+$ rock
2711	sym NH_3^+ bend + $\text{CH}_3\text{-NH}_3^+$ rock
2488	2x $\text{CH}_3\text{-NH}_3^+$ rock
2375	C-N stretch + $\text{CH}_3\text{-NH}_3^+$ rock
1840	C-N stretch + $\text{CH}_3\text{-NH}_3^+$ rock
1719	asym. NH_2 bend
1577	Asym. NH_3^+ bend
1482	sym. NH_2 bend
1469	sym NH_3^+ bend
1422	Asym. CH_3 bend
1249	$\text{CH}_3\text{-NH}_3^+$ rock
962	C-N stretch
910	$\text{CH}_3\text{-NH}_3^+$ rock

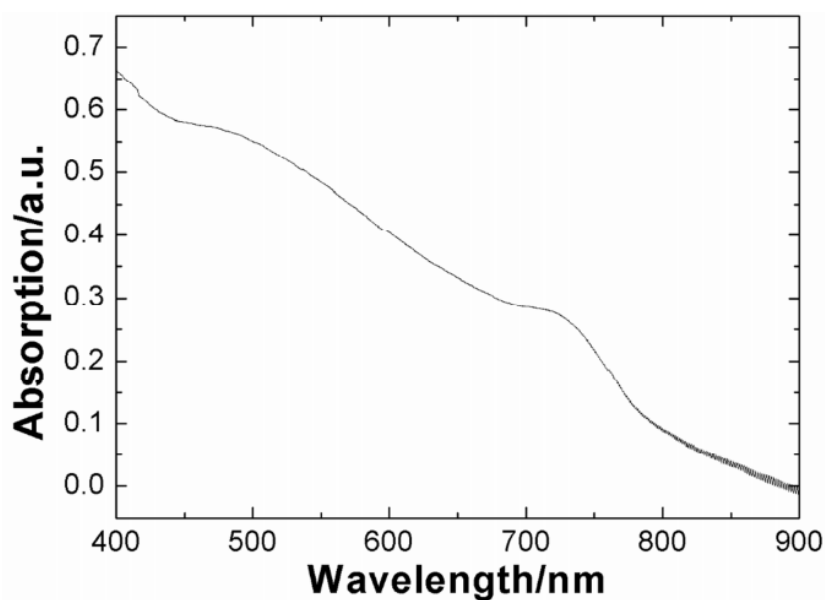


Figure S2. A representative UV-vis spectrum of MAPbI₃/KBr with KBr as the background at room temperature. The light absorption starts ~800 nm, which is consistent with the bandgap of MAPbI₃ (1.54 eV). The UV-vis spectrum did not show a bump at ~540 nm. This indicates that PbI₂ content (bandgap 2.3 eV, 540 nm) is negligible in the film.

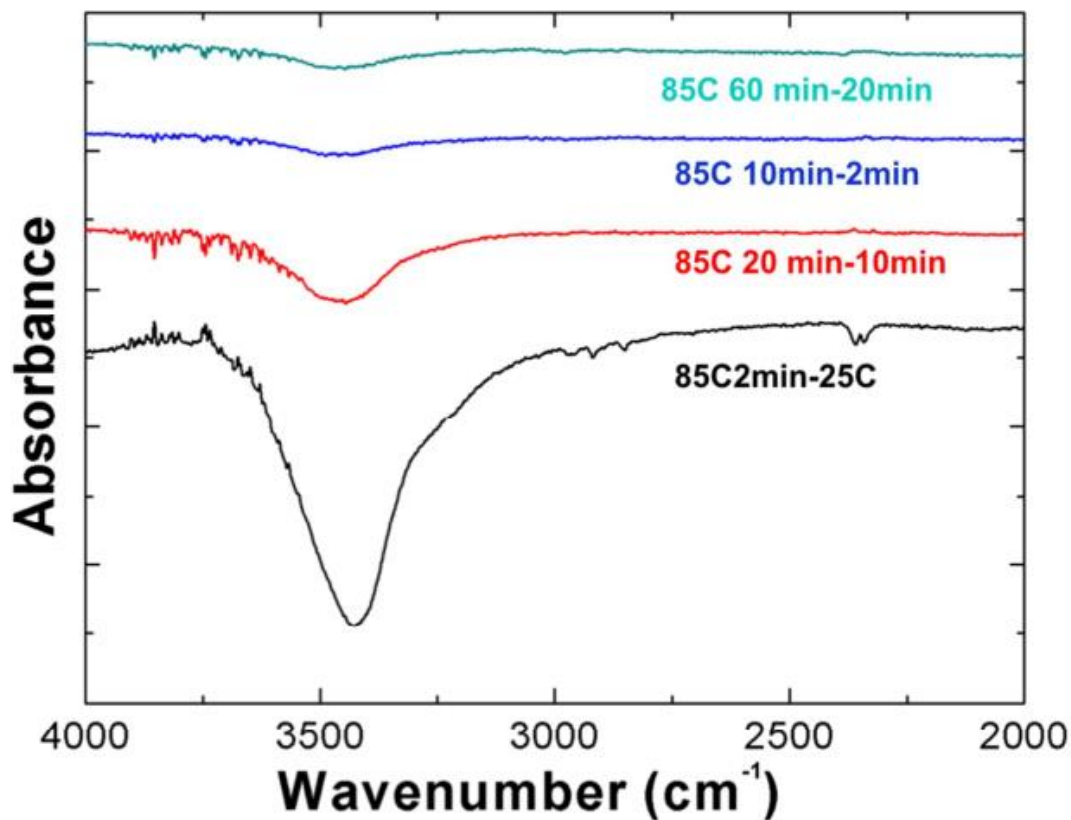


Figure S3. Differential spectra of pure KBr at 85°C. Negative peaks of -OH suggest the removal of water. Most of water is removed during the first 10 min.

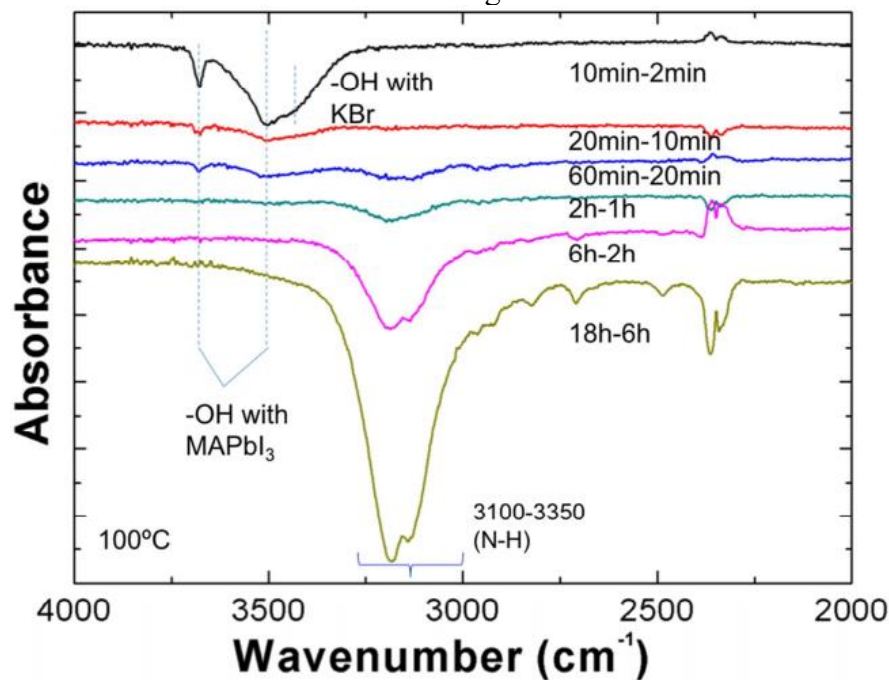


Figure S4. Differential spectra after sitting at 100°C for different periods. The critical feature is that majority of –OH groups is removed during the initial 60 min. The major removal of N-H does not accompany with a significant removal of –OH groups.

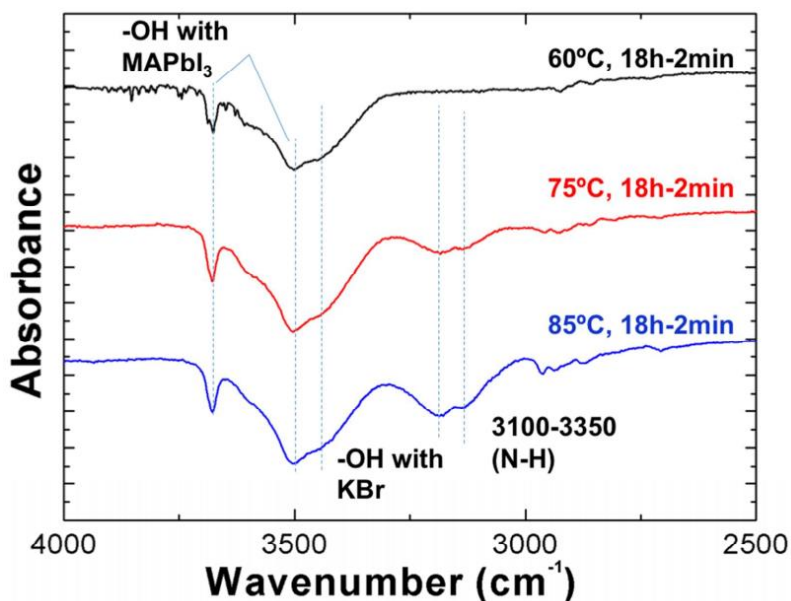


Figure S5. Differential spectra of samples after 18h at 60°C, 75°C, and 85°C with the spectra at 2min as the reference. The change of N-H stretching mode is negligible for 60°C and is noticeable at 75°C and 85°C. These results suggest that the decomposition of MAPbI₃ is negligible after 18h at 60°C

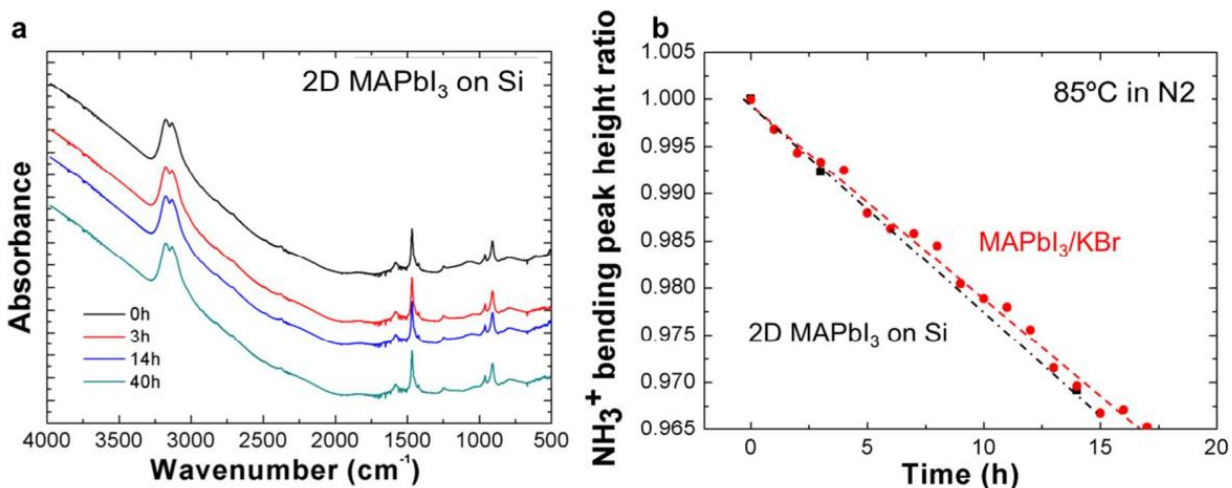


Figure S6. a) IR spectra of MAPbI₃ thin film on Si after annealing at 85°C in N₂ for different periods. b) Intensities of –N-H bending band at ~1468 cm⁻¹ for MAPbI₃ film on Si (a) and MAPbI₃/KBr from Figure S6. The Line is for the guidance of eyes. The degradation rate of MAPbI₃ film on Si is ~ 0.23%/h, which aligns with the degradation rate of MAPbI₃/KBr 0.17± 0.06%/h. The relative amount of MAPbI₃ is calculated by the height of NH₃⁺ bending peak (1469 cm⁻¹), instead of using N-H stretching mode (3179 cm⁻¹). It is because the baseline between 2000 and 4000 cm⁻¹ is tilted while the baseline for NH₃⁺ bending peak is flat as shown in figure (a).

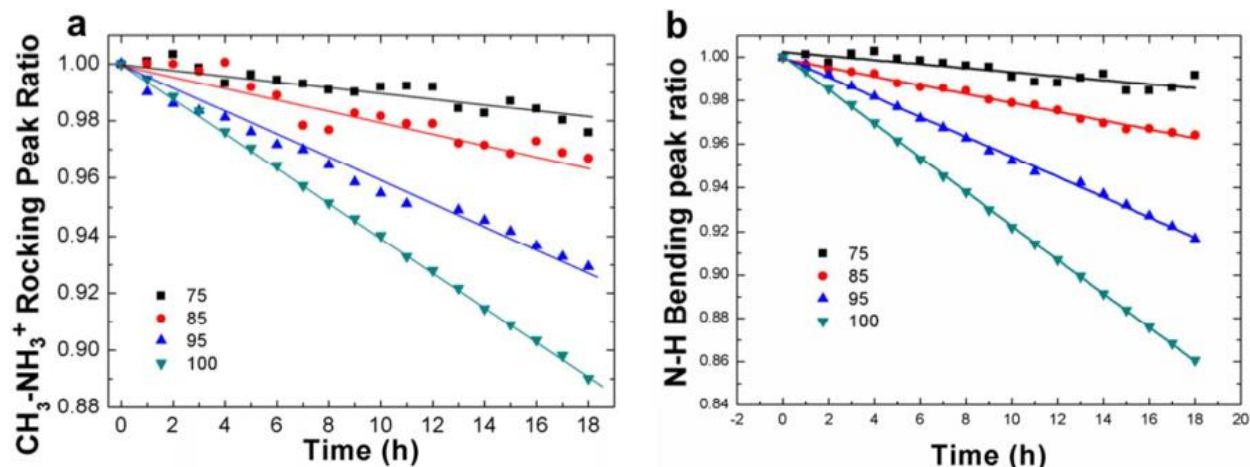


Figure S7. a) The change of C-N rocking band at $\sim 962\text{ cm}^{-1}$ with reaction time; b) The change of N-H bending band at 1468 cm^{-1} with reaction time. The degradation rates at various temperatures obtained from N-H bending mode (b) match well with the corresponding rates from N-H stretching mode. There are small differences between degradation rates from C-N rocking mode and N-H modes at 90°C and 100°C . The differences are incorporated into the degradation rates as standard deviation. The differences may due to the impact of hydrogen bonding on N-H mode.

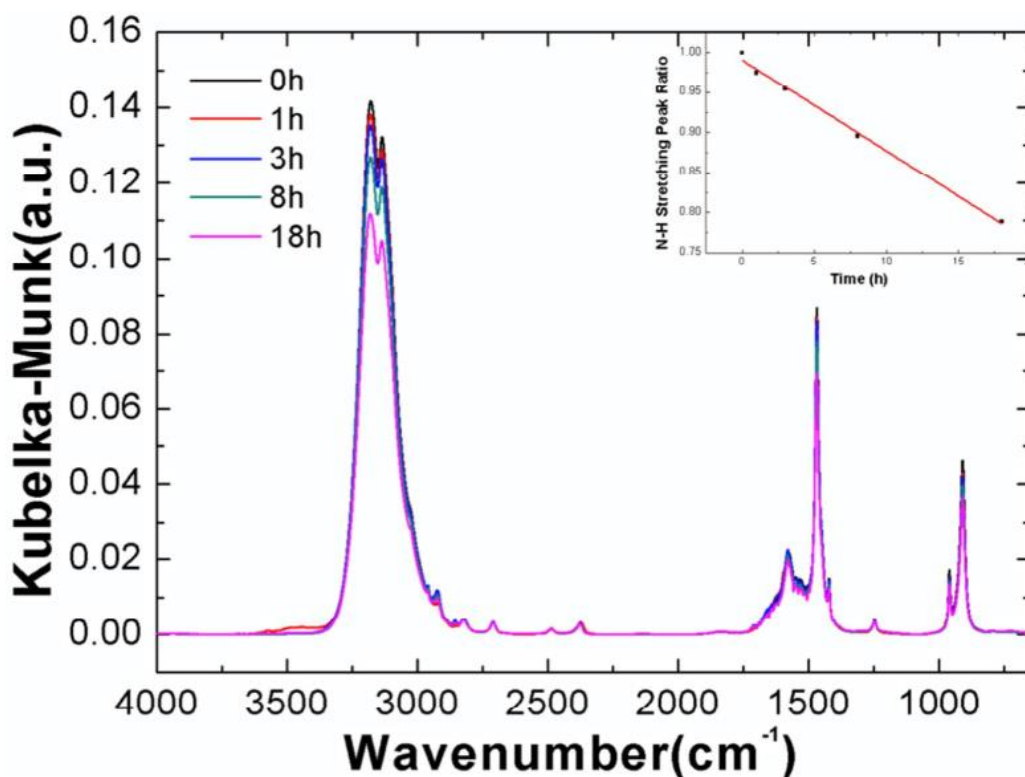


Figure S8. The IR spectra of MAPbI₃/KBr after degradation in O₂ without laser at 85°C with KBr at 25°C as the background. The degradation rate is $\sim 1.1\%/h$, which is faster than the corresponding rate in N₂ at 85°C ($< 0.3\%/h$) shown in the inset figure.

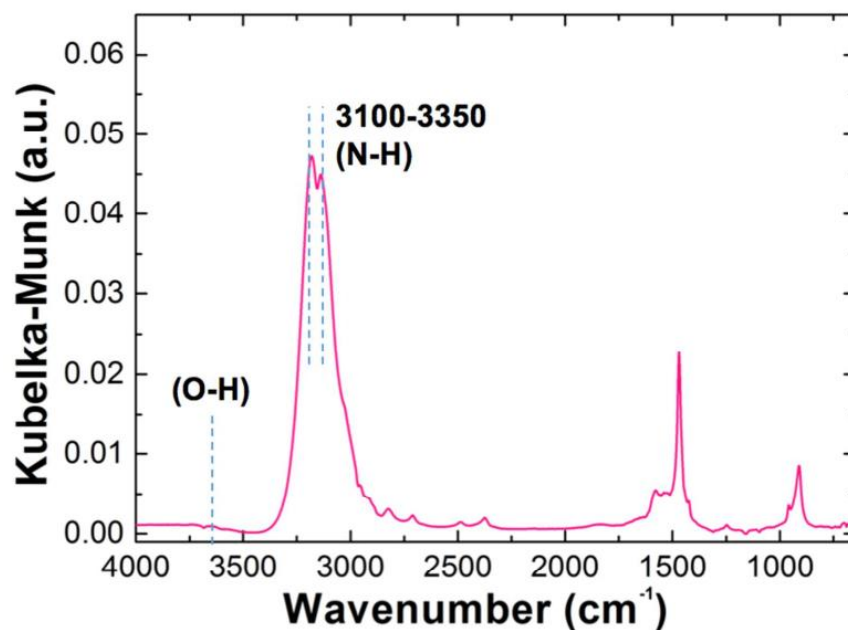


Figure S9. The IR spectra of MAPbI₃ after 50% degradation in O₂ with photon of 633nm at 85°C with KBr at 25°C as the background. We observed removal of H₂O peak after heating. The spectrum is largely same as the spectrum of pristine MAPbI₃.

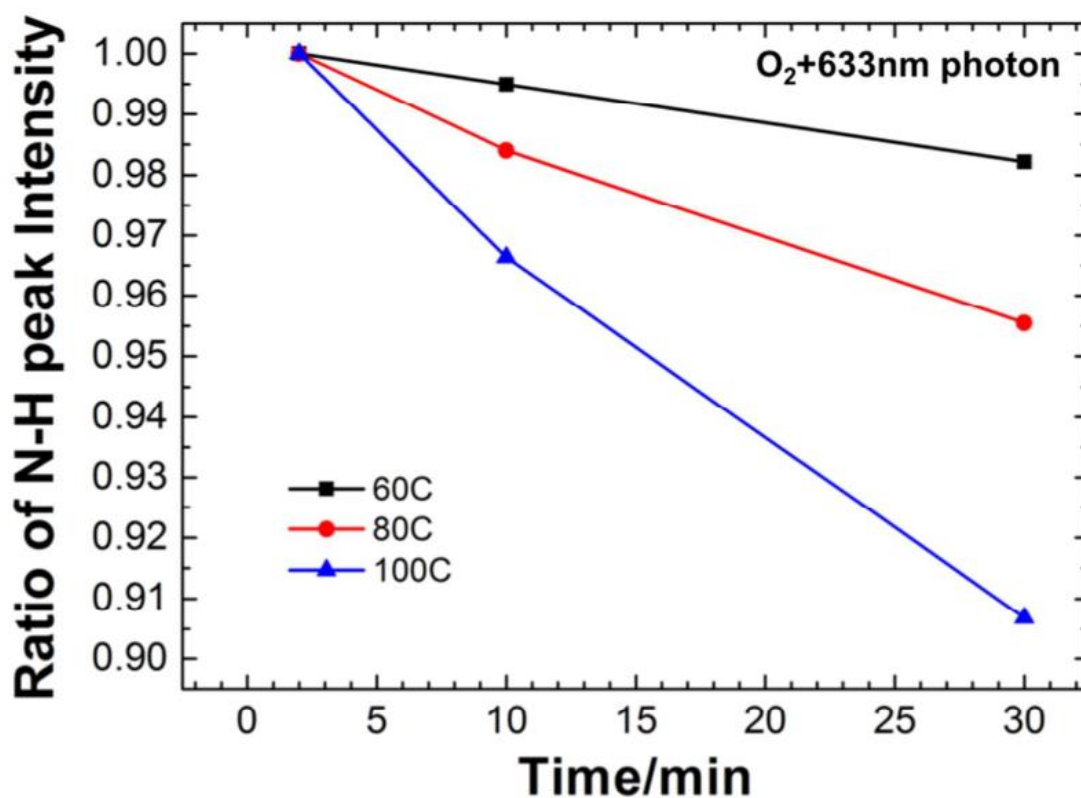


Figure S10. The change of N-H stretching mode at (3179 cm⁻¹) of MAPbI₃/KBr with annealing time in O₂ with a laser (633 nm) at 60°C, 80°C, and 100°C.

CHAPTER 4 : INSPECT THE SURFACE PROPERTY OF MAPBI₃ BY PROBE MOLECULAR OF PYRIDINE

4.1 Introduction.

Methyl amine lead iodide perovskite (CH₃NH₃PbI₃) shows promise for applications in solar cells,¹⁰⁸ light-emitting diodes,¹⁰⁹ lasers,¹¹⁰ and chemical sensors.^{111,112} Its large-scale deployment for these applications faces several challenges, including toxicity of Pb, environmental stability, charge recombination, and scalable processing of the material. Its chemical reaction with pyridine (C₅H₅N)^{113,114} has been explored to address these challenges. For instance, it is claimed that pyridine can improve the photoluminescence and solar cell performance of CH₃NH₃PbI₃ by passivating its surface coordinate-unsaturated sites (*CUS*) of Pb²⁺ through the formation of pyridine (Py-Pb²⁺).¹¹³ On the other hand, auto-generated pyridine vapor, right above liquid pyridine, can dramatically improve the conformality and crystallinity of a CH₃NH₃PbI₃ thin film within 1 min in ambient at room temperature.¹¹⁴ In addition, a similar exposure of pyridine vapor is shown to cause the optical bleach of the whole film.^{112,114} These results contradict each other as surface *CUS* passivation demands the reaction to be surface-limited or confined at surface region, but recrystallization and optical-bleach requires the transformation of the bulk film. The origin of these inconsistent results is not clear due to a lack of systematic study of the reaction behavior between pyridine and CH₃NH₃PbI₃. For example, although the passivation of Pb²⁺ *CUS* site on CH₃NH₃PbI₃ by pyridine is ascribed to its enhanced photoluminescence, the direct chemical evidence is missing. On the other hand, although the changes of morphology, crystallinity, and optical appearance of CH₃NH₃PbI₃ confirms its bulk transformation by the exposure of pyridine vapor, it is challenging to

draw a conclusive mechanism from these experiments as the impact of moisture in ambient on the chemisorption of pyridine is unknown. More importantly, no research has been done to understand the effect of partial pressure of pyridine on its reaction with $\text{CH}_3\text{NH}_3\text{PbI}_3$ even though the reaction behavior is dependent on its partial pressure. In addition, the time-evolved reaction behavior is not understood despite the fact that the extent of the reaction depends on the reaction time. These missing understandings are critical to choosing right conditions to passivate the surface and transform the bulk of a $\text{CH}_3\text{NH}_3\text{PbI}_3$ film by pyridine vapor, and to apply $\text{CH}_3\text{NH}_3\text{PbI}_3$ to sense pyridine vapor.

In this study, we show that the reaction behavior between pyridine vapor and $\text{CH}_3\text{NH}_3\text{PbI}_3$ depends strongly on the partial pressure of pyridine. When pyridine's pressure is 1.15 torr or below, the reaction takes place at the surface region of $\text{CH}_3\text{NH}_3\text{PbI}_3$ and generates PbI_2 around the surface of $\text{CH}_3\text{NH}_3\text{PbI}_3$ core. Pyridinium ion (Py^+H) is the main final product from pyridine and bonds to the surface of $\text{CH}_3\text{NH}_3\text{PbI}_3$ and PbI_2 . When pyridine's pressure is 1.3 torr or higher, the pyridine vapor can transform the whole $\text{CH}_3\text{NH}_3\text{PbI}_3$ film after a short incubation period. The reaction rate increases several-hundred times after the incubation period. The dramatically increased rate is ascribed to a liquid-like layer that is formed when the partial pressure of pyridine is 1.3 torr or higher. In the liquid-like layer, the mobility of species is increased so that they can work in concert to catalyze the reaction between pyridine and $\text{CH}_3\text{NH}_3\text{PbI}_3$. In bulk transformation, pyridine is also mainly converted into Py^+H through the proton transfer reaction between CH_3NH_3^+ and pyridine. The formed Py^+H molecules transform $\text{CH}_3\text{NH}_3\text{PbI}_3$ into undefined crystals. Our results, for the first time, show the sensitivity of reaction behaviors to the partial pressure of undersaturated pyridine vapor, that is, i.e., its free energy. Our findings highlight the critical role of fundamental studies in guiding the chemical treatment of $\text{CH}_3\text{NH}_3\text{PbI}_3$.

4.2 Results and discussions.

Exposure to Autogenic Pyridine Vapor (20 torr, 25 °C) in a Glovebox (P_20 torr Treatment).

Figure 4.1 shows the change of optical appearance of a typical $\text{CH}_3\text{NH}_3\text{PbI}_3$ film (dark) on an FTO glass ($\text{CH}_3\text{NH}_3\text{PbI}_3/\text{FTO}$) before, during, and after the exposure of pyridine vapor. The dark film becomes gray after 10 s exposure to a pyridine vapor in a glove box ($\text{H}_2\text{O} < 0.1$ ppm and $\text{O}_2 < 0.1$ ppm). The pressure of pyridine vapor is estimated to be ~ 20 torr, the saturated vapor pressure of pyridine at 25 °C and 1 atm. After 1 min exposure to this pyridine vapor, the film becomes transparent. For convenience, we will refer this treatment as P_20torr. After the removal of the pyridine vapor, the transparent film turns into brownish within 1 min in glove box, not yet fully recovered to the original dark color even after 30 min back into the N_2 filled glove box. Although the changes of optical appearance of $\text{CH}_3\text{NH}_3\text{PbI}_3$ film is generally consistent with previous reports,^{112,114} the recovery of $\text{CH}_3\text{NH}_3\text{PbI}_3$ from the pyridine bleached film is much slower in our experiment than that in other reports. The slow rate is due to the moisture free environment in the glove box (**Figure S1**).

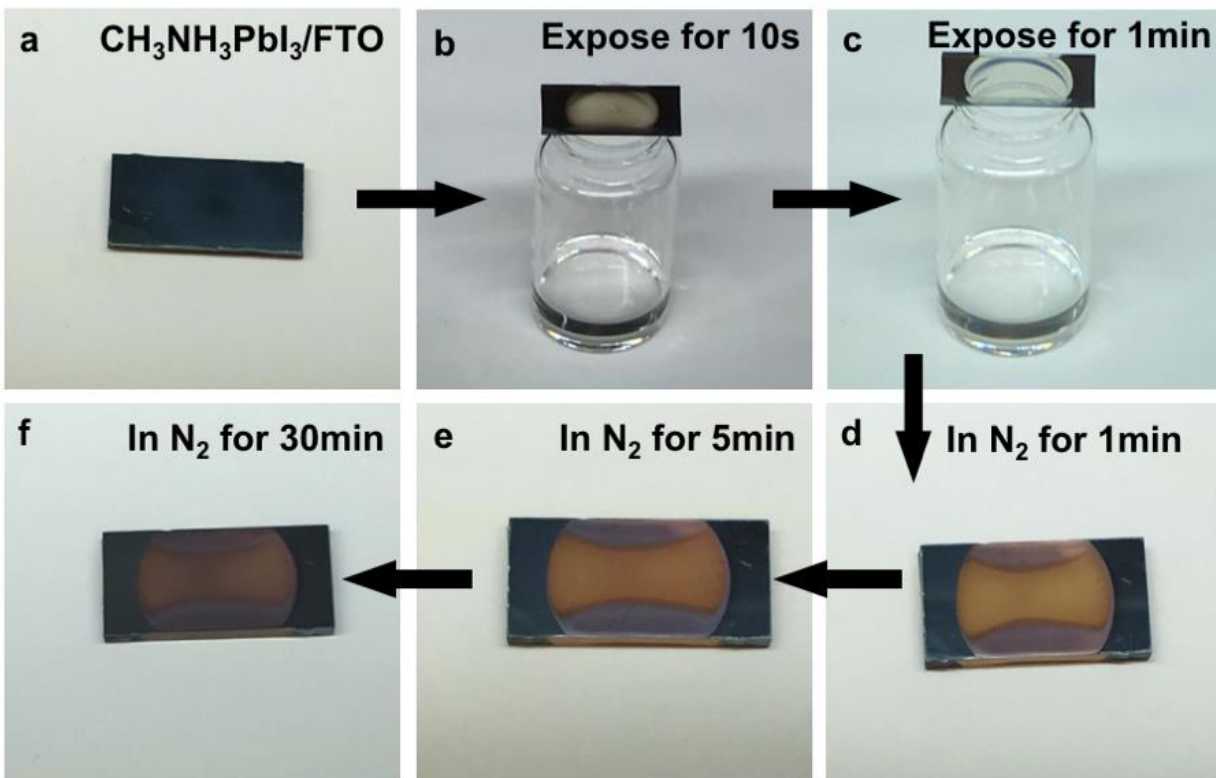


Figure 4.1. Optical images of a $\text{CH}_3\text{NH}_3\text{PbI}_3/\text{FTO}$ sample (a) before pyridine exposure; (b, c) after 10 s and 1 min of exposure to autogenic pyridine vapor (~ 20 torr at 25°C) in a glovebox; (d–f) 1, 5, and 30 min in N_2 (glovebox) after removal of the pyridine vapor.

Figure 4.2 presents the IR spectra of a $\text{CH}_3\text{NH}_3\text{PbI}_3$ film on Si substrate ($\text{CH}_3\text{NH}_3\text{PbI}_3/\text{Si}$) before and after P_20torr treatment. All of these IR spectra use Si as the reference. The clean $\text{CH}_3\text{NH}_3\text{PbI}_3/\text{Si}$ shows only the characteristic peaks of $\text{CH}_3\text{NH}_3\text{PbI}_3$ ^{115,116}: asymmetric and symmetric stretching modes of N-H (3179 and 3125 cm^{-1}), asymmetric and symmetric C-H stretching modes (2958 and 2921 cm^{-1}), C-H bending mode (1422 cm^{-1}), asymmetric and symmetric N-H bending modes of NH_3^+ (1577 and 1469 cm^{-1}), $\text{CH}_3\text{-NH}_3^+$ rocking modes (1249 and 910 cm^{-1}), C-N stretching mode (962 cm^{-1}),²²⁻²⁴ This IR spectrum is consistent with $\text{CH}_3\text{NH}_3\text{PbI}_3$. After the pyridine treatment of P_20 torr, the $\text{CH}_3\text{NH}_3\text{PbI}_3/\text{Si}$ sample after P_20torr treatment is quickly transferred from the glove box to the dry air purged IR chamber. The whole transfer process takes less than 1 min with a brief ambient exposure that is less than 30 s.

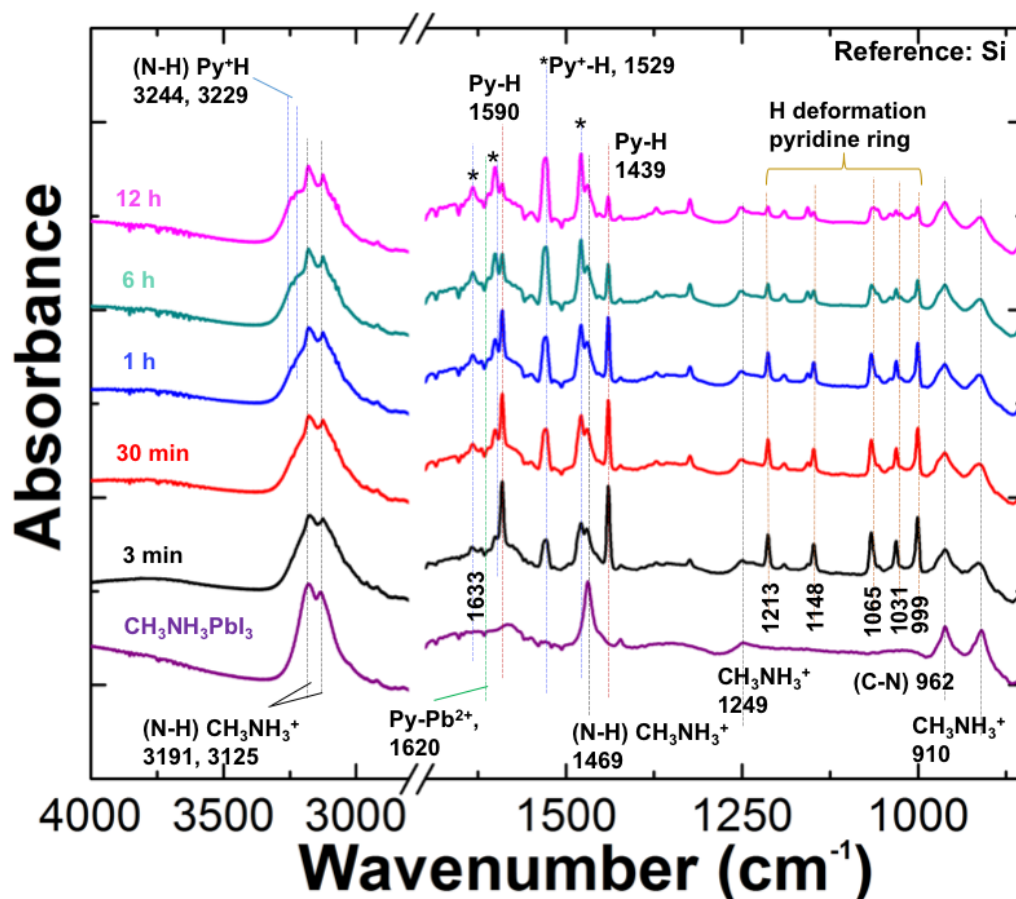


Figure 4.2. Time-evolved IR spectra of a $\text{CH}_3\text{NH}_3\text{PbI}_3/\text{Si}$ after P_{20} torr treatment. The spectra were recorded at 3 min, 30 min, 1, 6, and 12 h in a dry-air purged IR chamber. IR spectrum of a clean $\text{CH}_3\text{NH}_3\text{PbI}_3/\text{Si}$ is added for the comparison. All spectra use Si as the reference. Blue dash lines are peaks from Py^+H . Red dash lines are peaks from Py-H . Green dash line is the ring-vibration mode from Py-Pb^{2+} . Brown dash lines are H-deformation from all pyridine species. Black dash lines are peaks from $\text{CH}_3\text{NH}_3\text{PbI}_3$. * represents the ring vibration modes of Py^+H .

After the P_{20} torr treatment, the IR spectra of $\text{CH}_3\text{NH}_3\text{PbI}_3/\text{Si}$ sample are recorded at 3 min, 30 min, 3 h, 6 h, and 12 h in dry air. The spectra show the time-evolved chemical composition of the sample in dry air. *First*, after P_{20} torr treatment, the film still has the peaks from $\text{CH}_3\text{NH}_3\text{PbI}_3$, 3175, 3132, 1469, 1249, 962, and 910 cm^{-1} . The absorbance of these peaks does not change much with time and is $\sim 73\%$ of the value from the original $\text{CH}_3\text{NH}_3\text{PbI}_3$. Therefore, a significant amount of CH_3NH_3^+ is still preserved inside the film, and its concentration is relatively stable during the 12 h in dry air. *Second*, Py^+H is generated inside of the film, and their absorbance

increases with time in dry air. According to the studies that use pyridine molecules to probe Lewis acid and Brønsted acid surface sites,¹¹⁷⁻¹²¹ the IR peaks at 1633, 1601, 1528 and 1478 cm^{-1} are the unique ring-vibration modes of pyridine in Py^+H . Their absorbance increases with time; it means more and more Py^+H molecules are generated, presumably, through the proton transfer reaction from CH_3NH_3^+ to pyridine. In addition, the N-H stretching mode of Py^+H ¹¹⁷⁻¹²¹, a shoulder peak at 3250 cm^{-1} , becomes clearer with time increasing; it confirms the continuous formation of Py^+H .

Third, there are $\text{Py}\text{-H}$ molecules inside the film and its concentration decreases with time. The positive peaks at 1590 and 1439 cm^{-1} belong to the ring-vibration modes of $\text{Py}\text{-H}$.¹¹⁷ The absorbance of these $\text{Py}\text{-H}$ peaks decreases with time, suggesting the reduction of $\text{Py}\text{-H}$'s concentration. It is a surprise that $\text{Py}\text{-H}$ molecules are still in the film even after 12 h in dry air. In addition, in the 3 min spectra, the broad N-H stretching modes (3000-3500 cm^{-1}) become broader than clean $\text{CH}_3\text{NH}_3\text{PbI}_3$. It is due to the hydrogen bonding formed between pyridine and CH_3NH_3^+ , namely $\text{Py}\text{-H}$.

Fourth, after $\text{P}_{-20\text{torr}}$ treatment, the concentration of $\text{Py}\text{-Pb}^{2+}$ is negligible, but increases very slowly with time. The ring-vibration mode of pyridine in $\text{Py}\text{-Pb}^{2+}$ is located at ~ 1610 cm^{-1} , whose absorbance is negligible in the 3 min spectrum and becomes detectible in the 6 h spectrum.

Fifth, pyridine is continuously removed from the film through desorption. In all pyridine related species, including Py^+H , $\text{Py}\text{-H}$, and $\text{Py}\text{-Pb}^{2+}$, pyridine ring has in-plane C-H deformation modes, whose IR peaks are located at 1213, 1148, 1066, 1030, and 1000 cm^{-1} . The absorbance of these peaks decreases with increasing the time in dry air. Because the concentrations of $\text{Py}\text{-Pb}^{2+}$ and Py^+H increases with time upto 12 h, the reduction of their absorbance is from the removal of $\text{Py}\text{-H}$ from the sample through the desorption. In summary, using the unique ring-vibrations of three types bonded pyridine, Py^+H , $\text{Py}\text{-H}$, and $\text{Py}\text{-Pb}^{2+}$,¹¹⁷⁻¹²¹ we are able to identify that $\text{Py}\text{-H}$ and Py^+H are the main components of pyridine inside of the $\text{CH}_3\text{NH}_3\text{PbI}_3$ film right after $\text{P}_{-20\text{torr}}$ treatment. We also show the continuous formation Py^+H in dry air through the proton transfer reaction from CH_3NH_3^+

to pyridine, with Py-H as intermediate compounds. Pyridine molecules can bond to the uncoordinated Pb^{2+} orbital in PbI_x^{x-2} to form Py-Pb^{2+} , which is a minor component in comparison with the formed Py^+H . This result disagrees with the previous claim of selective formation of Py-Pb^{2+} by treating $\text{CH}_3\text{NH}_3\text{PbI}_3$ with pyridine molecules.¹¹³

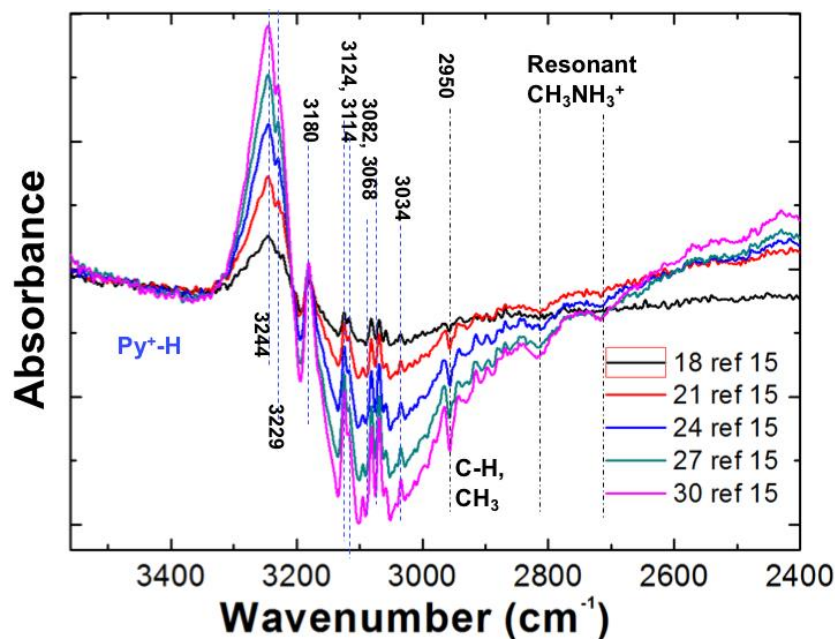


Figure 4.3. Differential IR spectra of $\text{CH}_3\text{NH}_3\text{PbI}_3/\text{Si}$ (after P_20 torr treatment) at 18, 21, 24, 27, and 30 min in dry air with the spectrum at 15 min in dry air as the reference. A negative peak means the related species is removed during the period in dry air. A positive peak means the related species are generated. Blue dash lines are peaks from Py^+H . The black dash lines are peaks from CH_3NH_3^+ . The broad negative peak centered around 3100 cm^{-1} is due to the removal of CH_3NH_3^+ .

To better illustrate the chemical change of $\text{CH}_3\text{NH}_3\text{PbI}_3/\text{Si}$ in dry air after P_20 treatment, we present, in **Figure 4.3**, the differential spectra of the sample within a short time frame. The sample after 15 min in dry air is used as the reference. The positive peaks at 3244 and 3229 cm^{-1} are N-H stretches from Py^+H that are bonded to PbI_x^{x-2} .¹¹⁷ The relatively small positive peaks at 3180 and 3124 are also N-H from the Py^+H molecules that are bonded to PbI_x^{x-2} .¹¹⁷ Peaks at 3114 , 3082 , 3068 , and 3034 cm^{-1} are probably the C-H stretches on pyridine ring in Py-H^+ . The large broad negative peak ranging from $2900 - 3200\text{ cm}^{-1}$ is N-H and C-H stretches from the consumed CH_3NH_3^+ molecules and removed pyridine molecules. The broad peak becomes larger with time

because CH_3NH_3^+ and pyridine are continuously removed from the substrate, but at a very slow rate. The negative peaks at 2820 and 2950 cm^{-1} are probably the resonant peaks from CH_3NH_3^+ . The complex N-H stretching modes of Py^+H indicates its complex bonding environment.

From these IR spectra, we conclude that major reaction pathway between pyridine and $\text{CH}_3\text{NH}_3\text{PbI}_3$ proceeds with the formation of Py-H bonded with CH_3NH_3^+ , shown in (Eq. 1). A portion of the Py-H molecules desorbs from the film as pyridine molecules (Eq. 1), the other portion is converted into Py^+H through the proton transfer reaction from CH_3NH_3^+ to pyridine (Eq. 2). These Py^+H molecules are mainly coordinated to PbI_x^{x-2} (Eq. 3). The absorbance of Py^+H in the 3 min spectrum is 0.1486. It takes 2 h to double its absorbance after the film is sitting in dry air (**Figure S1** and **Figure 4.2**). It suggests that the formation rate of Py^+H is much faster during the 1 min exposure of pyridine vapor of 20 torr than that from the film that is removed from the 20 torr pyridine vapor. It is partially due to the low concentration of Py-H in the film in dry air and partially due to the restriction of movement of ionic species.

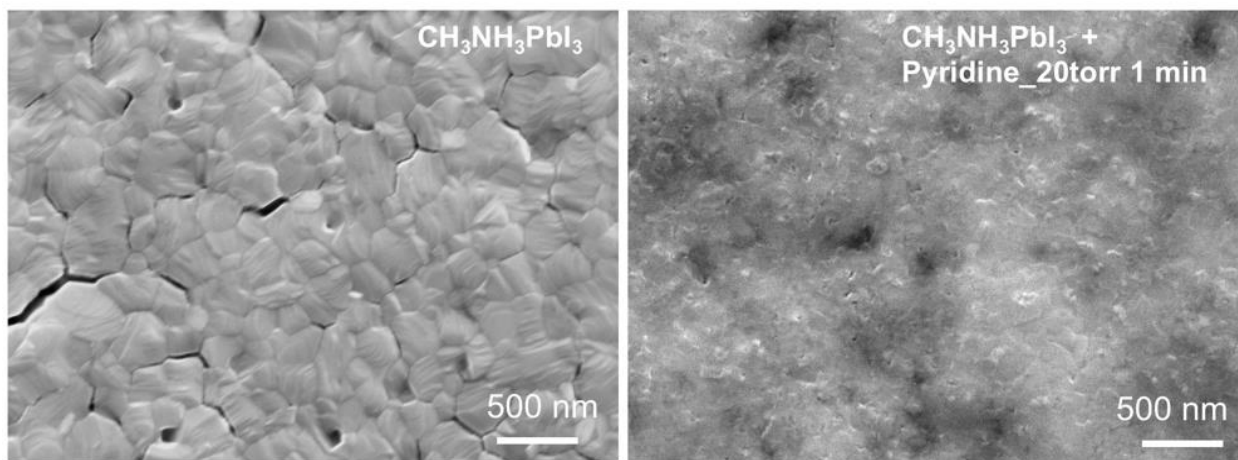
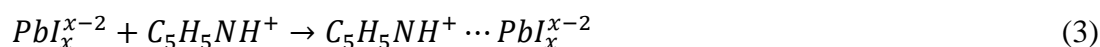
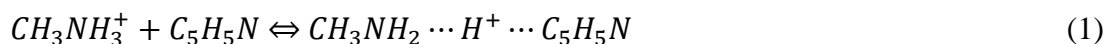


Figure 4.4. SEM images of a pure $\text{CH}_3\text{NH}_3\text{PbI}_3/\text{Si}$ sample (a) and $\text{CH}_3\text{NH}_3\text{PbI}_3/\text{Si}$ after P_20 torr treatment and sitting in N_2 for 30 min (b). The SEM images show that P_20 torr treatment changes the surface morphology of $\text{CH}_3\text{NH}_3\text{PbI}_3$.

Figure 4.4 presents the SEM image of the $\text{CH}_3\text{NH}_3\text{PbI}_3/\text{Si}$. The sample consists of grains. There are randomly distributed cracks in the film. The morphology of sample changes dramatically after P_20torr treatment and sitting in N_2 for 30 min. The texture of grains disappears. The cracks are healed. These changes are due to the movement of ions that is triggered by the pyridine vapor.

Figure 4.5 shows the XRD spectrum of $\text{CH}_3\text{NH}_3\text{PbI}_3/\text{Si}$ after P_20torr treatment sitting in glove box for 30 min. The XRD spectra of $\text{CH}_3\text{NH}_3\text{PbI}_3$, $\text{CH}_3\text{NH}_3\text{I}$, and PbI_2 are added for comparison. The pure $\text{CH}_3\text{NH}_3\text{PbI}_3$ film has diffraction peaks at 14.1, 20.0, 23.5, 24.4, 26.5, 28.4, 31.8, 33.7, 34.9, 37.7, 40.7, and 43.2 degree, which are consistent with literature report.^{114,122,123} After P_20torr treatment, the $\text{CH}_3\text{NH}_3\text{PbI}_3/\text{Si}$ thin film shows a major new peak at ~ 12.4 degree and small new peaks at 11.0, 14.1, 19.0, 21.5, and 22.3 degree. These new peaks do not belong to either PbI_2 or $\text{CH}_3\text{NH}_3\text{I}$, for PbI_2 film shows peaks at 14.7 and 45.1 degree, and pure $\text{CH}_3\text{NH}_3\text{I}$ film shows peaks at 11.4, 22.8, and 34.2 degree.^{114,122,123} These new peaks probably result from Py^+H coordinated PbI_x^{x-2} cluster^{45,124}. Our finding is different from the previously reported result,¹¹⁴ which claims $\text{CH}_3\text{NH}_3\text{I}$ as the product after $\text{CH}_3\text{NH}_3\text{PbI}_3$ is bleached by pyridine. In addition, in our recovered film, the intensity of all peaks from $\text{CH}_3\text{NH}_3\text{PbI}_3$ are dramatically reduced. This result is also in contrast with the previous report, where the recovered $\text{CH}_3\text{NH}_3\text{PbI}_3$ shows dramatically improved crystallinity. These differences may due to the difference in moisture level in recrystallizing the $\text{CH}_3\text{NH}_3\text{PbI}_3$ after the pyridine treatment, because in our experiment sample is recovered in H_2O free glove box, while in the previous reports, the sample recovery is done in a controlled dry air environment. In our control experiments, the formation rate of PyH^+ and removal rate of Py-H are dramatically enhanced in the moisture environments (**Figure S1**).

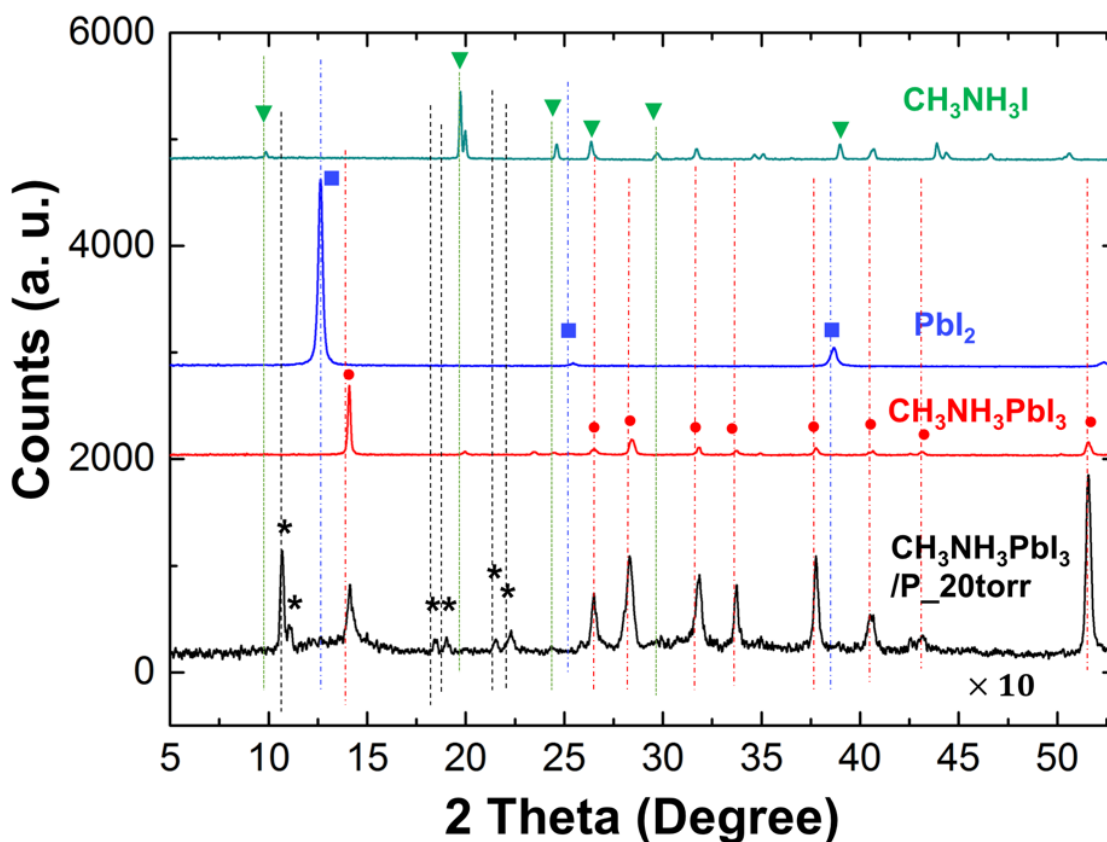


Figure 4.5. XRD patterns of $\text{CH}_3\text{NH}_3\text{PbI}_3$ (red, ●, red dash-dot lines) and $\text{CH}_3\text{NH}_3\text{PbI}_3/\text{Si}$ after P_20 torr treatment and sitting in N_2 for 30 min (black, *, black dashlines) after. The XRD patterns of $\text{CH}_3\text{NH}_3\text{I}$ (green, ▼, green dashlines) and PbI_2 (blue, ■, blue dash-dot lines) are shown for comparison.

Exposure to Pulses of Pyridine Vapor (<0.5 torr) in a Vacuum Reactor (Pulse Treatment).

To further understand the reaction between pyridine and $\text{CH}_3\text{NH}_3\text{PbI}_3$, we studied the isothermal pyridine sorption onto $\text{CH}_3\text{NH}_3\text{PbI}_3$ films. We first tried the pulsing mode, in which 1 s pulse of room temperature pyridine vapor is injected into the N_2 carrier gas stream. An in-situ quartz crystal microbalance is used to record the mass change onto a $\text{CH}_3\text{NH}_3\text{PbI}_3$ film induced by pyridine vapor in a vacuum reactor. The injection of pyridine vapor causes a spike of pressure of 0.3 - 0.5 torr on top of the process pressure (~ 0.9 torr, 250 sccm N_2). As shown by **Figure 4.6a**, the first pulse of pyridine vapor causes a spike of mass gain onto $\text{CH}_3\text{NH}_3\text{PbI}_3$ surface at 25 °C. A portion of the gained mass is removed during the following purge step with only N_2 . The removed mass is due to the removal of weakly bonded physisorbed pyridine. The net mass gain that

survives the purge step is from the chemically-bonded pyridine onto $\text{CH}_3\text{NH}_3\text{PbI}_3$ surface. Then, another 15 pulses of pyridine vapor are introduced onto the sample. The mass gain behavior in these pulses similar as the 1st pulse, except that the magnitude of mass gain and removal in each pulse decrease with increasing the pulse number. The net mass gain from No. 16 pulse is negligible, suggesting no more reaction after 16 of 1 s pulse of pyridine vapor. After 16 pulses of pyridine vapor, the total chemically bonded pyridine reaches $\sim 0.35 \mu\text{g}/\text{cm}^2$ (**Figure 4.6a**).

As shown in **Figure 4.6b**, the intensity of XRD peaks from $\text{CH}_3\text{NH}_3\text{PbI}_3$ is barely affected after the multiple pyridine pulses, except the generation of a small peak of PbI_2 . In addition, as shown by the **Figure 4.6c** and **4.6d**, these pulses of pyridine vapor have a marginal impact on the surface morphology of a $\text{CH}_3\text{NH}_3\text{PbI}_3$ film. The subtle difference of the surface morphology is due the variation of surface morphology of the sample at the different locations. The $\text{CH}_3\text{NH}_3\text{PbI}_3$ film has a large amount of cracks before and after the 16 pulses of pyridine vapor. These cracks are not healed by the pulses of pyridine. The XRD and SEM results are consistent with the QCM results, confirming that multiple 1 s pulses pyridine vapor (0.3 - 0.5 torr) reacts with a $\text{CH}_3\text{NH}_3\text{PbI}_3$ film at the surface region. The IR analyses (**Figure 4.7**) shows the formation of Py^+H and removal of CH_3NH_3^+ , without presence of Py-H .

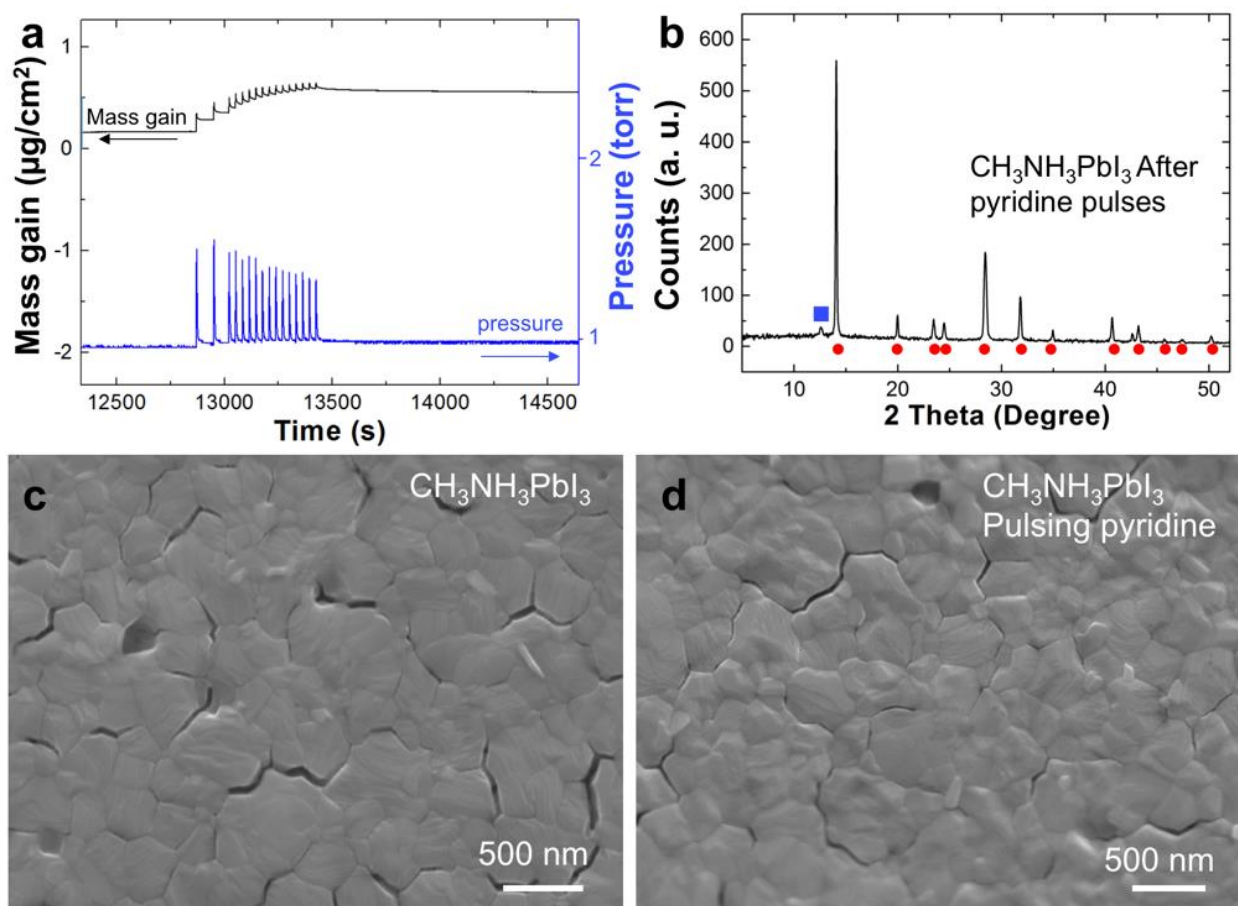


Figure 4.6. (a) The mass gain occurred on a $\text{CH}_3\text{NH}_3\text{PbI}_3$ film measured by QCM in exposure to 16 pulses of pyridine vapor (1 s each). The blue trace is the reactor's pressure, with the spike from pyridine pulses, and the black trace is the mass gain from the in situ QCM. (b) XRD pattern of $\text{CH}_3\text{NH}_3\text{PbI}_3/\text{Si}$ after 16 pyridine pulses. (blue, \blacksquare) and (red, \bullet) are peaks from PbI_2 and $\text{CH}_3\text{NH}_3\text{PbI}_3$. (c, d) SEM images show that surface morphology of $\text{CH}_3\text{NH}_3\text{PbI}_3/\text{Si}$ sample is similar before (c) and after (d) the pyridine pulses

On the basis of the ex situ IR and XRD measurements, the low-pressure pyridine vapor generates mainly Py^+H and PbI_2 and removes CH_3NH_3^+ from the $\text{CH}_3\text{NH}_3\text{PbI}_3$. According to the reaction, the net mass gain is 48 g/mol Py^+H . If we assume the packing density of CH_3NH_3^+ sites are 1×10^{15} molecules/ cm^2 , a monolayer of bonded pyridine weighs 0.077 $\mu\text{g}/\text{cm}^2$. The obtained mass is ~ 0.350 $\mu\text{g}/\text{cm}^2$ and is larger than 0.077 $\mu\text{g}/\text{cm}^2$. This discrepancy is partially due to the cracks in the $\text{CH}_3\text{NH}_3\text{PbI}_3$ film (**Figure 6c,d**) and roughness of $\text{CH}_3\text{NH}_3\text{PbI}_3$ film. It is important to note that the 1 cm^2 area is the projected area. Roughness and cracks mean more sites in a projected 1 cm^2 area than sites in a projected 1 cm^2 area than the solid flat surface. In solid flat surface. In

addition, the initial $\text{CH}_3\text{NH}_3\text{PbI}_3$ film has a mass of $260 \pm 25 \mu\text{g}/\text{cm}^2$, which is $0.42 \pm 0.04 \mu\text{mol}/\text{cm}^2$ of $\text{CH}_3\text{NH}_3\text{PbI}_3$. If we assume all CH_3NH_3^+ are replaced by Py^+H , the net mass gain would be $20 \pm 2 \mu\text{g}/\text{cm}^2$ (for details of calculation, see [Supporting Information](#)). Because this value is much larger than the $0.35 \mu\text{g}/\text{cm}^2$, the reaction between multiple pulses of pyridine vapor and $\text{CH}_3\text{NH}_3\text{PbI}_3$ is confined close to the surface region of $\text{CH}_3\text{NH}_3\text{PbI}_3$. Therefore, we demonstrate that pulsing pyridine vapor is a reliable way to modify the surface of $\text{CH}_3\text{NH}_3\text{PbI}_3$.

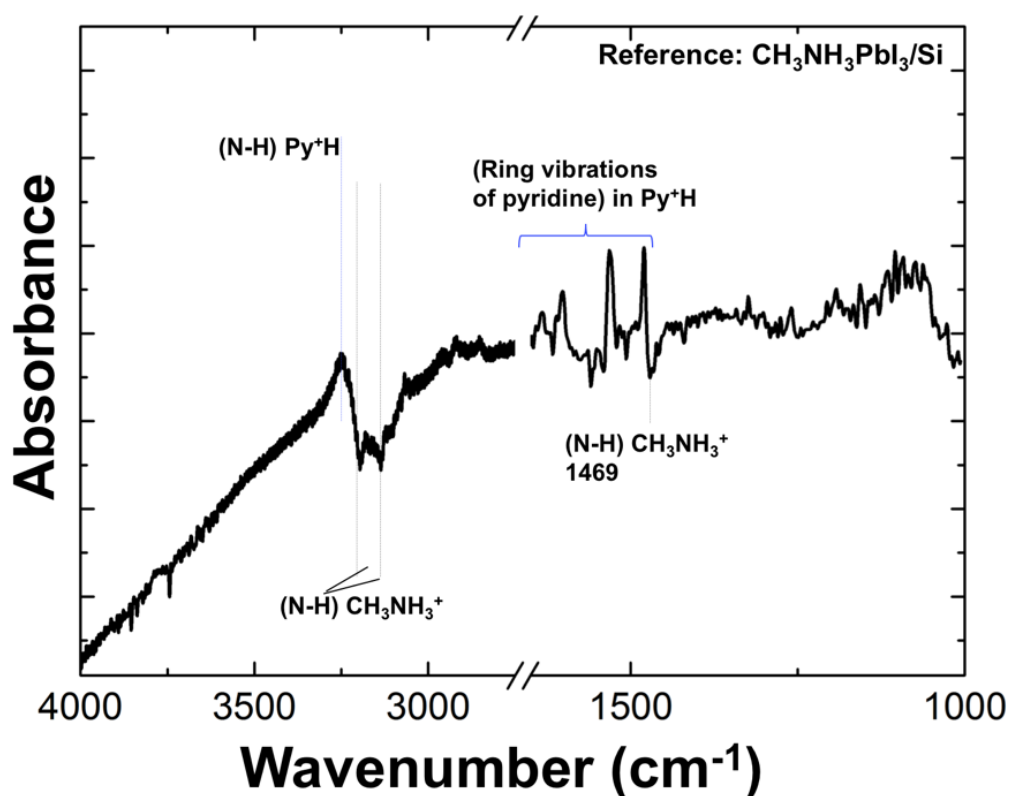


Figure 4.7. IR spectrum of $\text{CH}_3\text{NH}_3\text{PbI}_3$ after 16 pulses of pyridine vapor. It shows that Py^+H is formed and CH_3NH_3^+ is removed.

Exposure to Pyridine Vapor of Different Pressure in a Vacuum Reactor

We further performed the isothermal experiment in a batch mode to understand the effect of pyridine vapor pressures on its reaction with $\text{CH}_3\text{NH}_3\text{PbI}_3$. Specifically, after evacuated to 50 mtorr and isolated from the processing pump, the vacuum reactor is quickly filled with pure pyridine vapor of a desired pressure. A QCM crystal records the mass change of a $\text{CH}_3\text{NH}_3\text{PbI}_3$ film throughout the whole process. As shown in **Figure 4.8**, before the pyridine exposure, the

$\text{CH}_3\text{NH}_3\text{PbI}_3$ film is stable inside vacuum reactor at 25 °C, as its mass is stable in this condition. Then the film is exposed to pyridine vapor of 0.5 torr for ~8700 s. The mass gain rate is high initially and decreases with time. After ~1 h of exposure, the mass gain rate is small and remains relatively constant. The $\text{CH}_3\text{NH}_3\text{PbI}_3$ film gains a mass of ~0.9 $\mu\text{g}/\text{cm}^2$ after 8700 s of exposure. The following N_2 purge step removes the pyridine vapor and the physically bonded pyridine molecules on the film. The final sustained mass is ~0.8 $\mu\text{g}/\text{cm}^2$, which is from chemically bonded pyridine. The $\text{CH}_3\text{NH}_3\text{PbI}_3$ film shows similar mass gain behavior when exposed to 0.3 torr pyridine for 10 000 s (**Figure S2**). This mass gain behavior is consistent with the results from pulsing pyridine vapor of similar pressure to $\text{CH}_3\text{NH}_3\text{PbI}_3$, except the mass gain here is higher than that in the pulsing mode. The higher mass gain is probably due to the long exposure of pyridine and higher surface area per 1 cm^2 of projected area. In long exposure of 0.5 and 0.3 torr pyridine, the mass gain keeps increasing with time but at a slower rate in the later stage. As pyridine's partial pressure and reaction temperature are not changing, the slow mass gain rate in the later stage is partially due to the reduced reactive sites on the substrate as the reaction proceeds and partially due to the formation of PbI_2 layer, which slows the reaction by limiting the diffusion of pyridine or CH_3NH_3^+ . The amount of mass gain and slow mass gain rate at the later stage indicate the reaction is still confined at the surface region of the $\text{CH}_3\text{NH}_3\text{PbI}_3$ film. This is confirmed by the XRD spectrum (**Figure S3**) of the sample after 8700 s of exposure to 0.5 torr pyridine. It shows a small peak of PbI_2 and largely unaffected peaks from $\text{CH}_3\text{NH}_3\text{PbI}_3$.

We further performed the isothermal experiment in a batch mode to understand the effect of pyridine vapor pressures on its reaction with $\text{CH}_3\text{NH}_3\text{PbI}_3$. Specifically, after evacuated to 50 mtorr and isolated from the processing pump, the vacuum reactor is quickly filled with pure pyridine vapor of a desired pressure. A QCM crystal records the mass change of a $\text{CH}_3\text{NH}_3\text{PbI}_3$ film throughout the whole process. As shown in **Figure 4.8**, before the pyridine exposure, the

CH₃NH₃PbI₃ film is stable inside vacuum reactor at 25 °C, as its mass is stable in this condition. Then the film is exposed to pyridine vapor of 0.5 torr for ~8700 s. The mass gain rate is high initially and decreases with time. After ~1 h of exposure, the mass gain rate is small and remains relatively constant. The CH₃NH₃PbI₃ film gains a mass of ~0.9 μg/cm² after 8700 s of exposure. The following N₂ purge step removes the pyridine vapor and the physically bonded pyridine molecules on the film. The final sustained mass is ~0.8 μg/cm², which is from chemically bonded pyridine. The CH₃NH₃PbI₃ film shows similar mass gain behavior when exposed to 0.3 torr pyridine for 10 000 s (**Figure S2**). This mass gain behavior is consistent with the results from pulsing pyridine vapor of similar pressure to CH₃NH₃PbI₃, except the mass gain here is higher than that in the pulsing mode. The higher mass gain is probably due to the long exposure of pyridine and higher surface area per 1 cm² of projected area. In long exposure of 0.5 and 0.3 torr pyridine, the mass gain keeps increasing with time but at a slower rate in the later stage. As pyridine's partial pressure and reaction temperature are not changing, the slow mass gain rate in the later stage is partially due to the reduced reactive sites on the substrate as the reaction proceeds and partially due to the formation of PbI₂ layer, which slows the reaction by limiting the diffusion of pyridine or CH₃NH₃⁺. The amount of mass gain and slow mass gain rate at the later stage indicate the reaction is still confined at the surface region of the CH₃NH₃PbI₃ film. This is confirmed by the XRD spectrum (**Figure S3**) of the sample after 8700 s of exposure to 0.5 torr pyridine. It shows a small peak of PbI₂ and largely unaffected peaks from CH₃NH₃PbI₃

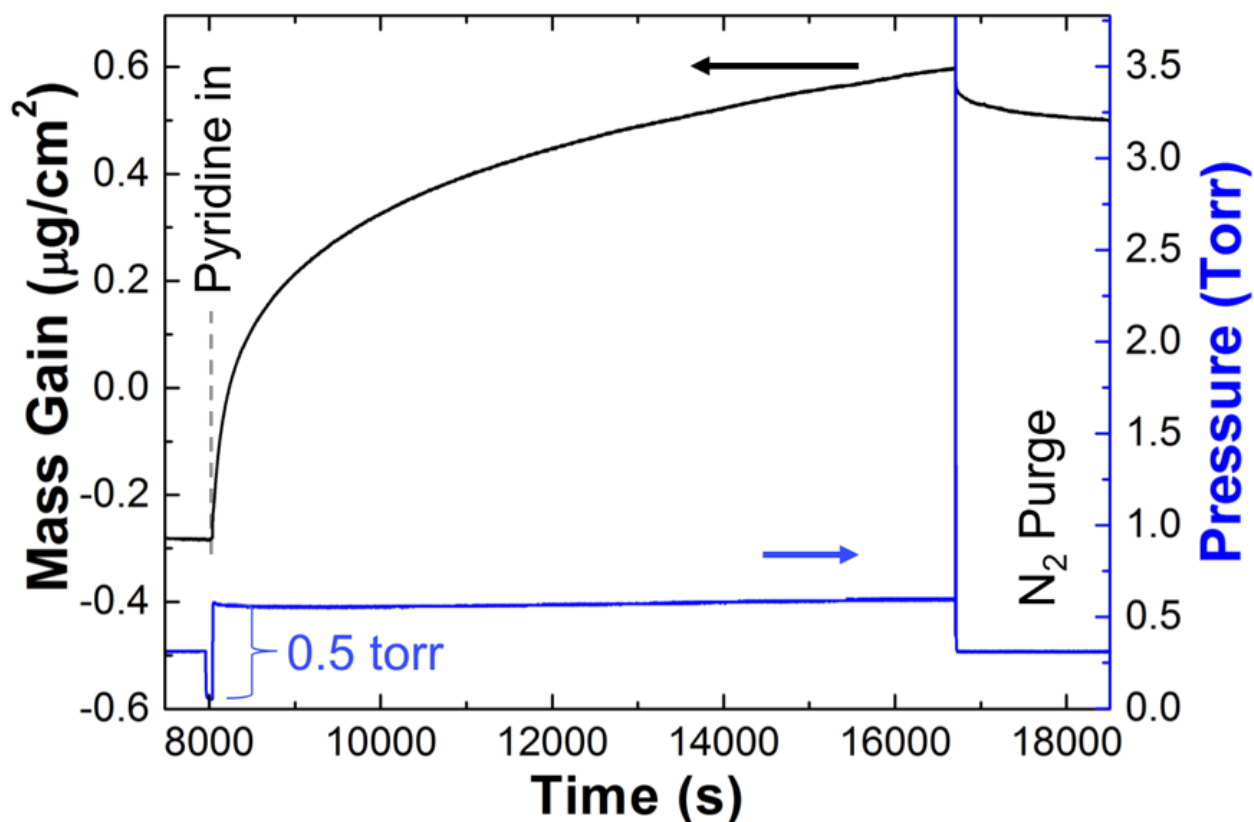


Figure 4.8. (a) Mass gain (black line) vs time for a $\text{CH}_3\text{NH}_3\text{PbI}_3$ film before, during and after exposure to pyridine vapor at partial pressures of 0.5 torr (blue).

With the exposure to a pyridine vapor of 1.3 torr, the typical time-evolved mass gain on a fresh $\text{CH}_3\text{NH}_3\text{PbI}_3$ film (**Figure 4.9**) is dramatically different than that with pyridine of 0.5 torr. The most pronounced features in **Figure 4.9a** are the abnormal jump of mass gain to $74 \times 10^3 \mu\text{g}/\text{cm}^2$ after ~ 1000 s exposure to the pyridine vapor. These abnormal mass gains are an artifact due to the formation of a short-circuit between the two originally isolated electrodes on the front and back sides of the QCM substrate. It is noteworthy that the $\text{CH}_3\text{NH}_3\text{PbI}_3$ film is only coated on the front electrode of the QCM substrate. There is a gap of couple of millimeters between the edge of the QCM substrate and the back electrode. Therefore, in order to short-out the front and back electrodes, a conductive fluid must flow to bridge the gap must flow across. According to these results, the product, after ~ 1000 s reaction, is an electrically conductive fluid. As $\text{CH}_3\text{NH}_3\text{PbI}_3$ is an insulating solid in dark vacuum reactor, the electrically conductive fluid is presumably due to the

increased mobility of ionic species caused by the reaction with pyridine. The evacuation of pyridine vapor fixes the short-circuit instantaneously, because the removal of pyridine converts the conductive fluid into an insulating material.

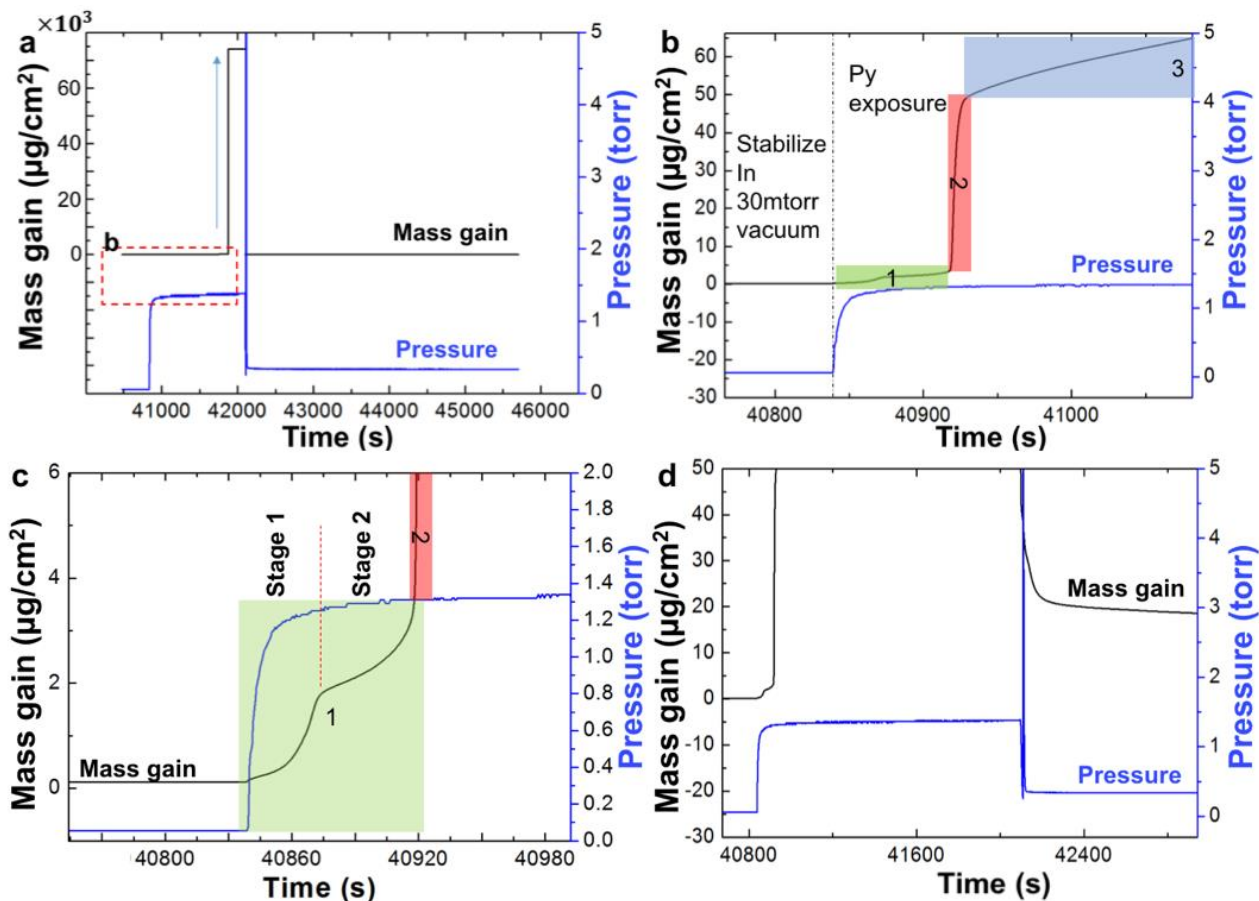


Figure 4.9. (a) Overall view of the time-evolved mass gain (black trace) occurred onto a $\text{CH}_3\text{NH}_3\text{PbI}_3$ film during the exposure of pyridine vapor of 1.38 torr in a vacuum reactor. It is termed P_1.3 torr treatment. The measured mass gain suddenly jumps to $74 \times 10^3 \mu\text{g}/\text{cm}^2$. It is an artifact due to the short of the back and front electrodes of QCM crystal by the reaction product. (b) The enlarged view of dash line window in (a). The mass gain behavior changes with reaction time and is categorized into three Zones (1–3) as shown by shadowed areas. (c) The enlarged view of transient mass gain behavior in Zone 1. Zone 1 consists of two Stages (1–2). (d) The transient mass gain behavior during the evacuation of the pyridine vapor. The mass gain stabilizes at $\sim 20 \mu\text{g}/\text{cm}^2$ and is from the absorbed pyridine molecules. (a–d) The mass gain is the black trace, and the pressure is the blue trace.

To understand the progress of reaction between pyridine vapor and $\text{CH}_3\text{NH}_3\text{PbI}_3$, we present the detail mass gain behavior before the electrodes are shorted. After the introduction of 1.3 torr pyridine vapor, the time-evolved mass gain can be categorized into three Zones (1–3) as marked

in **Figure 4.9b**. Zone 1 lasts ~ 80 s and is the incubation period. The mass gain from Zone 1 is ~ 1.6 $\mu\text{g}/\text{cm}^2$, and the reaction in Zone 1 is largely confined to the surface region but with an additional complexity, which will be discussed later in **Figure 4.9c**. In Zone 2, right after the incubation period, the mass gain rate dramatically increases to 9 $\mu\text{g}/(\text{cm}^2 \text{ s})$, which is ~ 350 times of the rate in Zone 1. The mass gain from Zone 2 is ~ 46 $\mu\text{g}/\text{cm}^2$. After that, the rate of mass gain decreases significantly to 0.1 $\mu\text{g}/(\text{cm}^2 \text{ s})$ in Zone 3. At this rate, more and more pyridine molecules are absorbed into the film until the QCM electrodes are shorted. It is important to note that the pressure of pyridine vapor is stable at 1.3 torr during the exposure; therefore, the change of mass gain rate is from the progression of the reaction. The growth behavior can be repeated well with 1.3 torr pyridine vapor (**Figure S4**). The amounts and rates of mass gain at each zone are not exactly the same during several experiments. This difference is due to the variation of $\text{CH}_3\text{NH}_3\text{PbI}_3$ film, including surface roughness and density of cracks and impurities.

A finer detail of Zone 1 is shown in **Figure 4.9c**. The transient mass gain in Zone 1 consists of two stages, both of which are concave to the axis of the mass gain. This is different than the reaction behavior of pyridine at a lower pressure (e.g., 0.5 torr). In the Stage 1, the reaction rate ramps up fast and then levels off into the second stage at ~ 1.6 $\mu\text{g}/\text{cm}^2$. The rate of mass gain in the second stage increases quickly with time and merges into Zone 2. Stage 1 and Stage 2, i.e., Zone 1, are the induction period of Zone 2. This mass gain behavior is dramatically different than that from the low-pressure pyridine experiments as well. On the basis of the amount of mass gain, the first concave curve is probably from the reaction between pyridine molecules and the exposed surface of the film. The $\text{CH}_3\text{NH}_3\text{PbI}_3$ sample is exposed to 1.3 torr pyridine vapor for ~ 1200 s before we start to pump out the pyridine vapor. As soon as we start pumping out the pyridine vapor from the reactor, the QCM crystal starts functioning again (**Figure 4.9d**), because the shorted electrodes become insulated. The removal of mass is probably due to the desorption of pyridine and

CH₃NH₂ molecules. The mass removal rate slows dramatically with increasing the pumping time (Figure 9d). The final attained stable mass gain is ~17 μg/cm².

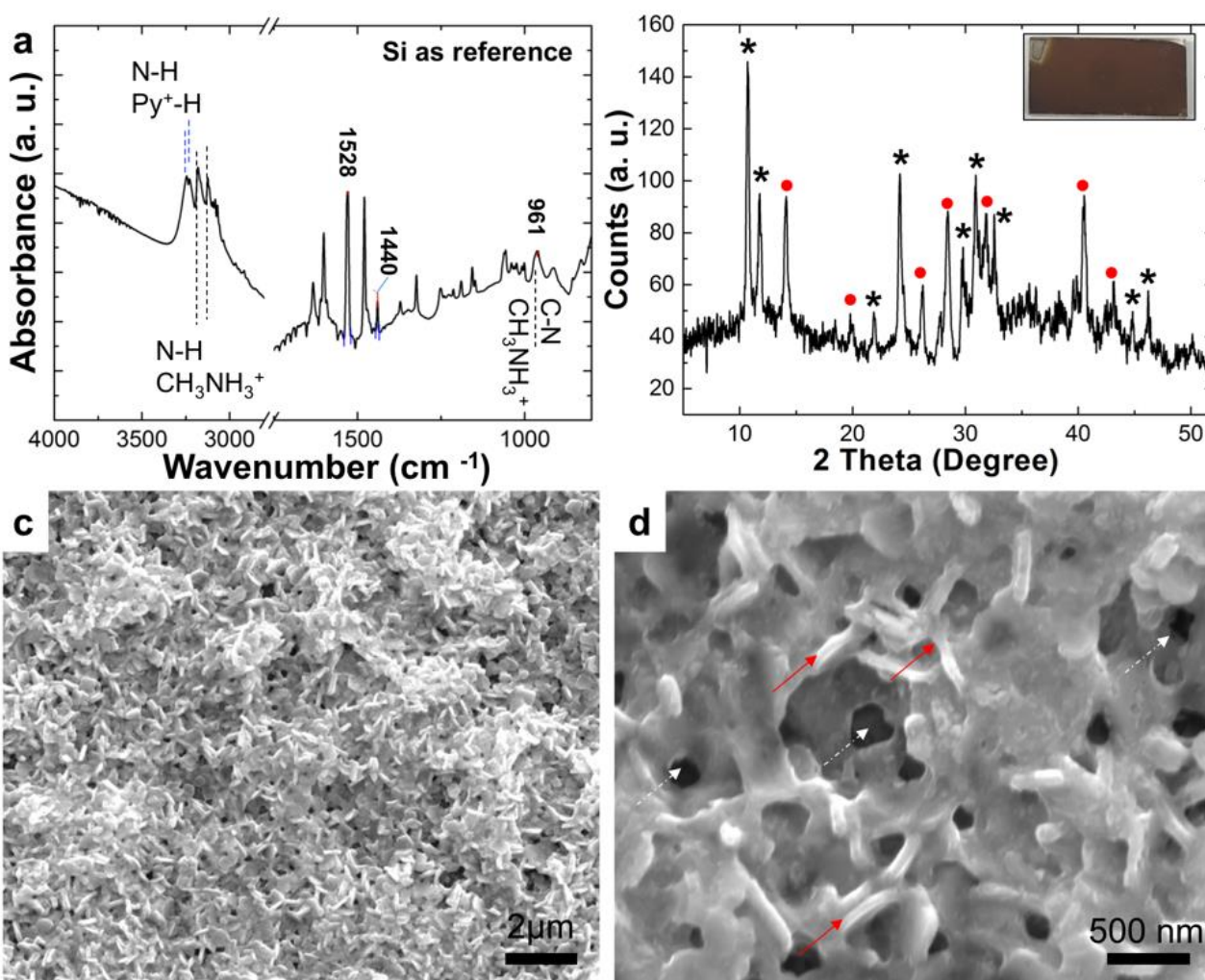


Figure 4.10. (a) IR spectrum of CH₃NH₃PbI₃/Si after the exposure to 1.3 torr pyridine vapor as shown in Figure 9. (b) XRD spectra of CH₃NH₃PbI₃/Si sample in (a). Inset Figure is the optical image CH₃NH₃PbI₃/FTO after 1.3 pyridine treatment (Brown). (Black, *) and (Red, ●) are peaks from new unknown species and CH₃NH₃PbI₃. (c, d) SEM images of the CH₃NH₃PbI₃/Si in (a) at different magnifications. Red arrows point to the flakes, and white arrows points to the voids.

Figure 4.10a shows the IR spectrum of the CH₃NH₃PbI₃ film after the P_1.3 torr treatment. The film now contains Py⁺H as a major product. In the range of 3000–3400 cm⁻¹, the double positive peaks at ~3250 cm⁻¹ are N–H stretches Py⁺H. The dual peaks at ~3200 cm⁻¹ are from CH₃NH₃⁺ inside the film. The spectrum in the range of 1400–1700 confirms the formation of Py⁺H in the film and existence of CH₃NH₃⁺, as well as the generation of a small amount of Py-H and Py-

Pb²⁺. The ratio of the absorbance of 1529 cm⁻¹ peak (Py⁺H) to the absorbance of 1440 cm⁻¹ peak (Py-H) is ~10 and is larger than that after P_20 torr treatment (0.5). It is partially due to the higher extent of reaction to Py⁺H because of the longer exposure to pyridine vapor in P_1.3 torr treatment (1200 s) than P_20 torr treatment (1 min) and partially due to the more effective removal of Py-H by evacuation than sitting in 1 atm dry air.

After the treatment of P_1.3torr shown in **Figure 4.9**, the XRD spectrum of the film (**Figure 4.10b**) shows new peaks at 10.7, 11.0, which do not belong to PbI₂ and CH₃NH₃I. These new peaks are not identified and are formed from the reaction with pyridine. There are also peaks from CH₃NH₃PbI₃, but with a significantly reduced intensity. After P_1.3 torr treatment, the dark CH₃NH₃PbI₃ film becomes brownish (the inset Figure in **Figure 4.10b**). This color change is due to the formation of new materials with larger bandgaps than CH₃NH₃PbI₃, for example, two-dimensional materials^{125,126}. As shown in **Figure 4.10c, d**, the treatment of P_1.3torr dramatically changes the film morphology. There are voids and flakes on the surface of the sample. The formation of voids is probably due to the fast removal of the dissolved Py-H and CH₃NH₂ in the evacuation step. The flakes resemble the common crystal morphology of two-dimensional materials, and are probably from the intercalated Py⁺HPbI₃.¹²⁵ The continuous phase is probably mainly CH₃NH₃PbI₃, but with an inferior crystallinity than the starting film.

Figure 4.11a shows the mass gain behavior a CH₃NH₃PbI₃ film with the exposure of pyridine vapor, whose pressure is increased stepwise from 0.5 torr to 1.3 torr. When the pressure is 1.15 torr and below, the total mass gain is less than 1.5 μg/cm². Shortly after the pressure of pyridine increases to 1.3 torr, the mass gain rate increases significantly and merges into Zone 2 type growth. While the reaction is still in the Zone 2, we start to remove part of the pyridine vapor. The stepwise reduction of pyridine pressure slowly reduces mass. It is probably due to the desorption of Py-H and CH₃NH₂ molecules. The zoom-in view of mass gain data before Zone 2 is shown in

Figure 4.11b. After the exposure to 0.5 torr pyridine for 21 min, the occurred mass gain is 0.45 $\mu\text{g}/\text{cm}^2$. Then additional pyridine is fed into the reactor, the partial pressure of pyridine increases to 0.8 torr. During the 36 min at 0.8 torr for 36 min, additional 0.38 $\mu\text{g}/\text{cm}^2$ is accumulated onto the sample. During the following 40 min at 1.15 torr, mass increases another 0.47 $\mu\text{g}/\text{cm}^2$. For all of these pressures, the mass gain versus time curve is concave to time axial, which is similar to the mass gain obtained at 0.3 and 0.5 torr pressure (**Figure 4.8**). Therefore, according to our experimental results, 1.3 torr is the transient point, which can trigger the Zone 2 type growth and activate a new chemistry, which does not take place at pressure 1.15 torr or below.

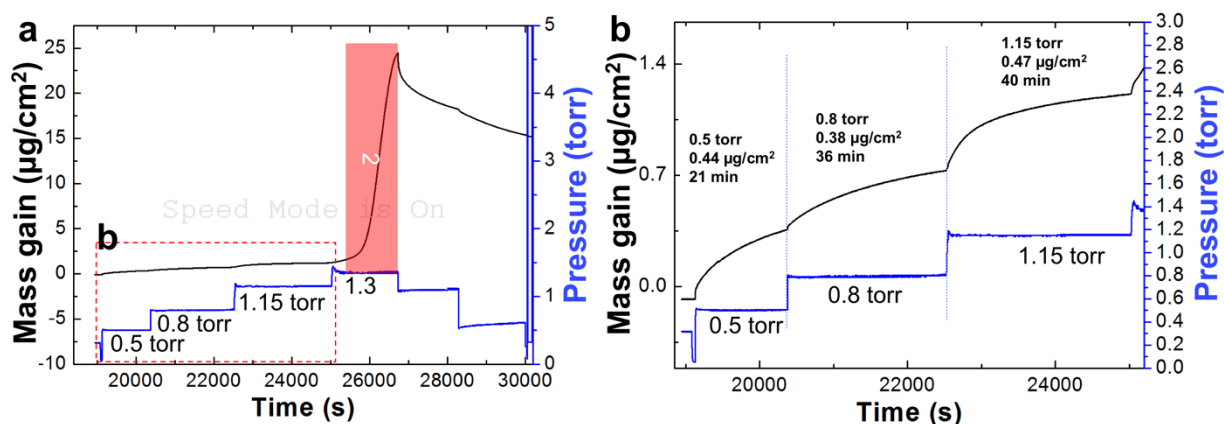


Figure 4.11. (a) QCM result from the stepwise increases of the partial pressure pyridine, 0.5, 0.8, 1.15, and 1.3 torr, then stepwise reduce the pressure of pyridine. Zone 2 region is shadowed. (b) Zoom-in view of the region enclosed by the dash-box in (a). The mass gain and duration at each pressure are labeled accordingly.

4.3 Discussion

According to our results, whether the reaction between pyridine vapor and $\text{CH}_3\text{NH}_3\text{PbI}_3$ is confined around its surface or into the bulk is strongly affected by the pressure of pyridine vapor as summarized in **Figure 4.12**. When the pressure of pyridine vapor is low, for example, 1.15 torr or less, pyridine vapor reacts with surface region of $\text{CH}_3\text{NH}_3\text{PbI}_3$ without disturbing the bulk properties. When a pyridine vapor has a higher pressure, for example, 1.3 torr or above, it transforms the bulk $\text{CH}_3\text{NH}_3\text{PbI}_3$ after a short incubation time (within a couple of minutes). A

recent study shows that the behavior of the reaction between NH_3 vapor and $\text{CH}_3\text{NH}_3\text{PbI}_3$ also depends on the pressure of NH_3 vapor¹²⁷: with 0.75 torr NH_3 , the reaction is confined around the surface region, while with 450 torr NH_3 , the whole $\text{CH}_3\text{NH}_3\text{PbI}_3$ substrate can be transformed into a NH_4PbI_3 film. Because Pb–I lattice window is 0.191 nm, NH_3 (<0.15 nm) can diffuse into $\text{CH}_3\text{NH}_3\text{PbI}_3$, but pyridine molecule (0.389 nm) cannot. It is also important to recognize that based on their proton affinity value, pyridine is a stronger base than CH_3NH_2 , while NH_3 is a weaker base than the CH_3NH_2 . Therefore, it is not the size and basicity of an amine that determines whether its reaction with $\text{CH}_3\text{NH}_3\text{PbI}_3$ is confined around the surface reaction or penetrates into the bulk of the substrate. Rather, it is determined by the pressure of the amine vapors as shown in our experiment and the experiment with NH_3 . There is additional indirect evidence in literature that supports our conclusion. For instance, CH_3NH_2 and butane amine of high pressure can transform the whole $\text{CH}_3\text{NH}_3\text{PbI}_3$.¹²⁸ The surface of $\text{CH}_3\text{NH}_3\text{PbI}_3$ can be functionalized by large amine molecules, such as benzyl amine, which have low vapor pressures and similar size as pyridine.^{14,129-131} The size of aniline has been attributed to the fact that aniline cannot cause bulky transformation of $\text{CH}_3\text{NH}_3\text{PbI}_3$ at room temperature even after 60 min of exposure.¹³² As aniline and benzyl amine have the similar cross-section size as pyridine molecules, our explanation is that surface functionalization by benzyl amine and aniline is due to their low vapor pressure rather than their bulky molecular size or their basicity. Therefore, it is critical to study the effect of pressure of an amine on its reaction with $\text{CH}_3\text{NH}_3\text{PbI}_3$.

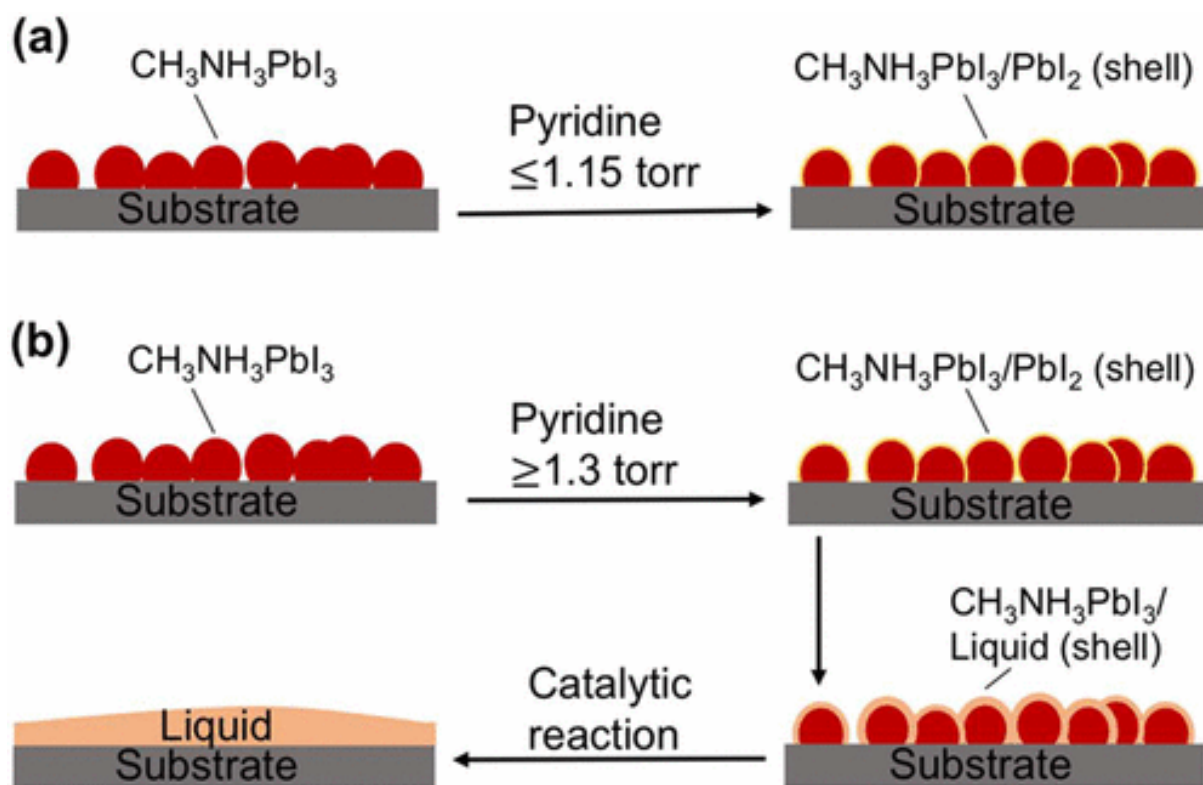


Figure 4.12. Schematic mechanism of the reaction between the pyridine vapor and $\text{CH}_3\text{NH}_3\text{PbI}_3$ when the vapor pressure of pyridine is 1.15 torr or lower (a) and 1.3 torr or higher (b). In (a), at low pressure, PbI_2 shell acts as a barrier to protect $\text{CH}_3\text{NH}_3\text{PbI}_3$ from pyridine. Liquid film and catalytic reaction are observed when pyridine vapor is 1.3 torr or higher.

For the reaction between $\text{CH}_3\text{NH}_3\text{PbI}_3$ and pyridine vapor, the core reaction is the proton transfer reaction between CH_3NH_3^+ and Py^+H , no matter what the pressure of pyridine is. This reaction is reversible, and its position of equilibrium can be moved to Py^+H by continuously supplying pyridine and removing CH_3NH_2 . However, when the pyridine vapor is 1.15 torr or lower, the extent of the reaction is limited by the kinetics rather than by thermodynamic equilibrium. As shown in **Figure 4.12a**, this pyridine vapor reacts with $\text{CH}_3\text{NH}_3\text{PbI}_3$ to form PbI_2 . As the reaction proceeds, more and more PbI_2 clusters are generated and form a conformation layer of PbI_2 ; the reaction rate is limited by the diffusion of pyridine molecules to the interface between PbI_2 and $\text{CH}_3\text{NH}_3\text{PbI}_3$.

When the pressure of pyridine vapor increases from 1.15 to 1.3 torr, its chemical free energy increases only 0.3 kJ/mol according to the equation of $RT \ln (1.3/1.15)$, where R is the gas constant, and T is the reaction temperature (298 K). It is fascinating that such a small change of chemical potential can cause a dramatic change of the reaction behavior between pyridine vapor and $\text{CH}_3\text{NH}_3\text{PbI}_3$. It is our hypothesis that when its pressure is 1.3 torr or higher, pyridine vapor generates a liquid-like layer on $\text{CH}_3\text{NH}_3\text{PbI}_3$ to enable dramatic increase of mass gain rate shown in Zone 2 (**Figure 4.12b**). This hypothesis is supported by the experimental results (**Figure S5**) that show the film morphology of $\text{CH}_3\text{NH}_3\text{PbI}_3$ changes at the beginning of Zone 2. It suggests the great mobility of surface species. In addition, as the pressure of pyridine vapor and reaction temperature are not changing throughout the experiment, the dramatically enhanced rate after the incubation period can only be explained by a reduction of activation energy for the reaction between pyridine and $\text{CH}_3\text{NH}_3\text{PbI}_3$. The liquid-like film increases the mobility of the species so that these species can move to the reaction sites and find the right configuration to catalyze the reaction, therefore lowering the activation energy. It has been observed that pyridine can catalyze the proton transfer reaction.¹³³ Furthermore, with 1.3 torr pyridine, the rate of mass gain increases with the extent of the reaction in Stage 2 and Zone 2. It suggests the reaction products work with pyridine molecules to dismantle the $\text{CH}_3\text{NH}_3\text{PbI}_3$ film. Otherwise, the growth behavior will be similar as the one with 0.5 torr pyridine vapor. The morphology of the final products also suggests that the whole film of the $\text{CH}_3\text{NH}_3\text{PbI}_3$ was turned into a liquid in P_1.3 torr and P_20 torr treatments. This hypothesis is also consistent with the experimental results from P_20 torr: the formation of Py^+H slows dramatically after removal of the pyridine vapor. According to the mechanism in **Figure 4.12b**, the liquid film that is formed during pyridine exposure is solidified, and the Py-H molecules are “frozen” in the film so that the catalytic reaction is not possible. Although liquid formation has been observed in the reaction between the CH_3NH_2 and $\text{CH}_3\text{NH}_3\text{PbI}_3$,¹²⁸ our report is the first

demonstration that the liquid or liquid-like film can be formed at a pressure far below the saturated vapor pressure of an amine and that its formation depends strongly on the amine's pressure, that is, its chemical free energy.

In terms of the formation mechanism of the liquid-like layer, we believe it is due to the interaction between the absorbed pyridine, PbI_x^{x-2} , Py^+H , and CH_3NH_3^+ . The incubation time means that the formation of liquid-like film takes time and is an accumulation result. We rule out the possibility that the liquid or liquid-like film is formed from the condensation of pyridine vapor with two reasons. First, 1.3 torr is far below the saturated vapor pressure of pyridine (20 torr at 25 °C). Second, although according to the Kelvin equation, capillaries can induce presaturation condensation, such condensation is expected to take place at different vapor pressures, as sizes of cracks on the film are randomly distributed. However, in all of our experiments, the Zone 2 type of growth starts only when the pressure is 1.3 torr or higher. In terms of why a small change of pressure at ~1.3 torr can change the state of the system; further research is needed to understand the underlying thermodynamics.

4.4 Conclusion

In summary, our results demonstrate that pressure of pyridine is a key parameter that defines its reaction behavior with $\text{CH}_3\text{NH}_3\text{PbI}_3$: if you want surface modification, use low pressure pyridine vapors; if you want bulk transformation use high pressure pyridine vapors. As this strong pressure-dependent growth behavior effect should be applicable for other amines as well, therefore it is critical to understand the reaction behavior in treating $\text{CH}_3\text{NH}_3\text{PbI}_3$ with amines. In addition, pyridine is a valuable probing molecule in studying the type of surface sites on $\text{CH}_3\text{NH}_3\text{PbI}_3$ and can potentially be used to analyze the effect of synthesis chemistry, temperature history, and surface modification on the surface chemistry of $\text{CH}_3\text{NH}_3\text{PbI}_3$. This information is invaluable in solving the stability issue and surface charge recombination problem that are currently facing halide

perovskites-based devices. In addition, according to our result, although it is possible to sense amine vapor by measuring the conductivity of a $\text{CH}_3\text{NH}_3\text{PbI}_3$ film,¹³⁴ its sensing capability may not be fully reversible and its response may not be linear to the pressure of pyridine.

Support information:

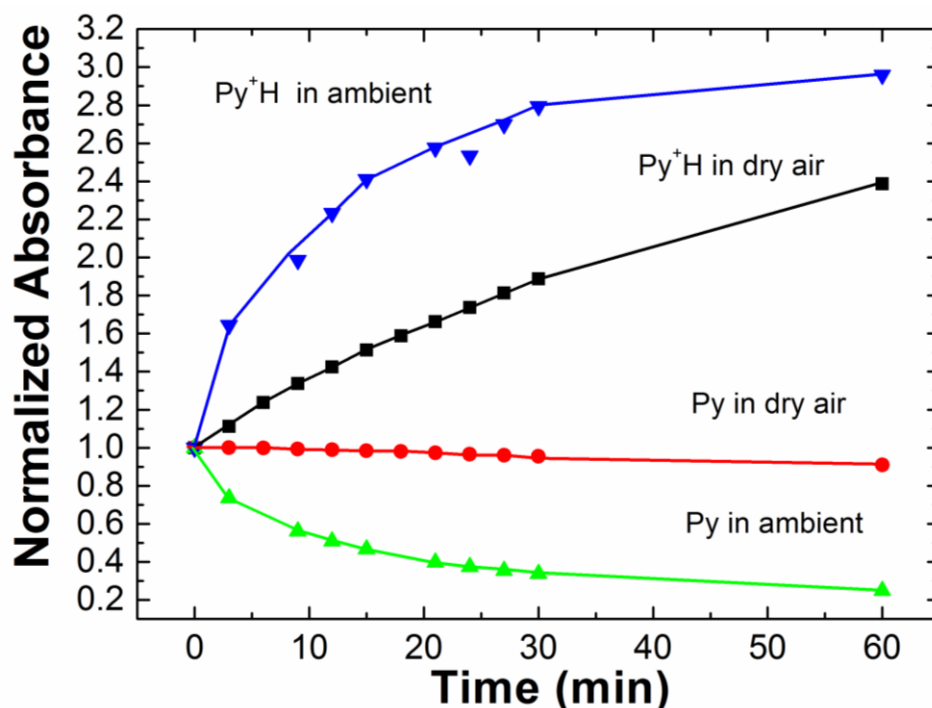


Figure S1. Time-evolved absorbance of ring-vibration of Py (at 1590 cm^{-1}) and Py^+H (at 1525 cm^{-1}) from pyridine treated $\text{CH}_3\text{NH}_3\text{PbI}_3$ film sitting in dry air and in ambient, within 60 min; For a direct comparison, we normalized the peaks' intensity to their intensity in the first spectra measured at 3 min (time zero in the figure) in the dry air purged IR chamber.

Effect of moisture of the rate of Py-H to Py^+H

Although finding optimal conditions of recrystallization is beyond the scope of this paper, we probed the effect of moisture on the chemical composition of $\text{CH}_3\text{NH}_3\text{PbI}_3$ after P_20torr. We monitored the two ring-vibration modes Py-H (1590 cm^{-1}) and Py^+H (1528 cm^{-1}) because they are the strongest one for the related species. More importantly, the effect of bonding environments on their absorbance is small as they are the nuclear resonances. Figure S1 shows the time-evolved absorbance of these ring-vibration modes in dry air and ambient air. For a direct comparison, their

absorbance at different times is normalized to the corresponding peak's absorbance that is obtained after the ambient air is cleared out from the IR chamber. This process generally takes 3 min. As shown in Figure S1, it takes a much shorter time to achieve the same level of removal of Py-H and production of Py⁺H in ambient air than in dry air. For instance, it takes only 3 min for the 30% of Py-H absorbance in ambient (Figure 5a), but 1 h for the 10% reduction in dry air. For Py⁺H, it takes less than 3 min in ambient to generate Py⁺H of normalized absorbance of 1.6, but a hefty of 30 min to get the same level Py⁺H if the film in dry air. These dramatically accelerated reaction rates in ambient suggest that H₂O can facilitate the conversion of Py-H to Py⁺H and removal of Py-H from the CH₃NH₃PbI₃/Si after P_20torr treatment, potentially acting as a catalyst. Therefore, our results clearly show the significant role of H₂O in the chemical transformation. The concentration of moisture is the reason that why our sample in glove box take a much long time to be converted back to CH₃NH₃PbI₃.

The theoretical mass change if all CH₃NH₃⁺ are replaced by Py⁺H.

The mass of CH₃NH₃PbI₃ film on QCM film is around 260 ± 25 μg/cm². If assume all CH₃NH₃⁺ are replaced by Py⁺H as shown in the Eq. (s1)



Then theoretical maximum net mass gain on the film can be calculated:

Moles of CH₃NH₃⁺ can be calculated from Eq. (s2), wherein 620 g/mol is the molar mass of CH₃NH₃PbI₃. As the mass of a CH₃NH₃PbI₃ film is 260 ± 25 μg/cm², $M_{CH_3NH_3^+}$ is 0.42 ± 0.04 μmol/cm² on a QCM crystal. According to Eq. (s3), the ultimate net mass gain (m_{net}) is 20 ± 2 μg/cm². In Eq. 2, 48 g/mol is the increase of the molar mass after replacing CH₃NH₃⁺(32 g/mol) by Py⁺H (80 g/mol). As the $M_{CH_3NH_3^+}$ is 0.42 ± 0.04 μmol/cm²,

$$\frac{m_{CH_3NH_3PbI_3}}{620g/mol} = M_{CH_3NH_3^+} \quad (s2)$$

$$M_{\text{CH}_3\text{NH}_3^+} \times \left(48 \frac{\text{g}}{\text{mol}}\right) = m_{\text{net}} \quad (\text{s3})$$

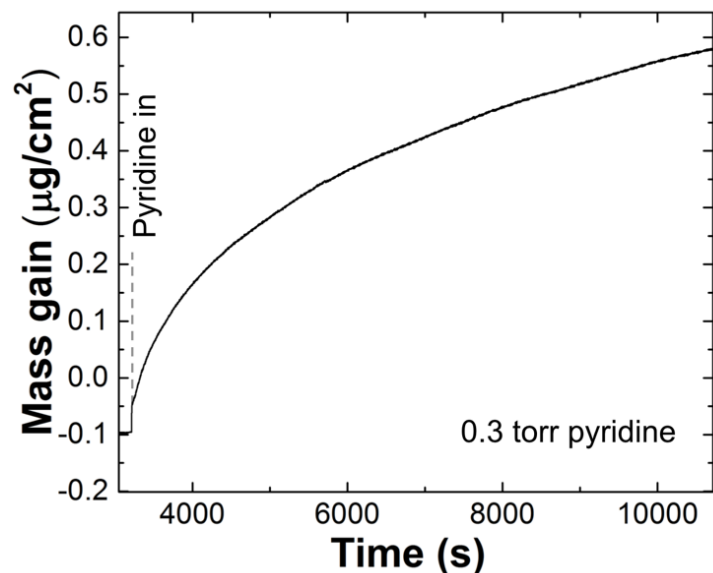


Figure S2. SEM image of a $\text{CH}_3\text{NH}_3\text{PbI}_3$ film measured by QCM with pyridine of vapor pressure 0.3 torr.

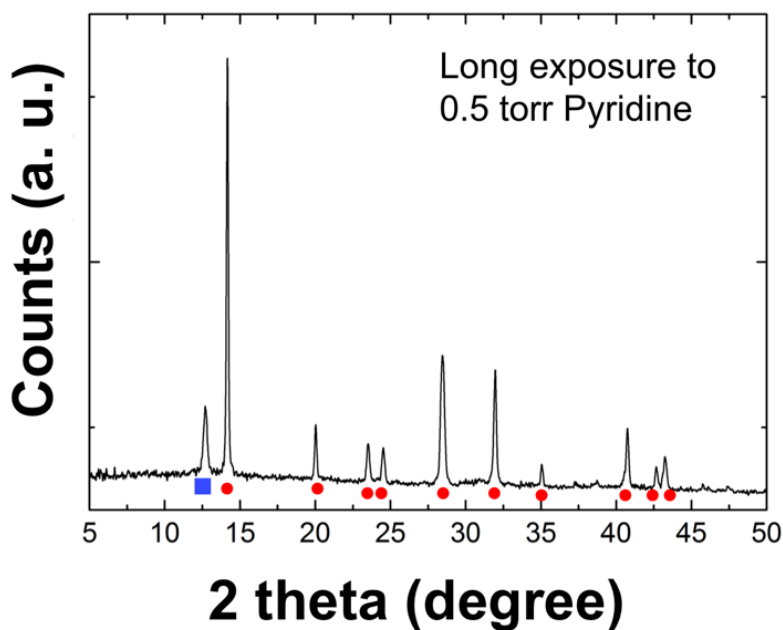


Figure S3. XRD spectrum of a $\text{CH}_3\text{NH}_3\text{PbI}_3$ film that is exposed to pyridine vapor of pressure 0.5 torr for ~ 8700 s. It shows that majority of $\text{CH}_3\text{NH}_3\text{PbI}_3$ (Red dots) is still in the film and some PbI_2 (Blue square) has been generated.

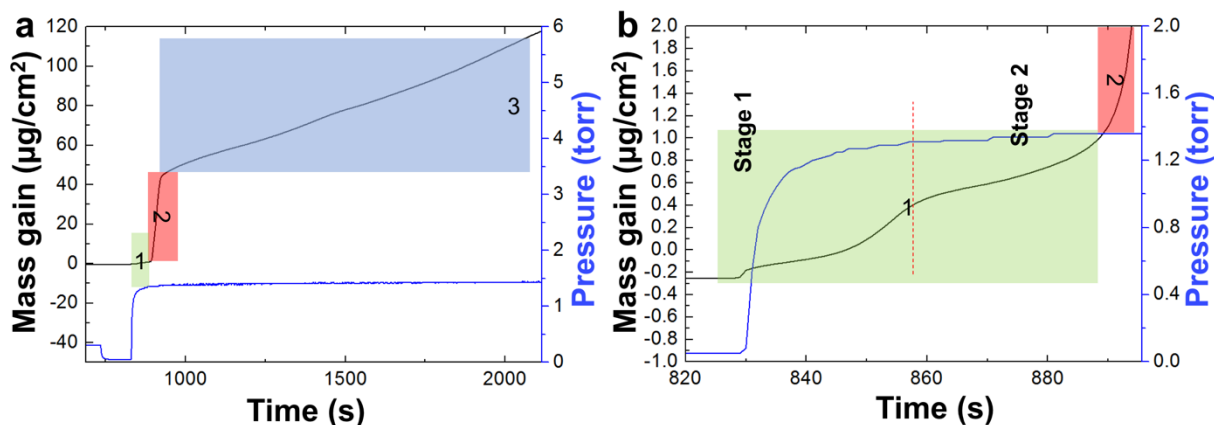


Figure S4. The overall view of the time-evolved mass gain (black trace) occurred onto a $\text{CH}_3\text{NH}_3\text{PbI}_3$ film during the exposure of pyridine vapor of 1.38 torr in a vacuum reactor from a different run than that in Figure 9. (b) Zoom-in view of Zone 1 in (a). Note, Stage 1 finished at $0.6 \mu\text{g}/\text{cm}^2$. Zone 2 finished around $50 \mu\text{g}/\text{cm}^2$.

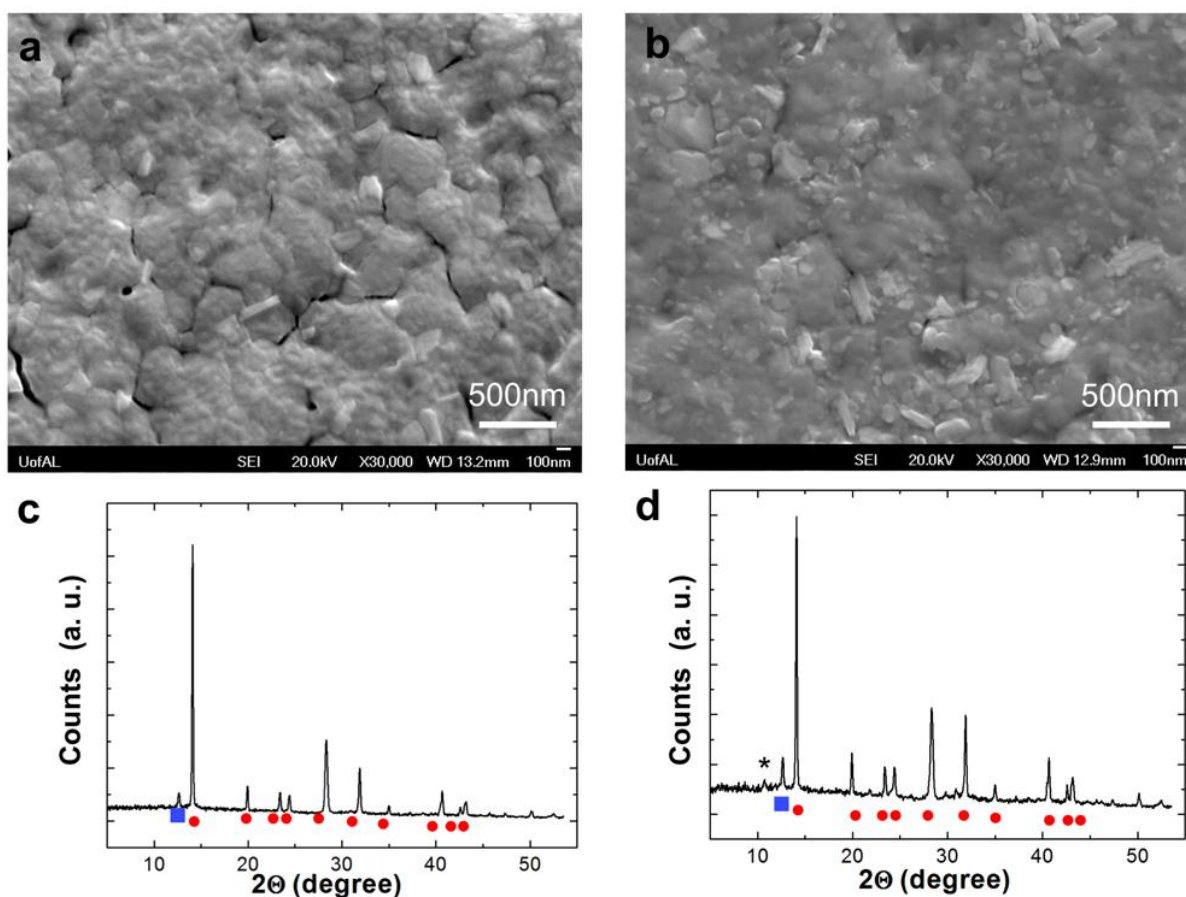
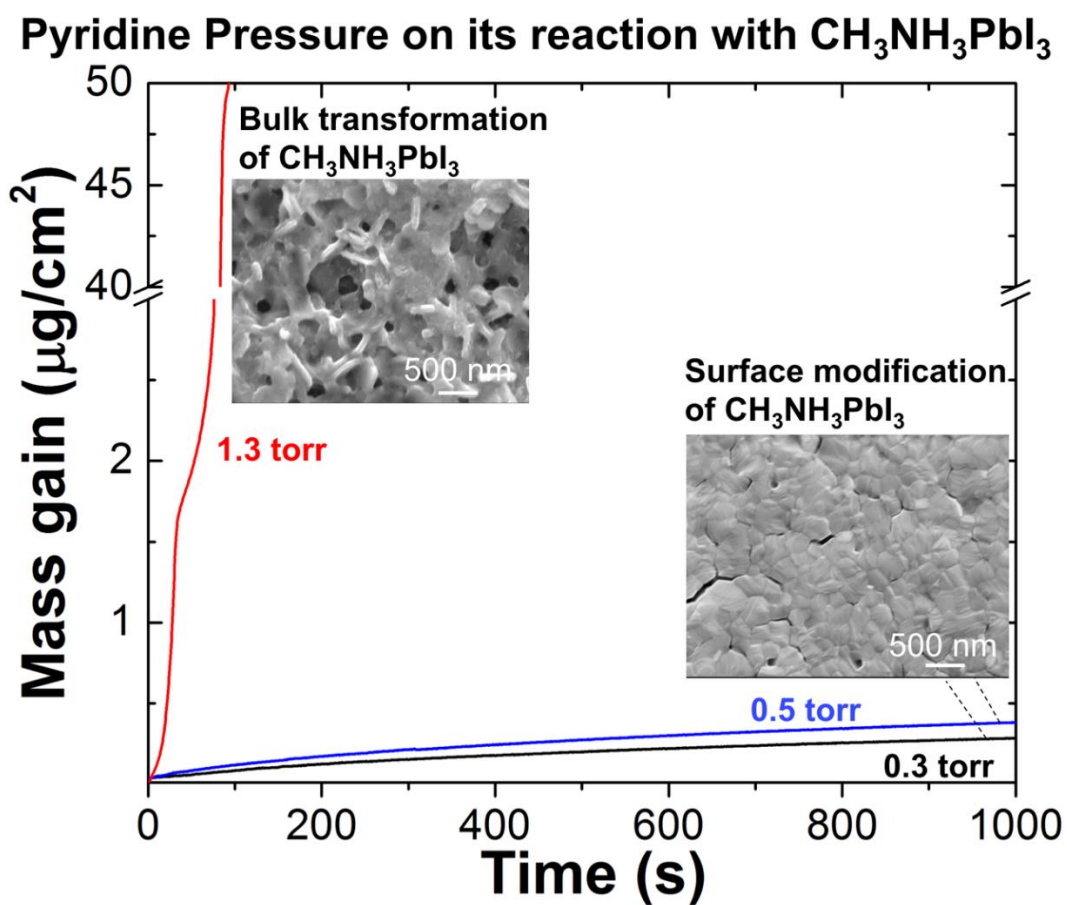


Figure S5. SEM images of $\text{CH}_3\text{NH}_3\text{PbI}_3$ films obtained after remove pyridine at Stage 2 (a) and (b) at the early stage of Zone 2 in P_1.3torr treatment. The SEM images show the surface morphology of a $\text{CH}_3\text{NH}_3\text{PbI}_3$ film does not change until the early stage of Zone 2. (c-d) are the XRD spectra from sample in (a) and (b) respectively. The XRD spectra show additional diffraction peak (Black, *) from new species other than PbI_2 (Blue, ■) and $\text{CH}_3\text{NH}_3\text{PbI}_3$ (Red, ●) in the sample obtained at the early stage of Zone 2.



CHAPTER 5: IMPROVE THE STABILITY OF METHYLAMINE LEAD PEROVSKITE BY ATOMIC LAYER DEPOSITION OF Al_2O_3 AT 25°C

5.1 Introduction

Halide perovskites have emerged as a class of low cost semiconductors for high efficient solar cells,^{109,135-140} LEDs,^{109,113,140,141} lasing,^{110,142} sensors,^{111,143,144} and computing chipsets.^{135,145} The power-conversion-efficiency (PCE) of $\text{CH}_3\text{NH}_3\text{PbI}_3$ solar cells reaches 22.1%, which is competitive with the high cost commercial silicon solar cells.¹⁰⁸ In order to commercialize $\text{CH}_3\text{NH}_3\text{PbI}_3$ -based devices on a large scale, the generation cost per kilowatt hour must be low enough to be competitive. It demands long life time of solar cell modules, owing to the high cost of installation of solar cells. However, $\text{CH}_3\text{NH}_3\text{PbI}_3$ has a poor stability in ambient,^{109,135-140} and the state-of-the-art lifetime of $\text{CH}_3\text{NH}_3\text{PbI}_3$ solar cells is less than a couple of years,¹⁴⁶⁻¹⁴⁸ which is much shorter than the lifetime (20 - 30 years) of commercial Si solar cells. A range of methods have been developed to improve the environmental stability of perovskites.¹⁴⁹⁻¹⁶⁰ For instance, engineering the composition of perovskites^{12,161} has been demonstrated as the most effective way to improve their stability. Encapsulating perovskite devices can also improve the stability of perovskites.¹⁶² Another method is to isolate $\text{CH}_3\text{NH}_3\text{PbI}_3$ from ambient by a thin diffusion barrier as moisture and oxygen degrade and accelerate the degradation of $\text{CH}_3\text{NH}_3\text{PbI}_3$.^{12,163,164} Currently, there is no winning solution that solved the stability problem of perovskites. It is possible that these methods and additional methods need to work in concert to solve the environmental stability issue of perovskites.

Among the various diffusion barrier layers that have been developed for perovskites,^{51,159,165-170} Al₂O₃ layers formed by atomic layer deposition (ALD) represent an attractive strategy. For instance, an Al₂O₃ layer, which was deposited on CH₃NH₃PbI₃ by 10 cycles of trimethyl aluminum (TMA)/H₂O chemistry at 100 °C, not only improves the environmental stability of the CH₃NH₃PbI₃ film, but also enhances the efficiency of CH₃NH₃PbI₃ solar cells.^{74,171} Al₂O₃ ALD (TMA/H₂O) films that were grown on CH₃NH₃PbI₃ at room temperature can greatly improve its stability.^{172,173} Chemisorption of triethyl aluminum (a similar chemical as TMA) at room temperature onto CH₃NH₃PbI₃ can improve its ambient stability.¹⁷⁴ However, there are also reports showing that Al₂O₃ ALD degrades CH₃NH₃PbI₃. For example, TMA/H₂O chemistry, at 100 °C, degrades CH₃NH₃PbI₃.¹⁶⁶ TMA vapor etches and degrades CH₃NH₃PbI₃ at 75 °C.¹⁷⁵ In summary, ALD Al₂O₃ may be effective in improving the stability of CH₃NH₃PbI₃, however these inconsistent results present a challenge in reliably using this method. These inconsistent results could be due to the poorly understood TMA/CH₃NH₃PbI₃ reaction, which is the key step determining the nucleation of ALD Al₂O₃ on CH₃NH₃PbI₃,^{171,173,175} because ALD is step-wise process.

In this study, we investigated the reaction between TMA and fresh CH₃NH₃PbI₃ by using in situ QCM (quartz crystal microbalance) and QMS (quadrupole mass spectrometer). We found that TMA/CH₃NH₃PbI₃ reaction does not follow the surface site-limited monolayer reaction as expected for ALD. Instead, the TMA/CH₃NH₃PbI₃ reaction proceeds into the CH₃NH₃PbI₃ substrate. Both reaction temperature and partial pressure of TMA strongly affect the TMA/CH₃NH₃PbI₃ reaction. Specifically, at 25°C, TMA vapor of ~ 0.1 torr reacts with CH₃NH₃PbI₃ to generate a saturated mass gain of 350 ng/cm², which is much larger than the saturated mass gain of TMA step on a metal oxide surface. The generated product layer supports the nucleation of Al₂O₃ ALD. In contrast, at 75°C, TMA vapor (~0.1 torr) continuously etches CH₃NH₃PbI₃ to generate PbI₂ and the

nucleation of the following Al₂O₃ ALD process is delayed. QMS measurements show that CH₃NH₂ is not the main gaseous byproduct at both reaction temperatures; Instead, CH₃I emerges as the byproduct after many pulses of TMA vapor on CH₃NH₃PbI₃ at both temperatures. In addition, when the partial pressure of TMA is higher than 0.5 torr, TMA etches CH₃NH₃PbI₃ even at 25°C and the extent of the etching reaction increases with increasing the partial pressure of TMA and reaction time. Based on these results, we hypothesize that TMA/CH₃NH₃PbI₃ reaction follows a core(perovskite)-shrinking model^{107,176}: the CH₃NH₃PbI₃ core is consumed by the TMA/CH₃NH₃PbI₃ reaction, which forms a product shell. The shell formed at 25 °C in the vacuum process can protect CH₃NH₃PbI₃ from TMA, but the product shell disintegrates at higher temperatures (e.g., 75 °C). The environmental stability of CH₃NH₃PbI₃ can be improved by one cycle of ALD Al₂O₃ that was done at 25°C with TMA of ~ 0.1 torr, followed by the air exposure.

5.2 Result and discussion

In situ QCM measurement shows that TMA (0.1 torr)/CH₃NH₃PbI₃ reaction approaches a saturated mass gain at 25°C. As shown in **Figure 5.1a**, the mass gain obtained from each TMA vapor pulse decreases with repeating the pulses of TMA vapor. This trend is clearly illustrated in **Figure 5.1b**. The mass gain from a TMA pulse approaches zero after 40 pulses of TMA vapor. The total net mass gain saturates at ~ 0.35 μg/cm² after 50 pulses of TMA (1_s TMA dose/30_s purge by N₂). The accumulated mass is from the reaction between TMA and CH₃NH₃PbI₃ because the mass gain cannot be removed by a long-term purge step with ultrahigh purity N₂ gas. This mass gain is ~3 times of the saturated mass gain that is obtained from multiple TMA pulses in QCM surface (**Figure S1** supporting information). This higher mass gain suggests that the reaction mechanism between TMA and CH₃NH₃PbI₃ is different from the submonolayer chemisorption of TMA on Al-OH surface in steady-state Al₂O₃ growth, because the surface of a CH₃NH₃PbI₃ film on a QCM crystal is smoother than a clean QCM crystal with 50 nm Al₂O₃ (**Figure S2**), indicating that the

$\text{CH}_3\text{NH}_3\text{PbI}_3$ substrate potentially has less amount surface sites per 1cm^2 projected area than the steady state Al_2O_3 film on a QCM crystal. This in situ QCM result suggest that the TMA (0.1 torr)/ $\text{CH}_3\text{NH}_3\text{PbI}_3$ reaction at 25°C has a saturated mass gain, which is much higher than that from the expected monolayer TMA chemisorption.

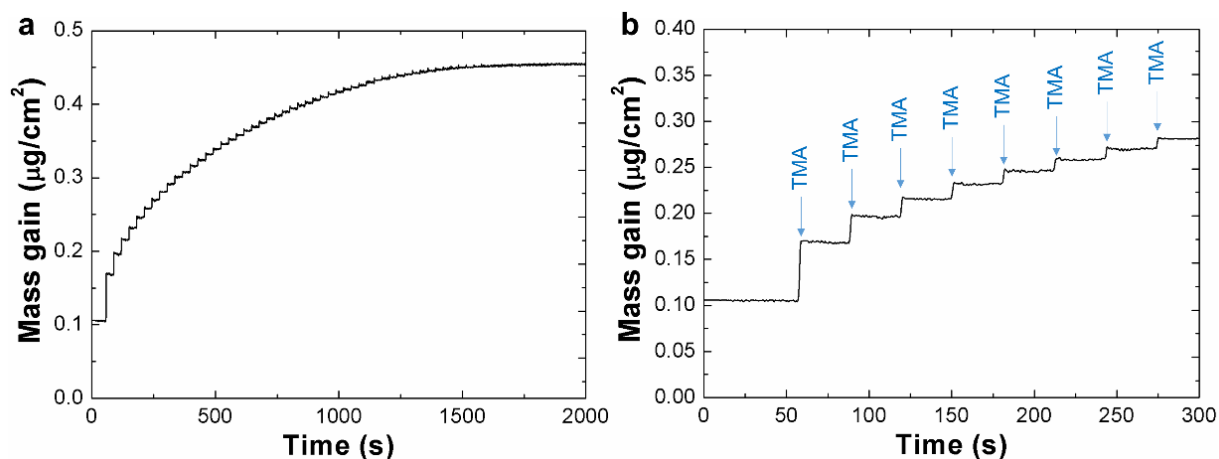


Figure 5.1. *In situ* QCM measurement of the mass gain behavior (a) during 50 pulses of TMA onto $\text{CH}_3\text{NH}_3\text{PbI}_3$ and (b) during the first eight pulses of TMA vapor on $\text{CH}_3\text{NH}_3\text{PbI}_3$. The experiment is carried at 25°C . Each TMA exposure step consists of 1s pulse of TMA vapor (partial pressure of ~ 0.1 torr) followed by 30s N_2 purge.

In situ QMS was applied to monitor the gas products during the TMA pulses (Figure 5.2). First, the mass signal from TMA ($m/z = 57$) is well resolved. The intensity of TMA signal does not change much for the 50 TMA pulses, because the partial pressure of TMA does not very much, and the majority of TMA does not participate in the reaction. Second, the main peak for CH_3NH_2 ($m/z = 30$) is negligible during the measurement. It means that CH_3NH_2 is probably not a byproduct from the reaction between TMA and $\text{CH}_3\text{NH}_3\text{PbI}_3$. Third, the intensity of mass signal of CH_4 ($m/z = 16$) gradually decreases by repeating the pulses of TMA vapor. After ~ 20 TMA pulses, the CH_4 signal becomes constant. The constant CH_4 signal is ascribed to the fragment from TMA molecules. In a control experiment of pulsing TMA vapor on the Al-OH surface in the steady-state ALD of Al_2O_3 , CH_4 signal becomes constant after ~ 16 pulses of TMA (Figure S3), suggesting that the surface reaction is limited by surface sites and the gradually reduced CH_4 signal is, at least partially, due to

the reaction between TMA and -OH on the wall of the reactor. The reaction between TMA and CH_3NH_3^+ could lead to the formation of CH_4 . After ~ 40 cycles of TMA, QMS measurement detects the signal from CH_3I ($m/z = 142$). It is interesting that when the CH_3I signal picks up, the CH_4 signal drops further. This trend of QMS signal indicates that the reaction between TMA molecules and $\text{CH}_3\text{NH}_3\text{PbI}_3$ changes with the progression of the reaction. In the first stage, TMA mainly reacts with surface sites groups, e.g., -OH or CH_3NH_3^+ , to generate CH_4 . At the second stage, the reaction generates CH_3I molecules, which desorb from the substrate. The desorbed CH_3I explains the negligible mass gain after ~ 40 pulses of TMA vapor (**Figure 5.1a**), as the mass loss from the desorbed CH_3I is balanced by the added mass from TMA.

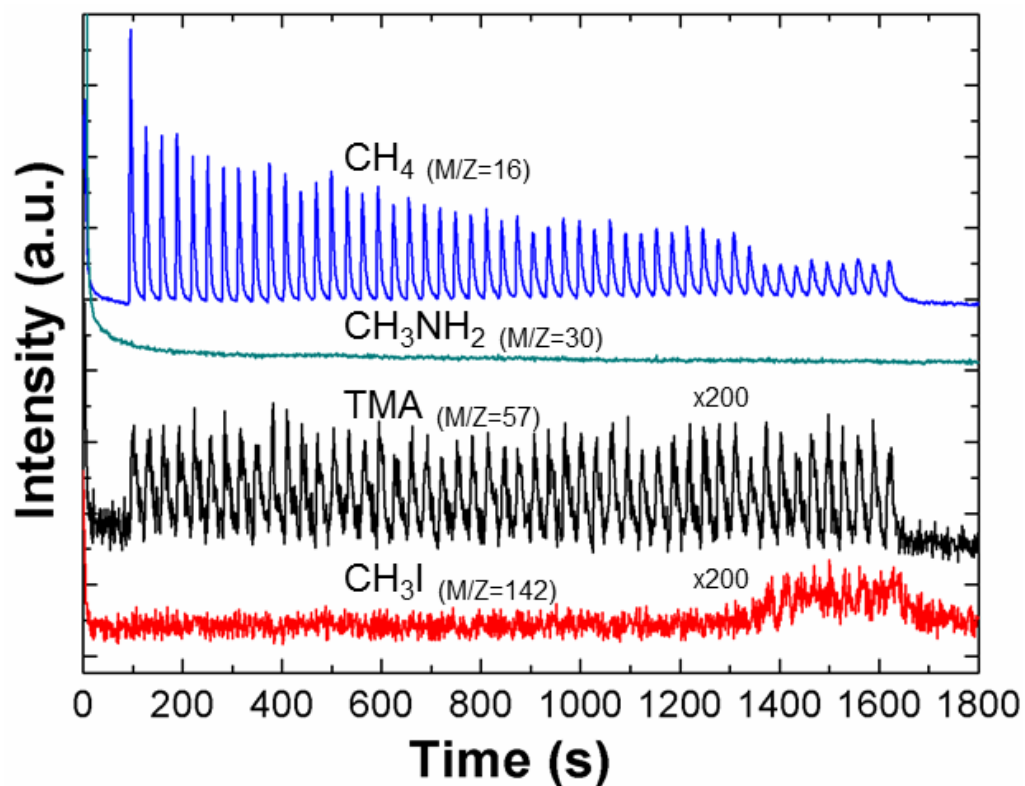


Figure 5.2. In situ QMS measurement of 50 pulses of TMA vapor on the $\text{CH}_3\text{NH}_3\text{PbI}_3$ powder at 25°C . The signal intensity of TMA ($m/z = 57$) and CH_3I ($m/z = 142$) is magnified by 200 times.

The 50 pulses of TMA vapor do not generate detectable PbI_2 on $\text{CH}_3\text{NH}_3\text{PbI}_3$ at 25°C (**Figure 5.3**). For the fresh $\text{CH}_3\text{NH}_3\text{PbI}_3$ sample, there are main peaks of $\text{CH}_3\text{NH}_3\text{PbI}_3$ at 14.1° , 28.4° and 32.2° , corresponding to the (110), (220) and (222) planes of a tetragonal perovskite

structure. After the exposure to 50 pulses of TMA vapor, no new peaks, such as PbI_2 , is detected by XRD. In addition, the full width at half maximum (FWHM) of the (110) peak at 14.1° does not change. Therefore, the sizes of $\text{CH}_3\text{NH}_3\text{PbI}_3$ crystals inside the film remain unchanged by the surface reaction with TMA vapor based on the Scherrer equation. Because TMA vapor does not generate PbI_2 and reduce the crystal size of $\text{CH}_3\text{NH}_3\text{PbI}_3$ while accumulate mass onto the substrate (Figure 5.1), we conclude that the reactions are confined at the surface region at 25°C .

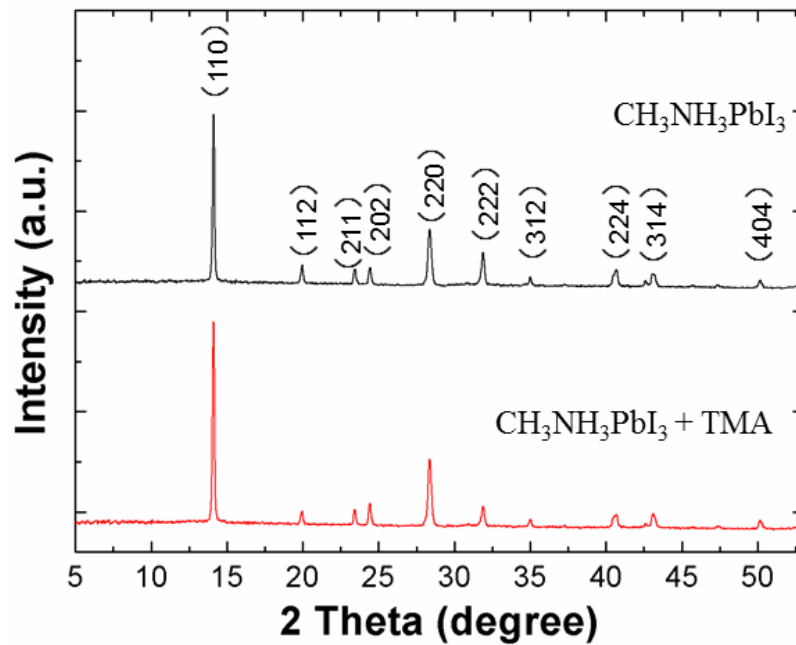


Figure 5.3. XRD spectrum of a $\text{CH}_3\text{NH}_3\text{PbI}_3$ film before (top) and after (bottom) 50 pulses of TMA vapor at 25°C .

The alternate exposures of TMA and H₂O vapor continuously add mass onto the CH₃NH₃PbI₃ substrate (**Figure 5.4**). As shown in **Figure 5.4a**, there is a short nucleation delay in the initial several cycles, where the average mass gain rate of each cycle is smaller than the steady-state rate in Al₂O₃ ALD. According to **Figure 5.4b**, the mass gain is mainly from the TMA exposure. The comparison of results from **Figure 5.1** and **Figure 5.4** suggest that H₂O is indispensable to refresh the surface sites to nucleate Al₂O₃ ALD. At 25°C, it is possible that the mass gain from TMA pulses is due to the physically bonded H₂O residue. However, H₂O pulses contribute negligible net mass gains (**Figure 5.4b**), suggesting physically bonded H₂O is negligible. Therefore, ALD Al₂O₃ at 25°C can readily nucleate on CH₃NH₃PbI₃ without significantly

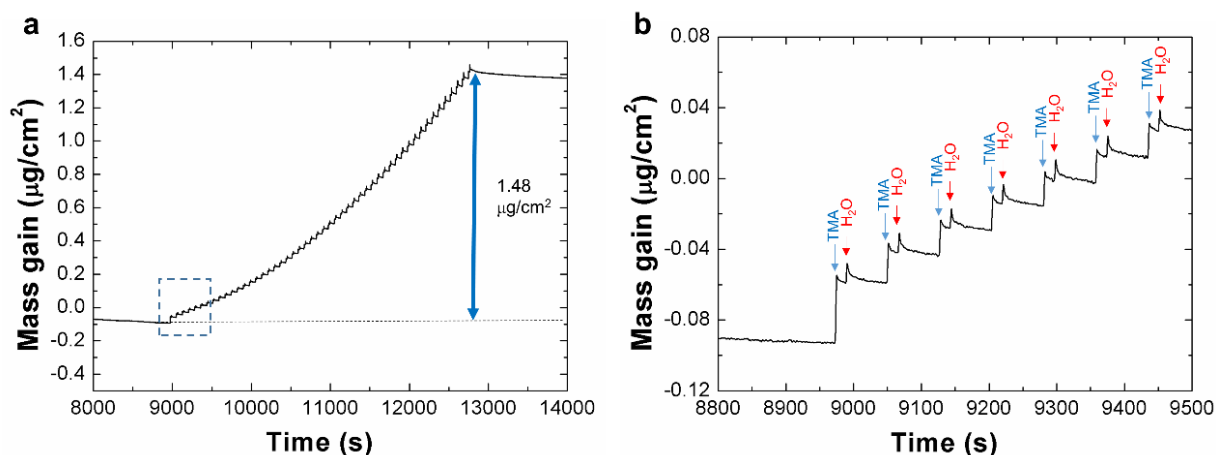


Figure 5.4. Nucleation and growth behavior of ALD Al₂O₃ on CH₃NH₃PbI₃ at 25 °C. (a) The overview of mass gain during 50 ALD Al₂O₃ cycles; (b) the detailed mass gain behavior during the initial 7 cycles.

Figure 5.5 shows the in-situ QCM measurement during TMA pulses on CH₃NH₃PbI₃ at 75°C. CH₃NH₃PbI₃ films are relatively stable at 1 torr, 75°C in N₂,¹⁷⁷ as QCM measurement (**Figure 5.5b**) shows the mass of the film is relatively stable before introducing TMA pulses. The first pulse of TMA on fresh CH₃NH₃PbI₃ produces a positive mass gain. This positive mass gain is mainly due to the reaction between TMA vapor and –OH groups on the surface, which is expected from air exposure. However, the following 30 pulses of TMA reduce the mass of CH₃NH₃PbI₃ at a

relatively constant rate (**Figure 5.5a**). The reduction of mass is completed within the 1 s TMA pulsing step and the mass of the film is stable during the following N₂ purging steps (30 s). This etching reaction behavior agrees with a previous QCM result,¹⁷⁵ and is dramatically different than that at 25°C (**Figure 5.1**)

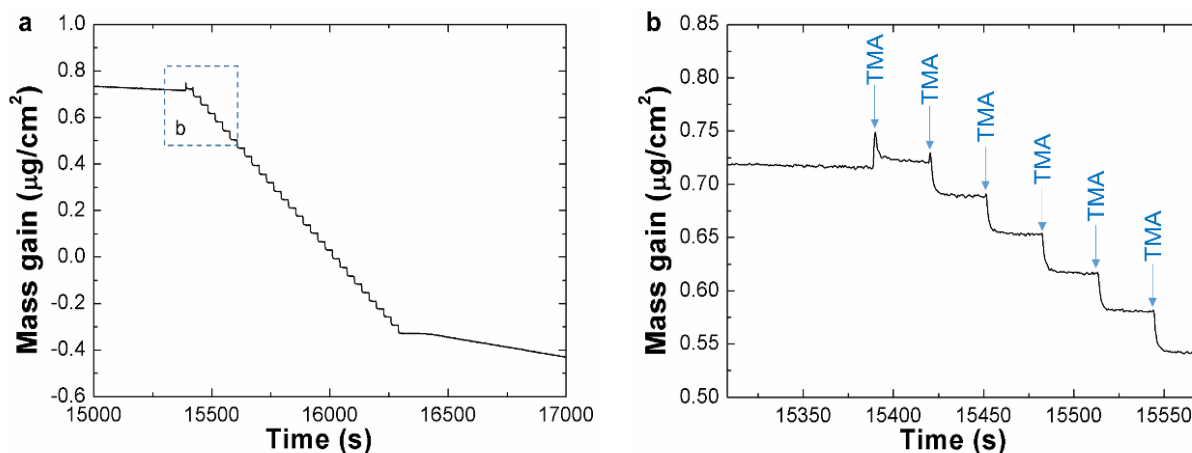


Figure 5.5. (a) The mass change during TMA pulse on CH₃NH₃PbI₃ at 75°C; (b) The mass change during the initial 6 pulses of TMA as shown by the dash box in (a).

Figure 5.6 shows QMS results from the reaction between CH₃NH₃PbI₃ and TMA at 75°C. The signal of CH₃NH₂ is not detectable while signals from TMA and CH₄ are clear. This result does not agree with a previous report,¹⁷⁵ which hypothesizes that CH₃NH₂ is the major byproduct. The intensity of CH₄ peak gradually decreases with repeating the TMA pulses and becomes constant after ~20 pulses of TMA. It suggests that no more CH₄ is generated from the reactions with either -OH or CH₃NH₃⁺. After the signal of CH₄ becomes constant, the CH₃I (m/z = 142) signal appears and increases with repeating TMA pulses. The QMS results suggest that the reaction between TMA and CH₃NH₃PbI₃ changes with repeating TMA pulses. The QMS measurement show a similar pattern as that from 25°C (**Figure 5.2**) although the mass gain behaviors are different. The detailed reasons will be presented in discussion.

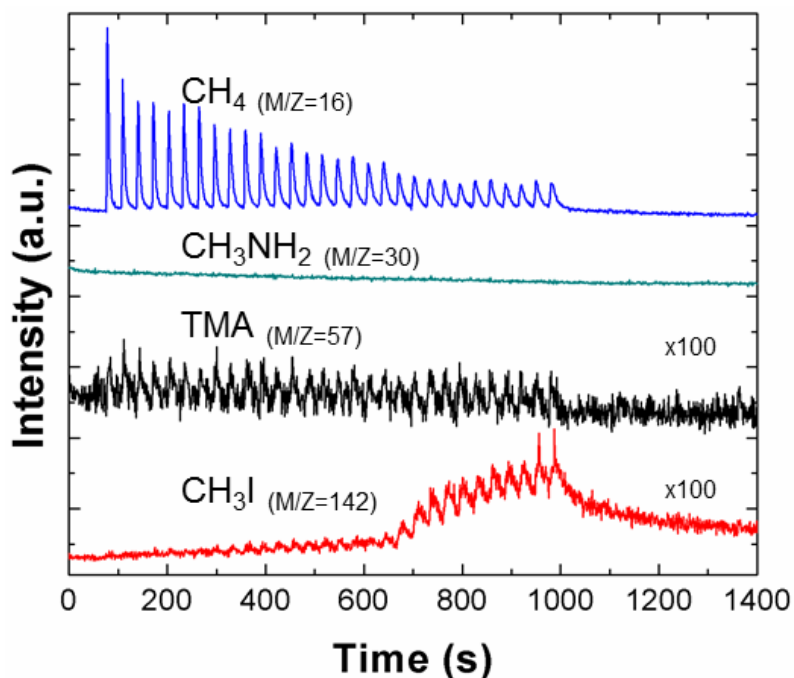


Figure 5.6. The gas product of the reaction between $\text{CH}_3\text{NH}_3\text{PbI}_3$ and TMA vapor at 75°C by QMS.

XRD measurement (**Figure 5.7**) shows that PbI_2 is produced onto $\text{CH}_3\text{NH}_3\text{PbI}_3$ after 50 pulses of TMA vapor at 75°C . The peak at 12.6° is due to the (110) plane of PbI_2 . Therefore, TMA molecules degrade $\text{CH}_3\text{NH}_3\text{PbI}_3$ to PbI_2 at 75°C . This result is different from that at 25°C and is consistent with the previous reports.^{166,175} Although TMA molecules etch $\text{CH}_3\text{NH}_3\text{PbI}_3$, Al_2O_3 ALD can still nucleate onto $\text{CH}_3\text{NH}_3\text{PbI}_3$ at 75°C . As shown in **Figure 5.8a**, it takes more than 10 Al_2O_3 ALD cycles to start accumulating mass onto a $\text{CH}_3\text{NH}_3\text{PbI}_3$ film. This delay of nucleation is better illustrated in **Figure 5.8b**. It is interesting that there are net mass gains during the 1st and 2nd ALD cycles, but the net mass gain approaches zero at the 3rd cycle and beyond. The nucleation delay is probably due to: (1) etching of $\text{CH}_3\text{NH}_3\text{PbI}_3$ by TMA (**Figure 5.5**); and (2) accumulating Al related species onto the substrate before $\text{CH}_3\text{NH}_3\text{PbI}_3$ film is fully isolated from the gaseous reactants. After 50 cycles of Al_2O_3 ALD, the $\text{CH}_3\text{NH}_3\text{PbI}_3$ film becomes unstable in vacuum as the film's mass decreases with time (**Figure 5.8a**). This result suggests that Al_2O_3 ALD at 75°C can degrade $\text{CH}_3\text{NH}_3\text{PbI}_3$ and is not suitable for modifying the surface of $\text{CH}_3\text{NH}_3\text{PbI}_3$.

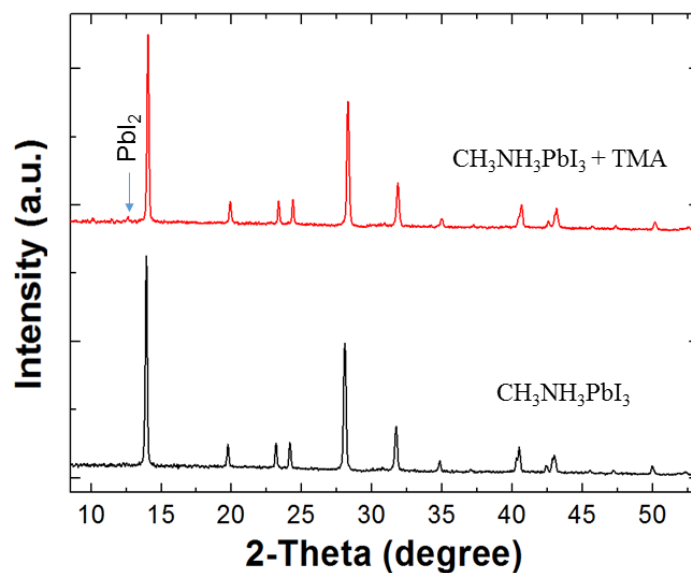


Figure 5.7. XRD spectrum of CH₃NH₃PbI₃ before (black) and after (red) TMA pulse treatment at 75°C. PbI₂ can be detected after 50 pulses TMA.

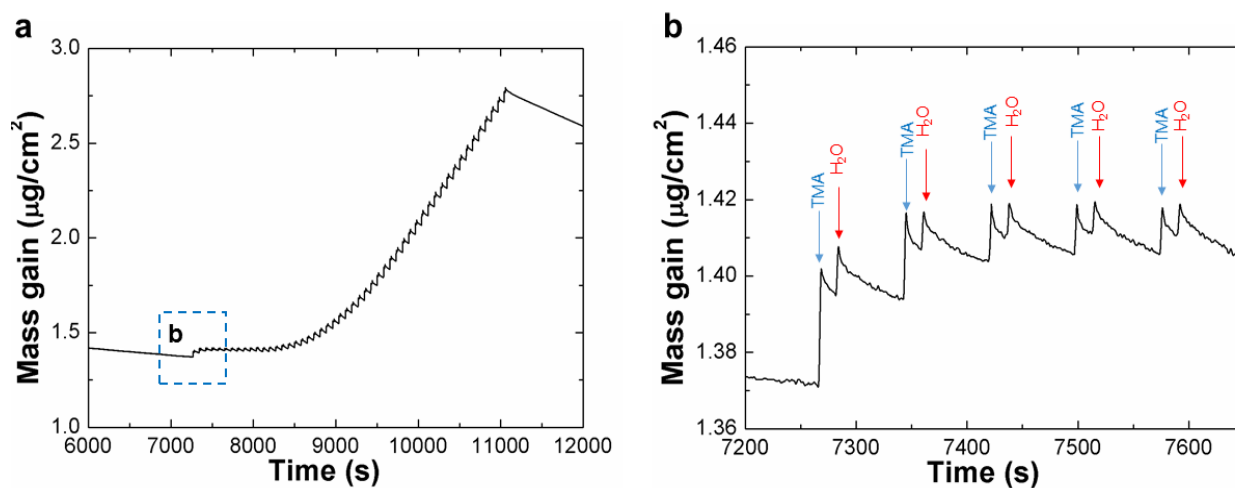


Figure 5.8. Nucleation and growth of Al₂O₃ ALD on CH₃NH₃PbI₃ at 75°C measured by *in situ* QCM, (a) successive 50 cycles; (b) initial 5 cycles.

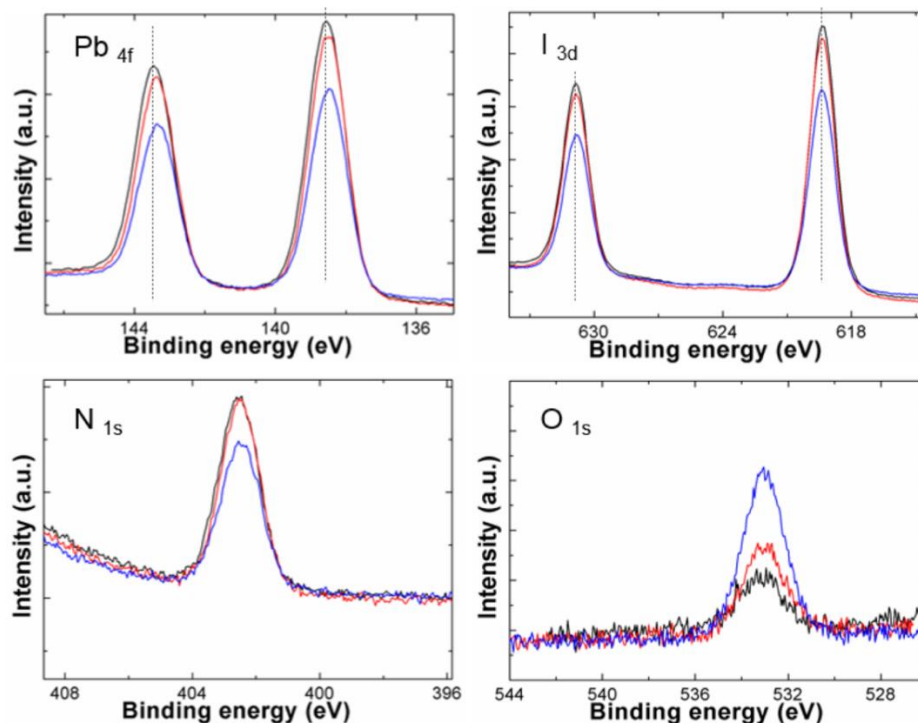


Figure 5.9. XPS spectrum of Pb_{4f} (a), I_{3d} (b), N_{1s} (c) and O_{1s} (d) in fresh CH₃NH₃PbI₃ (black trace) and after treated by 50 pulses TMA vapor at 25°C (red trace) and 75°C (blue trace). For all spectra, the lower C_{1s} peak is set at 284.8 eV.

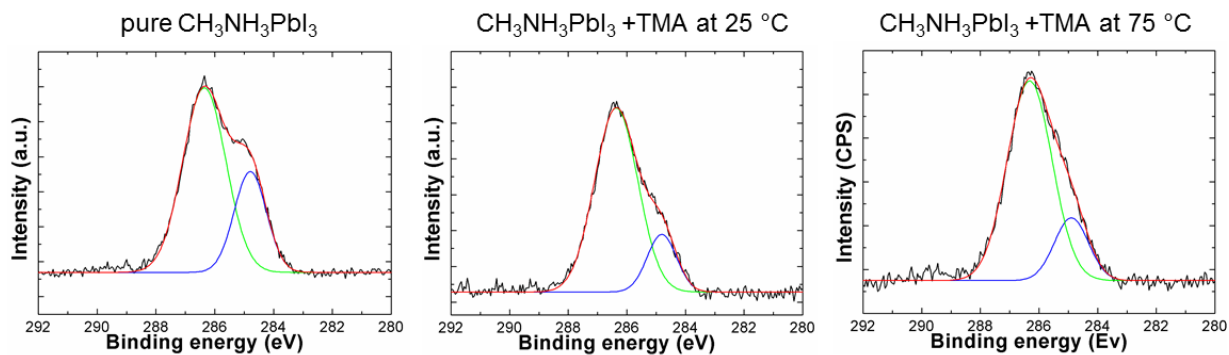


Figure 5.10. XPS spectrum of CH₃NH₃PbI₃ before (a) and after treated by 50 pulses TMA vapor at 25°C (b) and 75°C (c).

XPS spectra in **Figure 5.9** show the binding energy of Pb_{4f}, I_{3d}, N_{1s}, and O_{1s} peaks before and after the 50 pulses of TMA vapor at 25°C and 75°C. The peak of Pb_{4f} shifts to a lower energy after the TMA treatments at both temperatures. For example, the apex of the peak of Pb_{4f7/2} shifts from 138.6 eV (Pb-I) to 138.4 eV. This shift may indicate the possible formation of Pb-O bonds (mixed Pb-I and Pb-O) as Pb_{4f7/2} in Pb-O is located at 138.0 eV. However, as the shift is within the

resolution limitation of the XPS, further analysis is needed. After the TMA vapor treatments at both temperatures, the O/Pb ratios increase. The oxygen is due to the reaction between TMA treated samples and moisture in ambient. This is consistent with the formation of Pb-O on the surface. The apexes of I and N peaks do not have measurable shifts. It is surprising that Al_{2p} peak is not detectable by the XPS instrument for both sets of samples after 50 pulses of TMA vapor, it suggests that the signal of Al is below the detection limit (~ 0.1 at. %) of the instrument. This is consistent with a previous report, in which grazing-angle synchrotron-based XPS measures very small Al concentration on CH₃NH₃PbI₃ after 5 cycles of Al₂O₃ ALD.¹⁷³ Note, the grazing-angle synchrotron-based XPS is much more surface sensitive than the XPS used in this work. For the sample treated at 25°C, the low concentration of Al is due to the surface confined reaction as shown by QCM (**Figure 5.1**). The negligible Al signal on sample at 75°C means the 50 pulses of TMA vapor accumulate a very small amount of Al on the sample surface. For both samples, the ratio of peak areas at 284.8 eV and 286.3 eV decreases. The peak at 286.3 eV comes from the C-N bonding. The peak at ~ 284.8 eV is due to the C_{1s} peak, which could originate from hydrocarbons (e. g., from ambient). The higher degree of reduction of C_{1s} peaks indicates that C-N related species have a higher concentration on the sample surface. This result also suggests that CH₃NH₃⁺ does not leave the surface as CH₃NH₂, because, if this is the case, the intensity ratio of C-N/C-H peaks should not change significantly or at least should decrease as TMA and air contamination will bring hydrocarbons onto the surface.

We further examined the effect of 50 pulses of TMA vapor on the ambient stability of CH₃NH₃PbI₃ film. As shown in **Figure 5.11**, CH₃NH₃PbI₃ film remains dark in color after the TMA treatment at 25°C and 75 °C. This result indicates the amount of PbI₂ is small, which is consistent with the XRD measurements (**Figure 5.3** and **Figure 5.7**). After 14 days exposure in the ambient environment (25°C and 40% relative humidity), all three samples become yellow due to

the degradation of $\text{CH}_3\text{NH}_3\text{PbI}_3$ to form PbI_2 . The $\text{CH}_3\text{NH}_3\text{PbI}_3$ film that was treated with 50 pulses of TMA vapor at 25°C shows the least amount of yellowish color, in comparison with pristine $\text{CH}_3\text{NH}_3\text{PbI}_3$ film and the film treated by TMA vapor at 75°C . Therefore, the treatment with a low pressure of TMA (~ 0.1 torr) at 25°C can improve the ambient stability of $\text{CH}_3\text{NH}_3\text{PbI}_3$.

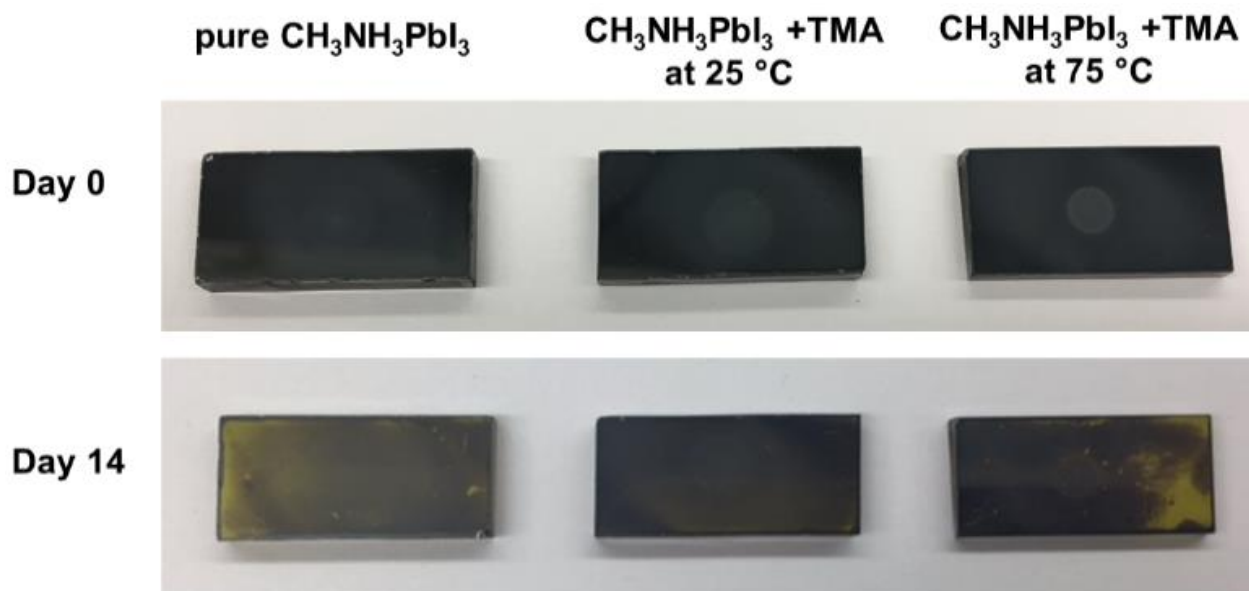


Figure 5.11. Optical image of $\text{CH}_3\text{NH}_3\text{PbI}_3$ and $\text{CH}_3\text{NH}_3\text{PbI}_3$ after treated by 50 pulses TMA vapor treatment at 75°C and 25°C . The samples are sitting in the lab ambient environment.

The morphology of the $\text{CH}_3\text{NH}_3\text{PbI}_3$ films after 50 pulses of TMA vapor at 25°C and 75°C are analyzed by SEM and presented in **Figure 5.12**. **Figure 5.12a** and **Figure 5.12b** show the change of surface morphology of $\text{CH}_3\text{NH}_3\text{PbI}_3$ films after 50 pulses of TMA vapor at 25°C . The fresh $\text{CH}_3\text{NH}_3\text{PbI}_3$ film (**Figure 5.12a**) shows clear crystal grain of $\text{CH}_3\text{NH}_3\text{PbI}_3$ and the grain boundaries. The 50 pulses of TMA treatment at 25°C generate hair-like surface texture (**Figure 5.12b**). The crystals and the grain boundaries can still be resolved. The 50 pulses of TMA treatment at 75°C also create the similar hair-like surface structures, which is denser than that is generated at 25°C . The grains cannot be easily differentiated after the treatment. These results suggest that the extent of reaction is higher at 75°C than at 25°C .

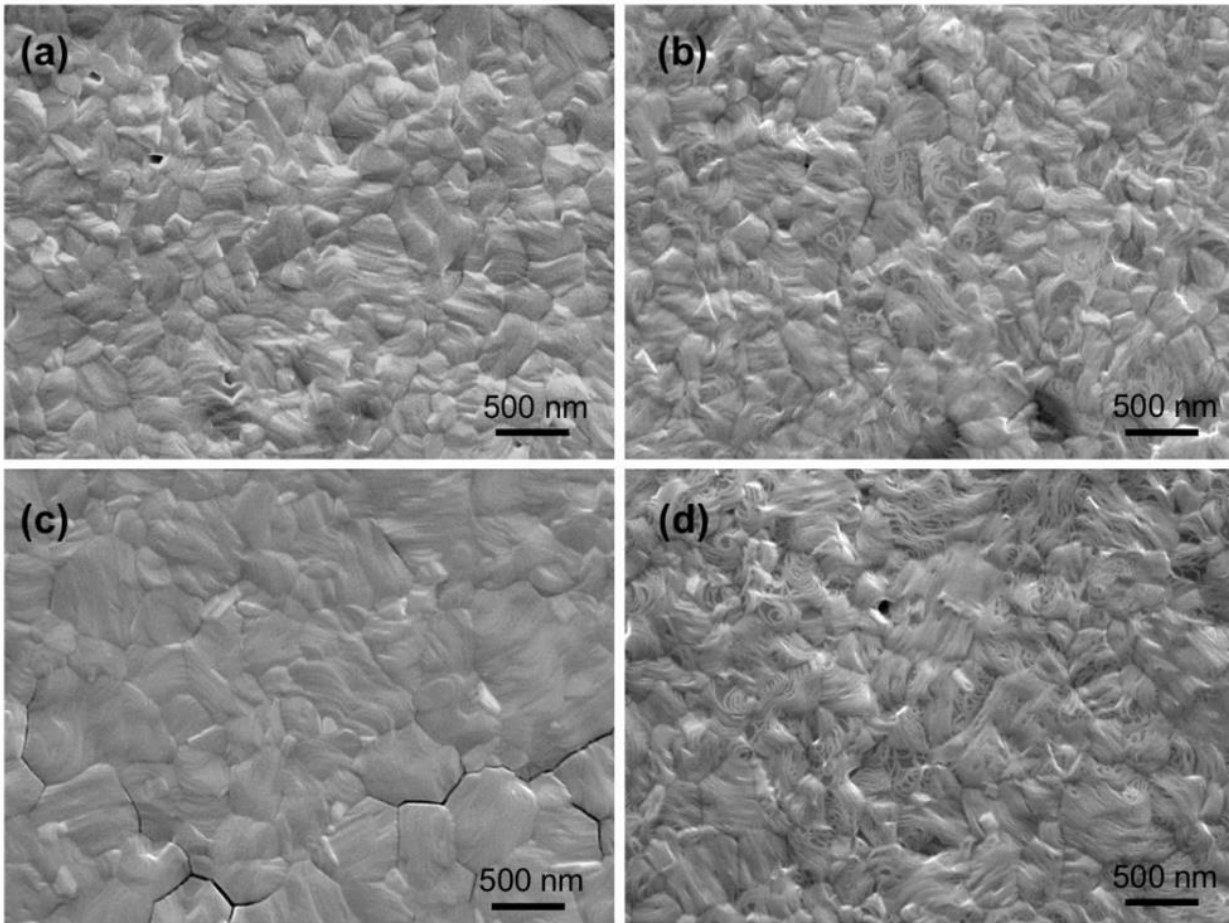


Figure 5.12. SEM images of top views of $\text{CH}_3\text{NH}_3\text{PbI}_3$ films grown on the silicon wafer, (a) before and (b) after 50 pulses of TMA vapor of 0.1 torr at 25°C , (c) before and (d) after TMA vapor of 0.1 torr at 75°C .

Effect of partial pressure of TMA

We further examined the effect of partial pressure of TMA vapor on the TMA/ $\text{CH}_3\text{NH}_3\text{PbI}_3$ reaction. If TMA/ $\text{CH}_3\text{NH}_3\text{PbI}_3$ reaction at 25°C is only limited by the sites on the external surface of $\text{CH}_3\text{NH}_3\text{PbI}_3$, the mass gain should not change with changing the partial pressure of TMA. The results in **Figure 5.13** show that the mass gain changes with partial pressure of TMA. With the exposure to TMA vapor of 0.5 torr, $\text{CH}_3\text{NH}_3\text{PbI}_3$ first gains mass, then loses mass during the first $\sim 60\text{s}$ exposure. In the following 140s exposure, the mass of $\text{CH}_3\text{NH}_3\text{PbI}_3$ is stable. By further increasing the partial pressure of TMA to ~ 1.2 torr, the mass is further reduced and stabilized with a net mass loss of $\sim 100\text{ ng/cm}^2$. The stabilized mass loss indicates that the reaction is confined at

the surface region. In addition, the sample color remains the same after these two treatments. In contrast, TMA vapor with a higher partial pressure (e.g., ~ 3 torr) continuously reduces the mass of $\text{CH}_3\text{NH}_3\text{PbI}_3$, suggesting the degradation of bulk of $\text{CH}_3\text{NH}_3\text{PbI}_3$ by TMA. In combination with the result in **Figure 5.1**, the data in **Figure 5.13** suggests that the reaction TMA/ $\text{CH}_3\text{NH}_3\text{PbI}_3$ at 25°C is strongly affected by the partial pressure of TMA vapor and the reaction is not limited by the sites on the external surface of $\text{CH}_3\text{NH}_3\text{PbI}_3$.

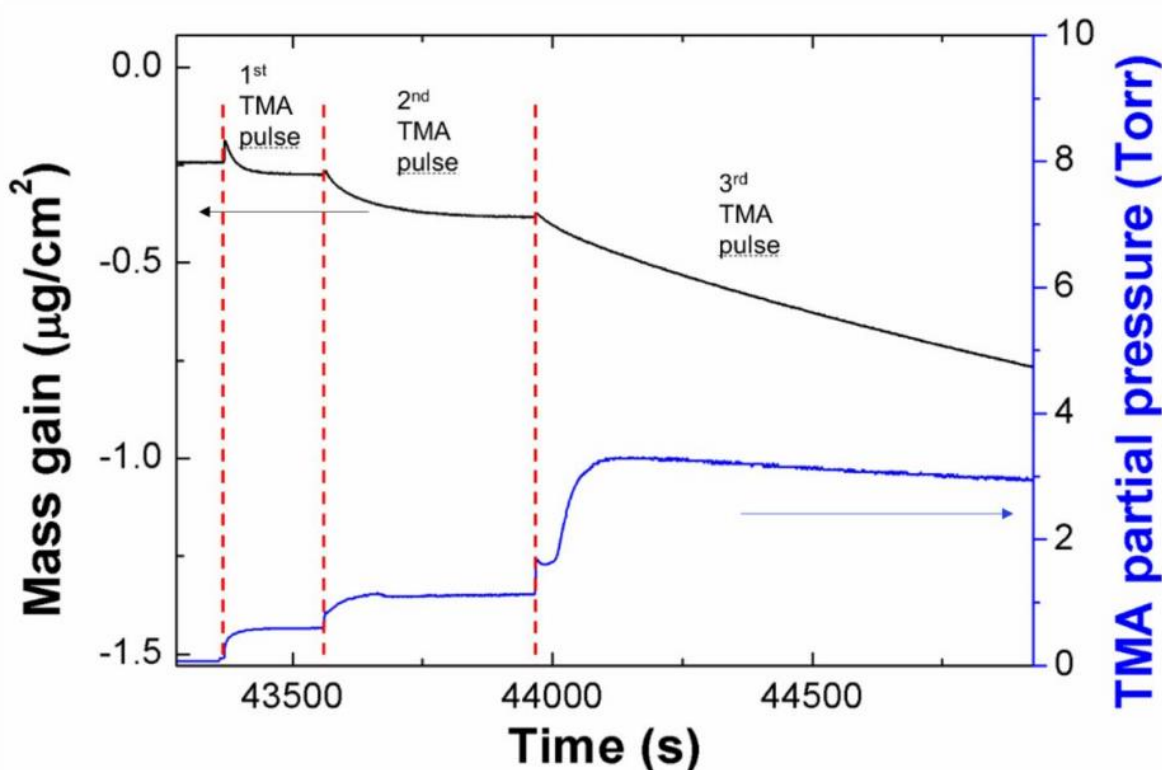


Figure 5.13. Mass change of $\text{CH}_3\text{NH}_3\text{PbI}_3$ during the long exposure to TMA vapor of high partial pressure at 25°C. Black line is the mass gain and blue trace is the partial pressure of TMA.

5.3 Discussion

Our results show that the reaction between TMA and $\text{CH}_3\text{NH}_3\text{PbI}_3$ can be dramatically affected by both the reaction temperature (**Figure 5.1** and **Figure 5.5**) and partial pressure of TMA (**Figure 5.1** and **Figure 5.13**). At 75 °C, TMA vapor of 0.1 torr continuously etches $\text{CH}_3\text{NH}_3\text{PbI}_3$;

At 25 °C, the reaction between TMA vapor of 0.1 torr and $\text{CH}_3\text{NH}_3\text{PbI}_3$ is limited and confined around the surface region. TMA vapor of a high partial pressure (e.g., 3 torr) can etch $\text{CH}_3\text{NH}_3\text{PbI}_3$ at 25 °C. These key findings suggest that the seemingly contradictory literature results^{74,166,171,173-175} could be due to the different processing conditions, including reaction temperature, partial pressure of TMA, and reaction times that are used in these papers. For instance, although TMA vapor will continuously etch $\text{CH}_3\text{NH}_3\text{PbI}_3$ at 100 °C,^{166,175} a short TMA exposure time will limit the extent of the etching reaction. Although Al_2O_3 ALD coating could be formed onto $\text{CH}_3\text{NH}_3\text{PbI}_3$ substrates at 75°C or 100°C, the interface between Al_2O_3 ALD coating and the $\text{CH}_3\text{NH}_3\text{PbI}_3$ substrate will be anything but a sharp interface. The composition and thickness of the interface will be affected by the processing temperature, TMA partial pressure, and reaction time. The interface's compositions and structures will be different in different experiments, the variation of interface properties could be one key reason that contradictory results are reported for the optoelectronic properties of Al_2O_3 ALD treated perovskites solar cells and their stability. Unfortunately, few of current literature carefully characterized the interface between Al_2O_3 ALD and $\text{CH}_3\text{NH}_3\text{PbI}_3$, whose properties will vary in different experimental conditions, and is the key to truly understand the correlations between ALD treatment and optoelectronics properties and stability of $\text{CH}_3\text{NH}_3\text{PbI}_3$ based devices.

Our experiment results show that TMA/ $\text{CH}_3\text{NH}_3\text{PbI}_3$ does not follow the simple surface-site-limited reaction modes.^{178,179} If $\text{CH}_3\text{NH}_3\text{PbI}_3$ is an impermeable and nondegradable substrate to TMA, the reaction between TMA and $\text{CH}_3\text{NH}_3\text{PbI}_3$ should be limited by surface sites and follow Langmuir isothermal adsorption behavior. The mass gain results should be that the higher the reaction temperature and the higher the partial pressure of TMA, the faster the TMA/ $\text{CH}_3\text{NH}_3\text{PbI}_3$ reaction approaches to monolayer saturation. However, the reaction shifts from accumulating mass (**Figure 5.1**) to removal of mass (**Figure 5.5**) with increasing the reaction temperature; the reaction also shifts from accumulation of mass (**Figure 5.1**) to removal of mass (**Figure 5.13**) by increasing

the partial pressure of TMA vapor. We know that $\text{CH}_3\text{NH}_3\text{PbI}_3$ is impermeable to TMA molecules as TMA is too big to diffuse into $\text{CH}_3\text{NH}_3\text{PbI}_3$. With our results, we hypothesize that the reaction between TMA and $\text{CH}_3\text{NH}_3\text{PbI}_3$ follows the core shrinking model of fluid-solid reaction,^{107,176} in which the reaction of TMA/ $\text{CH}_3\text{NH}_3\text{PbI}_3$ generates a product shell, which is much thicker than a monolayer, and the reaction frontier moves towards the core of $\text{CH}_3\text{NH}_3\text{PbI}_3$ until the product shell fully cover the underlying $\text{CH}_3\text{NH}_3\text{PbI}_3$ and block the TMA from reacting with the underlying $\text{CH}_3\text{NH}_3\text{PbI}_3$. This core-shrinking model can explain the experimental results. At 25°C, TMA/ $\text{CH}_3\text{NH}_3\text{PbI}_3$ reaction can gradually generate a conformal product shell over $\text{CH}_3\text{NH}_3\text{PbI}_3$ substrate to block TMA molecules from reaching the underlying $\text{CH}_3\text{NH}_3\text{PbI}_3$. However, the TMA/ $\text{CH}_3\text{NH}_3\text{PbI}_3$ reaction cannot form a conformal and dense shell to protect $\text{CH}_3\text{NH}_3\text{PbI}_3$ from TMA at 75°C or at 25°C with high partial pressure of TMA. We believe that the reaction proceeds through similar pathways, but the composition of the product layer is sensitive to the reaction temperature and partial pressure of TMA. We draw our hypothesis based on the following reasons. First, at both temperatures, QMS measurements show the same gaseous species and the same transition, in which CH_3I appears when CH_4 signal decreases to a constant value (**Figure 5.2** and **Figure 5.6**). Second, the ex-situ XPS shows similar changes of surface compositions of $\text{CH}_3\text{NH}_3\text{PbI}_3$ after TMA treatment at both temperatures (**Figure 5.9** and **Figure 10**), followed by the air exposure.

Although we cannot nail down the exact reaction pathways between TMA and $\text{CH}_3\text{NH}_3\text{PbI}_3$, our results advance the current understandings in the following aspects. First, our QMS measurement show that although CH_3NH_3^+ is removed from $\text{CH}_3\text{NH}_3\text{PbI}_3$ by TMA at 75°C, the reaction product is not CH_3NH_2 (**Figure 5.6**). As QMS can detect CH_3I as desorbed byproducts, QMS should be able to detect CH_3NH_2 if it is a main byproduct as CH_3NH_2 has a higher vapor pressure (boiling point is -6°C compared with 45°C of CH_3I) and probably higher ionization cross-

section than CH_3I .¹⁸⁰ Although TMA could take a proton from CH_3NH_3^+ as TMA is a strong Lewis acid and CH_3NH_3^+ ,¹⁸¹ the as-formed CH_3NH_2 will react with other TMA molecules, because TMA could coordinate with R-NHx (R: alkyl) to form stable complexes,^{182,183} including $(\text{CH}_3)_2\text{AlNHCH}_3$ ($m/z=87$), $(\text{CH}_3)_2\text{AlNH}_2\text{CH}_3^+$ ($m/z=88$), $(\text{CH}_3)_3\text{AlNH}_3$ ($m/z=89$), $(\text{CH}_3)_2\text{AlCH}_2\text{I}$ ($m/z=198$), $(\text{CH}_3)_2\text{Al}(\text{NH}_2\text{CH}_3)_2^+$ ($m/z=104$). Some of these complexes could present in the product layer as QMS did not detect these species (**Figure S4**). However, the Al in the product layer is below the detection limitation of XPS. Further experiments with in-situ IR coupled with $\text{CH}_3\text{NH}_3\text{PbI}_3$ powders of a high surface area could help identify the Al species produced from the reaction because if TMA coordinates with N-H, infrared (IR) peaks from $-\text{CH}_3$ will increase and N-H peaks could shift. In addition, TMA could also react with $\text{CH}_3\text{NH}_3\text{PbI}_3$ to form compounds containing I, such as AlI_3 or complexes based on AlI_3 and methyl ammonium, whose mass signals are close to and beyond the detection limit of our mass spectrometer ($m/z=200$). Second, we show that CH_3I is not the volatile byproduct that is responsible for the mass reduction at 75°C in **Figure 5.5**,^{27,184} because CH_3I is detected by QMS in the later pulses of TMA vapor rather than in the earlier pulses (**Figure 5.6**). CH_4 is probably generated from the reaction between TMA and CH_3NH_3^+ , however it cannot explain the mass loss. Further studies are needed to understand the chemical identity of volatile compounds from the reaction between TMA and $\text{CH}_3\text{NH}_3\text{PbI}_3$. Such understanding will help us understand the surface reactivity of $\text{CH}_3\text{NH}_3\text{PbI}_3$. Third, our results suggest that the reaction between $\text{CH}_3\text{NH}_3\text{PbI}_3$ and TMA changes with pulses of TMA vapors, meaning the surface chemistry changes by repeating TMA pulses. CH_3I is generated in the later stage of the reaction between TMA and decomposed products, for instance, transferring of $-\text{CH}_3$ ligand from TMA to I- as the Al center is a strong Lewis acid. No literatures have mentioned such dynamics of surface reactions. Further studies of the exact surface reactions mechanism could help improve the stability of $\text{CH}_3\text{NH}_3\text{PbI}_3$.

5.4 Conclusions

The reaction of TMA/ $\text{CH}_3\text{NH}_3\text{PbI}_3$ is not limited by sites on the external surface of $\text{CH}_3\text{NH}_3\text{PbI}_3$ substrates. Instead, the reaction is strongly affected by the reaction temperature and partial pressure of TMA and proceeds towards to the core of $\text{CH}_3\text{NH}_3\text{PbI}_3$ presumably through the core-shrinking mode of fluid-solid reactions. A layer of products will be formed at the interface between Al_2O_3 ALD coating and $\text{CH}_3\text{NH}_3\text{PbI}_3$. The properties of the layer of materials deserve more detailed studies in order to reliably apply TMA/ $\text{CH}_3\text{NH}_3\text{PbI}_3$ for modifying the surface of perovskite in a controllable and desirable way without significant changing its bulk. It is possible that other vapor/ $\text{CH}_3\text{NH}_3\text{PbI}_3$ reactions could advance towards the core of $\text{CH}_3\text{NH}_3\text{PbI}_3$ as well and generate a layer of products. The composition of these layers would be strongly affected by the processing conditions of these experiments. As shown by our results, the kinetics of the reactions could be harnessed to control the composition, thickness and microstructure of these generated interfaces, thereby to obtain the desired optoelectronic properties of perovskite devices. The heterogeneous reactions on $\text{CH}_3\text{NH}_3\text{PbI}_3$ and other halide perovskite are not well studied, and many assumptions have been made in literature and not yet confirmed. As hybrid halide perovskites have unique surface chemistry, their heterogeneous reactions will be interesting and complex, and the understanding of these heterogeneous reactions is essential to finding new methods to enable commercially viable perovskite devices.

Supporting information:

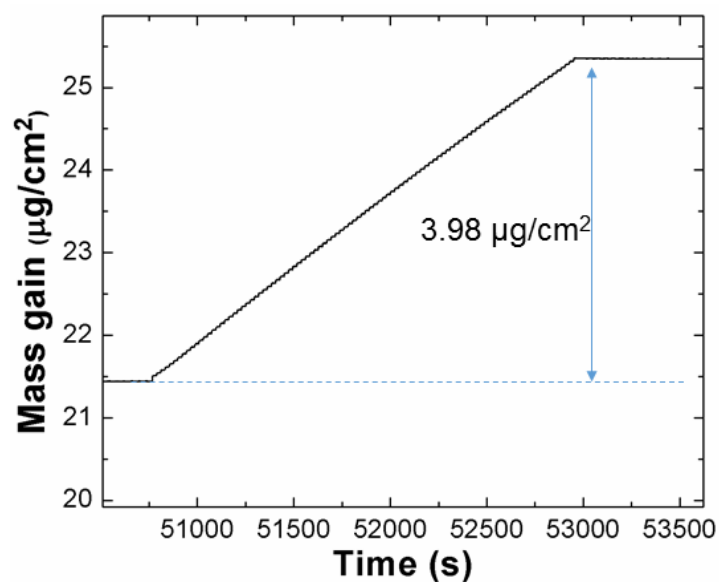


Fig.S1. Mass gain of 100 cycles of ALD Al₂O₃ at 75°C. The crystal was coated with 200 cycles of ALD Al₂O₃ before the measurement. The mass gain of each cycle stabilizes at 39.8 ng/cm².

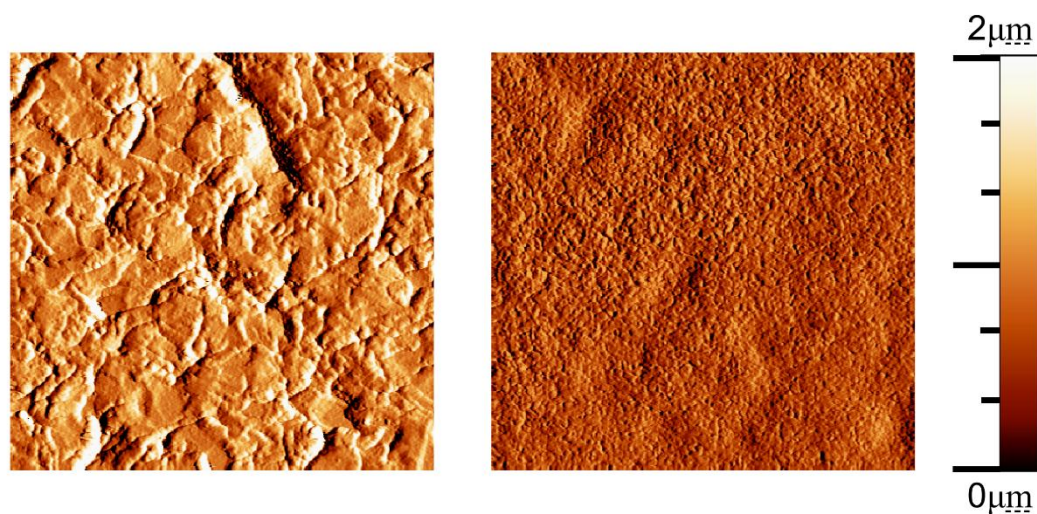


Fig. S2. AFM image of a clean QCM crystal without (left) and with CH₃NH₃PbI₃ film (right). The sampling area is 20µm×20µm for both images.

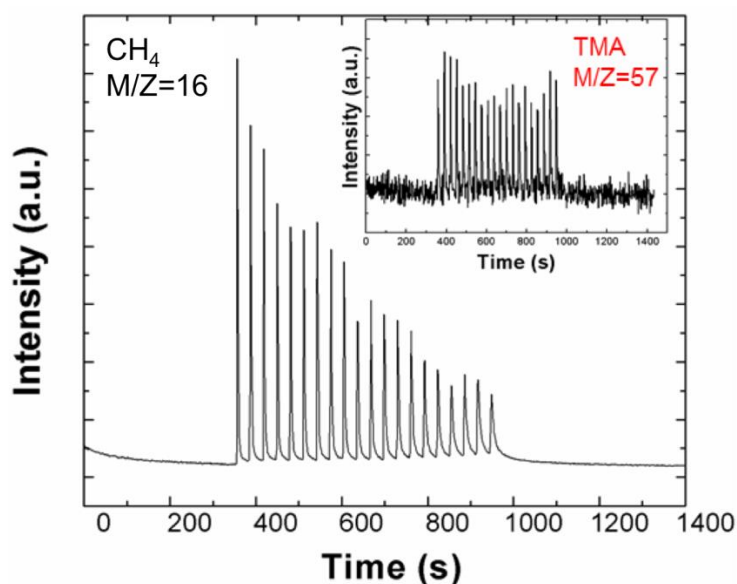


Fig. S3. The QMS signal during TMA pulsed into the reactor chamber that does not containing CH₃NH₃PbI₃ powder at 25°C. The signal intensity of CH₄ (m/z = 16) decreases by repeating TMA vapor pulses and then becomes constant after ~ 16 pulses. The intensity of TMA (m/z = 57) signal remains relative constant.

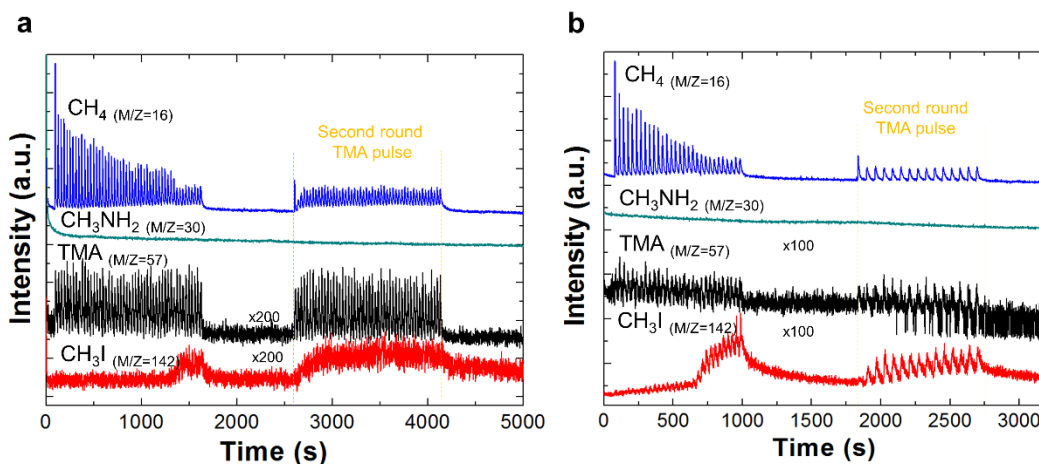


Fig.S4. In situ QMS measurement of successive two rounds TMA pulsing on the CH₃NH₃PbI₃ powder, the experiment was carried at (a) 25 °C and (b) 75°C. At 25C, to prove this hypothesis, a second train of TMA vapor pulses is pulsed onto CH₃NH₃PbI₃ powder after it had stayed in the vacuum chamber for ~ 1000s (Fig. S4a). Only the 1st pulse of TMA vapor pulses, in the second train, generate CH₄ from the signal of produced CH₄ is detected, which signal of CH₃I is not observed but CH₄ due to the TMA reaction priority with surface –OH group. The signal intensity of CH₃I increases to constant after a couple pulses of TMA vapor. During this 1000s storing, the surface group of perovskites reorganized, and water molecule bonded on the surface of perovskite and instrument again due to the low-vacuum of our reactor (1 torr).

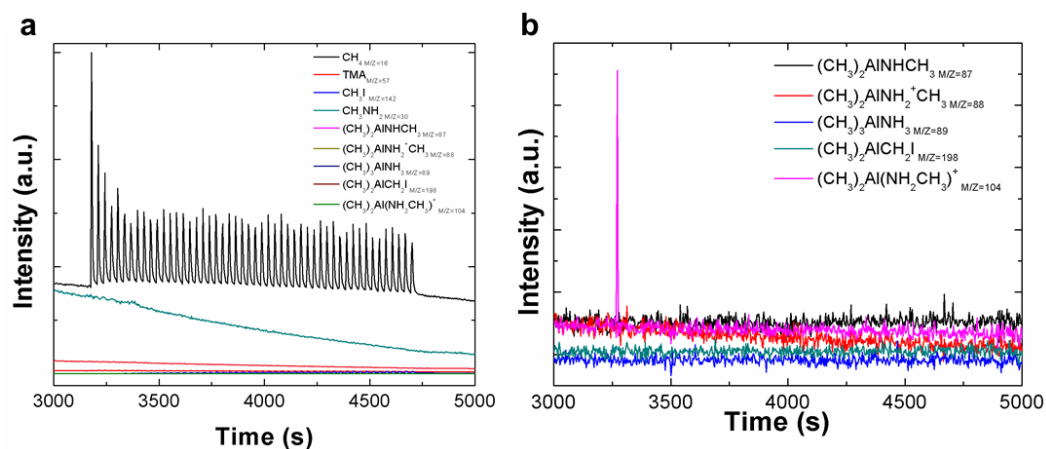


Fig.S5. (a) The possible gas byproducts from the reaction between TMA and $\text{CH}_3\text{NH}_3\text{PbI}_3$ at 75°C ; (b) Zoom-in spectrum of the main m/z peaks of the hypothesized gas byproducts of $(\text{CH}_3)_2\text{AlNHCH}_3$, $(\text{CH}_3)_2\text{AlNH}_2\text{CH}_3^+$, $(\text{CH}_3)_3\text{AlNH}_3$, $(\text{CH}_3)_2\text{AlCH}_2\text{I}$, $(\text{CH}_3)_2\text{Al}(\text{NH}_2\text{CH}_3)_2^+$.

CHAPTER 6: IMPROVE THE STABILITY OF HYBRID HALIDE PEROVSKITE VIA ATOMIC LAYER DEPOSITION ON ACTIVATED PHENYL-C61 BUTYRIC ACID METHYL ESTER

6.1 Introduction

[6, 6]-phenyl-C61 butyric acid methyl ester (PCBM) is one of the most widely used and studied n-type charge transport material for polymer solar cells¹⁸⁵ and hybrid perovskite solar cells^{146,186} due to its high electron transporting efficiency and solution-processible properties. Recently, it has been proposed and demonstrated by several groups that PCBM can help nucleate the formation of pinhole free oxide films by atomic layer deposition (ALD) when it is applied onto $\text{CH}_3\text{NH}_3\text{PbI}_3$ surface. The resulted pinhole free PCBM/ALD oxide film can block O_2 and water from diffusing and degrading $\text{CH}_3\text{NH}_3\text{PbI}_3$, therefore shows a great promise in improving the stability of halide hybrid perovskite, e.g., $\text{CH}_3\text{NH}_3\text{PbI}_3$, in the outdoor environment. For instance, Yu-Chia Chang *et al.* reported that ALD ZnO film on the surface of PCBM⁷⁷ not only provides excellent electron extraction and transport properties but also supply excellent air stability for more than 1 month. What`s more, Martinson *et al.* claimed that ALD TiO_2 onto PCBM film⁷³ can improve the thermal stability of $\text{CH}_3\text{NH}_3\text{PbI}_3$ and even protect the underlying $\text{CH}_3\text{NH}_3\text{PbI}_3$ from contacting water droplet. McGehee *et al.* demonstrate that PCBM/ALD SnO_2 not only serves as a good electron transporting layer, but also extends the lifetime of $\text{CH}_3\text{NH}_3\text{PbI}_3$ solar cell to 1000-hour in the damp heat test at 85 °C and 85% relative humidity environment.^{169,187} These results are very encouraging for using PCBM/ALD coatings to address the poor stability of halide hybrid perovskite. However, none of these studies examined the fundamental nucleation mechanisms about these ALD oxides on

PCBM. The growth behavior and surface reaction mechanism of ALD oxide film on PCBM is not yet understood. As ALD relies on heterogeneous surface reactions to grow the film, this missing information is critical to reliably apply PCBM/ALD coatings to address the poor stability of hybrid halide perovskites.

In this paper, we investigate the nucleation of ALD ZnO on $\text{CH}_3\text{NH}_3\text{PbI}_3$ and $\text{CH}_3\text{NH}_3\text{PbI}_3/\text{PCBM}$. Our results show that diethyl zinc (DEZ, a precursor for ALD ZnO) etches $\text{CH}_3\text{NH}_3\text{PbI}_3$ in the temperature range of 25°C - 100°C . PCBM overcoating on $\text{CH}_3\text{NH}_3\text{PbI}_3/\text{PCBM}$ slows down the etching reaction by DEZ dramatically because the PCBM layer blocks DEZ molecules from reaching the underlying $\text{CH}_3\text{NH}_3\text{PbI}_3$. Moreover, our in-situ measurement shows that ZnO ALD cannot nucleate onto the PCBM film because PCBM does react with DEZ or H_2O . We further identify that ALD Al_2O_3 can grow reliably on the PCBM film and generate reactive sites for ALD ZnO growth. The PCBM/ Al_2O_3 -ZnO coating dramatically enhances the stability of $\text{CH}_3\text{NH}_3\text{PbI}_3$ in ambient, even in contact with liquid water droplets. This new reliable chemical route can be further improved and applied onto other hybrid perovskite materials to extend the lifetime of solar cell in the working environment.

6.2 Results and discussion

ALD ZnO on $\text{CH}_3\text{NH}_3\text{PbI}_3$

We first examined ZnO ALD on $\text{CH}_3\text{NH}_3\text{PbI}_3$. As illustrated by the data in **Figure 6.1a**, the mass of $\text{CH}_3\text{NH}_3\text{PbI}_3$ is reduced continuously by repeating ALD ZnO for 100 cycles, suggesting that direct growth of ZnO on $\text{CH}_3\text{NH}_3\text{PbI}_3$ can degrade $\text{CH}_3\text{NH}_3\text{PbI}_3$. The mass reduction is in sharp contrast to mass gain rate of $\sim 100 \text{ ng/cm}^2$ per cycle during steady state ALD ZnO (**Figure S2**). As shown by **Figure 6.1b**, the reduction of mass results solely from the DEZ step. The water pulse steps do not affect the mass in a noticeable way because of the low concentration of water vapor (0.1 Torr, relative humidity of 0.4% at 25°C). This result is consistent with previous

reports.¹⁸⁸⁻¹⁹¹ It is interesting to note that the first DEZ half cycle produces a net mass gain on the fresh $\text{CH}_3\text{NH}_3\text{PbI}_3$ substrate. It is probably due to the net effect from the mass accumulation reaction between DEZ with surface $-\text{OH}$ species and mass reduction reaction between DEZ and $\text{CH}_3\text{NH}_3\text{PbI}_3$.

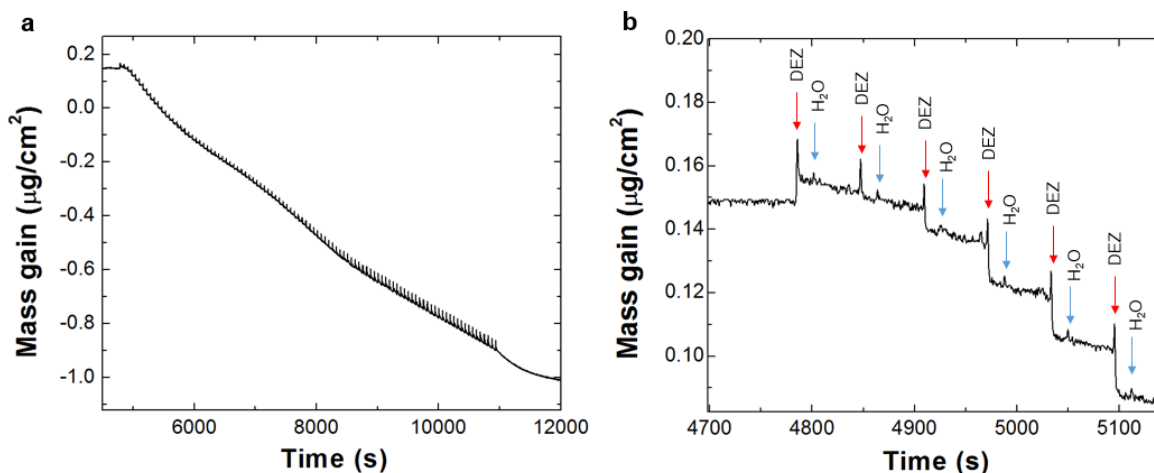


Figure 6.1. (a) Mass change measured by QCM in 100 cycles ALD ZnO on $\text{CH}_3\text{NH}_3\text{PbI}_3$ at 25°C (DEZ and water), (b) the initial 6 cycles of ALD ZnO on $\text{CH}_3\text{NH}_3\text{PbI}_3$

Our results in **Figure 6.1** provide direct results that ZnO ALD can degrade $\text{CH}_3\text{NH}_3\text{PbI}_3$, which is consistent with several other reports^{189,191} In contrast, there is one report which showed the feasibility of depositing ZnO on the bare $\text{CH}_3\text{NH}_3\text{PbBr}_3$ with atmospheric pressure ALD ZnO.¹⁹² This difference of experimental results may be due to the better intrinsic thermal stability of $\text{CH}_3\text{NH}_3\text{PbBr}_3$ than $\text{CH}_3\text{NH}_3\text{PbI}_3$.¹⁹³ In addition, in atmosphere pressure ALD, it is possible to form ZnO in vapor phase because it is much harder to remove the gas phase reactants from the reactor at atmospheric pressure than under vacuum condition as the boundary layer of gas flow increases with pressure.

The differential FTIR spectrum (**Figure 6.2**) confirms that CH_3NH_3^+ is removed from the $\text{CH}_3\text{NH}_3\text{PbI}_3$ substrate by ZnO ALD. Negative peaks of N–H stretching (3179 and 3132 cm^{-1}), N–H bending (1469 cm^{-1}), and C–N stretching (960 cm^{-1}) are from the removed CH_3NH_3^+ groups. On the basis of relative peak intensity of N–H stretching (3179 cm^{-1}) and N–H bending (1496 cm^{-1})

before and after the ALD process, ~20% of CH_3NH_3^+ are removed by the 100 DEZ/water cycles (shown in **Figure S3**). However, no $-\text{OH}$ group could be observed after 100 ALD ZnO cycles. It could be due to the limited sensitivity of the IR instrument for the thin film.

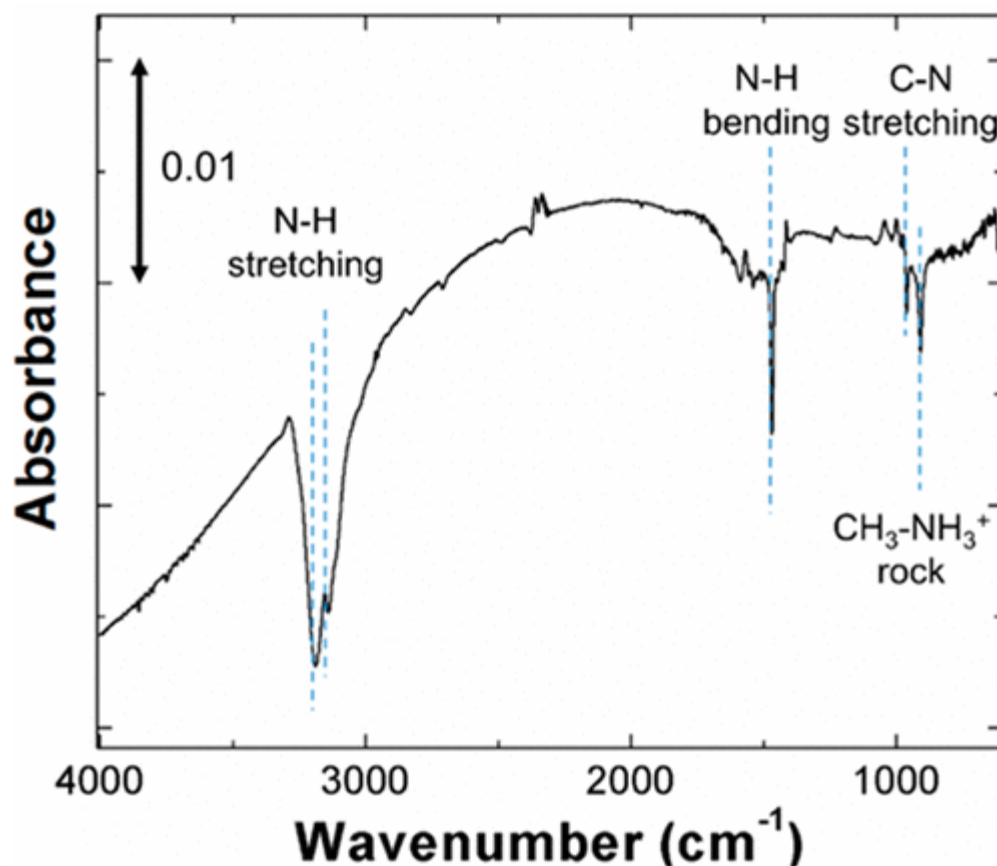


Figure 6.2. Differential IR spectrum of $\text{CH}_3\text{NH}_3\text{PbI}_3$ after 100 cycles of ALD ZnO at 25 °C. The fresh $\text{CH}_3\text{NH}_3\text{PbI}_3$ is used as the reference. Negative peaks represent removed species.

Figure 6.3 shows the mass gain behavior by repeating DEZ half cycles onto $\text{CH}_3\text{NH}_3\text{PbI}_3$ substrate. Every pulse of DEZ vapor reduces the mass from $\text{CH}_3\text{NH}_3\text{PbI}_3$. It suggests that the etching reaction between DEZ and $\text{CH}_3\text{NH}_3\text{PbI}_3$ is not limited by the surface sites. The reduction of mass is absent during the purge step, where only N_2 flows, suggesting that the products from the reaction does not cause further mass reduction. The mass reduction during the first DEZ pulse is different from that at 25 °C (**Figure 6.1**), which shows mass gain during the first pulse of DEZ. The different behavior is due to the higher rate of etching by DEZ at 60 °C. After the 50

pulses of DEZ vapor, the decomposition product is PbI_2 as indicated by the yellowish color in the optical image of QCM crystals (inset image of **Figure 6.3** and XRD **Figure S4**).

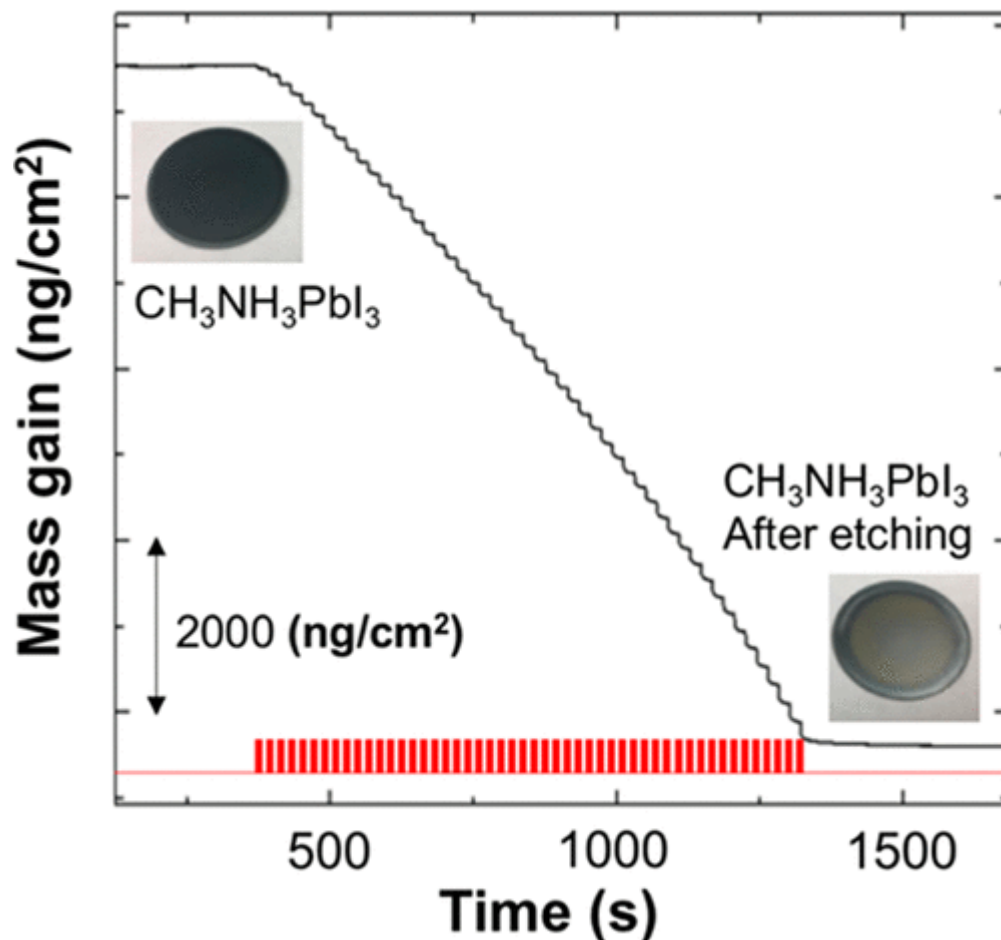


Figure 6.3. Mass change on the $\text{CH}_3\text{NH}_3\text{PbI}_3$ substrate by repeating pulses of DEZ vapor at 60°C . The inset image (top left) is QCM crystal with a fresh $\text{CH}_3\text{NH}_3\text{PbI}_3$ film. The same sample after 50 pulses of DEZ vapor is shown in the inset image (bottom right). Bottom red trace illustrates the DEZ pulses.

Figure 6.4 shows the mass gain behavior during ALD ZnO on $\text{CH}_3\text{NH}_3\text{PbI}_3/\text{PCBM}$, in which PCBM is over-coated on $\text{CH}_3\text{NH}_3\text{PbI}_3$. As shown by the top trace in **Figure 6.4**, $\text{CH}_3\text{NH}_3\text{PbI}_3/\text{PCBM}$ is quite stable in vacuum at 80°C as the mass change is only $\sim 10\text{ ng/cm}^2$ for more than 30 min. As shown by the middle trace, 100 cycles of ALD ZnO reduce the mass of $\text{CH}_3\text{NH}_3\text{PbI}_3/\text{PCBM}$ by $\sim 60\text{ ng/cm}^2$, which is higher than the mass loss of $\text{CH}_3\text{NH}_3\text{PbI}_3/\text{PCBM}$

caused by vacuum only. This mass reduction is presumably due to the surface reaction during ALD ZnO; however, there is no clear mass change during the pulses of DEZ and water. Coupled with the results in **Figure 6.1**, these data suggest that PCBM coating can block DEZ from etching $\text{CH}_3\text{NH}_3\text{PbI}_3$. However, the absence of mass gain during ALD ZnO suggests that DEZ/ H_2O ALD chemistry could not nucleate on PCBM.

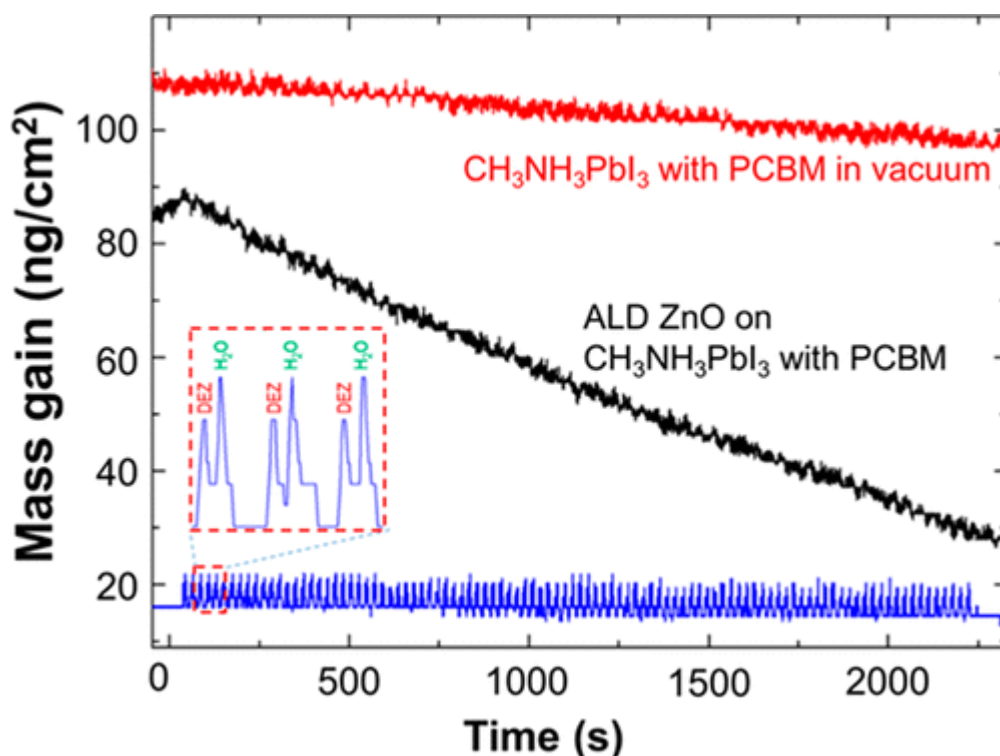


Figure 6.4. Mass change during ALD ZnO ($\text{DEZ}/\text{N}_2/\text{H}_2\text{O}/\text{N}_2 = 1:5:1:15\text{s}$) on the $\text{CH}_3\text{NH}_3\text{PbI}_3$ substrate with PCBM coating (~ 65 nm) at 80°C (black). The reference is the mass change of a similar sample in the vacuum at 80°C without ZnO ALD (red). The bottom trace (blue) shows the transient pressure increase during the pulse of DEZ and H_2O .

Figure 6.5 shows the IR spectra of the $\text{CH}_3\text{NH}_3\text{PbI}_3/\text{PCBM}$ sample before and after 200 cycles ALD ZnO. The locations of characteristic peaks of $\text{CH}_3\text{NH}_3\text{PbI}_3$ in fresh $\text{CH}_3\text{NH}_3\text{PbI}_3/\text{PCBM}$ align well with those from the pure $\text{CH}_3\text{NH}_3\text{PbI}_3$.^{194,195} The small positive peak at 1735 cm^{-1} is due to the $\text{C}=\text{O}$ bonding of PCBM.¹⁹⁶ The 200 ZnO ALD cycles do not change the locations and intensity of the peaks from $\text{CH}_3\text{NH}_3\text{PbI}_3$, confirming that the PCBM layer protects the underlying

CH₃NH₃PbI₃ from being corroded by the DEZ/H₂O chemistry at 80 °C for at least 200 cycles. The 200 cycles of ZnO ALD does not affect the intensity of the peak at 1735 cm⁻¹ neither, which is expected as DEZ is a weak Lewis acid and cannot activate C=O.⁷⁵ **Figure 6.6** shows that the mass gain is negligible during 100 cycles of DEZ/H₂O ALD chemistry on a PCBM film that is directly coated on QCM, supporting that both DEZ and H₂O cannot react with PCBM. Therefore, on the basis of the IR and QCM data, we conclude that ZnO ALD cannot nucleate on CH₃NH₃PbI₃/PCBM and PCBM. This result does not agree with the literature report, which shows that 100 cycles ZnO ALD was able to nucleate onto PCBM-coated CH₃NH₃PbI₃.¹⁹⁷ The difference could be due to the impurities in the PCBM, as impurities can act as nuclei to grow ALD film.¹⁹⁸

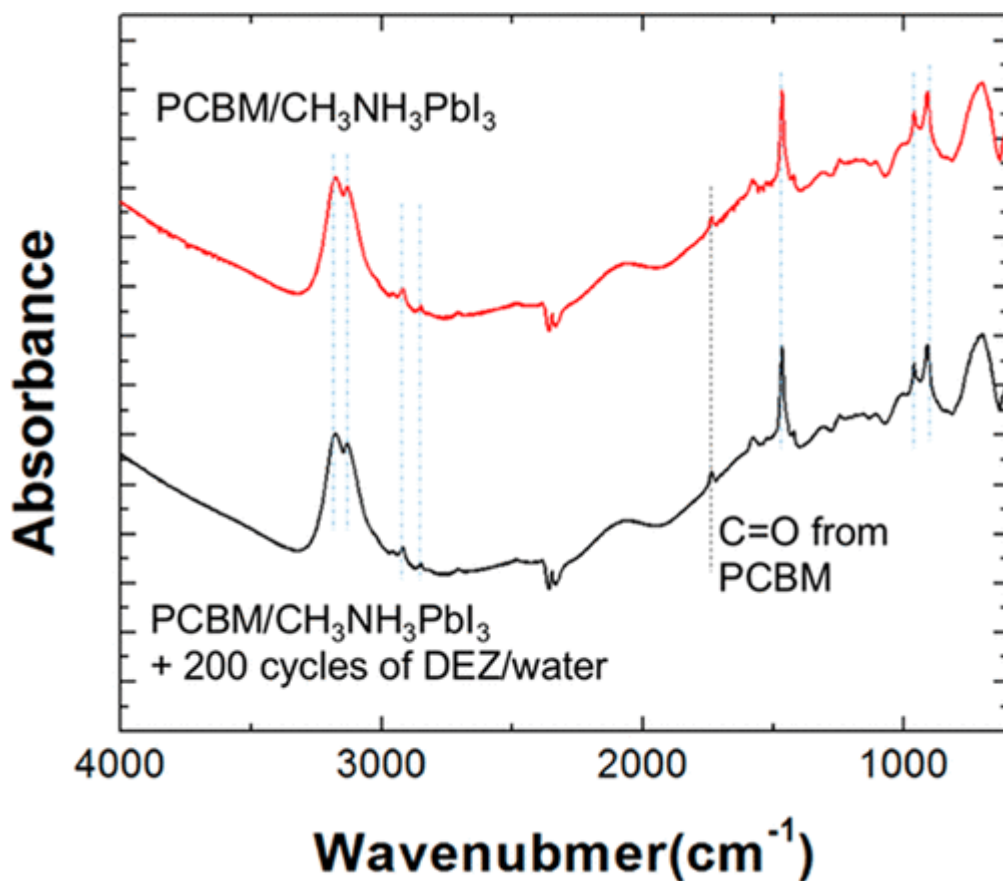


Figure 6.5. IR spectra of fresh CH₃NH₃PbI₃/PCBM before and after 200 cycles of ZnO ALD process at 80 °C. Dash-dot lines are peaks from CH₃NH₃PbI₃ and black dash line is the peak from PCBM. A clean Si substrate was used as the reference.

To nucleate ZnO ALD onto PCBM, a strategy would be activating the sites on PCBM. TMA/H₂O chemistry can potentially react with C=O on PCBM^{199,200} to provide nucleation sites. **Figure 6.7a** shows that each ALD Al₂O₃ cycle accumulates mass onto a CH₃NH₃PbI₃/PCBM substrate, suggesting that TMA/H₂O chemistry can grow on PCBM. The reaction during TMA exposure on CH₃NH₃PbI₃/PCBM produces net mass gain, which is different from the mass loss, that is, etching reaction, which is induced by TMA on a bare CH₃NH₃PbI₃ film.¹⁸⁸ It suggests that PCBM overcoating can block TMA from etching CH₃NH₃PbI₃. The 40 cycles of Al₂O₃ ALD accumulate 430 ng/cm² mass and the last Al₂O₃ cycle has a mass gain rate of ~15 ng/cm², which is one-third of the mass gain rate (~45 ng/cm²) in steady state Al₂O₃ ALD on an atomically smooth surface. It means that 40 cycles Al₂O₃ ALD does not form a continuous Al₂O₃ coating on PCBM yet, instead generates Al_xO_y nanoparticles that are decorated on PCBM. These Al_xO_y nanoparticles can help nucleate ALD ZnO as evidenced by the gradually increased mass gain rate with ALD cycles (**Figure 6.7b**). The mass gain of the last ZnO cycle is <50 ng/cm², which is only a half of mass gain (~100 ng/cm²) during the steady state ZnO ALD, suggesting that the 40 cycles of ZnO ALD does not yet cover the surface of PCBM with a continuous ZnO film. We are aware that Al₂O₃ is an insulator and understand that the thinner the Al₂O₃ layer is, the better it is for charge extraction. **Figure S5** shows that less Al₂O₃ ALD cycles (e.g., 20 cycles) can also nucleate the ZnO ALD process but with a longer nucleation period.

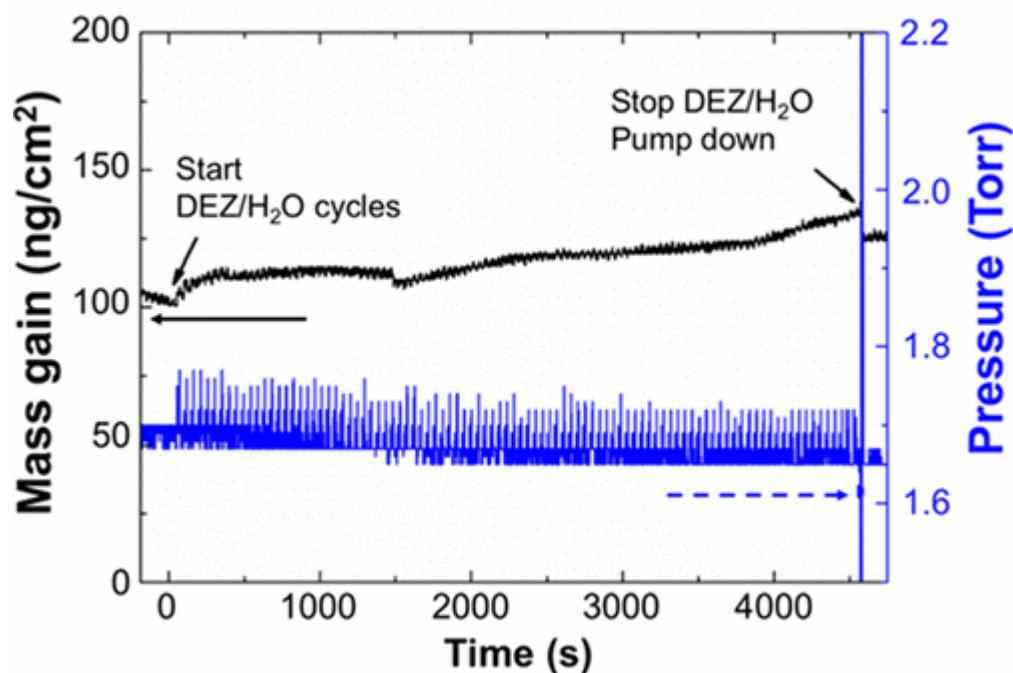


Figure 6.6. Mass change during ALD ZnO on PCBM at 100 °C.

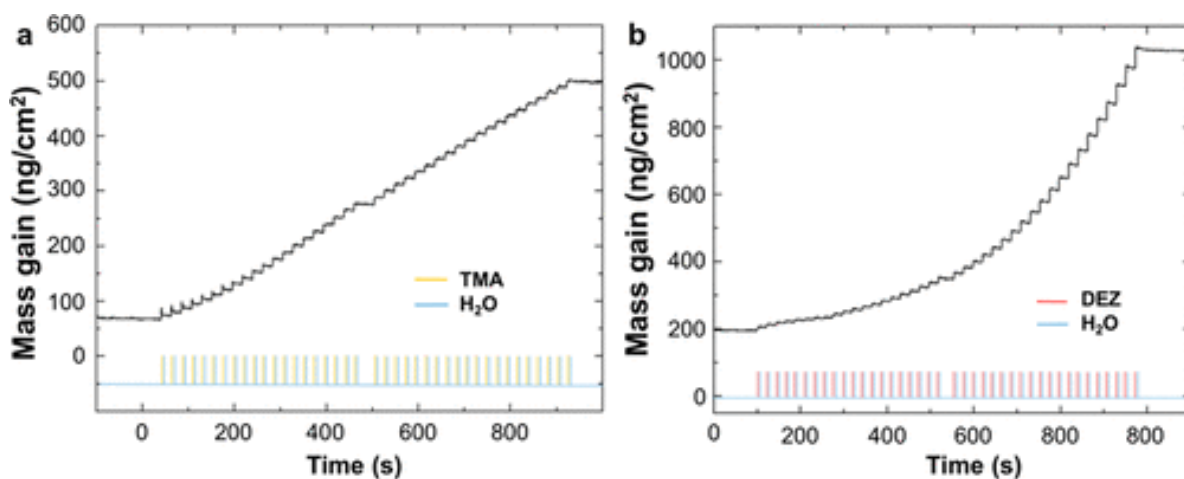


Figure 6.7. Mass change on the surface of the $\text{CH}_3\text{NH}_3\text{PbI}_3/\text{PCBM}$ substrate: (a) during 40 cycles of ALD Al_2O_3 and (b) following ALD ZnO cycles.

It is interesting to probe the mass gain during a long exposure of TMA as PCBM film because it is known that Lewis acid, as strong as TMA, reacts with $\text{C}=\text{O}$ slowly. **Figure 6.8a** shows the mass gain behavior during a long exposure of TMA vapor on a PCBM film, which has a mass gain of $33 \mu\text{g}/\text{cm}^2$, corresponding to $\sim 0.054 \mu\text{mol}$ PCBM coating on the QCM crystal surface.

When the PCBM film is exposed to TMA vapor of a partial pressure of ~ 1 Torr, the mass gain increases quickly and then slows down even when more TMA (a higher partial pressure) is added into the reactor. The initial mass is due to the diffusion and adsorption of TMA and the following slow mass uptake is ascribed to the slow reaction between TMA and PCBM. During the following purge step, the removal of mass is small, indicating that most of the obtained mass is from the chemical reaction. The net mass gain from the half cycle of TMA vapor is $\sim 0.35 \mu\text{g}/\text{cm}^2$, which is much larger than the mass gain ($< 20 \text{ ng}/\text{cm}^2$) resulting from the TMA exposure of much shorter time and smaller partial pressure (**Figure 6.7a**). This result suggests that the reaction between TMA and PCBM is limited by the reaction kinetics between TMA and PCBM. The differential IR spectrum (**Figure 6.8b**) show that the C=O peak is negative, which is due to the consumption of C=O groups ($\sim 1735 \text{ cm}^{-1}$) by TMA during the long exposure. It is important to note that C–H stretching peaks (2964 and 2923 cm^{-1}) increase a little, suggesting that the negative C=O peak is not due to a thinner PCBM film from misalignment of the sample. In addition, the film of PCBM is pretty uniform on Si (**Figure S1**), and therefore, the IR absorbance should be uniform throughout the sample. The small but positive peak at $\sim 1625 \text{ cm}^{-1}$ is assigned to the C–O stretches. On the basis of the IR evidence and the QCM results (**Figure 6.8a**), the reaction between TMA and C=O in PCBM probably follows the same mechanism as the reaction between TMA and C=O in polymers as shown **Figure 6.8c**.^{199,201,202} With this reaction mechanism and mass gain from the TMA exposure, reacted TMA molecules is $\sim 0.003 \mu\text{mol}$, which equals to $\sim 6\%$ of C=O groups in the PCBM film.

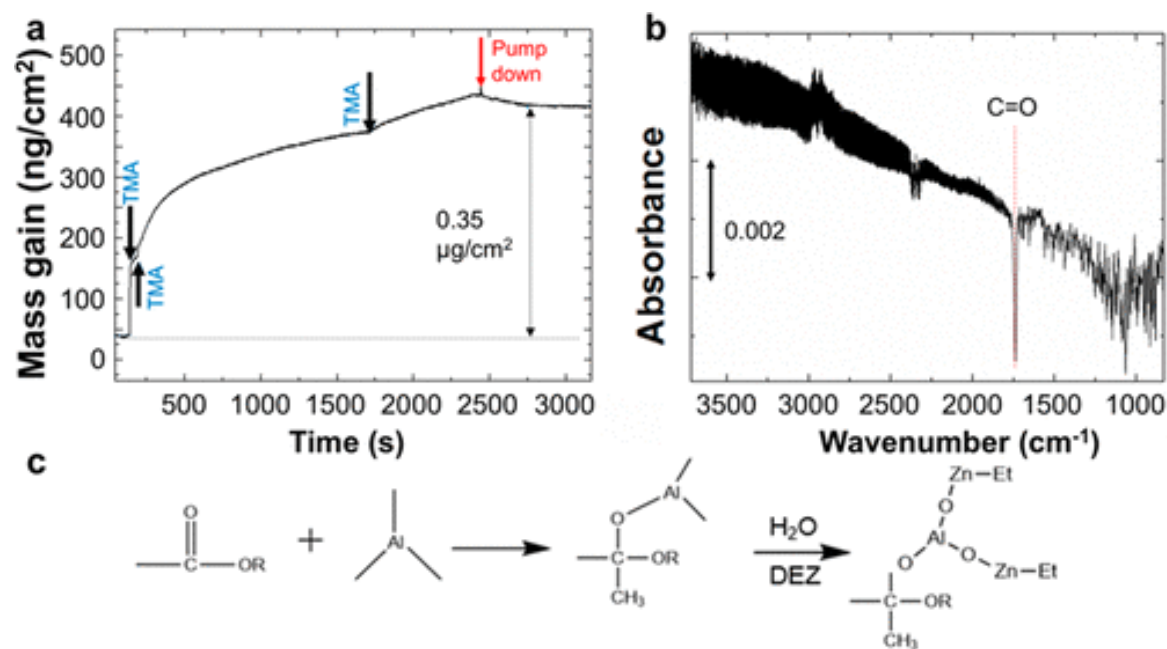


Figure 6.8. (a) Mass change during the long exposure of TMA vapor on PCBM at 100 °C; (b) differential FTIR spectrum of PCBM after TMA vapor treatment with reference to the PCBM film, and (c) mechanism for the improved nucleation of ALD ZnO on PCBM by TMA.

The treatment of Al_2O_3 ALD followed by ZnO ALD has dramatically different impacts on $\text{CH}_3\text{NH}_3\text{PbI}_3$ and $\text{CH}_3\text{NH}_3\text{PbI}_3/\text{PCBM}$. As shown in the IR spectrum in **Figure 6.9a**, without the PCBM overlayer, CH_3NH_3^+ in $\text{CH}_3\text{NH}_3\text{PbI}_3$ can be totally removed by ALD processes. All the peaks associated with CH_3NH_3^+ in $\text{CH}_3\text{NH}_3\text{PbI}_3$ are removed by 40 cycles ALD Al_2O_3 , followed by 200 cycles ALD ZnO. The ALD processes generate a peak at $\sim 3500 \text{ cm}^{-1}$, which is from the hydrogen bonded $-\text{OH}$ groups. These $-\text{OH}$ groups can come from the $-\text{OH}$ groups in ALD oxide²⁰³ and $\text{Pb}-\text{OH}$ groups.²⁰⁴ The broader peak (at $<1000 \text{ cm}^{-1}$) is due to the IR stretches of metal oxides.²⁰⁵ In sharp contrast to the results on $\text{CH}_3\text{NH}_3\text{PbI}_3$, after these ALD processes, the $\text{CH}_3\text{NH}_3\text{PbI}_3/\text{PCBM}$ substrate maintains the characteristic IR peaks of CH_3NH_3^+ , as shown in **Figure 6.9b**. This, again, witness the role of PCBM in blocking the ALD metal–organic precursors from the underlying $\text{CH}_3\text{NH}_3\text{PbI}_3$. In addition, the peak from $\text{C}=\text{O}$ is largely preserved, as ALD Al_2O_3 consumes only a small amount of $\text{C}=\text{O}$ bonding. Interestingly, the $\text{CH}_3\text{NH}_3\text{PbI}_3/\text{PCBM}$ sample did not show clear $-\text{OH}$ signals after the ALD treatments. This result

suggests that the ALD processes produce a much smaller amount of –OH groups on the $\text{CH}_3\text{NH}_3\text{PbI}_3/\text{PCBM}$ sample than on $\text{CH}_3\text{NH}_3\text{PbI}_3$.

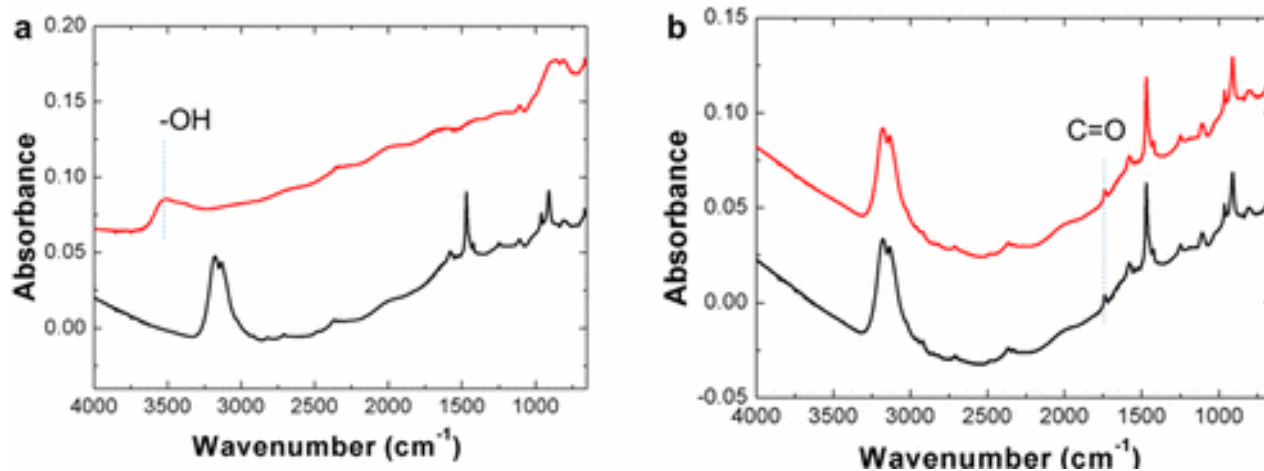


Figure 6.9. (a) IR spectra of (a) $\text{CH}_3\text{NH}_3\text{PbI}_3$ and (b) $\text{CH}_3\text{NH}_3\text{PbI}_3/\text{PCBM}$ before (black) and after (red) 40 cycles of ALD Al_2O_3 and then 200 cycles of ALD ZnO at 100°C . A clean Si substrate was used as the reference.

Stability of Materials

The results in **Figure 6.10** show that PCBM/ALD can dramatically improve the ambient stability of $\text{CH}_3\text{NH}_3\text{PbI}_3$. As shown in **Figure 6.10a**, $\text{CH}_3\text{NH}_3\text{PbI}_3$ degrades in ambience as evidenced by the color change from dark red to pale transparent. This is consistent with literature results.^{206,207} $\text{CH}_3\text{NH}_3\text{PbI}_3/\text{ALD}$ is transparent in color because of the degradation caused by ALD treatment. Although PCBM overcoating help improve the stability of $\text{CH}_3\text{NH}_3\text{PbI}_3$, but degradation is still significant as evidenced by the yellow color of the sample (**Figure 6.10c**). The ambient stability of $\text{CH}_3\text{NH}_3\text{PbI}_3/\text{PCBM}$ is dramatically improved by ALD treatment (40 cycles ALD $\text{Al}_2\text{O}_3/200$ cycles ALD ZnO), in comparison with the other three samples (**Figure 6.10a–c**). After 2 weeks in ambience, the $\text{CH}_3\text{NH}_3\text{PbI}_3/\text{PCBM}/\text{ALD}$ maintains its dark red color. The $\text{CH}_3\text{NH}_3\text{PbI}_3/\text{PCBM}/\text{ALD}$ sample is also stable with the water droplet (**Figure 6.10e**). Bare $\text{CH}_3\text{NH}_3\text{PbI}_3$ turns into yellow color as soon as it contacts with liquid water droplets. With the PCBM/ALD coating, the sample underneath the water droplet maintains its dark red color for more than 20 min. After that, scattered yellow spots start to show up. This improved stability is due to the

dense ALD film that has a limited number of pinholes in the film. The liquid water eventually penetrates through the ALD film through the defects in the film given enough time. The pinholes in the ALD film can be further reduced or eliminated with further engineering the ALD film (e.g., increasing ALD ZnO cycles).

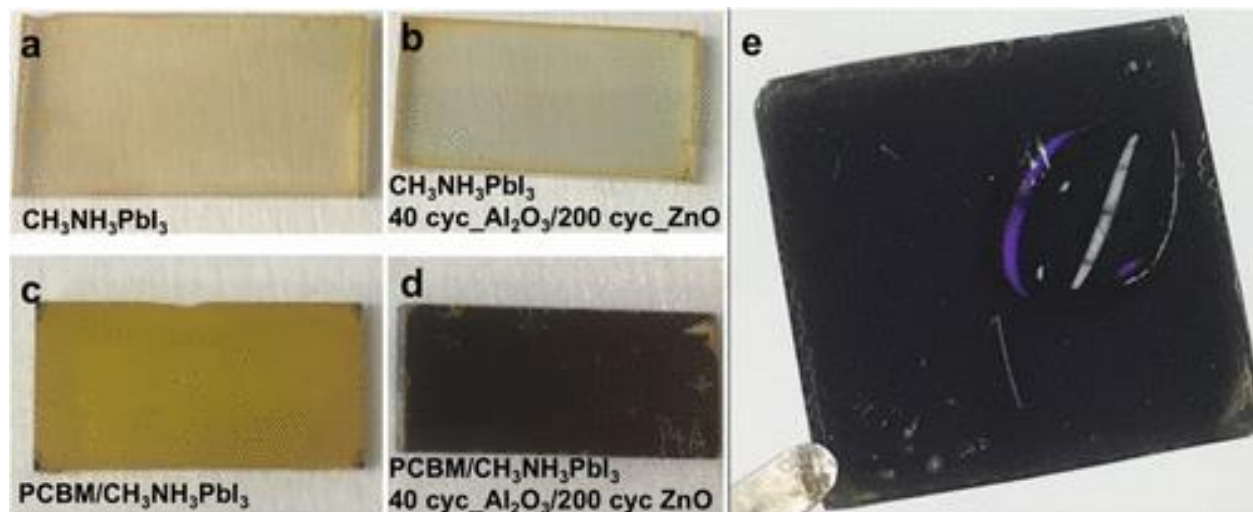


Figure 6.10. (a,b) Optical image of $\text{CH}_3\text{NH}_3\text{PbI}_3$ with and without the ALD treatment; (c,d) $\text{CH}_3\text{NH}_3\text{PbI}_3/\text{PCBM}$ with and without the ALD treatment. These images were taken after the samples sit in ambience (20°C and $40\% \text{RH}$) for 14 days. (e) Stability of $\text{CH}_3\text{NH}_3\text{PbI}_3/\text{PCBM}$ with ALD treatment under the impact of a water droplet. ALD treatment: 40 cycles of ALD Al_2O_3 and 200 cycles of ALD ZnO.

6.3 Conclusion

In summary, we find that PCBM is chemically inert to ALD ZnO chemistry. TMA, a strong Lewis acid, reacts with C=O groups in PCBM to generate nucleation sites for growing ZnO by ALD. Because PCBM only have C=O and C60 sites and most of ALD precursors are not able to react with these sites, PCBM may be inert to other ALD oxide chemistries such as TiO_2 and SnO_2 as well. Therefore, the TMA activation chemistry can be applied to nucleate other ALD oxides onto PCBM surface. We demonstrate the PCBM/ALD Al_2O_3 -ZnO oxide film can dramatically improve the ambient stability of $\text{CH}_3\text{NH}_3\text{PbI}_3$. Our results show that the nucleation of ALD oxides is critical to apply PCBM/ALD method to address the stability issue of perovskites. We further hypothesize

that it is possible to enhance the nucleation of ALD oxides on PCBM by engineering its composition - for instance adding [6,6]-Phenyl C61 butyric acid, C60-Catechol, or C60 derivatives,¹⁸⁵ to provide –OH groups.

Support information:

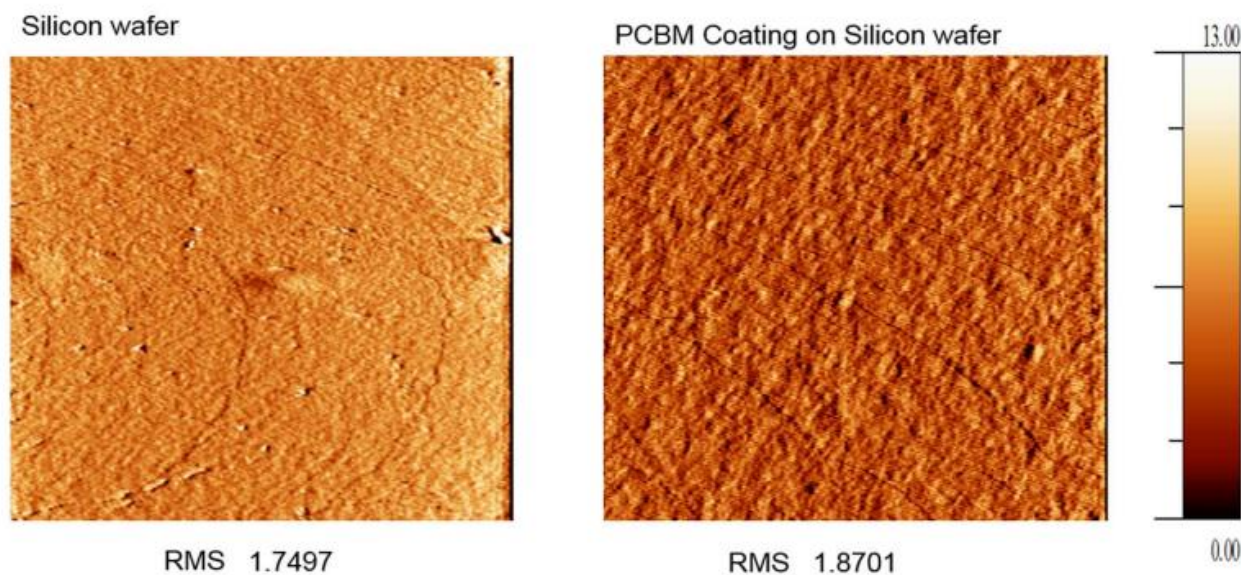


Figure S1. AFM image of clean silicon wafer and PCBM coating on silicon wafer.

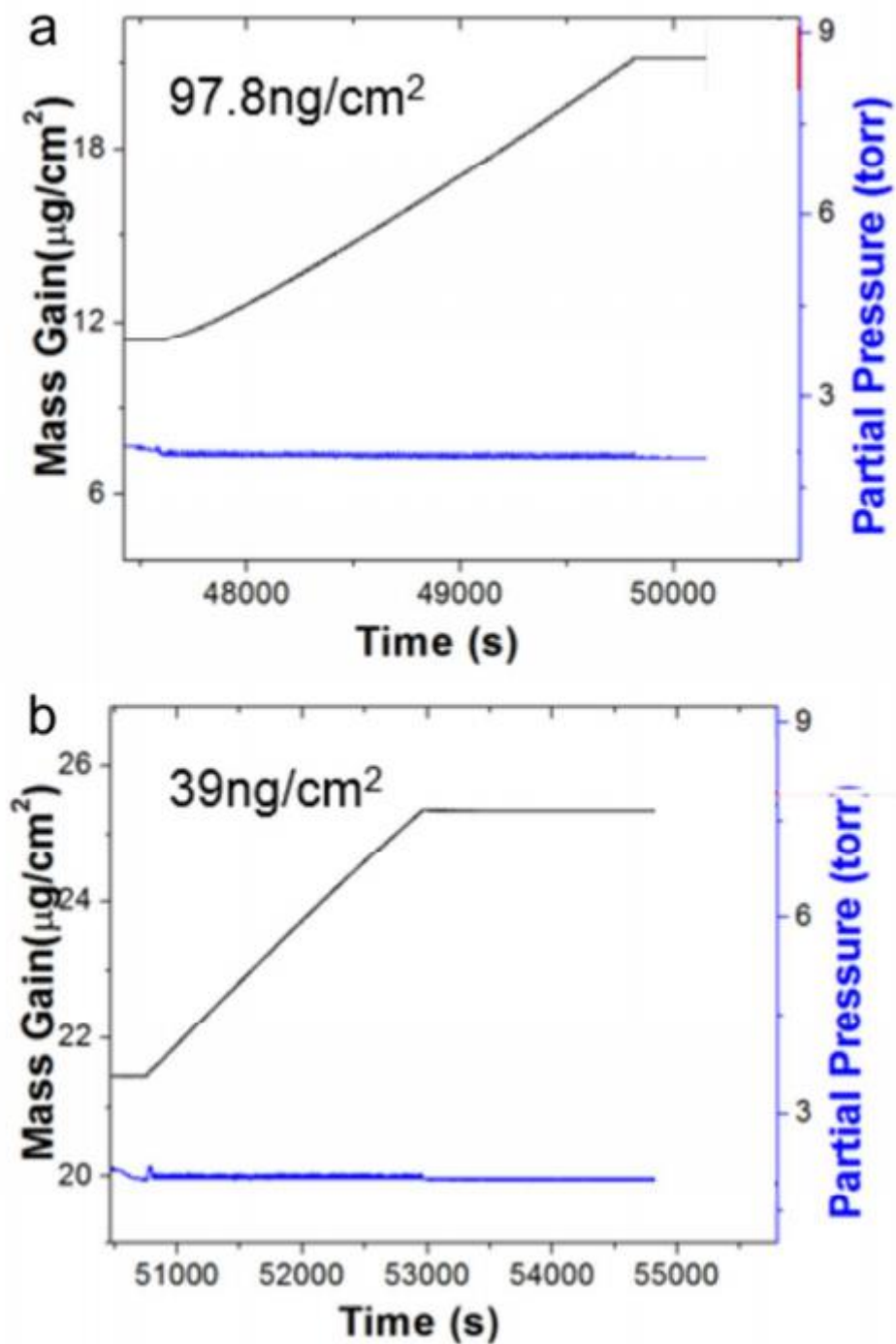


Figure S2. The baseline of the mass gain of (a) ALD ZnO and (b) Al₂O₃ on clean AT-cut QCM crystal purge at 100°C. Black lines represents the mass gain during the ALD growth. The blue traces represent the pressure change during the pulses of reactants. It is clear that ZnO and Al₂O₃ ALD can grow in a steady state mode on bare QCM crystal.

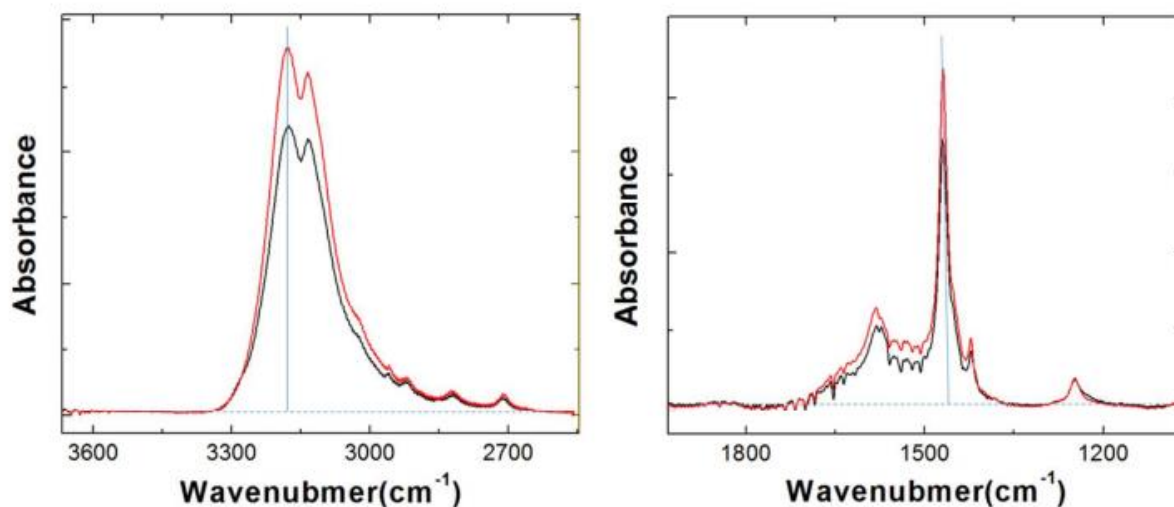


Figure S3. 100 cycles of ALD ZnO at 25 °C reduces the peak height of N-H stretching (3179 cm^{-1}) and N-H deformation (1468 cm^{-1}) by ~22%. $\text{CH}_3\text{NH}_3\text{PbI}_3$ film is coated on Si wafers.

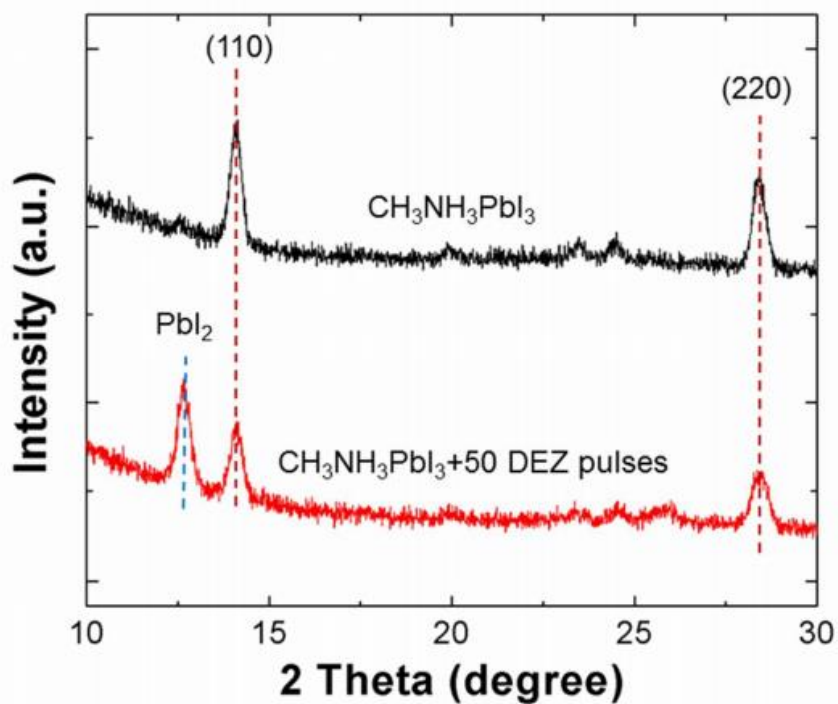


Figure S4. XRD of $\text{CH}_3\text{NH}_3\text{PbI}_3$ before and after 50 pulses of DEZ at 60 °C

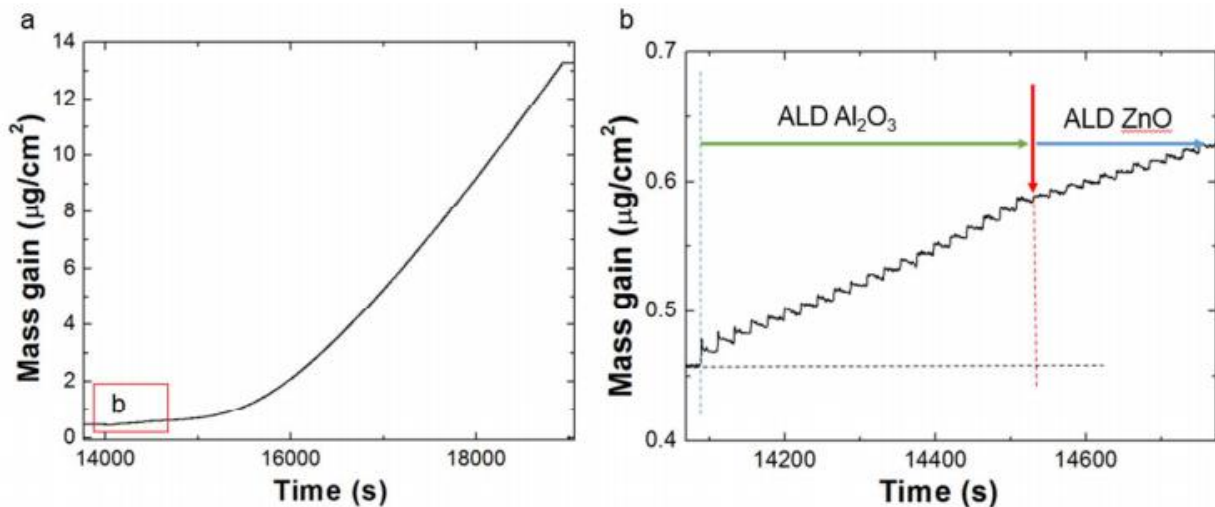
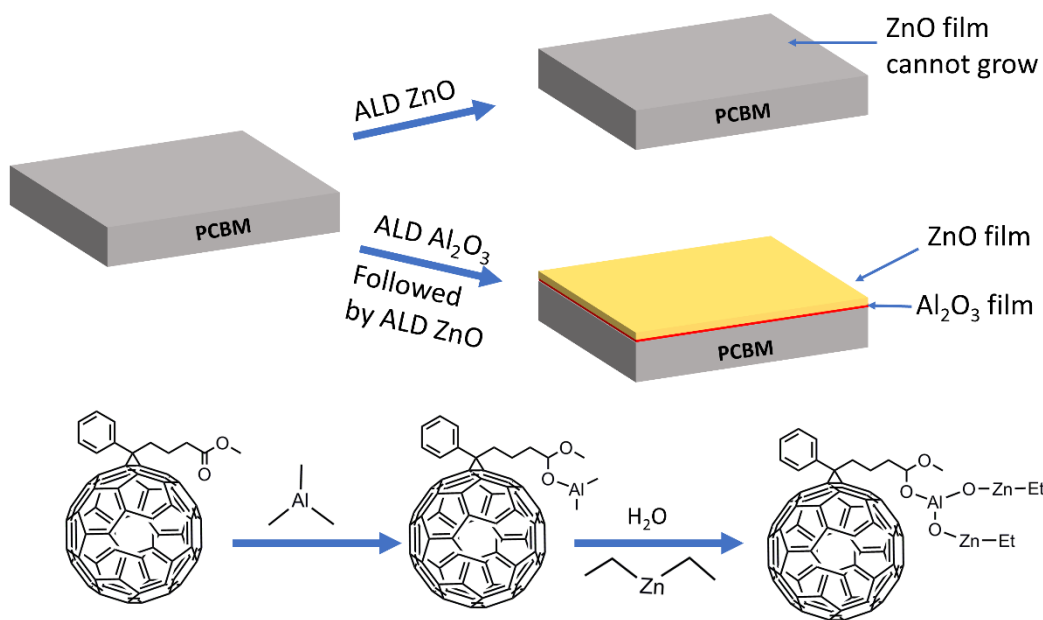


Figure S5. (a) Mass change occurred on PCBM during 20 cycles of ALD Al₂O₃ then ALD ZnO at 100 °C. The detailed mass gains in red window in (a) is shown in (b). (b) the detailed mass gain occurred during the beginning of the process. It shows that 20 cycles of Al₂O₃ ALD can seed the nucleation of ZnO ALD as well.

Table of content



CHAPTER 7: SUMMARY AND FUTURE DIRECTION

7.1 Summary:

In this dissertation, we have shined a light on the degradation mechanism and surface reaction mechanism of perovskite and applied ALD to enhance the stability of perovskite. We briefly review the history of the solar cell and the advantage of perovskite solar cell absorber. The stability problem is the biggest barrier to push organic-inorganic hybrid perovskite material to the market. The degradation mechanisms under different environmental factors and the potential methods to enhance the lifetime of perovskite material were summarized respectively. We emphasized the crucial role of surface modification in improving the stability and efficiency of perovskite. We carried out a comprehensive study in understanding surface coating behavior on the perovskite related substrate including the initial thermal degradation mechanism at different package gas environment, surface reaction property with amine chemical, ALD metal oxide nucleation and growth behavior on perovskite and PCBM film. This dissertation will provide fundamental understanding about ALD process on organic-inorganic hybrid perovskite which will contribute to the following encapsulation and large-scale fabrication of perovskite solar cell device.

In chapter 3, we are first to discuss the thermal degradation kinetics of hybrid perovskite in N_2 and O_2 gas. Our result indicated the fragile chemistry stability of $MAPbI_3$ which will degrade slowly at $85^\circ C$. The degradation rate is very sensitive to the temperature. The IR results also confirm that low humidity has no effect on the stability of $MAPbI_3$. In the dark environment, perovskite degrades faster in O_2 than N_2 . The synergistic effect between O_2 and solar irradiation may increase the decomposition rate further. However, this chapter did not have direct evidence to

show the degradation mechanism, whether MAPbI₃ degrade to CH₃NH₂ gas and PbI₂ need further exploration.

In chapter 4, we are first to probe surface chemistry of perovskite by vapor molecular Pyridine. Our results indicated the reaction between perovskite with Amine is very sensitive to the partial pressure of Amine. The IR results indicate when MAPbI₃ film is exposed to a low partial pressure of Py gas, Py molecular just passivates the surface of MAPbI₃. However, when exposed to high pressure (>1.3 torr) Py gas, CH₃NH₃⁺ would form H-bond with Py molecular immediately, after that Py will grab the proton from CH₃NH₃⁺ and finally forms PyH⁺ ion to bond with Pb-I matrix. The reaction between high partial pressure Py gas with MAPbI₃ is not reversible. The extra Py gas will form a liquid layer with Pb-I matrix and finally turn perovskite into liquid resulting in the totally change of the film morphology.

In chapter 5 and 6, we aim to enhance the stability of hybrid perovskite by applying ALD metal oxide film to encapsulate the surface of MAPbI₃ perovskite and the PCBM layer which is a wide-used electron acceptor. We found that temperature dramatically affects the reaction between TMA/water with MAPbI₃ perovskite. At 25°C, TMA could bond on the surface of perovskite following a self-limit model. How, at 75°C, TMA will etch the perovskite film by forming CH₃I. We also found, contrary to people`s wisdom, DEZ/water chemistry cannot nucleate on the surface of PCBM. We applied an ultra-thin ALD Al₂O₃ layer to supply active sites for the following ALD ZnO on the PCBM layer. With the encapsulation of ALD Al₂O₃ or ZnO on the perovskite solar cell surface, the stability of the film in ambient dramatically improved. After 40 cycles of ALD Al₂O₃ followed by 200 cycles of ALD ZnO onto PCBM/MAPbI₃ substrate, the film could keep stable upon direct contact with a droplet of water.

To sum up, this dissertation aimed to enhance the stability of organic-inorganic hybrid perovskite by surface reaction or surface coating. This dissertation takes a deep glance in

understanding the gas-solid reaction between Lewis amine and acid with perovskite surface. We carry out systematic research about ALD growth behavior and nucleation mechanism on the surface of hybrid perovskite. We believe our study will pave the way to discover a better method to the encapsulation of perovskite device and ultimately realize its commercialization.

7.2 Future direction:

Currently, the research of organic-inorganic hybrid perovskite focuses on developing new perovskite chemistry and synthesizing perovskite with different nanocrystal structures. However, the stability of these materials still blocks their development. ALD metal oxide is a very promising method to form a dense film or core-shell structure to encapsulate the surface. Thus, we studied the ALD process onto FAPbI₃ film and MAPbI₃ quantum dots system.

7.2.1 ALD Al₂O₃ on formamidinium lead iodide (FAPbI₃)

Surface site-limited reaction is critical for ALD process to form a dense and pinhole free film onto the perovskite surface. However, no surface site-limited reaction on MAPbI₃ perovskites has been demonstrated and confirmed. FAPbI₃ was proved to have better thermal stability than MAPbI₃. The NH₂CH=NH₂⁺ ion in FAPbI₃ not only has more H-band connecting with PbI₆⁴⁻ to stabilize the crystal structure but also supply a conjugation site for the ALD precursor. We hypothesize that TMA will bind to the surface of FAPbI₃ with a self-limited model by forming a coordinated complex of aluminum compounds with N, N'-disubstituted carbodiimides (**Figure 7.1**). The unique coordinated structure not only keeps the perovskite from the etching of TMA but also supply nucleation sites for the following ALD processing. Our preliminary experimental result indicated that there was strong coordination between FA⁺ and TMA. The mass growth behavior follows the self-limiting model (**Figure 7.2**). In this work, *in situ* QCM and *in situ* FTIR will be used to explore the surface reaction between TMA and FAPbI₃.

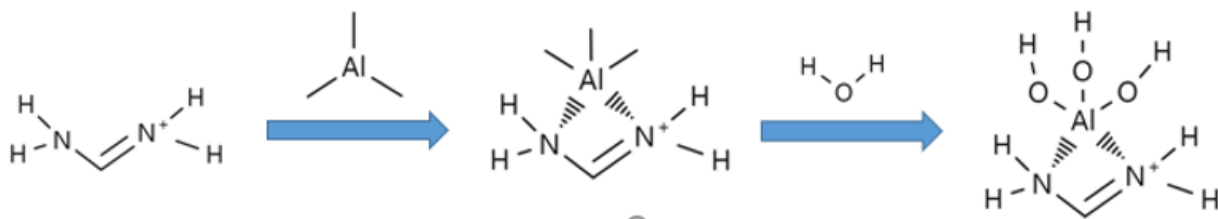


Figure 7.1. The proposed reaction mechanism of FA⁺ with TMA/water chemistry.

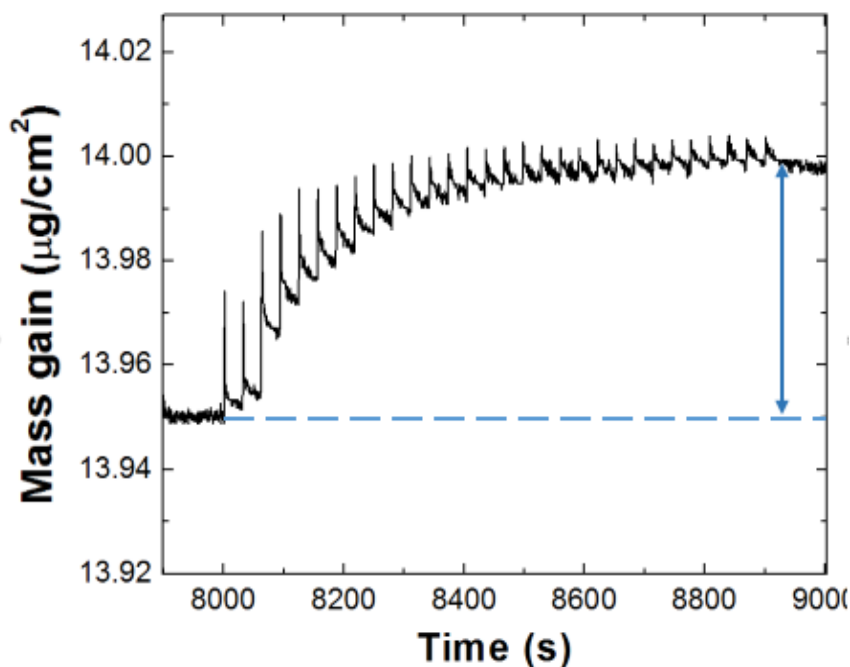


Figure 7.2. In situ QCM measurement of (a) the overall mass gain behavior during 30 pulses of TMA (1 s, partial pressure 0.1 torr, followed by 30s N₂ purge) onto FAPbI₃ at 75 °C.

7.2.2 ALD on MAPbI₃ quantum dots (QDs)

Because of the wide wavelength tunability (400-800 nm) and narrowband emission (full width at half-maximum, FWHM ~20 nm), hybrid perovskites have also been of great interest as emissive components in emitting diodes (LED), low threshold lasers, and electroluminescence (EL) devices.²⁰⁸⁻²¹⁴ However, the nanometer-size of QDs dramatically accelerate the degradation rate, resulting in a full degradation in only a couple of seconds in ambient environment. Based on the previous results, ALD Al₂O₃ can form an encapsulation layer onto MAPbI₃ and FAPbI₃ film at 25 °C without degrading them. Moreover, the surface ligand of QDs additives such as oleic acid and

butylamine will also supply plenty of active sites for ALD process. Thus, we propose that low-temperature ALD Al_2O_3 will form an oxide shell on the surface of QDs to stop the degradation of QDs from O_2 and water molecular. Our preliminary studies showed that without ALD, MAPbI_3 QDs will degrade in ambience after 15s. However, after 500 cycles of ALD Al_2O_3 , MAPbI_3 QDs could keep photoluminescence property in ambience for more than 15 min (**Figure 7.3**). *In-situ* QCM and FTIR will be used to measure the growth behavior of ALD Al_2O_3 and reaction mechanism of TMA with MAPbI_3 QDs surface ligand. Transmission electron microscopy (TEM) will be used to observe the morphology change of QDs before and after the ALD process. Photoluminescence spectroscopy and UV-Vis will be used to characterize the PL performance and band gap of QDs.

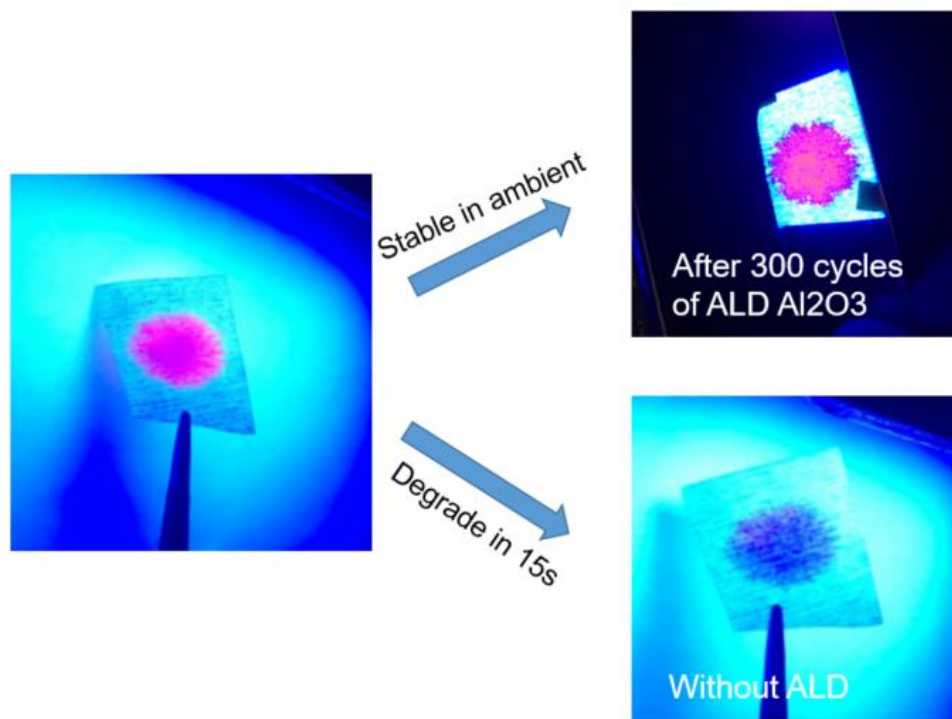


Figure 7.3 the PL performance of MAPbI_3 before and after ALD Al_2O_3 .

REFERENCES

- (1) Docampo, P.; Bein, T. A Long-Term View on Perovskite Optoelectronics. *Acc Chem Res* 2016, 49, 339-346.
- (2) Scholz, S.; Kondakov, D.; Lussem, B.; Leo, K. Degradation Mechanisms and Reactions in Organic Light-Emitting Devices. *Chem Rev* 2015, 115, 8449-8503.
- (3) Cheng, P.; Zhan, X. Stability of organic solar cells: challenges and strategies. *Chem Soc Rev* 2016, 45, 2544-2582.
- (4) El Chaar, L.; Lamont, L. A.; El Zein, N. Review of photovoltaic technologies. *Renewable and Sustainable Energy Reviews* 2011, 15, 2165-2175.
- (5) Burschka, J.; Pellet, N.; Moon, S. J.; Humphry-Baker, R.; Gao, P.; Nazeeruddin, M. K.; Gratzel, M. Sequential deposition as a route to high-performance perovskite-sensitized solar cells. *Nature* 2013, 499, 316-319.
- (6) Jeon, N. J.; Noh, J. H.; Yang, W. S.; Kim, Y. C.; Ryu, S.; Seo, J.; Seok, S. I. Compositional engineering of perovskite materials for high-performance solar cells. *Nature* 2015, 517, 476-480.
- (7) Liu, M.; Johnston, M. B.; Snaith, H. J. Efficient planar heterojunction perovskite solar cells by vapour deposition. *Nature* 2013, 501, 395-398.
- (8) Bush, K. A.; Palmstrom, A. F.; Yu, Z. J.; Boccard, M.; Cheacharoen, R.; Mailoa, J. P.; McMeekin, D. P.; Hoyer, R. L. Z.; Bailie, C. D.; Leijtens, T.; Peters, I. M.; Minichetti, M. C.; Rolston, N.; Prasanna, R.; Sofia, S.; Harwood, D.; Ma, W.; Moghadam, F.; Snaith, H. J.; Buonassisi, T.; Holman, Z. C.; Bent, S. F.; McGehee, M. D. 23.6%-efficient monolithic perovskite/silicon tandem solar cells with improved stability. *Nature Energy* 2017, 2.
- (9) Diao, Y.; Tee, B. C.; Giri, G.; Xu, J.; Kim, D. H.; Becerril, H. A.; Stoltenberg, R. M.; Lee, T. H.; Xue, G.; Mannsfeld, S. C.; Bao, Z. Solution coating of large-area organic semiconductor thin films with aligned single-crystalline domains. *Nat Mater* 2013, 12, 665-671.
- (10) Gratzel, M. The Light and Shade of Perovskite Solar Cells. *Nat. Mater.* 2014, 13, 838.
- (11) Rong, Y.; Hu, Y.; Mei, A.; Tan, H.; Saidaminov, M. I.; Seok, S. I.; McGehee, M. D.; Sargent, E. H.; Han, H. Challenges for commercializing perovskite solar cells. *Science* 2018, 361.

- (12) Wang, Z.; Shi, Z.; Li, T.; Chen, Y.; Huang, W. Stability of Perovskite Solar Cells: A Prospective on the Substitution of the A Cation and X Anion. *Angew Chem Int Ed Engl* 2017, 56, 1190-1212.
- (13) Eperon, G. E.; Stranks, S. D.; Menelaou, C.; Johnston, M. B.; Herz, L. M.; Snaith, H. J. Formamidinium lead trihalide: a broadly tunable perovskite for efficient planar heterojunction solar cells. *Energy & Environmental Science* 2014, 7, 982.
- (14) Liang, K. N.; Mitzi, D. B.; Prikas, M. T. Synthesis and Characterization of Organic-Inorganic Perovskite Thin Films Prepared Using a Versatile Two-Step Dipping Technique. *Chem. Mater.* 1998, 10, 403.
- (15) Boix, P. P.; Agarwala, S.; Koh, T. M.; Mathews, N.; Mhaisalkar, S. G. Perovskite Solar Cells: Beyond Methylammonium Lead Iodide. *J Phys Chem Lett* 2015, 6, 898-907.
- (16) Noh, J. H.; Im, S. H.; Heo, J. H.; Mandal, T. N.; Seok, S. I. Chemical management for colorful, efficient, and stable inorganic-organic hybrid nanostructured solar cells. *Nano Lett* 2013, 13, 1764-1769.
- (17) Chen, Q.; De Marco, N.; Yang, Y.; Song, T.-B.; Chen, C.-C.; Zhao, H.; Hong, Z.; Zhou, H.; Yang, Y. Under the spotlight: The organic-inorganic hybrid halide perovskite for optoelectronic applications. *Nano Today* 2015, 10, 355-396.
- (18) Jeon, N. J.; Noh, J. H.; Yang, W. S.; Kim, Y. C.; Ryu, S.; Seo, J.; Seok, S. I. Compositional engineering of perovskite materials for high-performance solar cells. *Nature* 2015, 517, 476.
- (19) Xiao, Z.; Dong, Q.; Bi, C.; Shao, Y.; Yuan, Y.; Huang, J. Solvent annealing of perovskite-induced crystal growth for photovoltaic-device efficiency enhancement. *Adv Mater* 2014, 26, 6503-6509.
- (20) Barrows, A. T.; Lilliu, S.; Pearson, A. J.; Babonneau, D.; Dunbar, A. D. F.; Lidzey, D. G. Monitoring the Formation of a $\text{CH}_3\text{NH}_3\text{PbI}_{3-x}\text{Cl}_x$ Perovskite during Thermal Annealing Using X-Ray Scattering. *Advanced Functional Materials* 2016, 26, 4934-4942.
- (21) Dualeh, A.; Tétreault, N.; Moehl, T.; Gao, P.; Nazeeruddin, M. K.; Grätzel, M. Effect of Annealing Temperature on Film Morphology of Organic-Inorganic Hybrid Perovskite Solid-State Solar Cells. *Advanced Functional Materials* 2014, 24, 3250-3258.
- (22) Liu, C.; Wang, K.; Yi, C.; Shi, X.; Smith, A. W.; Gong, X.; Heeger, A. J. Efficient Perovskite Hybrid Photovoltaics via Alcohol-Vapor Annealing Treatment. *Advanced Functional Materials* 2016, 26, 101-110.
- (23) Nguyen, L. H.; Hoppe, H.; Erb, T.; Günes, S.; Gobsch, G.; Sariciftci, N. S. Effects of Annealing on the Nanomorphology and Performance of Poly(alkylthiophene):Fullerene Bulk-Heterojunction Solar Cells. *Advanced Functional Materials* 2007, 17, 1071-1078.
- (24) Xiao, S.; Bai, Y.; Meng, X.; Zhang, T.; Chen, H.; Zheng, X.; Hu, C.; Qu, Y.; Yang, S. Unveiling a Key Intermediate in Solvent Vapor Postannealing to Enlarge Crystalline

Domains of Organometal Halide Perovskite Films. *Advanced Functional Materials* 2017, 27, 1604944.

(25) Rong, Y.; Liu, L.; Mei, A.; Li, X.; Han, H. Beyond Efficiency: the Challenge of Stability in Mesoscopic Perovskite Solar Cells. *Advanced Energy Materials* 2015, 5, 1501066.

(26) Dualeh, A.; Gao, P.; Seok, S. I.; Nazeeruddin, M. K.; Grätzel, M. Thermal Behavior of Methylammonium Lead-Trihalide Perovskite Photovoltaic Light Harvesters. *Chem. Mat.* 2014, 26, 6160-6164.

(27) Juarez-Perez, E. J.; Hawash, Z.; Raga, S. R.; Ono, L. K.; Qi, Y. Thermal degradation of $\text{CH}_3\text{NH}_3\text{PbI}_3$ perovskite into NH_3 and CH_3I gases observed by coupled thermogravimetry–mass spectrometry analysis. *Energy & Environmental Science* 2016, 9, 3406-3410.

(28) Conings, B.; Drijkoningen, J.; Gauquelin, N.; Babayigit, A.; D'Haen, J.; D'Olieslaeger, L.; Ethirajan, A.; Verbeeck, J.; Manca, J.; Mosconi, E.; Angelis, F. D.; Boyen, H.-G. Intrinsic Thermal Instability of Methylammonium Lead Trihalide Perovskite. *Advanced Energy Materials* 2015, 5, 1500477.

(29) Frost, J. M.; Butler, K. T.; Brivio, F.; Hendon, C. H.; van Schilfgaarde, M.; Walsh, A. Atomistic Origins of High-Performance in Hybrid Halide Perovskite Solar Cells. *Nano Lett.* 2014, 14, 2584.

(30) Leguy, A. M. A.; Hu, Y.; Campoy-Quiles, M.; Alonso, M. I.; Weber, O. J.; Azarhoosh, P.; van Schilfgaarde, M.; Weller, M. T.; Bein, T.; Nelson, J.; Docampo, P.; Barnes, P. R. F. Reversible Hydration of $\text{CH}_3\text{NH}_3\text{PbI}_3$ in Films, Single Crystals, and Solar Cells. *Chem. Mat.* 2015, 27, 3397-3407.

(31) Müller, C.; Glaser, T.; Plogmeyer, M.; Sendner, M.; Döring, S.; Bakulin, A. A.; Brzuska, C.; Scheer, R.; Pshenichnikov, M. S.; Kowalsky, W.; Pucci, A.; Lovrinčić, R. Water Infiltration in Methylammonium Lead Iodide Perovskite: Fast and Inconspicuous. *Chem. Mat.* 2015, 27, 7835-7841.

(32) Zhu, Z.; Hadjiev, V. G.; Rong, Y.; Guo, R.; Cao, B.; Tang, Z.; Qin, F.; Li, Y.; Wang, Y.; Hao, F.; Venkatesan, S.; Li, W.; Baldelli, S.; Guloy, A. M.; Fang, H.; Hu, Y.; Yao, Y.; Wang, Z.; Bao, J. Interaction of Organic Cation with Water Molecule in Perovskite MAPbI_3 : From Dynamic Orientational Disorder to Hydrogen Bonding. *Chem. Mat.* 2016, 28, 7385-7393.

(33) Yang, J. L.; Siempelkamp, B. D.; Liu, D. Y.; Kelly, T. L. Investigation of $\text{CH}_3\text{NH}_3\text{PbI}_3$ Degradation Rates and Mechanisms in Controlled Humidity Environments Using in Situ Techniques. *ACS Nano* 2015, 9, 1955.

(34) Leijtens, T.; Eperon, G. E.; Pathak, S.; Abate, A.; Lee, M. M.; Snaith, H. J. Overcoming ultraviolet light instability of sensitized TiO_2 with meso-superstructured organometal tri-halide perovskite solar cells. *Nat Commun* 2013, 4, 2885.

- (35) Sun, Y.; Fang, X.; Ma, Z.; Xu, L.; Lu, Y.; Yu, Q.; Yuan, N.; Ding, J. Enhanced UV-light stability of organometal halide perovskite solar cells with interface modification and a UV absorption layer. *Journal of Materials Chemistry C* 2017, 5, 8682-8687.
- (36) Zhang, L.; Sit, P. H. L. Ab initio study of the role of oxygen and excess electrons in the degradation of $\text{CH}_3\text{NH}_3\text{PbI}_3$. *J Mater Chem A* 2017, 5, 9042-9049.
- (37) Hao, W.; Chen, X.; Li, S. Synergistic Effects of Water and Oxygen Molecule Co-adsorption on (001) Surfaces of Tetragonal $\text{CH}_3\text{NH}_3\text{PbI}_3$: A First-Principles Study. *The Journal of Physical Chemistry C* 2016, 120, 28448-28455.
- (38) Bryant, D.; Aristidou, N.; Pont, S.; Sanchez-Molina, I.; Chotchunangatchaval, T.; Wheeler, S.; Durrant, J. R.; Haque, S. A. Light and oxygen induced degradation limits the operational stability of methylammonium lead triiodide perovskite solar cells. *Energy & Environmental Science* 2016, 9, 1655-1660.
- (39) Binek, A.; Hanusch, F. C.; Docampo, P.; Bein, T. Stabilization of the Trigonal High-Temperature Phase of Formamidinium Lead Iodide. *J Phys Chem Lett* 2015, 6, 1249-1253.
- (40) Eperon, G. E.; Paternò, G. M.; Sutton, R. J.; Zampetti, A.; Haghighirad, A. A.; Cacialli, F.; Snaith, H. J. Inorganic caesium lead iodide perovskite solar cells. *J Mater Chem A* 2015, 3, 19688-19695.
- (41) Lee, J.-W.; Kim, D.-H.; Kim, H.-S.; Seo, S.-W.; Cho, S. M.; Park, N.-G. Formamidinium and Cesium Hybridization for Photo- and Moisture-Stable Perovskite Solar Cell. *Advanced Energy Materials* 2015, 5, 1501310.
- (42) Jiang, Q.; Rebollar, D.; Gong, J.; Piacentino, E. L.; Zheng, C.; Xu, T. Pseudohalide-induced moisture tolerance in perovskite $\text{CH}_3\text{NH}_3\text{Pb}(\text{SCN})_2\text{I}$ thin films. *Angew Chem Int Ed Engl* 2015, 54, 7617-7620.
- (43) Ono, L. K.; Juarez-Perez, E. J.; Qi, Y. Progress on Perovskite Materials and Solar Cells with Mixed Cations and Halide Anions. *ACS Appl Mater Interfaces* 2017, 9, 30197-30246.
- (44) Yi, C.; Luo, J.; Meloni, S.; Boziki, A.; Ashari-Astani, N.; Grätzel, C.; Zakeeruddin, S. M.; Röthlisberger, U.; Grätzel, M. Entropic stabilization of mixed A-cation ABX_3 metal halide perovskites for high performance perovskite solar cells. *Energy & Environmental Science* 2016, 9, 656-662.
- (45) Stoumpos, C. C.; Cao, D. H.; Clark, D. J.; Young, J.; Rondinelli, J. M.; Jang, J. I.; Hupp, J. T.; Kanatzidis, M. G. Ruddlesden-Popper Hybrid Lead Iodide Perovskite 2D Homologous Semiconductors. *Chem. Mater.* 2016, 28, 2852.
- (46) Lv, Y.; Si, D.; Song, X.; Wang, K.; Wang, S.; Zhao, Z.; Hao, C.; Wei, L.; Shi, Y. Pseudohalogen-Based 2D Perovskite: A More Complex Thermal Degradation Mechanism Than 3D Perovskite. *Inorganic Chemistry* 2018.
- (47) Quan, L. N.; Zhao, Y.; Garcia de Arquer, F. P.; Sabatini, R.; Walters, G.; Voznyy, O.; Comin, R.; Li, Y.; Fan, J. Z.; Tan, H.; Pan, J.; Yuan, M.; Bakr, O. M.; Lu, Z.; Kim, D.

- H.; Sargent, E. H. Tailoring the Energy Landscape in Quasi-2D Halide Perovskites Enables Efficient Green-Light Emission. *Nano Lett* 2017, 17, 3701-3709.
- (48) Quan, L. N.; Yuan, M.; Comin, R.; Voznyy, O.; Beauregard, E. M.; Hoogland, S.; Buin, A.; Kirmani, A. R.; Zhao, K.; Amassian, A.; Kim, D. H.; Sargent, E. H. Ligand-Stabilized Reduced-Dimensionality Perovskites. *J Am Chem Soc* 2016, 138, 2649-2655.
- (49) Zhou, P.; Fang, Z.; Zhou, W.; Qiao, Q.; Wang, M.; Chen, T.; Yang, S. Nonconjugated Polymer Poly(vinylpyrrolidone) as an Efficient Interlayer Promoting Electron Transport for Perovskite Solar Cells. *ACS Appl Mater Interfaces* 2017, 9, 32957-32964.
- (50) Guo, Y.; Shoyama, K.; Sato, W.; Nakamura, E. Polymer Stabilization of Lead(II) Perovskite Cubic Nanocrystals for Semitransparent Solar Cells. *Advanced Energy Materials* 2016, 6, 1502317.
- (51) Habisreutinger, S. N.; Leijtens, T.; Eperon, G. E.; Stranks, S. D.; Nicholas, R. J.; Snaith, H. J. Carbon nanotube/polymer composites as a highly stable hole collection layer in perovskite solar cells. *Nano Lett* 2014, 14, 5561-5568.
- (52) Sun, C.; Guo, Y.; Fang, B.; Yang, J.; Qin, B.; Duan, H.; Chen, Y.; Li, H.; Liu, H. Enhanced Photovoltaic Performance of Perovskite Solar Cells Using Polymer P(VDF-TrFE) as a Processed Additive. *The Journal of Physical Chemistry C* 2016, 120, 12980-12988.
- (53) Kim, M.; Motti, S. G.; Sorrentino, R.; Petrozza, A. Enhanced solar cell stability by hygroscopic polymer passivation of metal halide perovskite thin film. *Energy & Environmental Science* 2018, 11, 2609-2619.
- (54) Zhao, Y.; Wei, J.; Li, H.; Yan, Y.; Zhou, W.; Yu, D.; Zhao, Q. A polymer scaffold for self-healing perovskite solar cells. *Nat Commun* 2016, 7, 10228.
- (55) Mei, A.; Li, X.; Liu, L.; Ku, Z.; Liu, T.; Rong, Y.; Xu, M.; Hu, M.; Chen, J.; Yang, Y.; Grätzel, M.; Han, H. A hole-conductor-free, fully printable mesoscopic perovskite solar cell with high stability. *Science* 2014, 345, 295-298.
- (56) Yeo, J.-S.; Kang, R.; Lee, S.; Jeon, Y.-J.; Myoung, N.; Lee, C.-L.; Kim, D.-Y.; Yun, J.-M.; Seo, Y.-H.; Kim, S.-S.; Na, S.-I. Highly efficient and stable planar perovskite solar cells with reduced graphene oxide nanosheets as electrode interlayer. *Nano Energy* 2015, 12, 96-104.
- (57) Wang, Q.; Chen, B.; Liu, Y.; Deng, Y.; Bai, Y.; Dong, Q.; Huang, J. Scaling behavior of moisture-induced grain degradation in polycrystalline hybrid perovskite thin films. *Energy & Environmental Science* 2017, 10, 516-522.
- (58) Ono, L. K.; Qi, Y. Surface and Interface Aspects of Organometal Halide Perovskite Materials and Solar Cells. *J Phys Chem Lett* 2016, 7, 4764-4794.
- (59) Mosconi, E.; Azpiroz, J. M.; De Angelis, F. Ab Initio Molecular Dynamics Simulations of Methylammonium Lead Iodide Perovskite Degradation by Water. *Chem. Mat.* 2015, 27, 4885-4892.

- (60) Noel, N. K.; Abate, A.; Stranks, S. D.; Parrott, E. S.; Burlakov, V. M.; Goriely, A.; Snaith, H. J. Enhanced Photoluminescence and Solar Cell Performance via Lewis Base Passivation of Organic–Inorganic Lead Halide Perovskites. *ACS Nano* 2014, 8, 9815-9821.
- (61) Abate, A.; Saliba, M.; Hollman, D. J.; Stranks, S. D.; Wojciechowski, K.; Avolio, R.; Grancini, G.; Petrozza, A.; Snaith, H. J. Supramolecular halogen bond passivation of organic-inorganic halide perovskite solar cells. *Nano Lett* 2014, 14, 3247-3254.
- (62) Lee, J. W.; Kim, H. S.; Park, N. G. Lewis Acid-Base Adduct Approach for High Efficiency Perovskite Solar Cells. *Acc Chem Res* 2016, 49, 311-319.
- (63) Wang, F.; Geng, W.; Zhou, Y.; Fang, H. H.; Tong, C. J.; Loi, M. A.; Liu, L. M.; Zhao, N. Phenylalkylamine Passivation of Organolead Halide Perovskites Enabling High-Efficiency and Air-Stable Photovoltaic Cells. *Adv Mater* 2016, 28, 9986-9992.
- (64) Yang, H.; Shan, C.; Li, F.; Han, D.; Zhang, Q.; Niu, L. Covalent functionalization of polydisperse chemically-converted graphene sheets with amine-terminated ionic liquid. *Chemical Communications* 2009, 3880-3882.
- (65) Abdelmageed, G.; Sully, H. R.; Bonabi Naghadeh, S.; El-Hag Ali, A.; Carter, S. A.; Zhang, J. Z. Improved Stability of Organometal Halide Perovskite Films and Solar Cells toward Humidity via Surface Passivation with Oleic Acid. *ACS Applied Energy Materials* 2018, 1, 387-392.
- (66) Li, B.; Fei, C.; Zheng, K.; Qu, X.; Pullerits, T.; Cao, G.; Tian, J. Constructing water-resistant CH₃NH₃PbI₃ perovskite films via coordination interaction. *J Mater Chem A* 2016, 4, 17018-17024.
- (67) Li, X.; Ibrahim Dar, M.; Yi, C.; Luo, J.; Tschumi, M.; Zakeeruddin, S. M.; Nazeeruddin, M. K.; Han, H.; Grätzel, M. Improved performance and stability of perovskite solar cells by crystal crosslinking with alkylphosphonic acid ω -ammonium chlorides. *Nature Chemistry* 2015, 7, 703.
- (68) Elam, J. W.; Routkevitch, D.; Mardilovich, P. P.; George, S. M. Conformal Coating on Ultrahigh-Aspect-Ratio Nanopores of Anodic Alumina by Atomic Layer Deposition. *Chem. Mat.* 2003, 15, 3507-3517.
- (69) Ellinger, C. R.; Nelson, S. F. Selective Area Spatial Atomic Layer Deposition of ZnO, Al₂O₃, and Aluminum-Doped ZnO Using Poly(vinyl pyrrolidone). *Chem. Mat.* 2014, 26, 1514-1522.
- (70) Kim, H. G.; Lee, H.-B.-R. Atomic Layer Deposition on 2D Materials. *Chem. Mat.* 2017, 29, 3809-3826.
- (71) Lee, H.-B.-R.; Mullings, M. N.; Jiang, X.; Clemens, B. M.; Bent, S. F. Nucleation-Controlled Growth of Nanoparticles by Atomic Layer Deposition. *Chem. Mat.* 2012, 24, 4051-4059.

- (72) Dong, X.; Hu, H.; Lin, B.; Ding, J.; Yuan, N. The effect of ALD-Zno layers on the formation of CH₃NH₃PbI₃ with different perovskite precursors and sintering temperatures. *Chem Commun (Camb)* 2014, 50, 14405-14408.
- (73) Kim, I. S.; Cao, D. H.; Buchholz, D. B.; Emery, J. D.; Farha, O. K.; Hupp, J. T.; Kanatzidis, M. G.; Martinson, A. B. F. Liquid Water- and Heat-Resistant Hybrid Perovskite Photovoltaics via an Inverted ALD Oxide Electron Extraction Layer Design. *Nano Lett.* 2016, 16, 7786-7790.
- (74) Koushik, D.; Verhees, W. J. H.; Kuang, Y.; Veenstra, S.; Zhang, D.; Verheijen, M. A.; Creatore, M.; Schropp, R. E. I. High-efficiency humidity-stable planar perovskite solar cells based on atomic layer architecture. *Energy & Environmental Science* 2017, 10, 91-100.
- (75) Peng, Q.; Tseng, Y. C.; Darling, S. B.; Elam, J. W. A Route to Nanoscopic Materials via Sequential Infiltration Synthesis on Block Copolymer Templates. *ACS Nano* 2011, 5, 4600.
- (76) Yu, X.; Yan, H.; Peng, Q. Improve the Stability of Hybrid Halide Perovskite via Atomic Layer Deposition on Activated Phenyl-C61 Butyric Acid Methyl Ester. *ACS Applied Materials & Interfaces* 2018, 10, 28948-28954.
- (77) Chang, C.-Y.; Lee, K.-T.; Huang, W.-K.; Siao, H.-Y.; Chang, Y.-C. High-Performance, Air-Stable, Low-Temperature Processed Semitransparent Perovskite Solar Cells Enabled by Atomic Layer Deposition. *Chem. Mat.* 2015, 27, 5122-5130.
- (78) Hultqvist, A.; Aitola, K.; Sveinbjörnsson, K.; Saki, Z.; Larsson, F.; Törndahl, T.; Johansson, E.; Boschloo, G.; Edoff, M. Atomic Layer Deposition of Electron Selective SnO_x and ZnO Films on Mixed Halide Perovskite: Compatibility and Performance. *ACS Applied Materials & Interfaces* 2017, 9, 29707-29716.
- (79) Li, G.; Rivarola, F. W.; Davis, N. J.; Bai, S.; Jellicoe, T. C.; de la Pena, F.; Hou, S.; Ducati, C.; Gao, F.; Friend, R. H.; Greenham, N. C.; Tan, Z. K. Highly Efficient Perovskite Nanocrystal Light-Emitting Diodes Enabled by a Universal Crosslinking Method. *Adv Mater* 2016, 28, 3528-3534.
- (80) Loiudice, A.; Saris, S.; Oveisi, E.; Alexander, D. T. L.; Buonsanti, R. CsPbBr₃ QD/AlO_x Inorganic Nanocomposites with Exceptional Stability in Water, Light, and Heat. *Angewandte Chemie International Edition* 2017, 56, 10696-10701.
- (81) Ahn, N.; Son, D. Y.; Jang, I. H.; Kang, S. M.; Choi, M.; Park, N. G. Highly Reproducible Perovskite Solar Cells with Average Efficiency of 18.3% and Best Efficiency of 19.7% Fabricated via Lewis Base Adduct of Lead(II) Iodide. *Journal of the American Chemical Society* 2015, 137, 8696-8699.
- (82) Yang, W. S.; Noh, J. H.; Jeon, N. J.; Kim, Y. C.; Ryu, S.; Seo, J.; Seok, S. I. High-performance photovoltaic perovskite layers fabricated through intramolecular exchange. *Science* 2015, 348, 1234-1237.

- (83) Yang, W. S.; Noh, J. H.; Jeon, N. J.; Kim, Y. C.; Ryu, S.; Seo, J.; Seok, S. I. High-Performance Photovoltaic Perovskite Layers Fabricated through Intramolecular Exchange. *Science* 2015, 348, 1234.
- (84) Stranks, S. D.; Snaith, H. J. Metal-Halide Perovskites for Photovoltaic and Light-Emitting Devices. *Nat. Nanotechnol.* 2015, 10, 391.
- (85) Chen, Q.; De Marco, N.; Yang, Y.; Song, T. B.; Chen, C. C.; Zhao, H. X.; Hong, Z. R.; Zhou, H. P.; Yang, Y. Under the spotlight: The organic-inorganic hybrid halide perovskite for optoelectronic applications. *Nano Today* 2015, 10, 355.
- (86) Gao, P.; Gratzel, M.; Nazeeruddin, M. K. Organohalide Lead Perovskites for Photovoltaic Applications. *Energy Environ. Sci.* 2014, 7, 2448.
- (87) Babayigit, A.; Ethirajan, A.; Muller, M.; Conings, B. Toxicity of Organometal Halide Perovskite Solar Cells. *Nat. Mater.* 2016, 15, 247.
- (88) Etgar, L.; Gao, P.; Xue, Z.; Peng, Q.; Chandiran, A. K.; Liu, B.; Nazeeruddin, M. K.; Graetzel, M. Mesoscopic CH₃NH₃PbI₃/TiO₂ Heterojunction Solar Cells. *J. Am. Chem. Soc.* 2012, 134, 17396.
- (89) Green, M. A.; Ho-Baillie, A.; Snaith, H. J. The Emergence of Perovskite Solar Cells. *Nat. Photonics* 2014, 8, 506.
- (90) Im, J. H.; Lee, C. R.; Lee, J. W.; Park, S. W.; Park, N. G. 6.5% Efficient Perovskite Quantum-Dot-Sensitized Solar Cell. *Nanoscale* 2011, 3, 4088.
- (91) Snaith, H. J. Perovskites: The Emergence of a New Era for Low-Cost, High-Efficiency Solar Cells. *J. Phys. Chem. Lett.* 2013, 4, 3623.
- (92) Leijtens, T.; Eperon, G. E.; Noel, N. K.; Habisreutinger, S. N.; Petrozza, A.; Snaith, H. J. Stability of Metal Halide Perovskite Solar Cells. *Adv. Energy Mater.* 2015, 5, 1500963.
- (93) Dualeh, A.; Gao, P.; Seok, S. I.; Nazeeruddin, M. K.; Grätzel, M. Thermal Behavior of Methylammonium Lead-Trihalide Perovskite Photovoltaic Light Harvesters. *Chem. Mater.* 2014, 26, 6160.
- (94) Christians, J. A.; Miranda Herrera, P. A.; Kamat, P. V. Transformation of the Excited State and Photovoltaic Efficiency of CH₃NH₃PbI₃ Perovskite upon Controlled Exposure to Humidified Air. *J. Am. Chem. Soc.* 2015, 137, 1530.
- (95) Aristidou, N.; Sanchez-Molina, I.; Chotchuangchutchaval, T.; Brown, M.; Martinez, L.; Rath, T.; Haque, S. A. The Role of Oxygen in the Degradation of Methylammonium Lead Trihalide Perovskite Photoactive Layers. *Angew. Chem., Int. Ed.* 2015, 54, 8208.
- (96) Bryant, D.; Aristidou, N.; Pont, S.; Sanchez-Molina, I.; Chotchunangatchaval, T.; Wheeler, S.; Durrant, J. R.; Haque, S. A. Light and Oxygen Induced Degradation Limits the Operational Stability of Methylammonium Lead Triiodide Perovskite Solar Cells. *Energy Environ. Sci.* 2016, 9, 1655.

- (97) Glaser, T.; Muller, C.; Sendner, M.; Krekeler, C.; Semonin, O. E.; Hull, T. D.; Yaffe, O.; Owen, J. S.; Kowalsky, W.; Pucci, A. Infrared Spectroscopic Study of Vibrational Modes in Methylammonium Lead Halide Perovskites. *J. Phys. Chem. Lett.* 2015, 6, 2913.
- (98) Onodayamamuro, N.; Matsuo, T.; Suga, H. Calorimetric and Ir Spectroscopic Studies of Phase-Transitions in Methylammonium Trihalogenoplumbates-(II). *J. Phys. Chem. Solids* 1990, 51, 1383.
- (99) Perez-Osorio, M. A.; Milot, R. L.; Filip, M. R.; Patel, J. B.; Herz, L. M.; Johnston, M. B.; Giustino, F. Vibrational Properties of the Organic Inorganic Halide Perovskite $\text{CH}_3\text{NH}_3\text{PbI}_3$ from Theory and Experiment: Factor Group Analysis, First-Principles Calculations, and Low-Temperature Infrared Spectra. *J. Phys. Chem. C* 2015, 119, 25703.
- (100) Halder, A.; Choudhury, D.; Ghosh, S.; Subbiah, A. S.; Sarkar, S. K. Exploring Thermochromic Behavior of Hydrated Hybrid Perovskites in Solar Cells. *J. Phys. Chem. Lett.* 2015, 6, 3180.
- (101) Muller, C.; Glaser, T.; Plogmeyer, M.; Sendner, M.; Doring, S.; Bakulin, A. A.; Brzuska, C.; Scheer, R.; Pshenichnikov, M. S.; Kowalsky, W.; Pucci, A. Water Infiltration in Methylammonium Lead Iodide Perovskite: Fast and Inconspicuous. *Chem. Mater.* 2015, 27, 7835.
- (102) Fuller, M. P.; Griffiths, P. R. Diffuse Reflectance Measurements by Infrared Fourier-Transform Spectrometry. *Anal. Chem.* 1978, 50, 1906.
- (103) Leguy, A. M. A.; Hu, Y.; Campoy-Quiles, M.; Alonso, M. I.; Weber, O. J.; Azarhoosh, P.; van Schilfgaarde, M.; Weller, M. T.; Bein, T.; Nelson, J.; Docampo, P. Reversible Hydration of $\text{CH}_3\text{NH}_3\text{PbI}_3$ in Films, Single Crystals, and Solar Cells. *Chem. Mater.* 2015, 27, 3397.
- (104) Tan, K.; Zuluaga, S.; Gong, Q. H.; Canepa, P.; Wang, H.; Li, J.; Chabal, Y. J.; Thonhauser, T. Water Reaction Mechanism in Metal Organic Frameworks with Coordinatively Unsaturated Metal Ions: MOF-74. *Chem. Mater.* 2014, 26, 6886.
- (105) O'Hanlon, J. F.: *A User's Guide to Vacuum Technology*, 2003.
- (106) Mosconi, E.; Azpiroz, J. M.; De Angelis, F. Ab Initio Molecular Dynamics Simulations of Methylammonium Lead Iodide Perovskite Degradation by Water. *Chem. Mater.* 2015, 27, 4885.
- (107) Khawam, A.; Flanagan, D. R. Solid-state kinetic models: Basics and mathematical fundamentals. *J. Phys. Chem. B* 2006, 110, 17315.
- (108) <https://www.nrel.gov/pv/assets/images/efficiency-chart.png>. National Renewable Energy Laboratory 2018.
- (109) Stranks, S. D.; Snaith, H. J. Metal-Halide Perovskites for Photovoltaic and Light-Emitting Devices. *Nat Nano* 2015, 10, 391-402.

- (110) Zhu, H. M.; Fu, Y. P.; Meng, F.; Wu, X. X.; Gong, Z. Z.; Ding, Q.; Gustafsson, M. V.; Trinh, M. T.; Jin, S.; Zhu, X. Y. Lead Halide Perovskite Nanowire Lasers with Low Lasing Thresholds and High Quality Factors. *Nat. Mater.* 2015, 14, 636-643.
- (111) Fang, Y.; Dong, Q.; Shao, Y.; Yuan, Y.; Huang, J. Highly Narrowband Perovskite Single-Crystal Photodetectors Enabled by Surface-Charge Recombination. *Nature Photonics* 2015, 9, 679-686.
- (112) Kim, J. H.; Kim, S.-H. Sub-Second Pyridine Gas Detection using a Organometal Halide Perovskite Functional Dye. *Dyes and Pigments* 2016, 134, 198-202.
- (113) Noel, N. K.; Abate, A.; Stranks, S. D.; Parrott, E. S.; Burlakov, V. M.; Goriely, A.; Snaith, H. J. Enhanced Photoluminescence and Solar Cell Performance via Lewis Base Passivation of Organic Inorganic Lead Halide Perovskites. *ACS Nano* 2014, 8, 9815-9821.
- (114) Jain, S. M.; Qiu, Z.; Häggman, L.; Mirmohades, M.; Johansson, M. B.; Edvinsson, T.; Boschloo, G. Frustrated Lewis pair-mediated recrystallization of CH₃NH₃PbI₃ for improved optoelectronic quality and high voltage planar perovskite solar cells. *Energy & Environmental Science* 2016, 9, 3770-3782.
- (115) Glaser, T.; Muller, C.; Sendner, M.; Krekeler, C.; Semonin, O. E.; Hull, T. D.; Yaffe, O.; Owen, J. S.; Kowalsky, W.; Pucci, A.; Lovrincic, R. Infrared Spectroscopic Study of Vibrational Modes in Methylammonium Lead Halide Perovskites. *J Phys Chem Lett* 2015, 6, 2913-2918.
- (116) Yu, X.; Qin, Y.; Peng, Q. Probe Decomposition of Methylammonium Lead Iodide Perovskite in N₂ and O₂ by in Situ Infrared Spectroscopy. *J. Phys. Chem. A* 2017, 121, 1169-1174.
- (117) Cook, D. Vibrational Spectra of Pyridinium Salts *Can. J. Chem.-Rev. Can. Chim.* 1961, 39, 2009-2024.
- (118) Parry, E. P. An Infrared Study of Pyridine Adsorbed on Acidic Solids Characterization of Surface Acidity. *J. Catal.* 1963, 2, 371-379.
- (119) Wong, K. N.; Colson, S. D. The FT-IR Spectra of Pyridine and Pyridine-D₅. *J Mol Spectrosc* 1984, 104, 129-151.
- (120) Barzetti, T.; Selli, E.; Moscotti, D.; Forni, L. Pyridine and Ammonia as Probes for FTIR Analysis of Solid Acid Catalysts. *Journal of the Chemical Society-Faraday Transactions* 1996, 92, 1401-1407.
- (121) Ferwerda, R.; vanderMaas, J. H.; vanDuijneveldt, F. B. Pyridine Adsorption onto Metal Oxides: An ab initio Study of Model Systems. *J Mol Catal a-Chem* 1996, 104, 319-328.
- (122) Stoumpos, C. C.; Malliakas, C. D.; Kanatzidis, M. G. Semiconducting Tin and Lead Iodide Perovskites with Organic Cations: Phase Transitions, High Mobilities, and Near-Infrared Photoluminescent Properties. *Inorganic Chemistry* 2013, 52, 9019-9038.

- (123) Liu, Y. C.; Yang, Z.; Cui, D.; Ren, X. D.; Sun, J. K.; Liu, X. J.; Zhang, J. R.; Wei, Q. B.; Fan, H. B.; Yu, F. Y.; Zhang, X.; Zhao, C. M.; Liu, S. Z. Two-Inch-Sized Perovskite $\text{CH}_3\text{NH}_3\text{PbX}_3$ ($X = \text{Cl, Br, I}$) Crystals: Growth and Characterization. *Adv. Mater.* 2015, 27, 5176-5183.
- (124) Saparov, B.; Mitzi, D. B. Organic-Inorganic Perovskites: Structural Versatility for Functional Materials Design. *Chem. Rev.* 2016, 116, 4558.
- (125) Saparov, B.; Mitzi, D. B. Organic-Inorganic Perovskites: Structural Versatility for Functional Materials Design. *Chem. Rev.* 2016, 116, 4558-4596.
- (126) Smith, I. C.; Hoke, E. T.; Solis-Ibarra, D.; McGehee, M. D.; Karunadasa, H. I. A Layered Hybrid Perovskite Solar-Cell Absorber with Enhanced Moisture Stability. *Angew. Chem. Int. Ed.* 2014, 53, 11232-11235.
- (127) Huang, W.; Manser, J. S.; Sadhu, S.; Kamat, P. V.; Ptasinska, S. Direct Observation of Reversible Transformation of $\text{CH}_3\text{NH}_3\text{PbI}_3$ and NH_4PbI_3 Induced by Polar Gaseous Molecules. *J. Phys. Chem. Lett.* 2016, 7, 5068.
- (128) Zhou, Z. M.; Wang, Z. W.; Zhou, Y. Y.; Pang, S. P.; Wang, D.; Xu, H. X.; Liu, Z. H.; Padture, N. P.; Cui, G. L. Methylamine-Gas-Induced Defect-Healing Behavior of $\text{CH}_3\text{NH}_3\text{PbI}_3$ Thin Films for Perovskite Solar Cells. *Angew. Chem., Int. Ed.* 2015, 54, 9705.
- (129) Wang, F.; Geng, W.; Zhou, Y.; Fang, H. H.; Tong, C. J.; Loi, M. A.; Liu, L. M.; Zhao, N. Phenylalkylamine Passivation of Organolead Halide Perovskites Enabling High-Efficiency and Air-Stable Photovoltaic Cells. *Adv. Mater.* 2016, 28, 9986.
- (130) Yang, S.; Wang, Y.; Liu, P.; Cheng, Y. B.; Zhao, H. J.; Yang, H. G. Functionalization of Perovskite Thin Films with Moisture-Tolerant Molecules. *Nat. Energy* 2016, 1, 15016.
- (131) Zhang, F.; Yi, C. Y.; Wei, P.; Bi, X. D.; Luo, J. S.; Jacopin, G.; Wang, S. R.; Li, X. G.; Xiao, Y.; Zakeeruddin, S. M.; Gratzel, M. A Novel Dopant-Free Triphenylamine based Molecular "Butterfly" Hole-Transport Material for Highly Efficient and Stable Perovskite Solar Cells. *Adv. Energy Mater.* 2016, 6, 1600401.
- (132) Jain, S. M.; Qiu, Z.; Haggman, L.; Mirmohades, M.; Johansson, M. B.; Edvinsson, T.; Boschloo, G. Frustrated Lewis Pair-Mediated Recrystallization of $\text{CH}_3\text{NH}_3\text{PbI}_3$ for Improved Optoelectronic Quality and High Voltage Planar Perovskite Solar Cells. *Energy Environ. Sci.* 2016, 9, 3770.
- (133) Klaus, J. W.; Sneh, O.; George, S. M. Growth of SiO_2 at Room Temperature with the Use of Catalyzed Sequential Half-Reactions. *Science* 1997, 278, 1934.
- (134) Hu, L.; Shao, G.; Jiang, T.; Li, D. B.; Lv, X. L.; Wang, H. Y.; Liu, X. S.; Song, H. S.; Tang, J.; Liu, H. Investigation of the Interaction between Perovskite Films with Moisture via in Situ Electrical Resistance Measurement. *ACS Appl. Mater. Interfaces* 2015, 7, 25113-25120.

- (135) Mitzi, D. B.: Synthesis, Structure, and Properties of Organic-Inorganic Perovskites and Related Materials. In *Progress in Inorganic Chemistry*; John Wiley & Sons, Inc., 2007; pp 1-121.
- (136) Snaith, H. J. Perovskites: The Emergence of a New Era for Low-Cost, High-Efficiency Solar Cells. *J. Phys. Chem. Lett.* 2013, 4, 3623-3630.
- (137) Gratzel, M. The Light and Shade of Perovskite Solar Cells. *Nat. Mater.* 2014, 13, 838-842.
- (138) Green, M. A.; Ho-Baillie, A.; Snaith, H. J. The Emergence of Perovskite Solar Cells. *Nature Photonics* 2014, 8, 506-514.
- (139) Park, N.-G. Perovskite Solar Cells: An Emerging Photovoltaic Technology. *Materials Today* 2014, 18, 65-72.
- (140) Chen, Q.; De Marco, N.; Yang, Y.; Song, T. B.; Chen, C. C.; Zhao, H. X.; Hong, Z. R.; Zhou, H. P.; Yang, Y. Under the Spotlight: The Organic-Inorganic Hybrid Halide Perovskite for Optoelectronic Applications. *Nano Today* 2015, 10, 355-396.
- (141) Tan, Z.-K.; Moghaddam, R. S.; Lai, M. L.; Docampo, P.; Higler, R.; Deschler, F.; Price, M.; Sadhanala, A.; Pazos, L. M.; Credgington, D.; Hanusch, F.; Bein, T.; Snaith, H. J.; Friend, R. H. Bright Light-Emitting Diodes Based on Organometal Halide Perovskite. *Nat Nano* 2014, 9, 687-692.
- (142) Xing, G.; Mathews, N.; Lim, S. S.; Yantara, N.; Liu, X.; Sabba, D.; Grätzel, M.; Mhaisalkar, S.; Sum, T. C. Low-Temperature Solution-Processed Wavelength-Tunable Perovskites for Lasing. *Nat Mater* 2014, 13, 476-480.
- (143) Zhuo, S. F.; Zhang, J. F.; Shi, Y. M.; Huang, Y.; Zhang, B. Self-Template-Directed Synthesis of Porous Perovskite Nanowires at Room Temperature for High-Performance Visible-Light Photodetectors. *Angew. Chem. Int. Ed.* 2015, 54, 5693-5696.
- (144) Dou, L. T.; Yang, Y.; You, J. B.; Hong, Z. R.; Chang, W. H.; Li, G.; Yang, Y. Solution-Processed Hybrid Perovskite Photodetectors with High Detectivity. *Nat. Commun.* 2014, 5, 5404.
- (145) Kagan, C. R.; Mitzi, D. B.; Dimitrakopoulos, C. D. Organic-Inorganic Hybrid Materials as Semiconducting Channels in Thin-Film Field-Effect Transistors. *Science* 1999, 286, 945-947.
- (146) Meng, L.; You, J. B.; Guo, T. F.; Yang, Y. Recent Advances in the Inverted Planar Structure of Perovskite Solar Cells. *Acc. Chem. Res.* 2016, 49, 155-165.
- (147) Meza, L. R.; Das, S.; Greer, J. R. Strong, Lightweight, and Recoverable Three-Dimensional Ceramic Nanolattices. *Science* 2014, 345, 1322-1326.
- (148) Li, X.; Tschumi, M.; Han, H. W.; Babkair, S. S.; Alzubaydi, R. A.; Ansari, A. A.; Habib, S. S.; Nazeeruddin, M. K.; Zakeeruddin, S. M.; Gratzel, M. Outdoor Performance

and Stability under Elevated Temperatures and Long-Term Light Soaking of Triple-Layer Mesoporous Perovskite Photovoltaics. *Energy Technology* 2015, 3, 551-555.

(149) Christians, J. A.; Schulz, P.; Tinkham, J. S.; Schloemer, T. H.; Harvey, S. P.; Tremolet de Villers, B. J.; Sellinger, A.; Berry, J. J.; Luther, J. M. Tailored interfaces of unencapsulated perovskite solar cells for >1,000 hour operational stability. *Nature Energy* 2018, 3, 68-74.

(150) Zeng, Q.; Zhang, X.; Feng, X.; Lu, S.; Chen, Z.; Yong, X.; Redfern, S. A. T.; Wei, H.; Wang, H.; Shen, H.; Zhang, W.; Zheng, W.; Zhang, H.; Tse, J. S.; Yang, B. Polymer-Passivated Inorganic Cesium Lead Mixed-Halide Perovskites for Stable and Efficient Solar Cells with High Open-Circuit Voltage over 1.3 V. *Adv. Mater.* 2018, 30, 1705393.

(151) Yang, X.; Zhang, X.; Deng, J.; Chu, Z.; Jiang, Q.; Meng, J.; Wang, P.; Zhang, L.; Yin, Z.; You, J. Efficient green light-emitting diodes based on quasi-two-dimensional composition and phase engineered perovskite with surface passivation. *Nature Communications* 2018, 9, 570.

(152) Wang, Z.; Lin, Q.; Chmiel, F. P.; Sakai, N.; Herz, L. M.; Snaith, H. J. Efficient ambient-air-stable solar cells with 2D–3D heterostructured butylammonium-caesium-formamidinium lead halide perovskites. *Nature Energy* 2017, 2, 17135.

(153) Bella, F.; Griffini, G.; Correa-Baena, J.-P.; Saracco, G.; Grätzel, M.; Hagfeldt, A.; Turri, S.; Gerbaldi, C. Improving efficiency and stability of perovskite solar cells with photocurable fluoropolymers. *Science* 2016, 354, 203-206.

(154) Correa-Baena, J.-P.; Saliba, M.; Buonassisi, T.; Grätzel, M.; Abate, A.; Tress, W.; Hagfeldt, A. Promises and challenges of perovskite solar cells. *Science* 2017, 358, 739-744.

(155) McMeekin, D. P.; Sadoughi, G.; Rehman, W.; Eperon, G. E.; Saliba, M.; Hörantner, M. T.; Haghighirad, A.; Sakai, N.; Korte, L.; Rech, B.; Johnston, M. B.; Herz, L. M.; Snaith, H. J. A mixed-cation lead mixed-halide perovskite absorber for tandem solar cells. *Science* 2016, 351, 151-155.

(156) Chen, W.; Wu, Y.; Yue, Y.; Liu, J.; Zhang, W.; Yang, X.; Chen, H.; Bi, E.; Ashraful, I.; Grätzel, M.; Han, L. Efficient and stable large-area perovskite solar cells with inorganic charge extraction layers. *Science* 2015, 350, 944-948.

(157) deQuilettes, D. W.; Vorpahl, S. M.; Stranks, S. D.; Nagaoka, H.; Eperon, G. E.; Ziffer, M. E.; Snaith, H. J.; Ginger, D. S. Impact of microstructure on local carrier lifetime in perovskite solar cells. *Science* 2015, 348, 683-686.

(158) Mei, A. Y.; Li, X.; Liu, L. F.; Ku, Z. L.; Liu, T. F.; Rong, Y. G.; Xu, M.; Hu, M.; Chen, J. Z.; Yang, Y.; Grätzel, M.; Han, H. W. A Hole-Conductor-Free, Fully Printable Mesoscopic Perovskite Solar Cell with High Stability. *Science* 2014, 345, 295-298.

(159) Bush, K. A.; Palmstrom, A. F.; Yu, Z. S. J.; Boccard, M.; Cheacharoen, R.; Mailoa, J. P.; McMeekin, D. P.; Hoyer, R. L. Z.; Bailie, C. D.; Leijtens, T.; Peters, I. M.; Minichetti, M. C.; Rolston, N.; Prasanna, R.; Sofia, S.; Harwood, D.; Ma, W.; Moghadam, F.; Snaith, H. J.; Buonassisi, T.; Holman, Z. C.; Bent, S. F.; McGehee, M. D. 23.6%-efficient

monolithic perovskite/silicon tandem solar cells with improved stability. *Nature Energy* 2017, 2.

(160) You, J. B.; Meng, L.; Song, T. B.; Guo, T. F.; Yang, Y.; Chang, W. H.; Hong, Z. R.; Chen, H. J.; Zhou, H. P.; Chen, Q.; Liu, Y. S.; De Marco, N.; Yang, Y. Improved air stability of perovskite solar cells via solution-processed metal oxide transport layers. *Nature Nanotechnology* 2016, 11, 75-+.

(161) Grancini, G.; Roldan-Carmona, C.; Zimmermann, I.; Mosconi, E.; Lee, X.; Martineau, D.; Narbey, S.; Oswald, F.; De Angelis, F.; Graetzel, M.; Nazeeruddin, M. K. One-Year stable perovskite solar cells by 2D/3D interface engineering. *Nature Communications* 2017, 8.

(162) Han, Y.; Meyer, S.; Dkhissi, Y.; Weber, K.; Pringle, J. M.; Bach, U.; Spiccia, L.; Cheng, Y.-B. Degradation observations of encapsulated planar CH₃NH₃PbI₃ perovskite solar cells at high temperatures and humidity. *J Mater Chem A* 2015, 3, 8139-8147.

(163) Berhe, T. A.; Su, W.-N.; Chen, C.-H.; Pan, C.-J.; Cheng, J.-H.; Chen, H.-M.; Tsai, M.-C.; Chen, L.-Y.; Dubale, A. A.; Hwang, B.-J. Organometal halide perovskite solar cells: degradation and stability. *Energy & Environmental Science* 2016, 9, 323-356.

(164) Li, B.; Li, Y.; Zheng, C.; Gao, D.; Huang, W. Advancements in the stability of perovskite solar cells: degradation mechanisms and improvement approaches. *RSC Advances* 2016, 6, 38079-38091.

(165) Seo, J.; Park, S.; Kim, Y. C.; Jeon, N. J.; Noh, J. H.; Yoon, S. C.; Sang, S. I. Benefits of very thin PCBM and LiF layers for solution-processed p-i-n perovskite solar cells. *Energy & Environmental Science* 2014, 7, 2642-2646.

(166) Kim, I. S.; Martinson, A. B. F. Stabilizing hybrid perovskites against moisture and temperature via non-hydrolytic atomic layer deposited overlayers. *J Mater Chem A* 2015, 3, 20092-20096.

(167) Cao, J.; Yin, J.; Yuan, S.; Zhao, Y.; Li, J.; Zheng, N. Thiols as interfacial modifiers to enhance the performance and stability of perovskite solar cells. *Nanoscale* 2015, 7, 9443-9447.

(168) Bai, Y.; Dong, Q.; Shao, Y.; Deng, Y.; Wang, Q.; Shen, L.; Wang, D.; Wei, W.; Huang, J. Enhancing stability and efficiency of perovskite solar cells with crosslinkable silane-functionalized and doped fullerene. *Nature Communications* 2016, 7, 12806.

(169) Eperon, G. E.; Leijtens, T.; Bush, K. A.; Prasanna, R.; Green, T.; Wang, J. T. W.; McMeekin, D. P.; Volonakis, G.; Milot, R. L.; May, R.; Palmstrom, A.; Slotcavage, D. J.; Belisle, R. A.; Patel, J. B.; Parrott, E. S.; Sutton, R. J.; Ma, W.; Moghadam, F.; Conings, B.; Babayigit, A.; Boyen, H. G.; Bent, S.; Giustino, F.; Herz, L. M.; Johnston, M. B.; McGehee, M. D.; Snaith, H. J. Perovskite-perovskite tandem photovoltaics with optimized band gaps. *Science* 2016, 354, 861-865.

- (170) Palmstrom, A. F.; Santra, P. K.; Bent, S. F. Atomic layer deposition in nanostructured photovoltaics: tuning optical, electronic and surface properties. *Nanoscale* 2015, 7, 12266-12283.
- (171) Kot, M.; Kegelmann, L.; Das, C.; Kus, P.; Tsud, N.; Matolinova, I.; Albrecht, S.; Matolin, V.; Schmeisser, D. Room-Temperature Atomic-Layer-Deposited Al₂O₃ Improves the Efficiency of Perovskite Solar Cells over Time. *ChemSusChem* 2018, 11, 3640-3648.
- (172) Kot, M.; Das, C.; Henkel, K.; Wojciechowski, K.; Snaith, H. J.; Schmeisser, D. Room temperature atomic layer deposited Al₂O₃ on CH₃NH₃PbI₃ characterized by synchrotron-based X-ray photoelectron spectroscopy. *Nuclear Instruments and Methods in Physics Research Section B: Beam Interactions with Materials and Atoms* 2017, 411, 49-52.
- (173) Kot, M.; Das, C.; Wang, Z.; Henkel, K.; Rouissi, Z.; Wojciechowski, K.; Snaith, H. J.; Schmeisser, D. Room-Temperature Atomic Layer Deposition of Al₂O₃: Impact on Efficiency, Stability and Surface Properties in Perovskite Solar Cells. *ChemSusChem* 2016, 9, 3401-3406.
- (174) Li, W.; Li, J.; Wang, L.; Niu, G.; Gao, R.; Qiu, Y. Post modification of perovskite sensitized solar cells by aluminum oxide for enhanced performance. *J Mater Chem A* 2013, 1, 11735.
- (175) Choudhury, D.; Rajaraman, G.; Sarkar, S. K. Self limiting atomic layer deposition of Al₂O₃ on perovskite surfaces: a reality? *Nanoscale* 2016, 8, 7459-7465.
- (176) Wen, C. Y. NONCATALYTIC HETEROGENEOUS SOLID-FLUID REACTION MODELS. *Industrial & Engineering Chemistry* 1968, 60, 34-54.
- (177) Li, Y.; Xu, X.; Wang, C.; Wang, C.; Xie, F.; Yang, J.; Gao, Y. Degradation by Exposure of Coevaporated CH₃NH₃PbI₃ Thin Films. *The Journal of Physical Chemistry C* 2015, 119, 23996-24002.
- (178) Miikkulainen, V.; Leskela, M.; Ritala, M.; Puurunen, R. L. Crystallinity of inorganic films grown by atomic layer deposition: Overview and general trends. *J Appl Phys* 2013, 113.
- (179) George, S. M. Atomic Layer Deposition: An Overview. *Chem. Rev.* 2010, 110, 111-131.
- (180) Rejoub, R.; Lindsay, B. G.; Stebbings, R. F. Electron-impact ionization of the methyl halides. *Journal of Chemical Physics* 2002, 117, 6450-6454.
- (181) Frost, J. M.; Butler, K. T.; Brivio, F.; Hendon, C. H.; van Schilfgaarde, M.; Walsh, A. Atomistic origins of high-performance in hybrid halide perovskite solar cells. *Nano Lett* 2014, 14, 2584-2590.
- (182) Bach, S. B. H.; Parent, D. C. Ion Molecule Reactions in Mixtures of Trimethylaluminum and Methylamines. *J Am Soc Mass Spectr* 1993, 4, 111-116.

- (183) Demchuk, A.; Simpson, S.; Koplitz, B. Exploration of the laser-assisted clustering and reactivity of trimethylaluminum with and without NH₃. *J Phys Chem A* 2003, 107, 1727-1733.
- (184) Xu, W.; Liu, L.; Yang, L.; Shen, P.; Sun, B.; McLeod, J. A. Dissociation of Methylammonium Cations in Hybrid Organic-Inorganic Perovskite Solar Cells. *Nano Lett* 2016, 16, 4720-4725.
- (185) Lai, Y.-Y.; Cheng, Y.-J.; Hsu, C.-S. Applications of Functional Fullerene Materials in Polymer Solar Cells. *Energy Environ. Sci.* 2014, 7, 1866-1883.
- (186) Liu, T. H.; Chen, K.; Hu, Q.; Zhu, R.; Gong, Q. H. Inverted Perovskite Solar Cells: Progresses and Perspectives. *Adv. Energy Mater.* 2016, 6, 1600457.
- (187) Bush, K. A.; Palmstrom, A. F.; Yu, Z. J.; Boccard, M.; Cheacharoen, R.; Mailoa, J. P.; McMeekin, D. P.; Hoyer, R. L. Z.; Bailie, C. D.; Leijtens, T.; Peters, I. M.; Minichetti, M. C.; Rolston, N.; Prasanna, R.; Sofia, S.; Harwood, D.; Ma, W.; Moghadam, F.; Snaith, H. J.; Buonassisi, T.; Holman, Z. C.; Bent, S. F.; McGehee, M. D. 23.6%-Efficient Monolithic Perovskite/Silicon Tandem Solar Cells with Improved Stability. *Nat. Energy* 2017, 2, 17009.
- (188) Choudhury, D.; Rajaraman, G.; Sarkar, S. K. Self Limiting Atomic Layer Deposition of Al₂O₃ on Perovskite Surfaces: A Reality? *Nanoscale* 2016, 8, 7459.
- (189) Zardetto, V.; Williams, B. L.; Perrotta, A.; Di Giacomo, F.; Verheijen, M. A.; Andriessen, R.; Kessels, W. M. M.; Creatore, M. Atomic Layer Deposition for Perovskite Solar Cells: Research Status, Opportunities and Challenges. *Sustainable Energy Fuels* 2017, 1, 30.
- (190) Zhu, Z.; Hadjiev, V. G.; Rong, Y.; Guo, R.; Cao, B.; Tang, Z.; Qin, F.; Li, Y.; Wang, Y.; Hao, F.; Venkatesan, S.; Li, W.; Baldelli, S.; Guloy, A. M.; Fang, H.; Hu, Y.; Yao, Y.; Wang, Z.; Bao, J. Interaction of Organic Cation with Water Molecule in Perovskite MAPbI₃: From Dynamic Orientational Disorder to Hydrogen Bonding. *Chem. Mater.* 2016, 28, 7385.
- (191) Hultqvist, A.; Aitola, K.; Sveinbjörnsson, K.; Saki, Z.; Larsson, F.; Törndahl, T.; Johansson, E.; Boschloo, G.; Edoff, M. Atomic Layer Deposition of Electron Selective SnO_x and ZnO Films on Mixed Halide Perovskite: Compatibility and Performance. *ACS Appl. Mater. Interfaces* 2017, 9, 29707.
- (192) Hoyer, R. L. Z.; Chua, M. R.; Musselman, K. P.; Li, G.; Lai, M. L.; Tan, Z. K.; Greenham, N. C.; MacManus-Driscoll, J. L.; Friend, R. H.; Credgington, D. Enhanced Performance in Fluorene-Free Organometal Halide Perovskite Light-Emitting Diodes using Tunable, Low Electron Affinity Oxide Electron Injectors. *Adv. Mater.* 2015, 27, 1414.
- (193) Nagabhushana, G. P.; Shivaramaiah, R.; Navrotsky, A. Direct Calorimetric Verification of Thermodynamic Instability of Lead Halide Hybrid Perovskites. *Proc. Natl. Acad. Sci. U.S.A.* 2016, 113, 7717.

- (194) Yu, X.; Qin, Y.; Peng, Q. Probe Decomposition of Methylammonium Lead Iodide Perovskite in N₂ and O₂ by in Situ Infrared Spectroscopy. *J. Phys. Chem. A* 2017, 121, 1169.
- (195) Yu, X.; Yan, H.; Peng, Q. Reaction between Pyridine and CH₃NH₃PbI₃: Surface-Confined Reaction or Bulk Transformation? *J. Phys. Chem. A* 2017, 121, 6755.
- (196) Yoo, S.; Kum, J.; Cho, S. Tuning the Electronic Band Structure of PCBM by Electron Irradiation. *Nanoscale Res. Lett.* 2011, 6, 545.
- (197) Chang, C. Y.; Lee, K. T.; Huang, W. K.; Siao, H. Y.; Chang, Y. C. High-Performance, Air-Stable, Low-Temperature Processed Semitransparent Perovskite Solar Cells Enabled by Atomic Layer Deposition. *Chem. Mater.* 2015, 27, 5122.
- (198) Ye, X.; Kestell, J.; Kisslinger, K.; Liu, M.; Grubbs, R. B.; Boscoboinik, J. A.; Nam, C. Y. Effects of Residual Solvent Molecules Facilitating the Infiltration Synthesis of ZnO in a Nonreactive Polymer. *Chem. Mater.* 2017, 29, 4535.
- (199) Parsons, G. N.; Atanasov, S. E.; Dandley, E. C.; Devine, C. K.; Gong, B.; Jur, J. S.; Lee, K.; Oldham, C. J.; Peng, Q.; Spagnola, J. C.; Williams, P. S. Mechanisms and Reactions during Atomic Layer Deposition on Polymers. *Coord. Chem. Rev.* 2013, 257, 3323.
- (200) Peng, Q.; Tseng, Y. C.; Darling, S. B.; Elam, J. W. Nanoscopic Patterned Materials with Tunable Dimensions via Atomic Layer Deposition on Block Copolymers. *Adv. Mater.* 2010, 22, 5129.
- (201) Biswas, M.; Libera, J. A.; Darling, S. B.; Elam, J. W. New Insight into the Mechanism of Sequential Infiltration Synthesis from Infrared Spectroscopy. *Chem. Mater.* 2014, 26, 6135.
- (202) Gong, B.; Parsons, G. N. Quantitative in situ infrared analysis of reactions between trimethylaluminum and polymers during Al₂O₃ atomic layer deposition. *J. Mater. Chem.* 2012, 22, 15672.
- (203) Goldstein, D. N.; McCormick, J. A.; George, S. M. Al₂O₃ Atomic Layer Deposition with Trimethylaluminum and Ozone Studied by in Situ Transmission FTIR Spectroscopy and Quadrupole Mass Spectrometry. *J. Phys. Chem. C* 2008, 112, 19530.
- (204) Kot, M.; Das, C.; Wang, Z.; Henkel, K.; Rouissi, Z.; Wojciechowski, K.; Snaith, H. J.; Schmeisser, D. Room-Temperature Atomic Layer Deposition of Al₂O₃: Impact on Efficiency, Stability and Surface Properties in Perovskite Solar Cells. *ChemSusChem* 2016, 9, 3401.
- (205) Thimsen, E.; Johnson, M.; Zhang, X.; Wagner, A. J.; Mkhoyan, K. A.; Kortshagen, U. R.; Aydil, E. S. High Electron Mobility in Thin Films Formed via Supersonic Impact Deposition of Nanocrystals Synthesized in Nonthermal Plasmas. *Nat. Commun.* 2014, 5, 5822.

- (206) Berhe, T. A.; Su, W. N.; Chen, C. H.; Pan, C. J.; Cheng, J. H.; Chen, H. M.; Tsai, M. C.; Chen, L. Y.; Dubale, A. A.; Hwang, B. J. Organometal Halide Perovskite Solar Cells: Degradation and Stability. *Energy Environ. Sci.* 2016, 9, 323.
- (207) Wang, Z.; Shi, Z.; Li, T.; Chen, Y.; Huang, W. Stability of Perovskite Solar Cells: A Prospective on the Substitution of the A Cation and X Anion. *Angew. Chem., Int. Ed.* 2017, 56, 1190.
- (208) Dirin, D. N.; Protesescu, L.; Trummer, D.; Kochetygov, I. V.; Yakunin, S.; Krumeich, F.; Stadie, N. P.; Kovalenko, M. V. Harnessing Defect-Tolerance at the Nanoscale: Highly Luminescent Lead Halide Perovskite Nanocrystals in Mesoporous Silica Matrixes. *Nano Letters* 2016, 16, 5866-5874.
- (209) Levchuk, I.; Osvet, A.; Tang, X.; Brandl, M.; Perea, J. D.; Hoegl, F.; Matt, G. J.; Hock, R.; Batentschuk, M.; Brabec, C. J. Brightly Luminescent and Color-Tunable Formamidinium Lead Halide Perovskite FAPbX₃ (X = Cl, Br, I) Colloidal Nanocrystals. *Nano Letters* 2017, 17, 2765-2770.
- (210) Protesescu, L.; Yakunin, S.; Bodnarchuk, M. I.; Krieg, F.; Caputo, R.; Hendon, C. H.; Yang, R. X.; Walsh, A.; Kovalenko, M. V. Nanocrystals of Cesium Lead Halide Perovskites (CsPbX₃, X = Cl, Br, and I): Novel Optoelectronic Materials Showing Bright Emission with Wide Color Gamut. *Nano Letters* 2015, 15, 3692-3696.
- (211) Fu, M.; Tamarat, P.; Trebbia, J.-B.; Bodnarchuk, M. I.; Kovalenko, M. V.; Even, J.; Lounis, B. Unraveling exciton-phonon coupling in individual FAPbI₃ nanocrystals emitting near-infrared single photons. *Nature Communications* 2018, 9, 3318.
- (212) Kovalenko, M. V.; Protesescu, L.; Bodnarchuk, M. I. Properties and potential optoelectronic applications of lead halide perovskite nanocrystals. *Science* 2017, 358, 745-750.
- (213) Demchyshyn, S.; Roemer, J. M.; Groß, H.; Heilbrunner, H.; Ulbricht, C.; Apaydin, D.; Böhm, A.; Rütt, U.; Bertram, F.; Hesser, G.; Scharber, M. C.; Sariciftci, N. S.; Nickel, B.; Bauer, S.; Głowacki, E. D.; Kaltenbrunner, M. Confining metal-halide perovskites in nanoporous thin films. *Science Advances* 2017, 3.
- (214) Li, X.; Cao, F.; Yu, D.; Chen, J.; Sun, Z.; Shen, Y.; Zhu, Y.; Wang, L.; Wei, Y.; Wu, Y.; Zeng, H. All Inorganic Halide Perovskites Nanosystem: Synthesis, Structural Features, Optical Properties and Optoelectronic Applications. *Small* 2017, 13, 1603996.

APPENDIX: LIST OF PUBLISHED, SUBMITTED, AND UNDER-PREPARATION PAPERS

Yu, X. Z.; Qin, Y.; Peng, Q. Probe Decomposition of Methylammonium Lead Iodide Perovskite in N₂ and O₂ by in Situ Infrared Spectroscopy. *J. Phys. Chem. A* 2017, 121, 1169-1174.

Yu, X. Z.; Yan, H. M.; Peng, Q. Reaction between Pyridine and CH₃NH₃PbI₃: Surface-Confined Reaction or Bulk Transformation? *J. Phys. Chem. A* 2017, 121, 6755-6765.

Yu, X. Z.; Yan, H. M.; Peng, Q. Improve the Stability of Hybrid Halide Perovskite via Atomic Layer Deposition on Activated Phenyl-C-61 Butyric Acid Methyl Ester. *ACS Appl. Mater. Interfaces* 2018, 10, 28948-28954.

Yu, X. Z.; Yan, H. M.; Peng, Q. Reaction Temperature and Partial Pressure Induced Etching of Methylammonium Lead Iodide Perovskite by Tri-methyl Aluminum. *Langmuir*, in revision 2019

Yu, X. Z.; Yan, H. M.; Peng, Q. Self-Limited Surface Reaction Stable Coordination between Strong Lewis Acid Trimethyl Aluminum and Formamidinium Lead Iodide Perovskite. in preparation